

Development of an Injectable Hybrid-Hydrogel using Oxidised-Alginate and N-Succinyl-Chitosan

by

Allan Rogalsky

A thesis
presented to the University of Waterloo
in fulfilment of the
thesis requirement for the degree of
Doctor of Philosophy
in
Mechanical and Mechatronics Engineering
(Nanotechnology)

Waterloo, Ontario, Canada

© Allan Rogalsky 2016

I hereby declare that I am the sole author of this thesis. This is a true copy of the thesis, including any required final revisions, as accepted by my examiners.

I understand that my thesis may be made electronically available to the public.

Abstract

A new oxidised-alginate / N-succinyl-chitosan hydrogel system with potential biomedical applications has been explored for precursor solution viscosities within the injectable range ($< \sim 0.2$ Pa·s). When fully developed, its advantages may include: 1) good mechanical properties due to covalent crosslinking; 2) increased degrees-of-freedom to tailor properties and unique stress strain response due to the hybrid structure; 3) suitability for cell encapsulation / use as an injectable gel due to biocompatibility / mild formation conditions; and 4) excellent adoptability due to readily available and low cost raw ingredients.

The current work is focused on two initial studies of the system: 1) development of hybrid hydrogel compositions to meet target viscosity and stiffness ranges that are appropriate for common hydrogel applications, and 2) development and validation of models to predict hydrogel swelling and stiffness behaviour.

As gel systems become more complex, predictive tools are crucial for more focused development work so that end users can tailor gel systems to their precise requirements. In this work, we have undertaken the development and/or advancement of three predictive models: 1) advancing current swelling models to apply to hybrid systems containing polyampholytes; 2) refining membrane osmometry models to handle polyampholytes and to incorporate modern corrections for non-ideal solutions; and 3) proposing a new stiffness model for hybrid gel systems. These models were verified using a comprehensive experimental program for which new experimental equipment was custom-designed and built.

To form the new gels, limit-oxidized alginate ($\sim 45\%$ repeat units modified) and six N-succinyl-chitosans (22 to 52% primary amine substitution) were synthesized from commercially available polymer. Solutions were prepared using phosphate buffered saline. A viscosity guideline of < 0.2 Pa·s was obtained from the injectability literature. This was easily met by oxidized-alginate solutions. N-succinyl-chitosan was limited to five substitutions (22 to 48%), with respective concentrations between 4.8 and 2.0 w/w%. Gels were formed by blending alginate and chitosan solutions at five different ratios (2:1 to 1:9). Gel stiffness was characterized in the ‘as cast’ state by compression testing. Swelling was characterized in phosphate buffered saline.

Our results showed that the stiffness model provided a good fit (largest p-value < 0.03). From the model it was found that limit-oxidized-alginate is 16 times less stiff than N-succinyl-chitosan. This combined with the restricted injectable concentration range resulted in a maximum stiffness of 7 kPa, which is below the target window for muscle tissue (i.e. between 10 to 30 kPa). To simultaneously achieve both targets further investigation is recommended using higher concentrations of lower molecular weight chitosan or stiffer oxidized polysaccharides. For N-succinyl-chitosan, the membrane osmometry model gave an excellent fit (largest p-value $\sim 10^{-7}$). A key finding was that the Manning-Oosawa model for ion condensation does not accurately predict behaviour. The relatively fast rate of oxidized-alginate degradation prevented osmometry from being used to collect empirical ion condensation data. Without this data, classical swelling theory could not adequately

predict experimental response. In future work, conductivity experiments are recommended to characterize ion condensation. Recent models by Trizac and O'Shaughnessy are recommended as improvements to the swelling theory.

The primary scientific contributions from this work are: 1) the first systematic characterization of the stiffness and swelling of injectable oxidised-alginate / N-succinyl-chitosan hydrogels; 2) the first analysis of polyampholyte ion condensation by membrane osmometry since the advent of modern ion activity models in the early 1990's; 3) the aforementioned advancement of osmometry and swelling theory; and 4) the proposal and successful experimental verification of a new model for hybrid gel stiffness.

In addition, a number of other contributions were also made, mainly: 1) a membrane osmometer was designed and built to characterize small samples of polyelectrolytes at elevated temperature and in concentrated chloride solutions, 2) N-succinylation was found to fit a log-linear empirical correlation with respect to input reagent concentrations; 3) a small increase in chitosan moisture affinity and thermal stability was observed with increasing N-succinyl substitution; 4) anomalous phase separation and rheological behaviour was observed in N-succinyl-chitosan solutions near the solubility limit; and 5) polyampholyte solution rheology was found to scale differently than that of polyelectrolytes.

Although the stiffness is below what was anticipated, the oxidised-alginate / N-succinyl-chitosan hydrogel system shows good potential. Provided the stiffness limitation can be overcome, the existence of high strain 'secondary stiffness' behaviour provides the potential for a much closer match to the non-linear elastic response of muscle tissue than is currently possible with single component systems. In addition, interesting phase behaviour near the N-succinyl-chitosan solubility limit may allow independent control of pore size and stiffness via a heterogeneous structure.

Acknowledgements

I would like to thank my advisers Dr. Pearl Sullivan and Dr. HJ Kown for their technical advice and financial assistance.

I acknowledge my Co-op Research Assistants: Mr. Ho Jae Cheang, Mr. Alex Vasile, and Mr. Anthony Silvaroli for their hard work and attention to detail while conducting routine experiments. Each in their own way went above and beyond the call of duty to save experiments and maintain ambitious testing schedules under less than ideal conditions.

I would like to thank my co-worker Mr. Geoff Rivers for providing a sceptical wall to bounce ideas off of.

I would like to thank Dr. Ariel Chan for her input on the presentation of chemical characterization results.

I would like to thank Ms. Marzieh Riahi (Dr. Neil McManus's Lab, Chemical Engineering, University of Waterloo) for characterizing the molecular weight of my polyvinyl alcohol validation sample using gel permeation chromatography.

I would like to thank Ms. Jan Venne (Department of Chemistry Nuclear Magnetic Resonance Technician) for running my NMR experiments.

I would like to thank Dr. Johan Wiklund (Dr. Roland Hall's Lab, Department of Biology, University of Waterloo) for help freeze drying my modified polymers.

I would like to thank Mr. Rick Forgett and the staff of the University of Waterloo Engineering Machine Shop for their training and advice on the manufacture of machined components.

I would like to thank my wife Christine Rogalsky for her perseverance through my long hours in the lab and her assistance proof reading and copy editing this manuscript.

I would also like to thank my father David Rogalsky for his final copy edit of this text.

Dedication

I dedicate this work to my family, in particular my daughter Tabitha who saw much less of her daddy than she would have liked during the writing process.

Table of Contents

List of Tables	xiv
List of Figures	xvi
Nomenclature	xviii
1 Introduction and Background	1
1.1 Motivation for Work	1
1.2 Project Outline and Scope	2
1.3 Proposed System Background	3
1.3.1 Polymer Type	4
1.3.2 Crosslink Type	6
1.3.3 Network Architecture - Relationships Between Stiffness Swelling and Pore Size	6
1.3.4 Required Model Parameters to Predict Swelling	7
1.3.5 Review of Related Systems	9
1.4 Application Literature Review	12
1.4.1 Injectability / Suitability for 3D Construct Casting	12
1.4.2 In Situ Biocompatibility and Degradation	14
1.4.3 Stiffness	16
1.4.4 Porosity and Swelling	16
1.4.5 Commercial Potential	17
1.5 Concluding Remarks	18

2	Models for Polyampholite Solutions and Gels	19
2.1	Overview	19
2.2	Gel Swelling and Membrane Osmometry	20
2.2.1	System Description and Balance Equations	20
2.2.2	Model Usage	22
2.3	Gel Stiffness - Theory of Rubber Elasticity	23
2.4	Polymer Solution Models	26
2.4.1	Osmotic Pressure - van't Hoff equation	26
2.4.2	Polymer Solution Mixing - Flory-Huggins Theory	28
2.4.3	Intra-chain Coulomb Potential	29
2.4.4	Solution Nonideality - Debye-Hückel and Pitzer	30
2.4.5	Counterion Condensation - Manning-Oosawa Theory	34
2.4.6	Weak Electrolyte Ionization Equilibrium	35
2.4.7	Gibbs-Donnan Equilibrium - Ion Partition due to Charged Polymers	37
2.4.8	Concentration Unit Conversions	39
2.5	Linearised Model Derivation for Membrane Osmometry	40
2.5.1	Salt Effects in Linearised Flory-Huggins Theory	41
2.5.2	Linear Donnan theory for Membrane Osmometry	42
2.5.3	Assembly as a Regression Model	44
2.5.4	Discussion	45
2.6	Numerical Simulations	46
2.6.1	Reference Solution Model	46
2.6.2	Polymer Ionization Model	47
2.6.3	Membrane Osmometry Monte Carlo Simulation	50
2.7	Concluding Remarks	55
3	Polymer Modification	56
3.1	Overview	56
3.2	Background	56
3.2.1	Chitosan Succinylation	56

3.2.2	Alginate Oxidation	58
3.2.3	Characterization by H-NMR	59
3.2.4	Salt Substitution by TGA	60
3.2.5	Moisture Content via Vacuum Drying	61
3.3	Materials and Methods	62
3.3.1	Materials	62
3.3.2	Chitosan Succinylation	62
3.3.3	Alginate Oxidation	63
3.3.4	Characterization by H-NMR	65
3.3.5	Salt Substitution by TGA	65
3.3.6	Moisture Content via Vacuum Drying	67
3.4	Results and Discussion	68
3.4.1	Polymer Modification	68
3.4.2	Salt Substitution	70
3.4.3	Moisture Content	71
3.4.4	Polymer Stability	71
3.5	Concluding Remarks	72
4	N-Succinyl-Chitosan Solution Rheology	73
4.1	Overview	73
4.2	Background	74
4.2.1	Polymer Solution Rheology	74
4.2.2	Injectability Evaluation	75
4.2.3	Instrument Selection and Operating Principals	75
4.3	Experimental	77
4.3.1	Experiment Design	77
4.3.2	Capillary Rheometer Description	78
4.3.3	Assumption and Safety Checks	81
4.3.4	Experimental Methods and Data Analysis	82
4.3.5	Chitosan Solution Preparation	83
4.4	Results and Discussion	84

5	Membrane Osmometer: Design and Validation	88
5.1	Overview	88
5.2	Background	88
5.2.1	Alternatives to In-House Fabrication	88
5.2.2	Design Constraints and Criteria	89
5.2.3	Membrane Osmometer Design Review	89
5.3	Initial Design - Fuoss-Mead Variant	91
5.3.1	Introduction	91
5.3.2	Design Description	91
5.3.3	Performance	93
5.4	Transducer Osmometer Design - Hansen Variant	94
5.4.1	Introduction	94
5.4.2	Core Design	94
5.4.3	Thermal Isolation and Stability	97
5.4.4	Membrane Hydraulic Conductivity	100
5.4.5	Final Cost and Performance	101
5.5	Setup and Operating Procedure	102
5.5.1	Setup	102
5.5.2	Solution Degas	103
5.5.3	Operation	104
5.6	Design Validation	105
5.6.1	Overview	105
5.6.2	PVA Property Estimates	106
5.6.3	Experimental Method	106
5.6.4	Validation Results	107
5.7	Concluding Remarks	107

6	Membrane Osmometry Experiments	109
6.1	Overview	109
6.2	Theory Background	109
6.2.1	Why Membrane Osmometry?	109
6.2.2	Osmometry Theory	110
6.3	Osmometer Experiments	113
6.3.1	Experimental Design	113
6.3.2	Materials	114
6.3.3	Buffer Solutions	114
6.3.4	Oxidised-Alginate Solution Preparation	115
6.3.5	N-Succinyl-Chitosan Solution Preparation	116
6.3.6	Final Sample Preparation	116
6.3.7	Membrane Osmometry	116
6.4	Results and Discussion	117
6.4.1	Oxidised-Alginate	117
6.4.2	N-Succinyl-Chitosan	117
6.5	Concluding Remarks	121
7	Gel Characterization: Swelling and Compression	123
7.1	Overview	123
7.2	Background	124
7.2.1	N-Succinyl-Chitosan / Oxidised-Alginate Hybrid Gels	124
7.2.2	Project Scope and Limitations	127
7.2.3	Theory for Gel Stiffness	128
7.2.4	Theory of Gel Swelling	129
7.3	Model Derivations	129
7.3.1	Hybrid Gel Elasticity	129
7.3.2	Network Functionality for Crosslinking Estimation	131
7.4	Simulation: Swelling Equilibrium	132
7.5	Experimental	134

7.5.1	Preliminary Experiments	134
7.5.2	Combined Study Plan	135
7.5.3	Materials	136
7.5.4	Sample Preparation	136
7.5.5	Compression Methodology	139
7.5.6	Swelling Methodology	140
7.6	Results and Discussion	140
7.6.1	Stress Strain Curves	140
7.6.2	Hybrid Gel Stiffness Model	142
7.6.3	Gel Failure Analysis	148
7.6.4	Equilibrium Swelling	148
7.6.5	Gel Appropriateness for Tissue Engineering Application	151
7.7	Concluding Remarks	152
8	Conclusions and Recommendations	153
8.1	Primary Scientific Contributions	153
8.2	Other Contributions	154
8.3	Recommendations for Future Work	155
	APPENDICES	156
A	Rheometer Design	157
A.1	Overview	157
A.2	Operating Procedure	157
A.3	Detail Design and Assembly	160
A.3.1	Design Tree	160
A.3.2	Engineering Drawings	160
B	Initial Osmometer Design	177
B.1	Overview	177
B.2	Design 4.0 - Drawings for Shop Quote	177
B.3	Design 4.2 - Changes For First Part Manufacture	194

B.4	Design 5.2 - Capillary Seating	198
B.5	Design 8.0 - Cast Silicone Gaskets	206
B.6	Design 9.0 - Glass Reference Snorkel	212
C	Transducer Osmometer Design	217
C.1	Top Level Assemblies	217
C.2	Core Design	220
C.3	Transducer Well	226
C.4	Thermal Isolation Spacer	231
C.5	Water Bath Components	237
C.6	Miscellaneous Tools	246
C.7	Solution Degassing	251
C.8	Detailed Setup Procedure	252
	References	254

List of Tables

1.1	Parameters Required to Predict Swelling	8
1.2	Literature Estimates for Alginate and Chitosan Model Parameters	10
1.3	Chitosan / Oxidised-Polysaccharide and Related Gels	11
1.4	Background Recommendations for Tissue Engineering Applications	13
1.5	Research Grade Polymer Cost	17
2.1	Models for Gel Swelling and Membrane Osmometry	21
2.2	Pitzer Interaction Parameters for Oppositely Charged Pairs	32
2.3	Pitzer Interaction Parameters for Like Pairs	32
2.4	Ionization Correlation Parameters for Phosphate Buffers	36
2.5	Density Estimation Parameters for Phosphate Buffered Saline	41
3.1	Chitosan ¹ H-NMR Spectrum Description	60
3.2	Chitosan and N-Succinyl-Chitosan ¹ H-NMR Peak Assignment	60
3.3	Chitosan Properties by Batch	63
3.4	Alginate Properties by Batch	64
4.1	Rheometry Study Statistical Design	78
4.2	Pressurised Rheometer Components	80
4.3	Viscosity Model Parameters and Regression Coefficients	86
4.4	Chitosan Solution Concentrations for Target Viscosity	87
5.1	Estimated Influence of Temperature Stability on Osmometer Baseline	101
5.2	Polyvinyl Alcohol Model Parameters	105
6.1	Osmometry Regression Model	111

6.2	Planned Model Inputs and Outputs	112
6.3	Osmometry Study Statistical Design	113
6.4	Chitosan Osmometry Results	119
7.1	Polymer Concentration used with each Chitosan	135
7.2	Blend Ratio Study Block	135
7.3	Typical Gel Experiment Schedule	137
7.3	Typical Gel Experiment Schedule	138

List of Figures

1.1	Thesis Overview	3
1.2	Alginate Structure	4
1.3	Chitosan repeat units	5
1.4	Crosslinking Reaction Scheme	5
1.5	Hydrogel Network Architectures	7
1.6	Common Hydrogel Polymers	18
2.1	Swelling and Osmometry System Schematic	20
2.2	Phosphate Species Present as a Function of pH	47
2.3	Pitzer Model Results	48
2.4	Ionization Model Results	51
2.5	Osmometer Statistical Design Selection	52
2.6	Effect of Replicates on Osmometer Resolution	52
2.7	Osmometer Polymer Concentration Selection	53
2.8	Model Predictions for Osmometer Ionic Strength Range	54
3.1	Chitosan Chemical Structure	57
3.2	Alginate Chemical Structure	58
3.3	Alginate NMR Results	66
3.4	Chitosan NMR Results	66
3.5	Chitosan TGA Results	67
3.6	Chitosan N-Succinylation Calibration Curve	69
3.7	Modification effect on Moisture Removal and Degradation Temperatures	71
4.1	Capillary Rheometer Schematic	79

4.2	Capillary Rheometer Core Detail	80
4.3	Rheometer Calibration Record	83
4.4	N-Succinyl-Chitosan Apparent Viscosity	85
5.1	Osmometer Initial Design	92
5.2	Transducer Osmometer Core Design	95
5.3	Initial Transducer Osmometer Temperature Control	98
5.4	Osmometer Thermal Lag	98
5.5	Improved Isolation and Temperature Control	99
5.6	Osmometer Setup Timeline	102
5.7	PVA Osmometry Results	107
6.1	Membrane Osmometry System Model	110
6.2	Alginate Degradation Time Series	117
6.3	Chitosan Osmometry Results: 21% Amine Substitution Polymer	118
6.4	Chitosan Osmometry Results: 34% Amine Substitution Polymer	119
7.1	Gel Formation Summary	125
7.2	Network Structure Schematic	126
7.3	Swelling and Compression Sample Moulding	139
7.4	Uniaxial Model Comparison	141
7.5	Elastic Modulus Results	142
7.6	Compression Curve Shape by Blend Ratio	143
7.7	Compression Curve Shape by Chitosan Modification	144
7.8	Elasticity model test	145
7.9	Elasticity model anomalous composition	146
7.10	Network Chain Stiffness Ratios	146
7.11	Polymer specific Elasticity Fit Constants	147
7.12	Gel Crosslinking Estimates	148
7.13	Compression Sample Failure Modes	149
7.14	Swelling Sample Optimization	149
7.15	Equilibrium Swelling Ratios	150

Nomenclature

α	fractional dissociation, positive polymeric ion
\bar{V}	partial molar volume
\bar{v}	partial specific volume
β	fractional dissociation, negative polymeric ion
χ_{ab}	Flory-Huggins interaction parameter: typically solvent takes subscript 1 and polymer(s) are numbered from 2 to n+1 for an n polymer system
$\Delta\mu_{a,b}$	change in chemical potential relative to standard reference state: subscript a defines the component of the mixture, subscript b provides the cause of the change
e	elementary electrical charge, $1.602\ 176\ 565(35) \times 10^{-19}\ C$ [1]
κ^{-1}	Debye length
λ	stretch ratio - rubber elasticity theory
λ_B	Bjerrum length
ν	mean number of negative charged groups on polymer molecule - Katchalsky theory
ν_e	number of crosslinks - rubber elasticity theory
Φ	volume fraction
ϕ	osmotic coefficient - ionic solution theory
ϕ_n	network functionality - rubber elasticity theory
Π	osmotic pressure
ρ_i^*	mass per volume concentration: subscript i indicates component of mixture
σ	true stress

ε	logarithmic strain
ε_0	permittivity of free space, $8.854\ 187\ 817 \times 10^{-12} \text{ Fm}^{-1}$ [1]
ε_r	relative dielectric constant of solvent
ξ	polymeric non-dimensional inverse charge density - Manning-Oosawa theory
ζ	mean number of positive charged groups on polymer molecule - Katchalsky theory
A_2	osmotic second virial coefficient
a_i	chemical activity: subscript i indicates component of mixture
c_i	molar concentration
f_ξ	Manning fraction
I	ionic strength
i	average monomer ionization
k_B	Boltzman constant, $1.380\ 6488(13) \times 10^{-23} \text{ JK}^{-1}$ [1]
m_i	molal concentration
M_n	number average molecular weight
M_w	weight average molecular weight
N_A	Avogadro constant, $6.022\ 141\ 29(27) \times 10^{23} \text{ mol}^{-1}$ [1]
pK_i	\log_{10} acid equilibrium constant: $(i = \alpha)$ low molecular weight compounds, $(i = \beta)$ negative polymeric functional groups and $(i = \beta)$ positive polymeric functional groups. For polymers, pK'_i is the apparent constant under experimental conditions. Without the prime it is the intrinsic constant which is roughly equivalent to the disassociation constant of the monomeric species.
Q	equilibrium swelling ratio
R	molar gas constant, $8.314\ 4621(75) \text{ Jmol}^{-1}\text{K}^{-1}$ [1]
T	temperature
x_i	mole fraction: subscript i indicates component of mixture
X_n	Number average degree of polymerization
z_i	charge on i^{th} ionic species

Chapter 1

Introduction and Background

1.1 Motivation for Work

Hydrogels consist of polymer networks swollen with water. In pharmaceutical science, injectable hydrogels provide sustained drug delivery to a physically limited target area [2], e.g. the cavity left after tumour removal, reducing both dosage and systemic toxicity [3]. For tissue engineering the similarities of hydrogels to natural cell supports make hydrogels ideal scaffold materials for developing tissue constructs such as replacement organs [2–5]. In both applications, the gels start with well defined properties tuned to the target environment, and then degrade at a well defined rate, disappearing when their purpose is served.

Both drug delivery and tissue engineering are multi-disciplinary fields. The end users (health care professionals), and developers (chemical engineers, chemists and biologists), are all dependent on each other for guidance outside of their own particular areas of expertise. An understanding of mechanical properties is not central to any of these disciplines yet has become important to further development work. The link between drug delivery and mechanical properties is not well understood. This may limit gel use in stressed locations, e.g. in and around joints [2]. In tissue engineering correct mechanical properties are particularly important as mechanical stimulation influences cell and tissue development [3, 4, 6, 7].

No single hydrogel system stands out as superior [2, 3, 5, 8]. Current trends include: 1) covalently crosslinked gels for better mechanical properties and usable life [2, 3, 7]; 2) hybrid gels, combining two or more polymers for more degrees of freedom to tailor properties [2, 9, 10]; and 3) injectable / castable systems to allow less intrusive delivery / cell encapsulation / formation of complex flow channels for 3D constructs [2, 8, 10–13]. Based on these trends we have explored the development of a hybrid gel composed of oxidised-alginate and N-succinyl-chitosan. An additional benefit is that both alginate and chitosan are inexpensive and readily available in sufficient quantities for widespread use.

In characterizing this material we seek to streamline efforts, by wherever possible, predicting properties from theoretical foundations. Much of the hydrogel literature is devoted to cataloguing gel performance using a phenomenological approach. This was useful for simple systems, however the phenomenological approach is running into decreasing returns. As system complexity increases (e.g. hybrid systems, attached pharmaceuticals or signalling molecules) it becomes impractical to adequately characterise all the permutations without predictive models. Swelling is one area that is often poorly characterised (See Section 1.4) and where predictive models exist [14–16].

1.2 Project Outline and Scope

As far as the author is aware, the oxidised-alginate and N-succinyl-chitosan system has yet to be developed. Our interest is to explore the development of a potential hybrid system that offers precursor solution viscosities within the injectable range of less than 0.2 Pa·s and stiffness values of at least 10 kPa. These target ranges are based on a review of common hydrogel applications as practical biomaterials. To initiate this development work, this thesis will build upon the existing swelling and stiffness models and wherever necessary, either refine them or offer new alternative models to predict property behaviour.

Membrane osmometry was selected to determine unknown model parameters for swelling prediction. This posed an enormous challenge as the technique fell out of favour in the early 1990's. Commercial instruments were unavailable making it necessary to build and validate an instrument in house. In addition, to analyse osmometry data it was necessary to assemble an updated model paralleling the approach that has been successful for gel swelling. A core component of this research study was to conduct membrane osmometry experiments to characterize, number average molecular weight, polymer/solvent interactions, and polyelectrolyte apparent ionization due to ion condensation. For stiffness characterization, uniaxial compression experiments were undertaken. To determine limiting concentrations for injectable formulations, additional rheological characterization was also necessary.

This thesis consists of eight chapters. Figure 1.1 provides a project overview. Modelling background, derivations and simulations are provided in Chapter 2. Modified polymer synthesis and characterization are found in Chapter 3. N-succinyl-chitosan solution rheology is investigated in Chapter 4, while membrane osmometer design and use are covered in Chapters 5 and 6. This provides the necessary background to answer the primary questions in Chapter 7. A summary of overall conclusions and recommendations is provided in Chapter 8. The remainder of the current chapter covers application and material specific background.

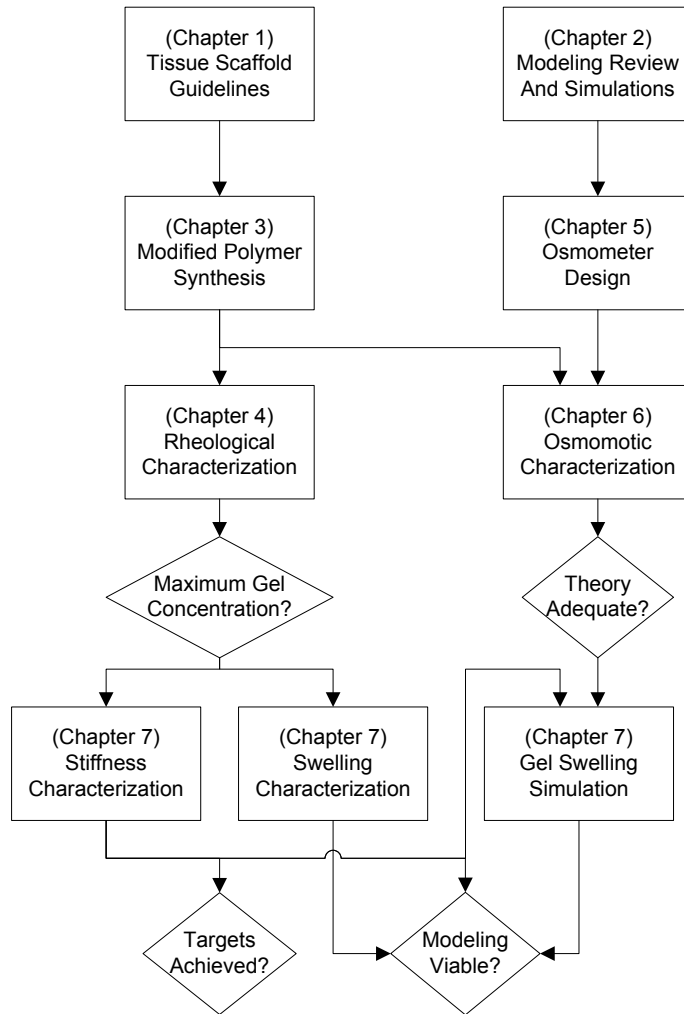


Figure 1.1: Thesis Overview

1.3 Proposed System Background

Hydrogels are weak elastic solids consisting of a volume spanning network and an aqueous sol phase. The network phase is generally the minor component (<5 w/w% is common). Good general reviews of polymeric hydrogels are provided by [17–19]. At this level of generalization it is possible to introduce three key physical proprieties, namely: 1) the gel elastic response primarily arises from the network; 2) the processability of precursor solutions is dominated by the contained polymer; and 3) gel construct dimensions are a strong function of solvent concentration (swelling). Swelling is controlled by a dynamic equilibrium between the network elastic response and the solution mixing physics. To identify related systems and gain insight into expected behaviour, further classification is required. Three categories are discussed, namely: 1) types of polymer, 2) network

crosslinking type, and 3) network architecture.

1.3.1 Polymer Type

Polymer type has a significant influence on the swelling behaviour of gels and the rheology of polymer solutions. Polymers must be hydrophilic to be soluble in water; however strong affinity for the solvent drives swelling. Water affinity is derived from polar groups. The most polar are charged polymers, which as a general class are called *polyelectrolytes*. These are further subdivided into simple polyelectrolytes, *polyampholytes* and *zwitterionic* polymers. Simple *anionic* or *cationic* polyelectrolytes carry only positive or negative charges, polyampholytes carry both positive and negative charges on the same polymer and zwitterionic polymers carry both positive and negative charges on the same monomer [20]. Correct classification is necessary when choosing model branches in later chapters. An important aspect of polyelectrolyte solution physics is the presence of oppositely charged *counterions*, which must be present to maintain overall electroneutrality.

Alginate is an anionic polysaccharide extracted from brown algae. It is a co-polymer of 1-4 linked β -D-mannuronic acid (M) and α -L-guluronic acid (G) residues (Figure 1.2). Long M and G blocks typically exist as well as alternating sequences [22, 23]. Both repeat units can be oxidised with sodium periodate. The resulting aldehyde functionality exists in equilibrium with hemiacetals formed with neighbouring repeat units [21] (Figure 1.2c and d). Similar to glucose this equilibrium is heavily biased towards the hemiacetal form.

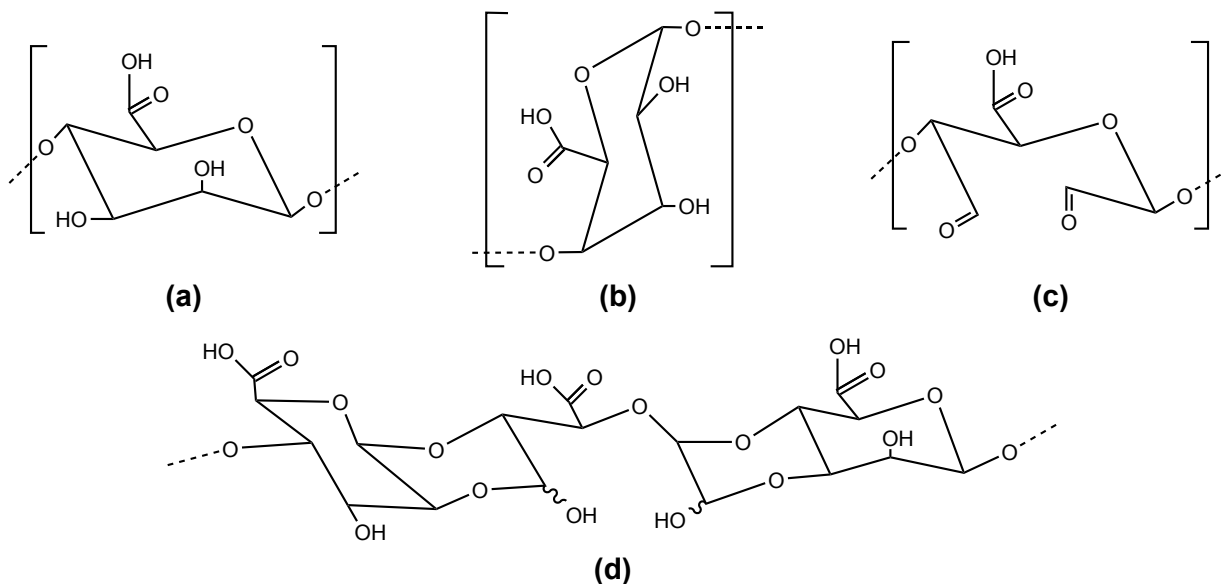


Figure 1.2: Alginate Structure; a) β -D-mannuronic acid (M), b) α -L-guluronic acid (G), c) oxidised M form, d) hemiacetal formed with neighbours. Adapted from [21].

Oxidation is limited to a maximum of 45% because rapidly forming hemiacetals shield adjacent repeat units against further attack [21]. Note that the oxidation reaction does not affect the charged moiety.

Chitosan is a cationic polyelectrolyte. It is unique among common polysaccharides in its amine functionality. Its primary repeat unit is 1-4 linked poly-D-glucosamine (Figure 1.3a). Chitosan is produced from the chitin in shrimp and crustacean shells by deacetylation, but almost always contains some residual acetylated repeat units [22] (Figure 1.3b). Chitosan is soluble in weak acids, but modification is necessary for solubility at physiological pH. In this work we use the ring opening polymerization reaction between succinic-anhydride and the chitosan amine to add carboxylic acid functionality (Figure 1.3c). The resultant N-succinyl-chitosan is a polyampholyte. The minimum succinylation extent for solubility is approximately 50% [24].

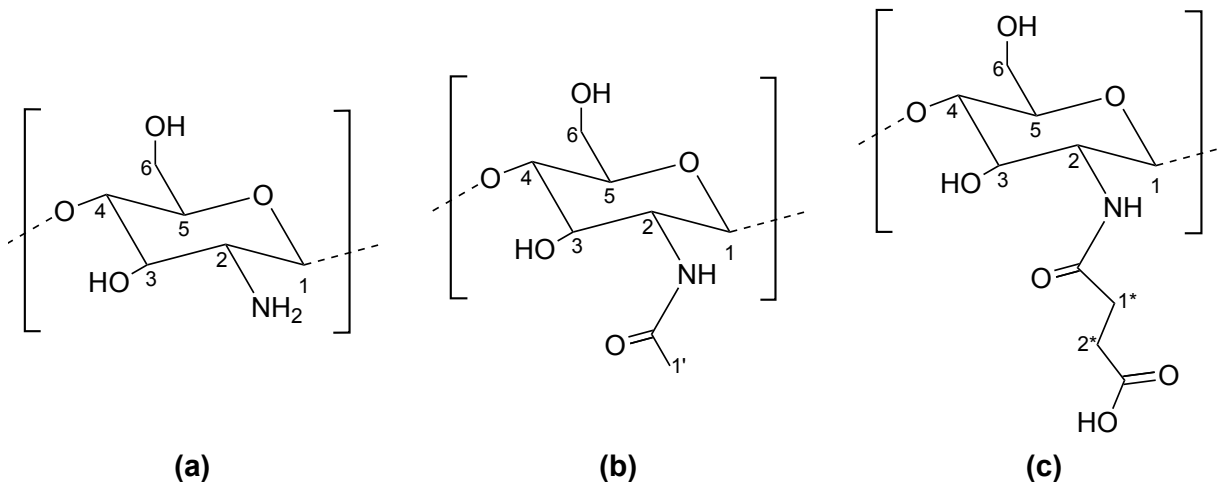


Figure 1.3: Chitosan repeat units; glucose-amine (a); acetylated (b); succinylated (c). Numbers beside carbons give H-NMR labelling convention

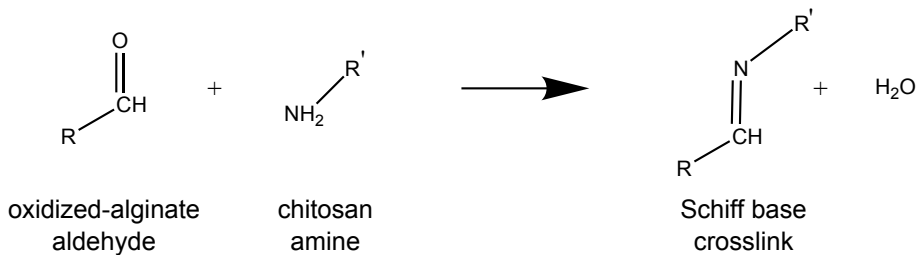


Figure 1.4: Crosslinking Reaction Scheme

1.3.2 Crosslink Type

A crosslink is a junction where three or more network chains join [19, 25, 26]. Crosslinks can be classified as chemical or physical in origin [17]. Physical crosslinks arise from ionic interactions, phase separation or conformational entanglements. These are generally sensitive to environmental factors resulting in rapid degradation and poor mechanical performance [2, 3, 7]. For this reason chemical crosslinking via covalent bonding has been recommended [2]. Oxidised-polysaccharide / chitosan systems, such as the one proposed, crosslink covalently using the Schiff base reaction (Figure 1.4) [27–33], following one of the preferred approaches for injectable gels [2, 34].

1.3.3 Network Architecture - Relationships Between Stiffness Swelling and Pore Size

In simple gels, network architecture is characterised by crosslink density, ν_e/V_o and the chain length between crosslinks, M_c [5, 19, 25, 35]. Though some independent control of these two parameters is possible, they are highly correlated resulting in effectively one degree of freedom for design [25]. For homogeneous networks, Equation 1.1 provides a scaling relationship between M_c and pore size, ξ [5, 19, 36]. Using the theory of rubber elasticity, a similar scaling relationship can be derived for stiffness (E' , Equation 1.2) [5, 18, 25]. The theory also predicts the stress-strain behaviour for simple gels, which is inherently less complex than those observed in natural tissues [7, 18, 25]. Swelling is only opposed by network stiffness, meaning for given polymer chemistry, degree of swelling (Q) will also be proportional to crosslink density [14, 19, 25]. Predictive theories for stiffness and swelling are discussed in greater detail in Chapter 2. The key point here is that the inability to independently vary gel physical properties means it is not possible to have a homogeneous single component gel with both a custom pore size and the desired stress-strain response.

$$\xi \propto Q^{1/3} M_c^{1/2} \quad (1.1)$$

$$E' \propto Q^{-1/3} M_c^{-1} \quad (1.2)$$

Multicomponent systems give more design degrees of freedom. Several different network architectures are depicted in Figure 1.5. Simple gels with a single polymer type have already been discussed. Gels with more than one polymer type are gaining popularity due to improved design degrees of freedom [37]. In this work we differentiate between multi-network gels (e.g. [37], Figure 1.5b) and hybrid-network gels (e.g. [9, 31, 33, 38, 39] 1.5c). Multi-network gels contain two or more interpenetrating networks which interact via physical entanglements, while hybrid-networks incorporate two or more distinct chain types forming the network analogue of a block co-polymer. The proposed alginate-chitosan material is of the latter type. Networks with distinct populations of chain lengths exhibit

increased toughness [25]. It is hypothesised that a similar mechanism may operate for hybrid networks with different chain stiffness's. This is discussed in much greater detail later, particularly Chapter 7 where results are interpreted in terms of a hybrid network structure.

Although homogeneous hybrid networks provide the potential to control the shape of the stress-strain curve and to improve toughness, they do not break the pore size / stiffness correlation. Using pore size theory provided by Chan [14] and stiffness relationships from Erman et al. [25] it can be shown that homogeneous oxidised-alginate / chitosan hydrogels with 10 to 30 kPa stiffness will have a pore size of less than 1 μm . This is outside the 2 to 100 μm range recommended for tissue scaffolds. Many techniques to improve porosity by introducing inhomogeneity have been developed [13]. One of the most promising approaches for injectable gels is the use of a gelatine based sacrificial porogen [13, 40]. A greatly desirable alternative is a thermodynamic approach which produces porosity through phase separation during crosslinking, e.g. [41]. This is preferable due to its simplicity of implementation once the right conditions have been found. The low solubility of chitosan and potential for control through N-succinylation suggests such a formulation might exist [2, 8, 11, 24].

1.3.4 Required Model Parameters to Predict Swelling

Published swelling models (e.g. [14–16, 26]), are covered in detail in Chapter 2. Swelling is driven by mixing and ionic potentials and opposed by the elastic potential. Equation 1.3 provides a simplified version of the equilibrium condition. Table 1.1 lists the respective material parameters that dominate each physics. Table 1.2 summarises the best available

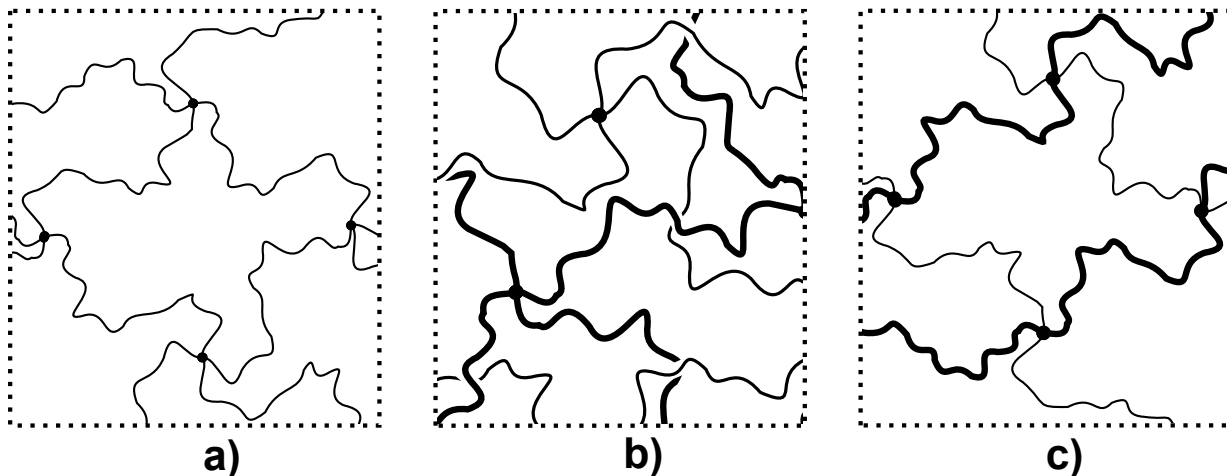


Figure 1.5: Hydrogel Network Architectures: a) Uniform-Network, b) Dual Network or Co-continuous, c) Hybrid-Network; Dots represent crosslinking points

Table 1.1: Parameters Required to Predict Swelling

Term	Parameter Group
Elastic	$E' \propto M_c^{-1} \propto (\nu_e/V_o)$
Mixing	$(\frac{1}{2} - \chi_{1,2}) \bar{v}^2 \propto A_2$
Ionic	$\gamma_f f_\xi i; \quad i = F(pK_\alpha, pK_\beta, 6h/h_0^2, l, r_{\min})$

estimates known to the author in the open literature. Enough data is available to plan experiments, but the available information is insufficient to expect quantitative agreement during modelling. As a result, three physical parameters have to be experimentally measured to verify the new models being developed in this work. These are the stiffness, E' , the osmotic second virial coefficient A_2 and the counterion condensation correction $\gamma_f f_\xi$. The later two are to be determined using membrane osmometry experiments.

$$\text{Elastic Potental} = \text{Mixing Potenal} + \text{Ionic Potential} \quad (1.3)$$

E' in the elastic term is the uniaxial zero deformation modulus. In the simplest theory it is proportional to the molecular weight between crosslinks M_c and crosslink density ν_e/V_o [25]. For the proposed system, polymer-polymer crosslinking makes prediction of crosslink density uncertain. Steric hindrance is expected to stop crosslinking after an unknown conversion. Parameters for the elastic term must therefore be determined independently for each gel.

Due their nature, mixing parameters must be for a specific solvent / polymer pair. The Flory-Huggins interaction parameter $\chi_{1,2}$ describes the affinity of the polymer for the solvent. As such it is expected to be the influential parameter when describing mixing physics [26, 42]. The partial specific volume \bar{v} is part of a correction for differences in solvent and monomer molar volumes. It includes information on mixing affinity via excluded volume affects; however these are second order when compared to the base affect of molecular size [43].

As can be seen in Table 1.2 literature values were only available for the unmodified polymers. These should be sufficient for modelling alginate, however those for chitosan are only suitable as a rough estimate for experiment planning. Because unmodified alginate is soluble under the required conditions (See Table 1.4), its parameters can be determined at the correct pH and ionic strength. Also, oxidation is not expected to have a significant affect on \bar{v} or $\chi_{1,2}$. The effect of oxidation on monomer molecular weight is very minor and a precedent exists for assuming $\chi_{1,2}$ is similar for both forms [44].

Chitosan modification has a significant effect on monomer molecular weight and polymer solubility. As such using $\chi_{1,2}$ values for unmodified chitosan is highly suspect and \bar{v}

estimates are likely to be low. Though both parameters can be determined via a number of experimental methods [26, 42, 43], membrane osmometry provides the potential to evaluate their combined contribution to swelling physics via a single experiment [26, 42, 45]. This is accomplished via the osmotic solubility parameter A_2 which also appears in swelling theory.

The ionic potential is dominated by the effective counterion concentration within charged polymer gels. $\gamma_f f_\xi$ corrects for counterions localised in the vicinity of the polymer chains due to the large net charge associated with polyelectrolytes. i is the average charge on a monomer and is proportional to the total number of counterions. Quantitative prediction of $\gamma_f f_\xi$ is still an open question. Rough published estimates are available for alginate [14]; however in the knowledge of the author estimates for N-succinyl-chitosan are not available in the open literature. Conductivity measurements and membrane osmometry are two known approaches to evaluate $\gamma_f f_\xi$ [46].

Quantitative estimation of i is possible. All the required parameters can be found in Table 1.2. Published alginate pK_α values indicate the polymer is almost fully dissociated in the pH range of interest, making i insensitive to the choice of model used for its prediction. Similar to alginate, the succinyl pK_α is far from the experimental range and therefore low resolution estimates are acceptable. The chitosan pK_β is close to the target pH range requiring that the relatively complex Katchalsky model be used [20, 47]. As the most influential parameters are independent of polymer modification they can be estimated from published data for unmodified chitosan.

1.3.5 Review of Related Systems

To predict the performance of the proposed system as an injectable gel / castable tissue scaffold, we look at oxidised-polysaccharide systems crosslinked via a Schiff base reaction. These are summarised in Table 1.3 and discussed relative to application guidelines in Section 1.4. This background study turned up two prior reports of network formation between oxidised-alginate and chitosan [48, 49]; however neither recognised the potential for injectability and both used extreme processing conditions incompatible with injectable formulations. The potential for an injectable formulation had been established by other authors using oxidised-hyaluronic acid [28] and oxidised-carboxymethyl-cellulose [29]; however to the best of our knowledge, our own study [31] represents the first report of an injectable / castable oxidised-alginate / chitosan system reported in the open literature. Since our initial report, the potential of the proposed system for the purposes of cell culture has been assessed by another group [50].

Table 1.2: Literature Estimates for Alginate and Chitosan Model Parameters

Symbol	Alginate	Chitosan	Units	Description
\bar{v}	0.45-0.49 ^a [51, 52]	0.57-0.58 ^b [51, 53]	cm ³ /g	Monomer Partial Specific Volume
$\chi_{1,2}$	0.233 ^c [14]	-0.01 ^d [54]	—	Polymer-Water Interaction Parameter
$\gamma_f f_\xi$	$\sim 0.4^a$ [14]	Unknown	—	Free Solution Charge Activity
pK_α	$\sim 3.52^e$ [55]	~ 4.65 [56, 57]	—	Negative Monomer Intrinsic Dissociation Constant
pK_β	—	6.13 ± 0.04^{fg}	—	Positive Monomer Intrinsic Dissociation Constant
$6h/h_0^2$	—	0.57 ± 0.12^{gh}	nm ⁻¹	Chain Extension Parameter ⁱ
l	0.515-0.53 ^j [14]	0.53 ^j	nm	Monomer Contour Length
r_{\min}	—	0.4[58]	nm	Ion Pair Average Centre Separation

^a Unmodified alginate

^b Unmodified chitosan

^c Unmodified alginate in water at physiological ionic strength

^d Unmodified chitosan in 0.3M aqueous acetic acid with and without 0.2M sodium acetate. Enthalpic contribution only, methodology suspect [59].

^e Average of 3.38 (M) and 3.65 (G) for unmodified alginate[55]. See Figure 1.2 for monomer types.

^r Average of 9 independent estimates obtained by fitting of Katchalsky ionization model (Section 2.4.6) to [60]. Error bars represent a 95% confidence interval on the average.

^t Estimate consistent with average apparent pKa value of 6.3 obtained by other authors [55, 56].

^h Contrary to expectations based on underlying form the estimate is largely independent of molecular weight.

ⁱ h is chain contour length. h_0 is rms end to end distance. Used in Katchalsky ionization model, Section 2.4.6 [61–63].

^j Distance between ether oxygen centres in the fully extended polymer. From a structural model based on simplified polysaccharide monomer geometry [26].

Table 1.3: Chitosan / Oxidised-Polysaccharide and Related Gels

Amine Polymer	Oxidised Polymer	Injec.	Cure	Stiff.	Swell.	Bio.	Degrad.	Ref.
adipic dihydrazide ^l	alginate	—	—	<i>hi</i>	Yes	—	Yes	[64–68]
poly(acrylamide-co-hydrazide)	alginate	Yes	—	<i>i</i>	Yes	—	Yes	[68]
hydrazide-hyaluronic-acid	methyl-cellulose	Yes	<i>j</i>	<i>g</i>	Yes	<i>c</i>	Yes	[69]
	carboxy-methyl-cellulose	Yes	<i>j</i>	<i>g</i>	Yes	<i>c</i>	Yes	[69]
	hydroxy-propyl-methyl-cellulose	Yes	<i>j</i>	<i>g</i>	Yes	<i>c</i>	Yes	[69]
	hyaluronic-acid	Yes	<i>j</i>	—	—	<i>c</i>	Yes	[70]
dexamethasone-hydrazide-hyaluronic-acid	hyaluronic-acid	Yes	<i>j</i>	<i>g</i>	yes	<i>c</i>	Yes	[71]
chitosan	alginate	—	—	—	Yes	<i>de</i>	Yes	[48, 49]
	sclerogucan	—	<i>k</i>	—	—	—	—	[27]
	starch	—	<i>k</i>	<i>g</i>	—	—	—	[30]
carboxymethyl-chitosan	alginate	Yes	<i>j</i>	—	Yes	<i>cdf</i>	—	[32, 72] ^b
N-succinyl-chitosan	alginate	Yes	<i>j</i>	<i>h</i>	—	<i>de</i>	—	[31] ^a [50] ^b
	RGD-peptide-alginate	Yes	—	—	—	<i>de</i>	—	[50] ^b
	carboxymethyl-cellulose	Yes	—	—	Yes	<i>d</i>	Yes	[29]
	hyaluronic-acid	Yes	<i>j</i>	<i>h</i>	Yes	<i>ef</i>	Yes	[28]
	starch	Yes	<i>j</i>	<i>g</i>	Yes	<i>e</i>	Yes	[33] ^b
dexamethasone-N-succinyl-chitosan	hyaluronic-acid	Yes	<i>j</i>	<i>h</i>	Yes	<i>ef</i>	Yes	[39] ^b

^a our initial report; ^b first available after acceptance of our initial report

^c biocompatibility in vivo; ^d in vitro cell viability and proliferation; ^e in vitro cell adhesion; ^f in vitro cell encapsulation

^g shear stiffness; ^h compressive stiffness; ⁱ indentation

^j single point formation time; ^k kinetics data

^l non-polymeric crosslinker

1.4 Application Literature Review

Translation of experimental systems to clinical practice has been identified as an ongoing challenge for injectable systems [8]. Any new material must meet well established guidelines. In tissue engineering design, as in other fields, failure is initiated by whatever property is limiting. Table 1.4 summarises recommendations collected from the many excellent reviews of the field [2–4, 6–8, 10, 11]. These are discussed and the oxidised-alginate / N-succinyl-chitosan systems potential is evaluated based on what is known from related systems. Discussion is divided into four topics namely: 1) injectability; 2) in situ degradation and biocompatibility; 3) physical properties (stiffness, swelling and porosity) and 4) commercialisability.

1.4.1 Injectability / Suitability for 3D Construct Casting

The material requirements for injectable systems and certain approaches to 3D construct design are almost identical. Uniform seeding of cells throughout a volume and maintaining adequate nutrient exchange are major challenges facing 3D construct manufacture [3]. These can be addressed by encapsulating cells within the scaffold material as it forms [11, 78] and including flow channels with active media circulation during construct manufacture [12, 13]. Cell encapsulation precludes processing steps that could harm cells while injectable systems must not harm surrounding tissue [2, 11, 78]. The resultant biocompatibility constraints are more or less identical. Requiring flow channels limits the available manufacturing options. Casting with degradable cores and three dimensional printing are two methods by which the complex internal geometries associated with flow channels can be produced. Precursor solutions with good fluidity are required for casting, while rapidly gelling or weakly gelled precursors that stay where they are placed are required for 3D printer ‘ink’. This mirrors the fluidity and cure rate requirements of injectable systems.

For ideal biocompatibility, a castable / injectable system must be non-toxic in its precursors and crosslinking process [2, 4]. The low molecular weight crosslinkers often used to produce ‘chemical gels’ are highly toxic preventing cell encapsulation and requiring post processing to neutralise or remove residual active groups [2]. The same chemical species are much less toxic when present on large molecules. For this reason, in order to produce adequate stiffness and an appropriate degradation rate without compromising biocompatibility, covalent bonding via polymer-polymer crosslinking has been recommended [2, 3, 7]. The proposed system conforms to this recommendation meaning precursor toxicity is very unlikely in the brief period required to form crosslinks. Longer term biocompatibility of oxidised-alginate and N-succinyl-chitosan are discussed further in the next section. Crosslink toxicity can be largely ruled out as the Schiff base crosslinking reaction is one of the ones recommended by the review [2] and cells have been successfully encapsulated using related systems [28, 39, 72].

Table 1.4: Background Recommendations for Tissue Engineering Applications

Injectable / Castable (Handling and Biocompatibility)	<0.2 Pa s precursor solution viscosity [2, 73] <1 min gel time for localised delivery [2, 8] All precursors non-toxic [2] No crosslink toxicity [2] Crosslinked in an environment suitable for cell viability. [3]
Biocompatibility (in situ)	Non-immunogenic [2–4, 11] Correct ^a Cell Signalling [3, 4, 41, 50] No toxic degradation products [2–4, 11] Maintains an environment suitable for cell viability. [3]
Environment for Cell Viability	pH 7.3-7.5 [74] Ionic strength 125-185 mmol/L [75, 76] Temperature 36.5-37.5 °C [77]
Stiffness	10 to 30 kPa at no load, equilibrium swelling [4, 6, 7, 11] Stress-strain curve similar to target tissue [7]
Swelling	No guidelines given; however volume changes are not desirable in injectable formulations.
Interconnected Porosity (diameter)	>8 nm therapeutic protein diffusion [14, 78, 79] >10 nm antibody diffusion [78, 79] >2 µm cell migration [80] 5-100 µm capillary formation [41]
Degradation	4 to 8 weeks to 50% mass loss [81] ~6 months to complete dissolution [82]
Commercialisability	Easy to Sterilise [8] Raw Material Availability [7]

^a Functionalization to control cell adherence, proliferation and differentiation is being recommended by a number of authors (e.g. [3, 4, 41, 50])

Forming gels under the environmental conditions listed in Table 1.4 has implications for physical properties and precursor processability. Evaluation of formulation injectability is a developing field [73, 83]. In this work an upper viscosity threshold of 0.2 Pa·s is used based on the guidelines provided by Martens et. al. [73]. Alginate is not expected to be limiting because it is easily soluble under the required conditions and oxidation is known to reduce solution viscosity [23, 32, 72, 84]. Chitosan solubility in the indicated pH range is reported to start at approximate 50% succinylation with weak physical gels (very high viscosity solutions) reported for insoluble chitosans [24]. As succinylation uses up amines necessary for crosslinking, an optimum balance is expected to exist between modification for solubility and amine concentration for crosslinking potential. Published viscosity data on N-succinyl-chitosan is sparse. The only report known to the author examines the effect of molecular weight at a single unspecified degree of succinylation [85]. A need for further study of N-succinyl-chitosan solution viscosity as a function of modification extent was identified.

The cure of polymer-polymer systems is characterised by a rapid second order reaction until gelation followed by a transition to zero-order kinetics [86]. Low conversion of reactive groups is expected due to the leash effect imposed by the polymer chain after incorporation into the growing network. As both reaction rate and final crosslink density are functions of initial reactant concentrations, independent control of physical properties and cure rate are not possible. Cure is one of the more well documented properties in Table 1.3. The two studies with kinetics data show the expected behaviour [27, 30]. A rate maximum was observed near pH 7 with study at higher pH limited by the solubility of unmodified chitosan [27]. Reported gel times between 3.5 s and 5 min are typical in crude single point gel time tests [28, 32, 39, 69, 71]. This suggests obtaining the required rate is plausible for the proposed system.

The proposed system is expected to meet the biocompatibility requirements for injectable gels. Handling requirements are more challenging due to low chitosan solubility and unknown cure kinetics. It is reasonable to expect some formulations will exhibit acceptable cure rate based on the range observed for related systems. It is recommended that N-succinyl-chitosan solution viscosity be characterised to ensure only formulations with the potential to be injectable are studied.

1.4.2 In Situ Biocompatibility and Degradation

Without appropriate biocompatibility, gel materials may not be used for drug delivery or tissue engineering [4, 7]. For this reason it would be irresponsible to proceed with gel development without evaluating the expected performance of the proposed system. The base biocompatibility requirement is no toxicity and no adverse immune response [3]. The adaptability of the mammalian immune system means that even very inert materials may eventually be recognised as foreign and attacked. One strategy to prevent this is to limit

scaffold materials to those that degrade and disappear, resulting in non-toxic by-products and leaving behind minimal residue [4, 10]. Inherent or added functionalization to control cell adherence, proliferation and differentiation is also recommended for tissue engineering applications [3, 4, 7].

Oxidised-alginate / N-succinyl-chitosan hydrogels are expected to primarily degrade via hydrolysis. Alginate is not degradable by human enzymes and though chitosan with a low deacetylation extent is degraded by lysozyme [11], this effect is limited in the 80 to 90% deacetylated material commonly available [87]. Degradation by hydrolysis is a random depolymerization process resulting in the release of fragments with a predictable molecular weight distribution [34]. The oxidised monomers are particularly susceptible, resulting in a relationship between oxidation extent and degradation rate [34, 88]. The relationship is not straightforward, as oxidation also increases crosslinking potential, and highly crosslinked formulations typically exhibit slower degradation [28, 64, 65, 67, 68]. Polymer-polymer crosslinking further complicates the issue as it has been proposed as a method to decouple degradation and mechanical properties in related systems [65]. Degradation times ranging from days to months are observed depending on the exact details of the formulation studied [28, 29, 64, 65, 67, 68]. Incubation in media bearing amines is observed to accelerate degradation, which was attributed to interaction between media and dangling aldehydes along the oxidised polymer reducing ability for fragments to re-crosslink to the network [64].

Though unmodified chitosan and alginate are well known to be non-toxic and non-immunogenic [3, 4, 7, 10] this does not mean derivatives are [72]. In vitro studies on oxidised polymers produce conflicting toxicity results. Two studies reported a dose-dependent decrease in cell viability [29, 69], while six others report no or beneficial effect [28, 39, 50, 71, 72, 89]. In the most significant negative report, cells were exposed to polymer solutions [69]. A related study found this approach had a similar effect regardless of polymer oxidation, suggesting that the methodology may be flawed [71]. Gel studies in live animals report no toxicity [69, 71, 72], no inflammatory response [72, 88] and good hemocompatibility [72]. Three of these were closely related to the proposed system [69, 71, 72] and one evaluated the effect of oxidised-alginate / N,O-carboxymethyl-chitosan on a wide range of organs and tissues over a 21 day period [72]. From this we conclude that oxidised-alginate is sufficiently biocompatible for use in this project. Biocompatibility of N-succinyl-chitosan was established in two studies which evaluated its biodisposition after direct injection of solutions into a mouse model and found no ill effect over the 35 day study period [90, 91].

Without modification the only expected cell interaction with the proposed system is an ability for attachment. This expectation highlights an advantage of the hybrid approach. Though alginate lacks biological recognition domains [3, 10], cells are observed to attach readily to high chitosan hybrid gels [28, 33, 39, 50]. A recent study studying cell attachment with and without RGD peptides on the proposed system only observed statistically significant differences in cell proliferation when both mechanical stimulation and peptide

modification were used [50]. This interaction with mechanical stimulation highlights the importance of substrate stiffness which is the topic of the next section.

1.4.3 Stiffness

Hydrogels and tissues are non-linear elastic. As such the deformation range at which stiffness measurements are quoted is important. When establishing attachment, cells typically only deform substrate materials by 3 to 4% regardless of substrate stiffness [6]; however larger deformations may result from muscle contractions (>20% [7]) and swelling may result in very large linear strains (>100%)[14, 68].

The stiffness targets in Table 1.4 are those of muscle tissue (both cardiac and skeletal) at swelling equilibrium and zero load [6, 7]. This focus is due to the relative shortage of scaffold materials within the required window compared to other tissues [6, 7]. As was previously noted, achieving “nonlinear elasticity that is similar to that of heart muscle” has been identified as the “most important challenge” facing tissue scaffold designers today [7]. Several benefits result from the correct substrate stiffness. In static culture, correct substrate stiffness promotes cell attachment and phenotype maintenance [6]. Correct cell alignment and improved growth are additional benefits imparted by the presence of mechanical stimuli [81, 92]. For heart repair via hydrogel injection, the best results are expected when material matching the stiffness of healthy tissues is used [7, 93–95].

Examining the related systems in Table 1.3, stiffness is generally characterised after swelling (ideally at equilibrium); however equilibrium is more often assumed than verified and the swelling extent of mechanical specimens is seldom quoted. Stiffness values between 10 and 30 kPa were reported by several authors [28, 33, 39, 68], though in some cases these were achieved by using unreasonably high polymer concentrations (e.g. 20 w/w% [33]). The N-succinyl-chitosan and oxidised-hyaluronic acid system stands out with stiffness centred on 20 kPa at only 2 w/v% polymer [28, 39]. This is very promising for the proposed system as alginate is very closely related to hyaluronic acid.

1.4.4 Porosity and Swelling

Porosity and swelling are both poorly characterised for injectable systems due to the tendency to freeze dry samples prior to testing. This allows the ‘dry polymer mass’ to be used as a baseline for swelling (e.g. [28, 29, 32, 33, 39]) and SEM analysis to be used for microstructure characterization (e.g. [28, 29, 32, 33, 39, 70]); however freeze drying is known to modify network structure by phase separation during ice formation [96]. In addition, polymer-polymer crosslinking is expected to be halted by steric hindrance. When network volume is drastically reduced further crosslinking can be reasonably expected during the

initial stages of swelling experiments. Though the freeze dried pore size and swelling measurements share a baseline, neither is directly applicable to an injectable system as the network architecture is expected to be heavily modified by the process.

Pore size requirements are well summarised in Table 1.4. As pore size characterization is beyond the scope of this work, discussion here will be brief. Reviewing related systems, pore size is only characterised by SEM. An ASTM standard listing more appropriate options is available [96]. It is significant to the suitability of the proposed system that correct pore size and stiffness are not expected unless low chitosan solubility introduces inhomogeneity. For this reason pore size measurements are recommended as a follow-up for any compositions where inhomogeneity is observed.

Swelling requirements are situation and system dependent. Swelling is generally not desirable in an injectable system as it has the potential to put pressure on surrounding tissue. In cast constructs, diffusion distances and therefore cell viability might change significantly due to swelling strains. Linear strains of 14 to 40% were reported for the only system in Table 1.3 that used ‘as-cast’ gels as a baseline for swelling ($Q = 1.5$ to 3.0 [69, 71]). The physics of this behaviour mean that eliminating swelling is not practical. Even if a base system with minimal swelling were developed, changes to system formulation encouraged to promote biocompatibility (e.g. RGD peptide modification) are also likely to modify swelling behaviour. For this reason swelling prediction is made a priority in this work. If swelling can be predicted its effects on dimensions, pore size and stiffness can be accounted for during construct design.

1.4.5 Commercial Potential

Several authors recommended that systems under development be readily adoptable or commercializable [4, 7, 8, 10]. Key factors determining adoptability include sterilizability [8, 10], availability [3, 7, 8, 10, 11] and cost [8, 10]. Based on these factors the proposed system is expected to be highly commercializable. Sterilization is not a challenge. The generally adopted approach for related systems is to irradiate dry polymer prior to solution preparation [28, 39, 50, 69, 72]. Irradiation or autoclaving in solution was also reported [29, 33]. Both alginate and chitosan are readily available. This is indicated in several reviews of the field [3, 7, 8, 10, 11] and also by how frequently they are used (see Table

Table 1.5: Research Grade Polymer Cost in 2011 (per gram)

PEG	PVA	Gelatin	Alginate	Chitosan	Hyaluronic Acid	Fibrin	Collagen	Peptide Based
\$0.07	\$0.12	\$0.13	\$0.24	\$0.81	\$39	\$71	\$1000	\$2000
[97]	[98]	[99]	[100]	[101]	[102]	[103]	[104]	[105]

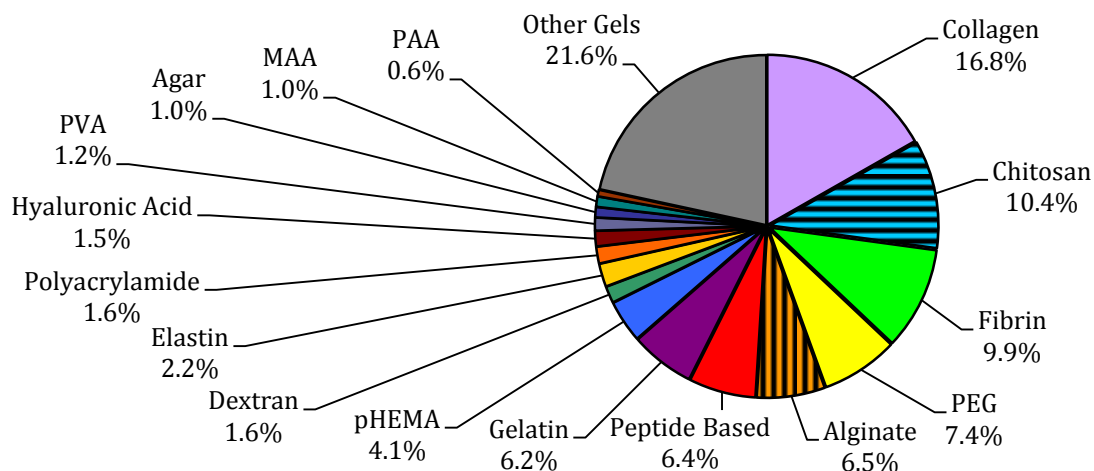


Figure 1.6: Hydrogel Frequency: Journal of Biomaterials (2009) Vol. 30, Issues 1-24

1.6). The cost of both polymers is also very competitive (See Table 1.5). It is worth noting that the cost differential is expected to narrow going from research grade to medical grade material; however this is not expected to significantly affect the analysis.

1.5 Concluding Remarks

The proposed oxidised-alginate / N-succinyl-chitosan system is expected to meet the stringent biocompatibility constraints imposed on injectable systems. Based on related systems, acceptable stiffness is also expected. Due to its hybrid nature, strength and toughness are not necessarily directly linked to stiffness and control of stress-strain curve shape may be possible. To insure formulations are representative of injectable systems, characterization of chitosan solution rheology as a function of modification is recommended. Though outside the scope of the current work, potential to use chitosan solubility to de-link stiffness and porosity was also identified. As N-succinyl-chitosan solubility and crosslinkability are inversely proportional a key challenge is that design degrees of freedom may be insufficient for simultaneous control of all variables (i.e. stiffness, fluidity and pore size). This would require moving to even more complex formulations, potentially by blending with related systems. As system complexity increases the need to move to a design approach for tissue construct development becomes more urgent. In light of this, swelling prediction was identified as an area where models are beginning to bear fruit. Stiffness measurements and membrane osmometry experiments are recommended to support the modelling work necessary to develop this proposed gel system.

Chapter 2

Models for Polyampholyte Solutions and Gels

2.1 Overview

The goal of this work is to find three types of mathematical models to describe the new gel behaviour. These are a model to describe hybrid gel stiffness, a model to predict polyampholyte gel equilibrium swelling, and a model to analyse polyampholyte solution membrane osmometry. To keep the scope of discussion manageable, greater emphasis is placed on the background required to support the proposed approach in later chapters. In line with tissue engineering approaches, the properties of phosphate buffered saline (PBS) are used when solvent data is required to decide between model branches.

The modelling work was inspired by a desire to narrow down the experimental field by estimating in advance which gel formulations were likely to be successful. Based on the quantitative agreement for gel swelling obtained by Chan [14], six key factors were identified, namely 1) elastic potential, 2) solution mixing, 3) ionic interactions, 4) electrolyte solution nonideality, 5) counterion condensation and 6) weak electrolyte ionization.

Parameters for 1) are determined by compression testing in Chapter 7. Models for this purpose are well known, although there is some inconsistency regarding their usage. Improved models for hybrid gels are recommended, a topic that is discussed further in Chapter 7.

Parameters for 2) and 5) are found by membrane osmometry in Chapter 6. The models used for these are the least well developed/documentated and therefore the osmometry experiment also represents a test of the theories. To assist in this work a Monte Carlo simulation is presented which is used to estimate error tolerance and compare statistical designs prior to conducting physical experiments. Despite or perhaps because of the fact that osmometry is a very old technique, the author was unable to find a suitably compre-

hensive model for analysing polyelectrolyte osmometry experiments. A suitable model was therefore assembled and is presented towards the end of this chapter.

Parameters for 4) and 6) are available in the literature. The models are well developed and suitable for the system under study. Simulations using these are presented to support experimental work in Chapters 4, 6, and 7.

2.2 Gel Swelling and Membrane Osmometry

2.2.1 System Description and Balance Equations

As can be seen in Figure 2.1, membrane osmometry and gel swelling are closely related topics. During gel swelling, polymer is prevented from mixing with the reference solution by network connectivity. In osmometry a semipermeable membrane separates the polymer containing sample from the reference solution. In both cases the solvent and ions can freely cross the boundary between the two phases but polymers cannot. In the system definition, the polymer side is often referred to as the “*internal*” or “*sample*” phase , e.g.[26], and the other side is the “*external*”, “*reference*” or “*surrounding*” phase. In both cases the driving forces are solution mixing and ionic interactions. Countering potentials come from elastic energy during swelling and membrane pressure in osmometry.

The thermodynamic model used in both cases treats the sample and reference phases as two independent thermodynamic systems with a shared boundary defined by the gel

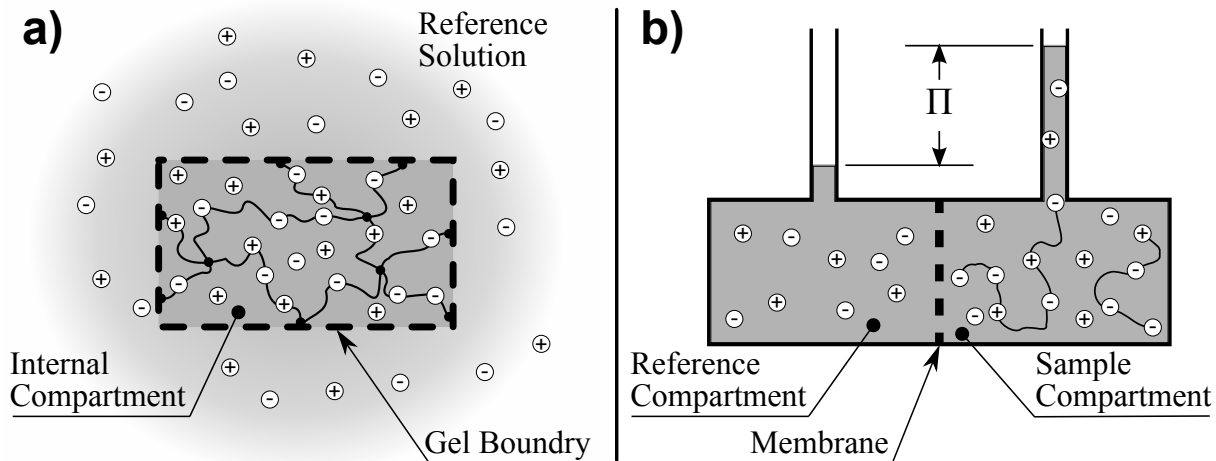


Figure 2.1: Swelling and Osmometry System Schematic: a) Gel Swelling b) Membrane Osmometry. Note three analogous pairs: 1) Reference Solution / Reference Compartment; 2) Gel Boundary / Membrane and 3) Internal Compartment / Sample Compartment

surface or semipermeable membrane. At equilibrium, the free energy of a thermodynamic system is constant, and any component that can cross the system boundary must have equal chemical potential on both sides [42, pp. 506-510].

Swelling model derivations often start with an equilibrium chemical potential balance on the solvent [16, 26, 106, 107]. Equation 2.1 is as presented by Flory [26, p. 591] for polyelectrolytes and is sufficiently general as to apply to polyampholyte systems as well. Here $\Delta\mu_{a,b}$ is the change in chemical potential across the system boundary and $\Delta\mu_{a,b}^c$ the change in ‘phase c ’ relative to the standard reference state. Subscript a defines the component of the mixture (solvent = 1) and b provides the cause of the change.

$$\Delta\mu_{1,ionic}^{gel} - \Delta\mu_{1,ionic}^{surroundings} = \Delta\mu_{1,mixing} + \Delta\mu_{1,elastic} \quad [26, p. 591] \quad (2.1)$$

To the best knowledge of the author, the membrane osmometry equivalent to Equation 2.1 does not appear in the open literature. The starting point for osmometry derivations is typically van’t Hoff’s equation, (e. g. [26, pp. 269-272], [42, pp. 568-575], see Section 2.4.1). This makes sense when the focus is on molecular weight; however other effects must be interpreted by models introduced partway through the linearization process. This leads to implicit approximations which may not always be justified. To better demonstrate the similarity between gel swelling and membrane osmometry and provide a clearer understanding of the interaction between the different physics, Equation 2.2 is proposed as the starting point in this work.

$$\Delta\mu_{1,ionic}^{sample} - \Delta\mu_{1,ionic}^{reference} = \Delta\mu_{1,mixing} + \Delta\mu_{1,osmotic\ pressure} \quad (2.2)$$

Equation 2.2 is determined by analogy to Equation 2.1 and is consistent with Flory’s swelling model derivation [26, p. 591], Himenz derivation of the van’t Hoff equation [42, p. 545] and Oosawa’s [108] discussion of additivity rules. It assumes various effects on solvent chemical potential are additive which has been observed experimentally since the 1960’s [109].

Table 2.1: Models for Gel Swelling and Membrane Osmometry

Term	Model	Section	References
$\Delta\mu_{1,elastic}$	theory of rubber elasticity	2.3	[15, 16, 19, 25, 26, 36, 110, 111]
$\Delta\mu_{1,osmotic\ pressure}$	van’t Hoff equation	2.4.1	[26, 42]
$\Delta\mu_{1,mixing}$	Flory-Huggins theory	2.4.2	[14, 16, 26, 42, 106]
$\Delta\mu_{1,ionic}^{sample} - \Delta\mu_{1,ionic}^{reference}$	Gibbs-Donnan equilibrium	2.4.7	[14, 16, 26, 42]

Terms for Equations 2.1 and 2.2.

2.2.2 Model Usage

For each term included in Equations 2.1 and 2.2 a model exists. A summary of the models and where they are discussed is found in Table 2.1. Both equations neglect the (usually small) electrostatic contribution from ions along the polymer backbone [106, 107]. This is discussed further in Section 2.4.3. For polyelectrolytes the Donnan term tends to dominate [20], see Chapter 6. In order to evaluate this term accurately three additional topics must be considered, namely: 1) solution nonideality (Section 2.4.4), counterion condensation (Section 2.4.5) and weak electrolyte ionization (Section 2.4.6).

Due to its relative importance to polyelectrolytes, how the Donnan term is evaluated is one of the key factors differentiating comparisons between theory and experiment. Two groups have obtained quantitative agreement, one by considering all three factors for equilibrium swelling [14] and the second by direct potentiometric evaluation of the Donnan term for a gel membrane [57, 112]. Qualitative agreement was obtained by considering solution nonideality but neglecting counterion condensation and weak electrolyte interaction effects during ionization [107, 113]. Neglecting condensation might be reasonable given the focus on charge balanced polyampholytes but according to Kudaibergenov [47] weak electrolyte interaction effects are significant. Other authors who discuss the full polyelectrolyte swelling model do not provide strong tests of theory. They either fit the model to their data [16, 114] or do not compare theory to experiment [15, 16, 26, 42, 106, 115].

The literature for polyelectrolyte osmometry is even more sparse. Based on the parameters in Table 1.2 and the Section 2.6.3 simulation, at physiologically significant ionic strength and pH, both salt and mixing effects were thought to be of similar importance for N-succinyl-chitosan. For a variety of reasons few authors consider both. Model derivations starting with the van't Hoff equation break the derivation into two cases: 1) a low salt regime where osmotic pressure is independent of mixing effects, and 2) a high salt regime where it is independent of ionic effects [26, 42]. This was in good agreement with early work (1960-1970) [109, 116–119]; however during this time ion activity models (solution nonideality effect [120]) were not sufficiently advanced to quantitatively investigate even the intermediate regime. The focus was therefore on the low salt regime, where mixing effects could be neglected. Though mixing effects are considered in a discussion of scaling relationships from the early 1980's [121], works published since 1991 when activity models appear to have matured [122] still focus on the low salt regime and therefore neglect a significant section of the physics [123, 124]. To the best knowledge of the author, a formal evaluation of the full osmometry model for electrolytes, including all the effects necessary for quantitative agreement with equilibrium gel swelling, does not appear in the open literature.

2.3 Gel Stiffness - Theory of Rubber Elasticity

The most successful model for hydrogel stiffness is the theory of rubber elasticity [15, 16, 19, 25, 26, 36, 110, 111]. According to the theory, the stiffness in network polymers has an entropic origin, similar to pressure in gasses. Any deformation of the gel perturbs network chains from their preferred configuration and a force must be exerted to maintain the perturbation. In accordance to this theory, gel stiffness is only dependent on chain conformational statistics and network architecture [25, 26]. Provided it can be modelled as a flexible random coil, the nature of the polymer backbone only effects stiffness indirectly via the number of monomers in a statistical segment.

The theory has been well reviewed by Erman and Mark [25]. To support its use in this work four topics must be covered, namely 1) the zero deformation reference state; 2) the assumed chain conformation statistical distribution; 3) the assumed constraint imposed by the network on connection points; and 4) deformation mode specific derivations (volumetric swelling and uniaxial compression).

In his 1953 textbook Flory notes that “the volume of the relaxed network” is the accurate reference state for volumetric changes [26, p. 578]. This is often referred to as the ‘unswollen’ state due to the original focus on natural rubber crosslinked in the absence of solvents. Some authors have therefore erroneously used the solvent free state as the reference state for hydrogels. Gel networks are typically formed in the presence of solvent out of polymer chains that are in their relaxed state. Assuming that crosslinking has a negligible effect on chain conformations, the correct reference state is the solvent concentration present at the time of formation [15, 16, 19, 25, 26].

Assuming Gaussian statistics allows network chain length to be eliminated from the model [26]. The resultant Helmholtz free energy function for deformation of an individual network chain (Equation 2.3) is only dependent on the unperturbed ($\langle r^2 \rangle_0$) and instantaneous (r) chain end to end distances [110]. Here k_B is the Boltzman constant and T is the absolute temperature.

$$\Delta F_{Chain} = \frac{3}{2} k_B T \frac{r^2}{\langle r^2 \rangle_0} \quad (2.3)$$

The Gaussian assumption holds for most polymers provided deformations are not large enough to fully extend network chains. Non-Gaussian versions of the theory are available [14, 16, 19, 25, 26]; but we can assume that the Gaussian approximation suffices for this work. Chan compared Gaussian and non-Gaussian approaches to modelling the volumetric swelling of covalently crosslinked alginate [14]. Her simulation results indicate the difference in elastic potential is significant for short chain lengths; however the effect on the equilibrium swelling ratio is small due to the rapid change in swelling potential near the equilibrium point. As will be demonstrated in Chapter 7, simple Gaussian models provide a good fit to uniaxial compression data for practically significant deformations of

N-succinyl-chitosan / oxidised-alginate hybrid gels. As such, only Gaussian models will be covered in detail here.

Two classical versions of the theory that are often used for hydrogels are the ‘affine’ and ‘phantom’ approaches. Equation 2.4 gives the Helmholtz free energy arising from elastic deformation of a network according to the respective theories [25, 110]. Here ν_e is the number of crosslinks, ϕ_n is the network functionality (number of chains originating at a crosslink), λ_i^2 are the principal stretch ratios, V is the instantaneous network volume and V_o is the reference state volume.

$$\Delta F_{Elastic} = \begin{cases} \frac{1}{2} \nu_e k_B T \left(\lambda_x^2 + \lambda_y^2 + \lambda_z^2 - 3 - \frac{4}{\phi_n} \ln \left(\frac{V}{V_o} \right) \right) & \text{afine} \\ \frac{1}{2} \left(1 - \frac{2}{\phi_n} \right) \nu_e k_B T \left(\lambda_x^2 + \lambda_y^2 + \lambda_z^2 - 3 \right) & \text{phantom} \end{cases} \quad (2.4)$$

The ‘affine’ and ‘phantom’ approaches have been demonstrated to represent limiting cases for the freedom of network junctions to move relative to the overall network [25]. The ‘affine’ theory assumes entanglements between chains provide sufficient constraint that network junctions move linearly with macroscopic deformation. ‘Phantom’ theory assumes that neighbouring chains do not interact; making junctions only subject to the ‘leash’ effect of the chains they connect. In practice, under tensile loading only very rigid thermosets exhibit the idealised ‘affine’ behaviour and most rubbers fall somewhere between the two limits. Hydrogel chains are well separated by solvent resulting in almost pure ‘phantom’ behaviour [25, 26]. From this it would appear the ‘phantom’ model is the correct form, although a key difference between the elastic free energy functions for the two models is suppressed in volume conserving deformation modes.

The volume term $\frac{V}{V_o}$ drops out of Equation 2.4 if incompressibility can be assumed. For hydrogels, an assumption of incompressibility equates to an assumption that local solvent concentration remains constant throughout the deformation [111]. Agreement between the ‘phantom’ theory and experimental results can be explained if solvent rearrangement within local pore spaces is rapid, but solvent movement from or into any portion of the gel is slow compared to the time scale of the experiment [111]. Therefore incompressibility can be assumed for tensile or compressive tests, but creep, stress-relaxation and swelling phenomena are all driven by solvent redistribution making this assumption more uncertain. This has led to the extensive use of the ‘affine’ model for swelling in hydrogels [15, 16, 19, 111].

To convert free energy into quantities measurable in specific deformation modes the following algorithm is followed: 1) geometry based simplifications are applied; 2) the expression is formulated in terms of the desired deformation measure; and 3) the result is differentiated to get the work associated with deformation.

Unconstrained uniaxial deformation with an assumption of incompressibility allows the Equation 2.5 geometric simplification to be used [110]. Force as function of instantaneous

length l is used as a stepping stone to stress as a function of some strain measure. The definition of the stretch ratio, Equation 2.6 contains l ; where l_o is undeformed length and ε is the more familiar logarithmic strain. Substituting Equations 2.5 and Equation 2.4 into Equation 2.7 and using Equation 2.6 to take the derivative with respect to l gives Equation 2.8 [25, 110].

$$\lambda_x = -\lambda_y^{1/2} = -\lambda_z^{1/2} = \lambda_e \quad \text{and} \quad V = V_o \quad (2.5)$$

$$\lambda = \frac{l}{l_o} = \exp(\varepsilon) \quad (2.6)$$

$$\sigma = \frac{1}{\text{Area}} \frac{\delta \Delta F_{Elastic}}{\delta \lambda_e} \frac{\delta \lambda_e}{\delta l} \quad (2.7)$$

$$\sigma = \begin{cases} k_B T \frac{\nu_e}{V_o} (\lambda_e - \lambda_e^{-2}) & \text{afine} \\ \left(1 - \frac{2}{\phi_n}\right) k_B T \frac{\nu_e}{V_o} (\lambda_e - \lambda_e^{-2}) & \text{phantom} \end{cases} \quad (2.8)$$

The equivalent simplification for unconstrained volumetric swelling is Equation 2.9 [110]. Here solvent chemical potential is required at equilibrium swelling as a function of instantaneous concentration. This can be accomplished via Equation 2.10, where the volume of the swollen network is expressed in terms of the number of additional solvent molecules n_1 . Here ' \bar{V}_1 ' is the partial molar volume of the solvent and N_A is the Avogadro constant.

$$\lambda_x = \lambda_y = \lambda_z = \lambda_s \quad \text{and} \quad \frac{V}{V_o} = \lambda_s^3 \quad (2.9)$$

$$\lambda_s^3 = \frac{V}{V_o} = \frac{V_o + \bar{V}_1 N_A^{-1} n_1}{V_o} = Q \quad (2.10)$$

$$\Delta \mu_{1,elastic} = \frac{\delta \Delta F_{Elastic}}{\delta Q} \frac{\delta Q}{\delta n_1} \quad (2.11)$$

$$\Delta \mu_{1,elastic} = \begin{cases} k_B T N_A^{-1} \frac{\nu_e}{V_o} \left(Q^{-1/3} - \frac{4}{\phi_n} Q^{-1} \right) & \text{afine} \\ \left(1 - \frac{2}{\phi_n}\right) k_B T N_A^{-1} \frac{\nu_e}{V_o} Q^{-1/3} & \text{phantom} \end{cases} \quad (2.12)$$

From a scaling analysis point of view the two theories are identical for uniaxial case. All differences are in the front factor which is a constant for any given network. Differences in scaling analyses appear in swelling where a second term appears for the predictor variable. All theoretical models discussed are for a single chain type in network. Theories incorporating more than one chain type exist [25] however they are less well developed and in knowledge of the author are not formulated for hybrid systems of the type covered here. A model derivation for the hybrid systems covered in this work is found in Chapter 7.

2.4 Polymer Solution Models

Polyelectrolyte solution properties are important for predicting gel swelling and analysing osmometry results. Four different models provide terms for the Section 2.2 energy balance, namely: 1) osmotic pressure via the van't Hoff equation, 2) solution mixing via Flory-Huggins theory, 3) polyampholyte Coulomb potential via a model proposed by English [107] and 4) ionic partition potentials via Donnan equilibrium. As is seen in Chapter 6 the Donnan term dominates. To accurately model it, three additional topics must be considered, namely: 1) solution nonideality, 2) counterion condensation and 3) weak electrolyte ionization. Diverse concentration units are used by the different models, necessitating a discussion of unit conversions if they are to be assembled into unified whole.

2.4.1 Osmotic Pressure - van't Hoff equation

Equation 2.13 is the usual form for osmometry where a_i is solvent activity, Π is osmotic pressure \bar{V} is partial molar volume, R is the molar gas constant and T is the absolute temperature.

$$-\ln(a_1) = \frac{\bar{V}_1 \Pi}{RT} \quad [42, \text{p. 545}] \quad (2.13)$$

This equation assumes solvent incompressibility but is otherwise exact. Derivations for van't Hoff's equation as it applies to osmotic equilibrium appear in Flory [26, pp. 269-272] and Hiemenz [42, pp. 545-548, 568-575]. The basic equation can be transformed without loss of generality for substitution into the Section 2.2 energy balance or linearised through a series of approximations for direct analysis of membrane osmometry data.

Linearization for Charged Polymers

Though a rough linearization is derived by Hiemenz [42] to demonstrate key points of polyelectrolyte physics, the complexity of polyelectrolyte solutions means the potential balance (Equation 2.2) is a better starting point. Hiemenz notes at least three regimes exist namely: 1) salt free, 2) low salt and 3) high salt. Results are interpreted in terms of Donnan equilibrium or Flory-Huggins theory depending on regime [42, 46, 118, 119, 121, 124, 125]. Using the thermodynamic definition of activity (Equation 2.30, see Section 2.4.4), Equation 2.13 can be alternatively stated as Equation 2.14. This reduces the pressure contribution equation to its term in the energy balance without loss of generality.

$$\Delta\mu_{1,osmotic\ pressure} = -\bar{V}_1 \Pi \quad [42, \text{p. 545}] \quad (2.14)$$

Linearization for Neutral Polymers

As similar approximations are used in the Section 2.5 model linearization, it is worth following the standard derivation in detail.

For osmometry experiments on neutral polymers Himenz [42] uses the following approach: 1) a two component system is defined with solvent and polymer having subscripts 1 and 2 respectively; 2) assuming a dilute solution allows solvent activity to be approximated by mole fraction, x_1 ; 3) the definition of mole fraction can be used to introduce polymer concentration; and 4) the logarithm is approximated through a series expansion.

$$\frac{\bar{V}_1 \Pi}{RT} \approx -\ln(x_1) = -\ln(1 - x_2) = x_2 + \frac{1}{2}B'x_2^2 + \frac{1}{3}C'x_2^3 + \dots \quad (2.15)$$

Himenz [42] then introduces number average molecular weight M_n , and converts between polymer mole fraction and polymer mass per volume concentration ρ_2^* through Equation 2.16. A series of approximations are required, made possible by repeated application of the dilute solution assumption: 1) polymer mass per volume concentration is defined; 2) the polymer volume contribution $n_2 \bar{V}_2$ is assumed insignificant; 3) the number of polymer molecules n_2 is assumed insignificant as a fraction of the total; and 4) polymer mole fraction is substituted for its definition.

$$\rho_2^* = \frac{n_2 M_n}{n_1 \bar{V}_1 + n_2 \bar{V}_2} \approx \frac{n_2 M_n}{n_1 \bar{V}_1} \approx \frac{n_2}{n_1 + n_2} \frac{M_n}{\bar{V}_1} = x_2 \frac{M_n}{\bar{V}_1} \quad (2.16)$$

Substituting Equation 2.16 into 2.15, rearranging and truncating after the second term, results in Equation 2.17.

$$\frac{\Pi}{RT \rho_2^*} \approx \frac{1}{M_n} + \frac{B' \bar{V}_1}{2M_n^2} \rho_2^* = \frac{1}{M_n} + A_2 \rho_2^* \quad [42, \text{p. 551}] \quad (2.17)$$

Equation 2.17 forms the basis for the ASTM standard approach to osmometry data analysis [45]. The linear form allows the unknown parameters M_n and A_2 to be obtained by regression based on a series of experiments conducted at different polymer concentrations. The approximation becomes exact in the limit as polymer concentration approaches zero [42, pp. 551-553]. The left hand side is known as the reduced osmotic pressure. A_2 is the osmotic second virial coefficient which describes the solution nonideality involved in polymer solvent mixing. As such A_2 is often interpreted using Flory-Huggins theory [42, pp. 559-560].

2.4.2 Polymer Solution Mixing - Flory-Huggins Theory

Flory-Huggins theory accounts for the portion of mixing free energy arising from mixing entropy and short range specific interactions between system components [26, 43]. It neglects the effects of long range Coulomb interactions which are considered elsewhere (see sections 2.4.3 and 2.4.7). The derivation uses a lattice model of the polymer solution. An implicit assumption in the derivation is that polymer segments are distributed randomly and homogeneously throughout the solution. This is reasonable in gels but is a source of inaccuracy when data is extrapolated to infinite dilution for osmometry [26, p. 511]. Monte Carlo simulations indicate the theory is less accurate at low volume fractions but still provides useful predictions [126].

A general theory for systems with an arbitrary number of components is found in [26, p. 549]. Using this theory the mixing contribution to the component 1, chemical potential may be estimated for two and three component systems by use of equations 2.18 [26, p. 511][127] and 2.19 [26, p. 549][127].

$$\Delta\mu_{1,mixing} = RT \left[\ln(\Phi_1) + \left(1 - \frac{1}{x_{12}}\right) \Phi_2 + \chi_{12} \Phi_2^2 \right] \quad (2.18)$$

$$\Delta\mu_{1,mixing} = RT \left[\ln(\Phi_1) + (\chi_{12} \Phi_2 + \chi_{12} \Phi_3)(\Phi_2 + \Phi_3) - \frac{\Phi_2}{x_{12}} - \frac{\Phi_3}{x_{13}} - \chi_{23} \frac{\Phi_2 \Phi_3}{x_{23}} \right] \quad (2.19)$$

Subscript 1 typically refers to the solvent and subscripts 2, 3 to solutes. Φ_i is volume fraction, χ_{ab} is the Flory-Huggins binary interaction parameter and x_{ab} is a size parameter measuring the volume of component b in terms of molecules of component a [26, 127]. As such it is given by Equation 2.20 where the polymer volume has been partitioned into the monomer partial molar volume $\bar{V}_{b,r}$ and the chain number average degree of polymerization $X_{n,b}$. Equation 2.21 provides the relationship between $dX_{n,b}$ and number average molecular weight, where M_r is the molecular weight of a monomer [42].

$$x_{1b} = \frac{\bar{V}_1}{\bar{V}_{b,r}} X_{n,b} \quad (2.20)$$

$$M_n = M_r X_n \quad (2.21)$$

For gel swelling x_{1b} 's are proportional to the nearly infinite polymer network degree of polymerization eliminating all related terms from the equations. In this work the theoretical debate over the polymer-polymer interaction term, $\chi_{23} \frac{\Phi_2 \Phi_3}{x_{23}}$ [128], can be avoided by

noting that osmometry experiments (Chapter 6) are only conducted using a single polymer. In swelling experiments where two polymers are used (Chapter 7) it is argued that the very small polymer volume fractions combined with the spacial constraint imposed by the gel network makes this term of negligible practical significance.

To interpret A_2 from Equation 2.17 the theory is linearised [42]. The derivation is intended for use with neutral polymers in pure solvent and as such starts with Equation 2.18. The definition of volume fraction is used (Equation 2.22), allowing a series expansion (Equation 2.23). After truncation, this results in Equation 2.24.

$$\Phi_1 = 1 - \sum_{i=2}^n \Phi_i \quad (2.22)$$

$$\ln(1 - x) = - \sum_{n=1}^{\infty} \frac{1}{n} x^n \quad (2.23)$$

$$\Delta\mu_{1,mixing} = \frac{\Phi_2}{x_{12}} + \left(\frac{1}{2} - \chi_{12} \right) \Phi_2^2 \quad (2.24)$$

Equation 2.25 can be used to convert concentration units without approximation and Equation 2.21 is used to introduce M_n . This results in the right hand side of Equation 2.17, showing that according to Flory-Huggins theory A_2 is related to χ_{12} via Equation 2.26 [42].

$$\Phi_2 = \bar{V}_2 M_n^{-1} \rho_2^* \quad (2.25)$$

$$A_2 = \left(\frac{1}{2} - \chi_{12} \right) \frac{\bar{V}_2^2}{\bar{V}_1 M_n^2} \quad (2.26)$$

Linearization of the theory only introduces series truncation error when used with neutral polymers in pure solvent; however if salts are present the definition of solvent volume fraction should include salts and the use of two component theory is incorrect. The appropriateness of its use with polyelectrolytes in salt solutions is discussed further in Section 2.5.1.

2.4.3 Intra-chain Coulomb Potential

The intra-chain Coulomb potential results in charge attraction (polyampholyte only) and repulsion within individual polymer chains. Osmometry is only indirectly affected via the shape of polymer in solution [46]. This can influence solution mixing via modified contact between the polymer and solvent [26] and Donnan equilibrium via modified counterion condensation [108]. During the swelling of polyelectrolyte gels, the apparent stiffness of the polymer network may be reduced by charge repulsion making extended

chain conformations and non-Gaussian elasticity more likely. In most cases the magnitude of the intra-chain Coulomb effect is expected to be small [106], particularly when the screening effect of physiological ionic strength is considered [46]. Highly charge-imbalanced polyampholyte gels are expected to behave similarly to polyelectrolyte gels. However for polyampholyte systems near the isoelectric point charge attractions can partially oppose swelling and therefore cannot be wholly neglected [107].

Equations 2.27 to 2.29 provide the free energy model for the Coulomb effect on polyampholyte gel swelling proposed by English [107]. Here r is the approximate nearest neighbour distance, N_e is the effective number of fixed charges giving rise to attractive interactions, z is the maximum number of oppositely charged nearest neighbours, V is the gel volume and N_+ , N_- are the respective numbers of the indicated charges carried by the gel network.

$$\Delta F_{\text{coulomb}} = -\frac{z}{2} N_e \lambda_B \frac{\exp(-\kappa r)}{r} \quad (2.27)$$

$$r \approx 2 \left(\frac{3V}{4\pi(N_+ + N_-)} \right)^{1/3} \quad (2.28)$$

$$N_e = N_+ + N_- - 2|N_+ - N_-| \quad (2.29)$$

The model is very rough, however it might serve to provide an order of magnitude estimate for the polyampholyte effect. It can be converted to solvent chemical potential following the same procedure as for the elastic free energy (see Equations 2.10 and 2.11). In this model λ_B and κ are electrostatic length scale parameters introduced in Section 2.4.4.

2.4.4 Solution Nonideality - Debye-Hückel and Pitzer

In ideal solutions chemical interactions and reactions are proportional to concentration. Due to long range ionic interactions, charged species in solution only act in this ideal manner at very low concentrations. This is particularly significant in Section 2.6.1 when evaluating phosphate buffer equilibrium. To address this, corrected concentrations or activities a_i are defined thermodynamically (Equation 2.30) such that the chemical potential change with activity in a nonideal solution is the same as its change with concentration in an ideal solution [42, 129]. Activities are treated as dimensionless but their value is influenced by the reference state by which they are defined. The reference state for molality m_i is 1 mol/kg while for molarity c_i it is 1 mol/L. Models for activity are typically expressed in terms of activity coefficients γ_i which are defined as in Equation 2.31 [122, 130].

$$\Delta\mu_i(m) = RT \ln a_i(m) \quad \text{OR} \quad \Delta\mu_i(c) = RT \ln a_i(c) \quad (2.30)$$

$$a_i(m) = \frac{\gamma_i m_i}{m_{ref}} \quad \text{OR} \quad a_i(c) = \frac{\gamma_i c_i}{c_{ref}} \quad (2.31)$$

Debye-Hückel Theory

To calculate activity coefficients the Debye-Hückel ionic cloud model (Equation 2.32) provides a starting point. As a model it is only useful at ionic strengths below 0.01 [129, p. 273] but it is the origin of many parameters necessary for more complex theories.

$$\ln \gamma_i = -\frac{1}{2} z_i^2 \lambda_B \kappa = -\ln(10) A z_i^2 I_{(c)}^{1/2} \quad (2.32)$$

In Equation 2.32 λ_B is the Bjerrum length given by Equation 2.33. λ_B is the separation distance at which the interaction energy between unscreened ions equals the average thermal energy [131]. This should not be confused with the inverse Debye length κ (Equation 2.34), which is a measure of the screening distance over which ions can 'see' one another in solution. The Debye-Hückel parameter (A , Equation 2.32), encompasses the portion of $(\lambda_B \times \kappa)$ which is a constant for a given solvent at a given temperature. It is used in a number of more complex theories [122, 129]. Where A and λ_B are solvent properties, κ is also function of overall charge density in solution. This is modelled using ionic strength I (Equation 2.35). I is very widely used and its significance was recognised before Debye [122].

$$\lambda_B = \frac{\epsilon^2}{4\pi \epsilon_r \epsilon_0 k_B T} \quad (2.33)$$

$$\kappa = (8\pi \lambda_B N_A I_{(c)})^{1/2} \quad (2.34)$$

$$I_{(m)} = \frac{1}{2} \sum_i m_i z_i^2 \quad \text{OR} \quad I_{(c)} = \frac{1}{2} \sum_i c_i z_i^2 \quad (2.35)$$

In Equations 2.32 to 2.35 z_i is the charge on species i , c_i or m_i is the concentration of the i^{th} ionic species in solution, N_A is the Avogadro constant, ϵ is the elementary electrical charge, ϵ_0 is the permittivity of free space, ϵ_r is the solvent relative permittivity, k_B is the Boltzman constant and T is absolute temperature.

Choice of Pitzer Model

Several relatively simple modifications to Equation 2.32 exist that extend the range of validity to $I \approx 0.1$ [76, 122, 129]; however for blood and sea water ($I = 0.16$, $I = 0.7$) more complex models are necessary [76, 122, 132]. Deciding which models to use has been a topic of debate, with ion association models favored based on physical significance and simplicity for pure systems [129] and ion interaction models (such as Pitzer's) favoured for computational simplicity in mixtures [132]. Models of both types show good agreement with experiment at very high ionic strength (NaCl, $c = 5$ mol/L ion association [129] or $m = 6$ mol/kg Pitzer ion interaction [122]).

Reviewing model usage in the open literature: English et al. [113] use the McMillan and Mayer approach [133] (an ion interaction predecessor to Pitzer) to model polyampholyte gel swelling; Chan [14] uses single-component Pitzer-Mayorga theory [120] to model covalent alginate gel swelling in PBS; and Covington et al. [76] use the mixed-system Pitzer equations [122] to propose a high ionic strength unified pH definition for phosphate buffers.

Between Pitzer [122] and Covington [76] a full set of model parameters is available for phosphate buffered saline at 25 °C (Tables 2.2 and 2.3). Further work by Partanen et al. [134, 135] determined that the Pitzer parameters for potassium phosphate exhibit very weak temperature dependence allowing accurate calculation of activities in their range of study (25 to 35 °C) using the 25 °C parameters.

Given usage, applicability to problem at hand and availability of model parameters, in this work the mixed-system Pitzer model is used (Equations 2.36 to 2.41). The three virial coefficients from the single-component Pitzer-Mayorga theory and first order mixing effects are considered. Following Covington [76], Equations 2.36 and 2.37 neglect Pitzer’s additional mixing parameter ${}^E\theta'_{ij}(I)$. Also neglected are OH⁻ / phosphate like charge interactions, three component interactions and neutral species interactions all of which are

Table 2.2: Pitzer Interaction Parameters for Oppositely Charged Pairs

M	X	β^0	β^1	C^ϕ
Na ⁺	Cl ⁻	0.0765	0.2664	0.001 27
Na ⁺	H ₂ PO ₄ ⁻	-0.0533	0.0396	0.007 95
Na ⁺	HPO ₄ ²⁻	-0.058 28	1.466	0.0147
K ⁺	Cl ⁻	0.048 35	0.2122	-0.000 84
K ⁺	H ₂ PO ₄ ⁻	-0.0678	-0.1042	0
K ⁺	HPO ₄ ²⁻	0.024 75	1.274	0.008 19

Parameters from [122] for Equations 2.39 to 2.41 and 2.45

Table 2.3: Pitzer Interaction Parameters for Like Charged Pairs

M	M'	$\Theta_{MM'} = \Theta_{M'M}$	X	X'	$\Theta_{XX'} = \Theta_{X'X}$
Na ⁺	K ⁺	-0.012[122]	Cl ⁻	H ₂ PO ₄ ⁻	0.1[76]
Na ⁺	H ₃ O ⁺	0.036[122]	Cl ⁻	HPO ₄ ²⁻	-0.07[76]
K ⁺	H ₃ O ⁺	0.005[122]	Cl ⁻	OH ⁻	-0.05[76]
			H ₂ PO ₄ ⁻	HPO ₄ ²⁻	-0.53[76]

Parameters for Equations 2.36, 2.37 and 2.44

expected to be negligible in the systems studied here.

$$\begin{aligned} \ln \gamma_M &= z_M^2 f^y + \sum_a m_a (2 B_{Ma} + Z C_{Ma}) + \sum_c m_c (2 \theta_{Mc}) \\ &+ \sum_a \sum_c m_a m_c (z_M^2 B'_{ca} + z_M C_{ca}) + \dots \end{aligned} \quad (2.36)$$

$$\begin{aligned} \ln \gamma_X &= z_X^2 f^y + \sum_c m_c (2 B_{cX} + Z C_{cX}) + \sum_a m_a (2 \theta_{aX}) \\ &+ \sum_a \sum_c m_a m_c (z_X^2 B'_{ca} - z_X C_{ca}) + \dots \end{aligned} \quad (2.37)$$

$$f^y = -A_\phi \left(\frac{I^{1/2}}{1 + b I^{1/2}} + \frac{2}{b} \ln (1 + b I^{1/2}) \right) \quad (2.38)$$

$$B_{MX} = \beta_{MX}^0 + \frac{2}{\alpha_1^2 I} (1 - (1 + \alpha_1 I^{1/2}) \exp(-\alpha_1 I^{1/2})) \beta_{MX}^1 \quad (2.39)$$

$$B'_{MX} = \frac{-2}{\alpha_1^2 I^2} \left(1 - \left(1 + \alpha_1 I^{1/2} + \frac{\alpha_1^2 I}{2} \right) \exp(-\alpha_1 I^{1/2}) \right) \beta_{MX}^1 \quad (2.40)$$

$$C_{MX} = \frac{C^\phi}{2(-z_M z_X)^{1/2}} \quad (2.41)$$

$$Z = \sum_i m_i |z_i| \quad (2.42)$$

In the equations I is the molal ionic strength given by 2.35. β_{MX}^0 , β_{MX}^1 and C_{MX}^ϕ are empirical pair parameters which can be found in Table 2.2. Empirical mixing parameters $\theta_{XX'}$, $\theta_{MM'}$ can be found in Table 2.3. z_i is the charge on species i . Subscripts M and X refer to the components of salt MX and are constants in a given equation. Subscripts a (positive) and c (negative) are summation variables across the species in solution with the respective charge. Subscript i in Equation 2.42 is for summation across all species in solution. Parameters $b = 1.2 \text{ kg}^{1/2} \text{ mol}^{-1/2}$ and $\alpha_1 = 2.0 \text{ kg}^{1/2} \text{ mol}^{-1/2}$ are constants for all salts studied [76, 122]. A_ϕ is the molal Debye-Hückel parameter which is tabulated over a wide temperature range by Pitzer and equals $0.4023 \text{ kg}^{1/2} \text{ mol}^{-1/2}$ at $40 \text{ }^\circ\text{C}$ [122].

Solvent Activity

For polyelectrolyte osmometry the effect of solution nonideality on the solvent is more significant than that of the ions (see Section 2.5.2). The osmotic coefficient ϕ as defined in Equation 2.43 provides a relationship between ion concentrations m_i and solvent activity a_s [43]. Here M_s is the solvent molecular weight. The Pitzer model for the osmotic coefficient is given by Equations 2.44 and 2.45 where the parameters have the same meaning as above.

$$\ln a_s = -\phi M_s \sum_i m_i \quad (2.43)$$

$$\begin{aligned} (\phi - 1) = \frac{2}{\sum_i m_i} \left[\frac{-A_\phi I^{3/2}}{1 + b I^{1/2}} + \sum_c \sum_a m_c m_a (B_{ca}^\phi + Z C_{ca}) \right. \\ \left. + \sum_{c < c'} \sum m_c m_{c'} \theta_{cc'} + \sum_{a < a'} \sum m_a m_{a'} \theta_{aa'} + \dots \right] \quad (2.44) \end{aligned}$$

$$B_{MX}^\phi = \beta_{MX}^0 + \exp(-\alpha_1 I^{1/2}) \beta_{MX}^1 \quad (2.45)$$

2.4.5 Counterion Condensation - Manning-Oosawa Theory

The counterions to a charged polymer typically exhibit lower activity in solution than would be accounted for by acid equilibrium stoichiometry and Debye-Hückel theory [131]. The physical cause has been attributed to the high charge density in the vicinity of the polymer. This can overcome the thermal energy, trapping a counterion atmosphere [108].

A systematic limiting theory (applicable at zero polymer concentration) was put forward by Manning [131] who credits the terminology “counterion condensation” to Oosawa [108]. Experiments [109] and extensions to the theory [108] indicate the concentration dependence is weak making the limiting theory useful even at finite polymer concentrations. The theory’s accuracy at physiological ionic strength is more questionable, however good agreement has been found at elevated ionic strength in some cases [131]. This has led to its wide use [14, 46] and extensions providing better quantitative agreement have only been put forward recently [136, 137]. As such only the limiting theory is discussed here.

According to the theory, the onset of counterion condensation occurs when the *non-dimensional inverse charge density* (ξ , Equation 2.33) exceeds the *inverse magnitude of the counterion charge*, $|z|^{-1}$ [14, 108, 131]. The fraction of free counterions f_ξ is given by

Equation 2.47. Here λ_B is the Bjerrum length and b is the average spacing between unit charges along the polymer contour.

$$\xi = \frac{\lambda_B}{b} \quad (2.46)$$

$$f_\xi = \begin{cases} 1 & \text{if } \xi < |z|^{-1} \\ (\xi z)^{-1} & \text{if } \xi > |z|^{-1} \end{cases} \quad (2.47)$$

As a result of counterion condensation the charge density on the polymer is reduced to the critical value. For the calculation of electrostatic interactions an effective charge parameter ξ_{eff} is defined in Equation 2.48 [131].

$$\xi_{\text{eff}} = \begin{cases} \xi & \text{if } \xi < z^{-1} \\ z^{-1} & \text{if } \xi > z^{-1} \end{cases} \quad (2.48)$$

Manning provides Equation 2.49 for the activity coefficient of free counterions [131]. Here c_e is the molar stoichiometric counterion concentration and κ (Equation 2.34) accounts for added salt only. Note that in Equation 2.50 the counterion activity a_e as a function of c_e must be calculated using the combined effects of ion condensation and solution nonideality.

$$\ln \gamma_f = -\frac{2\pi N_A \lambda_B \xi_{\text{eff}} c_e}{1000 \kappa^2} \quad (2.49)$$

$$a_e = \gamma_f f_\xi c_e \quad (2.50)$$

To derive Equation 2.49 Manning uses the Debye-Hückel approximation for the screened potential and assumes the polymer can be modelled as a line charge within the screening radius. These assumptions are expected to break down at high ionic strength [131].

2.4.6 Weak Electrolyte Ionization Equilibrium

The phosphate in PBS and all polymers in this work are weak electrolytes. As noted in Section 2.4.4 the phosphate dissociation equilibrium influences ionic strength. The charge density on the polymeric species is a function of their degree of dissociation, influencing Coulomb interactions (Section 2.4.3), counterion condensation (Section 2.4.5) and Donnan equilibrium (Section 2.4.7).

The non-polymeric weak acid dissociation equilibrium is modelled using the Henderson-Hasselbalch Equation 2.51 [14, 16]. Here, to correct for solution nonideality, activities are substituted for the more commonly used concentrations [76, 122]. In Equation 2.51, pK_a is the negative logarithm of the acid dissociation constant K_a and a_{A^-} (dissociated), a_{AH} (associated) are the activities of the acid species.

$$pH = pK_a + \log \left(\frac{a_{A^-}}{a_{AH}} \right) \quad (2.51)$$

The pK_a of phosphate buffer solutions can be modelled in a manner consistent with the Pitzer activity model using Equation 2.52 [1, 43, 122, 138]. Here T is the temperature in Kelvin, R is the molar gas constant and all other parameters are as found in Table 2.4.

$$pK_{a,T} = \frac{pK_{a,\theta} R \ln(10) \frac{T}{T_\theta} - \Delta_r H_{p,\theta}^o \left(\frac{1}{T_\theta} - \frac{1}{T} \right) - \Delta_r C_{p,\theta}^o \left(\frac{T_\theta}{T} - 1 + \ln \left(\frac{T}{T_\theta} \right) \right)}{R \ln(10)} \quad (2.52)$$

Polymeric weak electrolytes including polyampholytes can be modelled using a modified form of the Henderson-Hasselbalch equation [47]. Here Equation 2.53 is for acid functional groups and Equation 2.54 is for bases where α and β are the respective fractional dissociations. In both cases pK'_i is the apparent acid dissociation constant of the species and may differ from pK_i , the intrinsic dissociation constant of the monomer [47, 139]. Provided a lower threshold is exceeded, pK'_i is only a weak function of ionic strength; however in polyampholyte systems it can be strongly influenced by the degree of acid/base substitution via neighbour interactions [47, 61, 62].

$$pH = pK'_\alpha + \log \left(\frac{\alpha}{1 - \alpha} \right) \quad (2.53)$$

$$pH = pK'_\beta + \log \left(\frac{1 - \beta}{\beta} \right) \quad (2.54)$$

To model pK'_i the approach of Katchalsky et al. [61–63] is highly recommended [20, 47]. Their simplest model (Equations 2.55 to 2.58) deals with polyampholytes with two types of monomers and assumes all species of one type have the other as a nearest neighbour. They assert that this assumption holds reasonably well provided the scarcest species does not represent more than a third of the total [61].

$$pK'_\alpha = pK_\alpha - \Delta pK_{\text{Short}} + \Delta pK_{\text{Long}} \quad (2.55)$$

$$pK'_\beta = pK_\beta + \Delta pK_{\text{Short}} + \Delta pK_{\text{Long}} \quad (2.56)$$

Table 2.4: Ionization Correlation Parameters for Phosphate Buffers

Reaction	$pK_{a,\theta}$	$\Delta_r H_{p,\theta}^o$ kJ mol ⁻¹	$\Delta_r C_{p,\theta}^o$ J mol ⁻¹ K ⁻¹	T_θ K
$\text{H}_3\text{PO}_4 \rightleftharpoons \text{H}^+ + \text{H}_2\text{PO}_4^-$	2.148	-8.0	-141	298.15
$\text{H}_2\text{PO}_4^- \rightleftharpoons \text{H}^+ + \text{HPO}_4^{2-}$	7.198	3.6	-230	298.15
$\text{HPO}_4^{2-} \rightleftharpoons \text{H}^+ + \text{PO}_4^{3-}$	12.35	16.0	-242	298.15

Parameters from [1] for use with Equation 2.52

$$\Delta p K_{\text{Short}} = 0.4343 \frac{\epsilon^2}{r D_E k_B T} \quad (2.57)$$

$$\Delta p K_{\text{Long}} = 0.8686 \lambda_B \frac{(\nu - \zeta)}{h} \ln \left(1 + \frac{6h}{\kappa h_0^2} \right) \quad (2.58)$$

Equation 2.55 models short range positive/negative neighbour interactions where r is the average distance between the centres of the charged groups, D_E is the effective dielectric constant in the vicinity of the charge couple, k_B is the Boltzman constant and T is the absolute temperature. D_E may be appreciably lower than the dielectric constant of the surrounding water [61].

Equations 2.58 models long range electrostatic effects. Here λ_B is the Bjerrum length (Equation 2.33), ζ (positive) and ν (negative) are the mean number of charged groups on a polymer molecule, κ is the inverse Debye length (Equation 2.34), h is the polymer end to end distance and h_0 is the root mean squared end to end distance in the absence of the electrostatic field [62, 63].

Parameter estimates for N-succinyl-chitosan and oxidised-alginate can be found in 1.2. Assumption checks regarding which parts of the Katchalsky model are significant for the system under study can be found in Section 2.6.2.

2.4.7 Gibbs-Donnan Equilibrium - Ion Partition due to Charged Polymers

Gibbs-Donnan equilibrium arises in systems where some charged groups are “fixed” in one phase but other ions can diffuse across the phase boundaries. This describes poly-electrolyte gel swelling and membrane osmometry (see Figure 2.1). The “fixed” charge constrains ion movement, repelling coions and keeping an excess of counterions on the polymer side of the boundary (*internal* phase). This is opposed by entropic driving forces which promote concentration equalization. The result is a mobile ion imbalance across the phase boundary which depends not only on the polymer concentration but also on the concentration of added salts.

Equations 2.59 or 2.60 are used to estimate the difference in solvent chemical potential arising from the mobile ion imbalance. Equation 2.59 provides the theoretically exact solution taking into account solution nonideality by using the formal definition of the osmotic coefficient ϕ (see Section 2.4.4) [26]. As far as the author is aware, this is not used to model hydrogel swelling anywhere in the open literature. Equation 2.60 is widely used [14, 16, 26] but similar to Equation 2.15 requires several dilute solution approximations in its derivation. Here quantities associated with the *surroundings* are denoted with a star as in ϕ^* , M_1 is the solvent molecular weight and \bar{V}_1 is the solvent specific volume. Mobile ionic species concentrations are given by m_i (molal) and c_i (molar). Note that the difference

in concentration units between the two equations is an artefact of usage. Though similar equations for each approach exist, ϕ is not frequently used with the molar system [43]

$$\Delta\mu_{1,ionic}^{internal} - \Delta\mu_{1,ionic}^{surroundings} = M_1 RT \left(\phi \sum_i m_i - \phi^* \sum_i m_i^* \right) \quad (2.59)$$

$$\Delta\mu_{1,ionic}^{internal} - \Delta\mu_{1,ionic}^{surroundings} \approx \bar{V}_1 RT \sum_i (c_i - c_i^*) \quad (2.60)$$

In his paper Donnan [140] derives a thermodynamic relationship for the ratio of mobile ion concentrations across the phase boundary. Though he limits discussion to ideal solutions, the approach is applicable to nonideal solutions [113], provided activities a_i are substituted for concentrations [14, 113, 141]. Equation 2.61 provides the equilibrium relationship between the Donnan ratio f_D and the activities of any mobile ionic species i [113, 140, 142]. Note the ion charge z_i is a signed quantity and that f_D has the same value for all *mobile* ions at equilibrium.

$$f_D = \left(\frac{a_i}{a_i^*} \right)^{1/z_i} \quad (2.61)$$

Polymer concentration is introduced to the model through the electroneutrality condition Equation 2.62 [14, 26, 113, 140, 141]. Note that the summation includes the polymer and that concentrations are used rather than activities [142]. For polyampholytes only the net charge on the polymer influences Gibbs-Donnan equilibrium [113, 142]. For polyelectrolytes and unbalanced polyampholytes, counterion condensation may have a significant effect; however according to Chan [14] this is neglected in the majority of literature derivations.

$$\sum_j z_j c_j = 0 \quad \text{OR} \quad \sum_j z_j m_j = 0 \quad (2.62)$$

From Equation 2.61 it can be seen that if f_D is known, the concentration of any ionic species can be calculated provided all the concentrations in one phase are also known. In practical experiments the concentrations in the *surroundings* can be known with reasonable certainty by use of an infinite reservoir approximation. f_D is therefore the primary unknown. The general solution (Equation 2.63) can be obtained by substituting Equations 2.31 and 2.61 into Equation 2.62, where c_e and f_ξ are polymer quantities from Manning-Oosawa theory (Section 2.4.5) and \pm is the sign of the polymer net charge.

$$\pm f_\xi c_e + \sum_i z_i \frac{\gamma_i^*}{\gamma_i} c_i^* f_D^{z_i} = 0 \quad (2.63)$$

Analytical solutions have been derived for special cases, most commonly 1:1 salts, where the relationship for f_D takes quadratic form, Equation 2.64 [14, 16, 107, 141, 142].

As $|b| < \sqrt{b^2 + 4ac}$ for all b and f_D must be positive, only the additive branch of the quadratic gives a physically valid solution. This is implicitly indicated in Chan's equations [14] but in the knowledge of the author is not explicitly stated anywhere in the open literature.

$$a = \sum_i \frac{\gamma_i^*}{\gamma_i} c_i^{*(+1)} \quad b = \pm f_\xi c_e \quad c = \sum_i \frac{\gamma_i^*}{\gamma_i} c_i^{*(-1)} \quad (2.64)$$

$$f_D = \frac{-b + \sqrt{b^2 + 4ac}}{2a}$$

The non-linear form of the equations is a challenge to practical usage in osmometry where f_ξ is an unknown of interest.

2.4.8 Concentration Unit Conversions

Three different concentration units are used in the above theories. Each has advantages and disadvantages: 1) molal concentration (m), is easiest to prepare and is used by Pitzer but may be difficult to convert to volumetric concentration, 2) volume fraction (Φ), is theoretically exact in Flory-Huggins theory but difficult to measure, and 3) mass per volume concentration (ρ^*), is unusual but must be used for polymers during osmometry due to unknown molecular weight. Exact conversions are possible from m to molar concentration (c) using Equation 2.65, c to Φ using Equation 2.66 and c to ρ^* using Equation 2.67 [42, 143]. The key parameters required for the conversions are solution density ρ_s , partial molar volume \bar{V} and molecular weight M . Note that in Equation 2.65 the solvent is given subscript 1 and for m in mol/kg, M must be expressed in kg/mol.

$$c_i = \frac{m_i \rho_s}{1 + \sum_{j=2}^n m_j M_j} \quad i \neq 1 \quad (2.65)$$

$$\Phi_i = \bar{V}_i c_i \quad (2.66)$$

$$\rho^* = c_i M_i \quad (2.67)$$

For the volume fraction conversion, \bar{V} can be calculated using Equations 2.68 and 2.69 provided solution density is known for a range of concentrations [43]. Here V_i is volume, n_i is number of moles and ${}^\Phi V_i$ is apparent molar volume. Subscript 1 is for the pure solvent, subscript 2 is for the solute and subscript s is for the solution.

$${}^\Phi V_2 = \frac{1}{n_2} (V_s - V_1) \quad (2.68)$$

$$\bar{V} = {}^\Phi V + m \frac{d{}^\Phi V}{dm} \quad (2.69)$$

Reference solution density can be calculated using Equations 2.70 to 2.73 [143]. (Here the logic has been extended to n component systems.) The equations are derived by considering hypothetical solution sub volumes each containing a single salt with concentrations and volumes selected such that the solvent has same partial molar volume in all partitions. Assuming components do not strongly interact and there is no phase change upon mixing this approach is consistent with that of Söhnel [143]. Temperature T is in in °C for all equations. $c_{s,i}$ is the molar concentration of the i^{th} salt. Pure solvent density (ρ_o) is given for water by Equation 2.71 [143]. α_i and β_i are fit coefficients to solutions of the pure components (Equations 2.72 and 2.73, with parameters Table 2.5) [143]. Note parameters for minor component divalent salts are not available at the 40°C test temperature however in PBS their contribution is very minor and therefore the error introduced using these values is small. These equations cannot be used for the sample as the polymer parameters are unknown.

$$\rho_s = \rho_o + \sum \alpha_i c_{s,i} - \left(\sum \beta_i^{2/3} c_i \right)^{3/2} \quad (2.70)$$

$$\rho_{H_2O} = 999.65 + 2.0438 \cdot 10^{-1} T - 6.1744 \cdot 10^{-2} T^{3/2} \quad (2.71)$$

$$\alpha_i = A + B T + C T^2 \quad \text{or} \quad G \quad (2.72)$$

$$\beta_i = D + E T + F T^2 \quad \text{or} \quad H \quad (2.73)$$

2.5 Linearised Model Derivation for Membrane Osmometry

The starting point for the derivation is provided by Equation 2.2, reproduced here:

$$\Delta\mu_{1,ionic}^{sample} - \Delta\mu_{1,ionic}^{reference} = \Delta\mu_{1,mixing} + \Delta\mu_{1,osmotic\ pressure}$$

Without approximation, Donnan equilibrium provides $\Delta\mu_{1,ionic}^{sample} - \Delta\mu_{1,ionic}^{reference}$ via Equation 2.59 and the van't Hoff equation provides $\Delta\mu_{1,osmotic\ pressure}$ via Equation 2.14.

In swelling models, the customary approach for the mixing term is to use Flory-Huggins theory, Equation 2.18, for $\Delta\mu_{1,mixing}$ [14–16, 26]; however doing so implicitly assumes the absence of salt. This is discussed in more detail in Section 2.5.1.

Considering all three terms, it is a challenge to getting this unwieldy theory into a form that “represents the facts with enough accuracy” while still being simple enough to use [122]. To approach this objective, the polymer will be treated in the dilute approximation, but solution nonideality due to physiologically significant ionic strength will be treated as precisely as feasible. Three major challenges exist: 1) linearization and interpretation of the $\ln(\Phi_1)$ term in Equation 2.18, given that the implicit presence of salt affects the solvent volume fraction, Φ_1 ; 2) extraction of the Donnan salt exclusion factor, f_D , from the Donnan equilibrium expression (cubic for phosphate buffer due to salts with -2 charge), and 3) standardization of concentration units across equations.

Table 2.5: Density Estimation Parameters for Phosphate Buffered Saline

Salt	A $\times 10^1$	B $\times 10^{-2}$	C $\times 10^{-4}$	D $\times 10^0$	E $\times 10^{-2}$	F $\times 10^{-3}$	G $\times 10^1$	H $\times 10^1$	Temp °C
KCl	4.971	-7.150	6.506	-2.376	0	0	—	—	0-100
NaCl	4.485	-9.634	6.136	-2.712	1.009	0	—	—	0-100
KH ₂ PO ₄	10.01	-58.70	70.83	-7.676	38.06	-4.561	—	—	0-80
NaH ₂ PO ₄	7.649	52.07	-61.42	1.086	-26.60	2.497	—	—	20-80
K ₂ HPO ₄	—	—	—	—	—	—	15.41	-15.28	18
Na ₂ HPO ₄	—	—	—	—	—	—	8.916	-8.060	25

Parameters from [143] for use with Equations 2.72 and 2.73

2.5.1 Salt Effects in Linearised Flory-Huggins Theory

To address ambiguity regarding the solution volume fraction term in Flory-Huggins theory $\ln(\Phi_1)$, we wish to linearise it here using the same approach used for neutral polymer theory but explicitly including salt. To do so we take a step back from the conventional approach and model the terms in Equation 2.74 using the three component Flory-Huggins theory Equation 2.19. Throughout the derivation starred parameters, e.g. $\Delta\mu_1^*$, are for the polymer-free reference solution, subscript 1 refers to solvent, subscript 2 to the sum of all salts treated as a single component and subscript 3 to the polymer. Precedence for using Flory-Huggins theory for solvated ion mixing exists [43]; however the approach taken here is in the author's knowledge, unique in the open literature.

$$\Delta\mu_1 - \Delta\mu_1^* = \Delta\mu_{1,ionic}^{sample} - \Delta\mu_{1,ionic}^{reference} - \Delta\mu_{1,mixing} \quad (2.74)$$

Using Equation 2.19 and noting $\Phi_3^* = 0$ results in Equation 2.75.

$$\begin{aligned} \frac{\Delta\mu_1 - \Delta\mu_1^*}{RT} &= \ln(\Phi_1) - \ln(\Phi_1^*) - \frac{\Phi_2 - \Phi_2^*}{x_{12}} - \chi_{12} \Phi_2^{*2} \\ &+ (\chi_{12} \Phi_2 + \chi_{12} \Phi_3)(\Phi_2 + \Phi_3) - \frac{\Phi_3}{x_{13}} - \chi_{23} \frac{\Phi_2 \Phi_3}{x_{23}} \end{aligned} \quad (2.75)$$

Substituting Equations 2.22 and 2.23 and truncating the series after the second term results in Equation 2.76, where the maximum truncation error is given by Equation 2.77.

$$\begin{aligned} \frac{\Delta\mu_1 - \Delta\mu_1^*}{RT} &= \frac{\Phi_3}{x_{13}} + \left(\frac{1}{2} - \chi_{13}\right) \Phi_3^2 \\ &- \left(1 - \chi_{13} - \frac{\chi_{23}}{x_{23}}\right) \Phi_2 \Phi_3 \\ &- \frac{\Phi_2 - \Phi_2^*}{x_{12}} - \left(\frac{1}{2} - \chi_{12}\right) (\Phi_2^2 - \Phi_2^{*2}) \end{aligned} \quad (2.76)$$

$$\%error = \frac{-x - \frac{1}{2}x^2 - \ln(1-x)}{\ln(1-x)} \times 100\% \quad ; \quad x = \Phi_2 - \Phi_3 \quad (2.77)$$

Examining the right hand side of Equation 2.76 the first line is the customary linearised form of the neutral polymer mixing term (Equation 2.24), the second line contains terms accounting for polymer salt interactions and the third line is the form nonideal Donnan equilibrium would take if the linearised activity equation were derived using the Flory-Huggins approach. Setting this part aside to be evaluated by the more accurate theory, the correct linear form for ionic polymer mixing is therefore:

$$\frac{\Delta\mu_{1,mixing}}{RT} = \frac{\Phi_3}{x_{13}} + \left(\frac{1}{2} - \chi_{13}\right) \Phi_3^2 - \left(1 - \chi_{13} - \frac{\chi_{23}}{x_{23}}\right) \Phi_2 \Phi_3 \quad (2.78)$$

Using experimental records, Equations 2.25 and Table 1.2 to estimate polymer volume fraction and Equations 2.66 and 2.68 through 2.73 to estimate the combined salt volume fraction, the most conservative estimate for series truncation error in osmometry experiments is less than 0.05% (I = 1.6, ~0.5 wt% polymer). From this we conclude experimental error and theory approximations far outweigh the linearization error.

2.5.2 Linear Donnan theory for Membrane Osmometry

Three challenges are addressed in formulating the linear theory, namely: 1) the extent to which solution nonideality must be considered, 2) the mathematical manipulations required to arrive at a simple enough equation to use, and 3) how to use the convenient 1:1 form when small fractions of 1:2 ions are present.

Osmotic and activity coefficients, ϕ and λ_i respectively, appear in the exact equations for the Donnan term ($\Delta\mu_{1,ionic}^{sample} - \Delta\mu_{1,ionic}^{reference}$, Equations 2.59, 2.61 and 2.31). Using Pitzer's model as described in Section 2.6.1 it is estimated that an error between 4 and 9% is produced by omitting the osmotic coefficient entirely. The same approach indicates that approximating osmotic coefficients and ion activity as identical in the sample and reference solutions is feasible ($\phi = \phi^*$, $\lambda_i = \lambda_i^*$). From the worst case low salt osmometry experiment in Chapter 6 a Donnan partition coefficient of $f_D = 1.04$ is obtained. This results in respective errors of 0.01% and 0.6% for ϕ^* and λ_i^* . Using these approximations Equation 2.79 can be written.

$$\Delta\mu_{1,ionic}^{internal} - \Delta\mu_{1,ionic}^{surroundings} = M_1 RT \phi^* \sum_i (f_D^{z_i} - 1) m_i^* \quad (2.79)$$

To allow further simplification an assumption of 1:1 ions is desirable. For the 1:1 case, with the approximations discussed above, Equation 2.64 can be written as Equation 2.80. Here the polymer equivalent charge concentration m_e is expressed in terms of average

repeat unit charge i and repeat unit molality $m_{3,r}$. Subscript 3 for the polymer is for consistency with the previous section.

$$a = \sum_i m_i^{*(+1)} \quad b = \pm f_\xi i m_{3,r} \quad c = \sum_i m_i^{*(-1)} \quad (2.80)$$

$$f_D = \frac{-b + \sqrt{b^2 + 4ac}}{2a}$$

Similarly Equation 2.79 can be written as Equation 2.81 and the electroneutrality condition (Equation 2.62) can be written for the sample and reference phases respectively as Equations 2.82 and 2.83. Here a , b and c have their Equation 2.80 definitions.

$$\Delta\mu_{1,ionic}^{internal} - \Delta\mu_{1,ionic}^{surroundings} = M_1 RT \phi^* \left(f_D a + \frac{1}{f_D} c - a - c \right) \quad (2.81)$$

$$b + f_D a = \frac{1}{f_D} c \quad (2.82)$$

$$a = c \quad (2.83)$$

From here a series of mathematical manipulations will result in the final simplified form. First, Equations 2.82 and 2.83 are substituted into Equation 2.81 eliminating c .

$$\Delta\mu_{1,ionic}^{internal} - \Delta\mu_{1,ionic}^{surroundings} = M_1 RT \phi^* (f_D a + b + f_D a - a - a) \quad (2.84)$$

Next the expression is simplified, Equation 2.80 is substituted for f_D and c is again eliminated using Equation 2.83.

$$\Delta\mu_{1,ionic}^{internal} - \Delta\mu_{1,ionic}^{surroundings} = M_1 RT \phi^* \left(2a \left(\frac{-b + \sqrt{b^2 + 4a^2}}{2a} \right) + b - 2a \right) \quad (2.85)$$

Finally the $2a$ terms associated with the ratio and b terms outside of square-root are cancelled with one another.

$$\Delta\mu_{1,ionic}^{internal} - \Delta\mu_{1,ionic}^{surroundings} = M_1 RT \phi^* \left(\sqrt{b^2 + (2a)^2} - 2a \right) \quad (2.86)$$

To expand the root a binomial series approximation is used (Equation 2.87). Truncating after the the second term and substituting in for a and b results in Equation 2.86. The truncation error is given by Equation 2.89. In this work the worst case osmometry experiment truncation error is less than 0.1 ppm indicating that the approximation is merited.

$$\sqrt{b^2 + (2a)^2} = 2a(1 + x)^{1/2} = 2a + ax + \dots, \quad x = \left(\frac{b}{2a} \right)^2 \quad (2.87)$$

$$\Delta\mu_{1,ionic}^{internal} - \Delta\mu_{1,ionic}^{surroundings} = M_1 RT \phi^* \frac{b^2}{4a} = \frac{1}{2} M_1 RT \phi^* (f_\xi i)^2 \frac{m_{r,3}^2}{\sum_i m_i^*} \quad (2.88)$$

$$\text{error in ppm} = \left(\frac{2a + \frac{1}{4}a^{-1}b^2}{\sqrt{b^2 + 4a^2}} - 1 \right) \times 10^6 \text{ ppm} \quad (2.89)$$

To use Equation 2.88 with PBS the issue of 1:2 ions must be addressed. A numerical approach is proposed here. First an initial guess d is selected for f_D (Equation 2.90). This allows summations involving $f_D^{z_i} z_i m_i$ to be written as in Equation 2.91. Examining the form we define 1:1 equivalents for the m_i and z_i of -2 ions.

$$f_D^{-2} = d f_D^{-1} \quad (2.90)$$

$$f_D^{-2} 2 m_i = f_D^{-1} 2 d m_i \quad (2.91)$$

$$m_i, \text{ 1:1 equivalent} = 2d m_i \quad , \quad z_i, \text{ 1:1 equivalent} = -1 \quad (2.92)$$

This approximate approach hinges on the assumption that -2 ions are not influential. The system can be solved by using an initial guess of $d = 1 \approx f_D$ to fit the full regression model, back calculating f_D using Equation 2.64 and iterating until convergence is reached. If the approximation is appropriate neither the coefficients nor error estimates obtained from the regression model should change significantly between the initial estimate and the final converged system.

2.5.3 Assembly as a Regression Model

The model is assembled by taking Equation 2.2 and substituting: 1) Equation 2.86 for the ionic term, 2) Equations 2.78 and 2.66 for the mixing term, and 3) Equation 2.14 for the pressure term. Dividing through by $\bar{V}_1 RT \rho_3^*$ results in the final form of the model.

$$\begin{aligned} -\frac{\Pi}{RT \rho_3^*} = & \frac{1}{X_n M_{r,3}} + \left(\frac{1}{2} - \chi_{13}\right) \frac{\bar{V}_{r,3}^2}{\bar{V}_1 M_{r,3}^2} \rho_3^* \\ & - \left[(1 - \chi_{13}) \frac{\bar{V}_{r,3} \bar{V}_2}{\bar{V}_1 M_{r,3}} - \chi_{23} \frac{\bar{V}_2^2}{\bar{V}_1 X_n M_{r,3}} \right] c_2 \\ & - \frac{M_1}{2 \bar{V}_1} (i f_\xi)^2 \frac{\phi^* m_{r,3}^2}{\rho_3^* \sum_i m_i^*} \end{aligned} \quad (2.93)$$

This equation is of the form given in Equation 2.94 where y is the reduced osmotic pressure and all three x 's are linearly independent of each other. Here $x_1 = \rho_3^*$ is the

polymer concentration, $x_2 = c_2$ is the salt concentration and $x_3 \approx x_1/x_2$ is the ratio of polymer and salt charge concentrations. Note: $m_{r,3} \approx c_{r,3} = \rho_3^*/M_{r,3}$ and $\sum_i m_i^* \approx c_2$.

$$y = \beta_0 + \beta_1 x_1 + \beta_2 x_2 + \beta_3 x_3 \quad (2.94)$$

x_3 should properly be given by Equation 2.95, however the largest uncertainty in the ionic term is the $(i f_\xi)$ value. Theoretically, $(i f_\xi)$ is expected to be constant with respect to polymer concentration and *nearly* constant with respect to salt concentration. Fitting with x_3^* provides an average value for $i f_\xi$ with respect to ionic strength and allows the theoretical uncertainty to be addressed. If the estimate is in good agreement with theory, a fit with the theoretical form for $i f_\xi$ can be used. Otherwise theoretical uncertainty is a source of overall error.

$$x_3 = (i f_\xi)^2 \frac{\phi^* m_{r,3}^2}{\rho_3^* \sum_i m_i^*} \approx \frac{(i f_\xi)^2 \phi^* \rho_3^*}{M_{r,3} c_2} \quad , \quad \beta_3 = -\frac{M_1}{2 \bar{V}_1} \quad (2.95)$$

$$x_3^* = (i f_\xi)^{-2} x_3 \quad , \quad \beta_3^* = (i f_\xi)^2 \beta_3 \quad (2.96)$$

Interpretation of the β 's is as follows: $\beta_0 = 1/M_n$ provides the number average molecular weight, β_1 can be recognised as the A_2 of classical osmometry, β_2 will be covered shortly, and β_3 is the Donnan term already discussed in terms of the x_3 definition.

2.5.4 Discussion

The regression model was assembled using mixed concentration units. The preferred approach would be to use the same units for all equations. Conversions are listed in Section 2.4.8; however the unknown polymer solution density must be used to convert between the volumetric concentrations required for Flory-Huggins theory and the gravimetric concentrations required to use Pitzer theory. As this cannot be accomplished without unacceptably high error, mixed concentration units must be used.

Mixed units are possible because all terms in Equation 2.2 are in the form of chemical potential differences. These *differences* are independent of the concentration units used to evaluate activity [43] provided each term is evaluated in an internally consistent manner (the scale base offset may change, but this is eliminated when the difference is taken). The implications for experiments are that both molar and molal concentrations need to be known so the correct units can be used when evaluating equations.

In the regression model β_2 is the salt effect on the polymer solvent interaction. It is often assumed to be 0 with the justification that all salt interactions are long range. β_2 comes in two halves. The first half is the impact of salt on polymer water contact which in the context of Flory-Huggins theory is not expected to be small (value on the order of 1).

The second half is the impact of polymer-salt interaction on the polymer water interaction which might be reasonably assumed negligible. It depends on the ratio of χ_{23}/X_n where the numerator is expected to be less than 1 and the denominator contains the degree of polymerization which is on the order of 100. Assuming second half is negligible might allow an internal check of theory based on $\bar{V}_{r,3}$ and χ_{13} .

The linear model derivation requires three key assumptions, namely: 1) solutions are dilute with respect to both polymer and total salt content, 2) ion activity coefficients and the solvent osmotic coefficient are identical in sample and reference compartments and 3) the effect of non 1:1 type ions is negligible. The first two were shown to introduce negligible error in this work. The last must be checked at the time of experiment.

2.6 Numerical Simulations

2.6.1 Reference Solution Model

The osmotic coefficient is needed to evaluate the ionic term during data analysis in Chapters 6 and 7. Ion activities are used to accurately model buffer ionization and to check linearization assumptions in Section 2.5.2.

In this work the reference solution is based on Dulbecco's phosphate buffered saline [144] with Ca and Mg omitted. NaCl is added or removed from the recipe to adjust ionic strength as needed. For analysis of experimental data, precise records of test conditions can be used. Molal concentrations are known for all species, and the hydronium activity is known via pH meter readings taken during solution preparation (adjusted to 7.40 at 40 °C). The latter factor means though total phosphate is known from experimental records, species partition must be calculated from a model.

Phosphate is polyprotic, however it can be treated as monoprotic with $\text{p}K_{a,2} = 7.61$ at 40 °C. Figure 2.2 shows the equilibrium species partition when all three ionization equilibria are considered. The two species involved in a single equilibrium reaction dominate the region between pH 5 and 10. When preparing the figure, ionic strength effects were not considered, however from full model results (not shown) the effect of ionic strength on the equivalence point is too small to invalidate the approximation. Noting that the figure uses a log scale, the error involved in the monoprotic approximation is expected to be completely negligible.

Sufficient information is available to solve the system, however phosphate concentration and activities interact via ionic strength. An iterative numerical solution was implemented in Excel VBA using the Pitzer Model (Section 2.4.4) and the Henderson-Hasselbalch equation (Section 2.4.6). To validate the simulation, results for pure salts were compared to a textbook reference (Figure 2.3a), and to a similar analysis conducted by Chan (Figure 2.3d) vs [14] Fig 2.6).

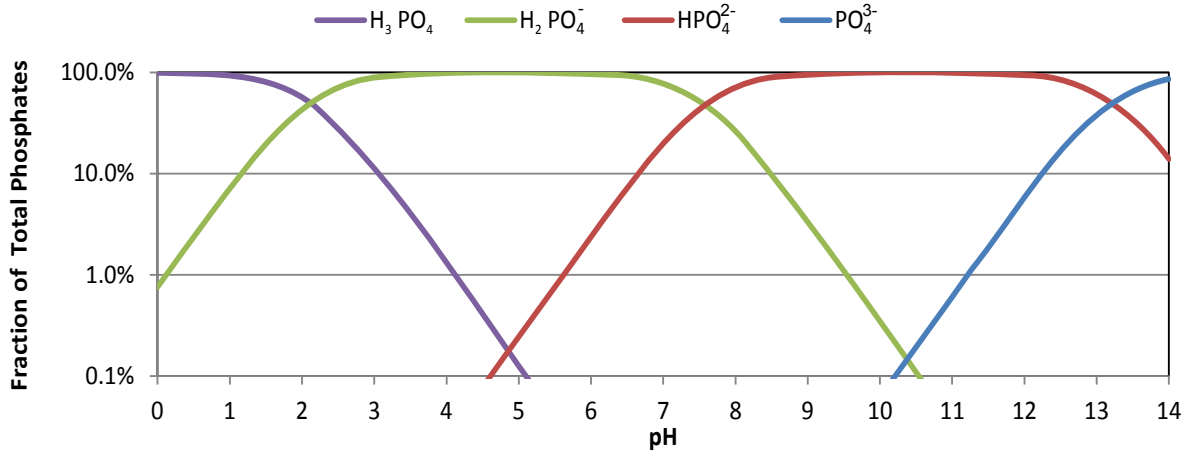


Figure 2.2: Phosphate Species Present as a Function of pH: Calculated using Equation 2.51, pKa values from Equation 2.52 at 40°C

2.6.2 Polymer Ionization Model

As recommended the Katchalsky model will be used in this work for polyampholyte ionization calculations. The long range interaction term (Equation 2.58) introduces three challenges, namely: 1) it does not account for ion condensation, 2) it contains molecular weight information, and 3) it introduces non-linearity by making fractional ionization dependent on polymer net charge.

Ion-Condensation

Incorporating ion-condensation is relatively easy. Katchalsky's work was part of the inspiration for Manning and strong similarities exist in the two theories. Comparing Katchalsky (Equation 2.58) to Manning (Equation 2.46) we find the Manning-Oosawa critical charge density ξ as a parameter group in the earlier theory (Equation 2.97). Based on this observation, Katchalsky theory can be modified to include ion condensation by substituting the apparent charge density fraction (ξ_f) for $\lambda_B \frac{\nu - \xi}{h}$ as in Equation 2.98.

$$\xi = \frac{\lambda_B}{b} = \lambda_B \frac{\nu - \xi}{h} = \lambda_B \frac{i}{l} \quad (2.97)$$

$$\Delta pK_{\text{Long}} = 0.8686 \xi_f \ln \left(1 + \frac{6h}{\kappa h_0^2} \right) \quad (2.98)$$

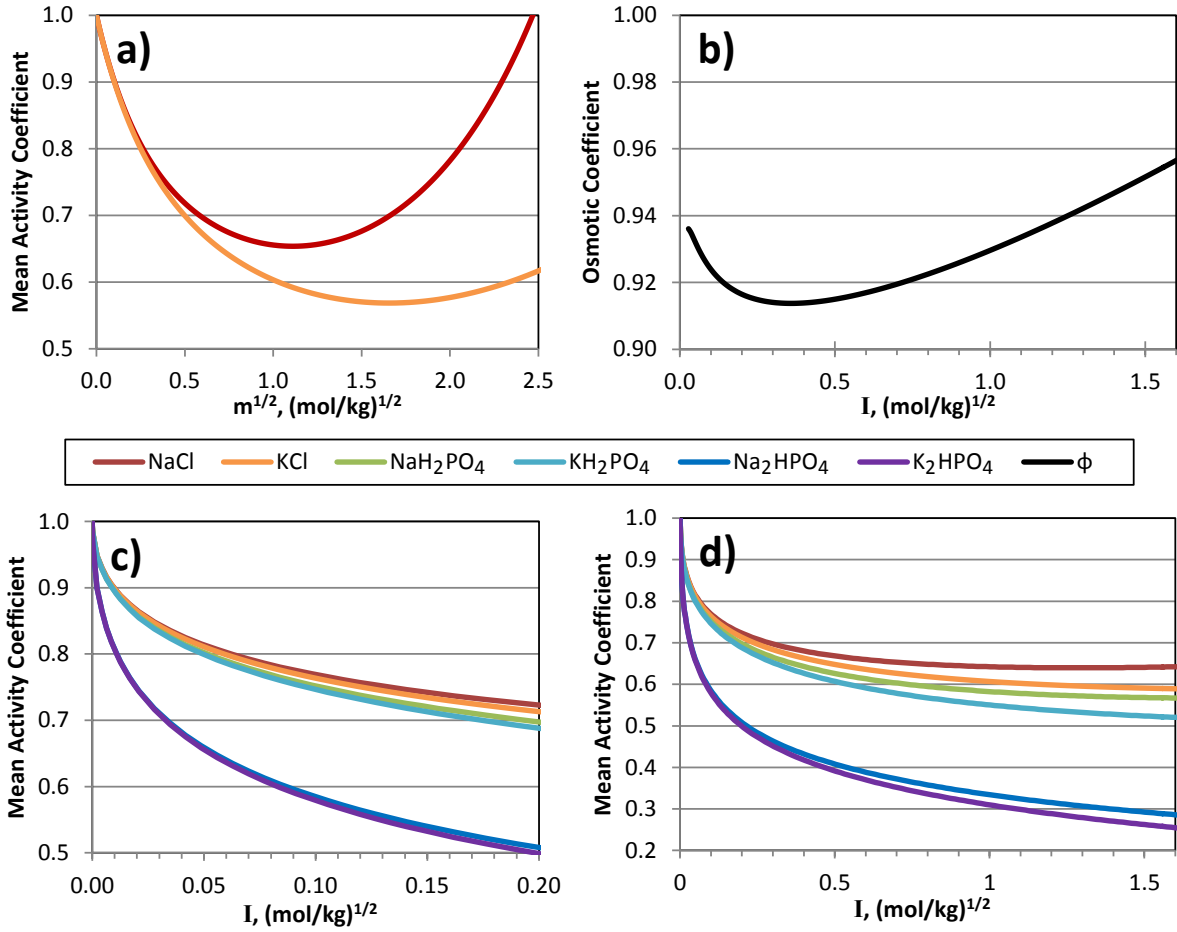


Figure 2.3: Pitzer Model Results: a) reproduction of [129, Fig. 3.28] to validate model, b) osmotic coefficient for full experimental range, c) and d) ion activities for Chapter 6 experimental ranges.

Molecular Weight Elimination and Model Setup

Via degree of polymerization X_n , molecular weight information is contained in three terms of Katchalsky's theory, namely: 1) the polymer length h , Equation 2.99 [26]; 2) the root mean squared polymer length h_o , Equation 2.100 [26], and 3) the average chain net charge $(\nu - \xi)$, Equation 2.101. All appear in ratios $(\nu - \xi)/h$ and h/h_o^2 allowing X_n to be eliminated and monomeric equivalents substituted.

$$h \approx l X_n \quad (2.99)$$

$$h_o \propto r_{rms} = \left[b^2 + (2a)^2 \frac{(1 - \cos \theta)}{(1 + \cos \theta)} \right]^{1/2} X_n^{1/2} \quad (2.100)$$

$$\nu - \xi = i X_n \quad (2.101)$$

The reference state for h_0 is a solution with all charges turned off but the “same solubility, steric hindrances, and hydrogen bonding” [63]. As such it is proportional to the root mean squared end to end distance r_{rms} but will not be exactly equal to the value calculated by Equation 2.100 which is for a completely unperturbed polymer [26].

Equation 2.100 assumes a simplified geometric model for 1-4 linked cellulosic polymers where only two bonds types are considered; 1) effective ether bonds with length $a = 0.2715$ nm, angle $\theta = 110^\circ$ and about which rotation can occur and 2) the saccharide ring, treated as an effective bond between the 1-4 carbons, with length $b = 0.2715$ nm, angle 90° , and about which rotation *cannot* occur.

In Equation 2.99, l is the monomer contour length which can be estimated from the same structural model used for Equation 2.100. It is approximately 0.53 nm for the fully extended chain.

The average monomer charge i is given by Equation 2.102. It allows calculation of m_e in Donnan theory (Section 2.5.2), and allows evaluation of ξ in Manning-Oosawa theory via the last form of Equation 2.97. For this calculation acidic (x_α) and basic (x_β) monomer degrees of substitution are determined in Chapter 3. The respective fractional ionizations α and β can be evaluated using Equations 2.55 and 2.56, but i is an input into these equations via Equation 2.97 making the system highly non-linear.

$$i = \alpha x_\alpha - \beta x_\beta \quad (2.102)$$

Term Significance Checks

Before embarking on a numerical solution it is wise to evaluate which terms of the model are significant. pK_{Short} (Equation 2.57) is only for polyampholytes and as such is only be significant for N-succinyl-chitosan. ΔpK_{Long} (Equation 2.98) is the salt / charge interaction and might be significant for both.

In ΔpK_{Short} , two polymer specific parameters exist, namely 1) the average ion size parameter r , and 2) the dielectric constant inside the polymer molecule D_E [61, 145]. From activity data, r is approximately ~ 0.4 nm for the primary-amine / carboxylic-acid pair in N-succinyl-chitosan [58, 146]. Due to a similar polar structure polysaccharides tend to have minimal effect on the dielectric constant of aqueous solutions[147] making that of water a good approximation in this case. Substituting these values into Equation 2.57 results in $\Delta pK \approx 0.80$.

To estimate the significance of ΔpK_{Long} estimates of f_ξ , κ^{-1} and $6h/h_0^2$ are required. At a first approximation, we consider the worst case scenario of extreme ionic strength

and a fully charged fully extended polymer. From experimental records in Chapter 6 and using Section 2.6.1, the ionic strength extremes in this work are $I = 0.075$ to 1.6 resulting in $\kappa^{-1} = 1.14$ to 0.25 nm. Using Equation 2.100 to estimate h_0 , and Equation 2.99 to estimate h for the fully extended chain, results in $6h/h_0^2 = 5.09$ nm⁻¹. From Manning theory $\xi_f \leq 1$. Substituting these values into Equation 2.98 gives $\Delta pK_{\text{Long}} = 1.4$ to 0.8 .

Noting that all experiments are conducted at a pH of 7.40 and examining the alginate and chitosan pK'_α estimates in Table 1.2, all interaction effects on acid group ionization are expected to be insignificant. At this pH the polymers are expected to have a predominantly negative charge. Under this condition the long and short range terms oppose each other for the acid groups. All acid groups are almost completely disassociated and a pK'_α shift of ± 1.4 will not change this significantly. The chitosan amine ionization is significantly affected. Its pK'_β is near the experimental range and for in this case the effect of both terms is additive.

Model Approach and Results

Parameter estimates to model polymer ionization are found in Table 1.2. The alginate ionization assumption was checked using Equation 2.53. As expected it was close to 1.00 for all cases. Equations 2.53 to 2.57, 2.98 were used to model N-succinyl-chitosan. The model was solved in Excel using the Gauss-Seidel method with a relaxation factor of 0.5 on β . To validate the model a simulation of Saito and Tanioka's experiment was conducted. When our simulation (Figure 2.4a) is compared to their results, reasonable agreement is observed, particularly for the location of the isoelectric point [56]. Ionization results across the whole experimental amine substitution range at the experimental pH of 7.40 are shown in Figure 2.4b. As expected α (not shown) is close to 1.00 for all compositions, pK_β varies with substitution and the isoelectric point is approached at high substitution. This model provides a predictor variable for rheology data in Chapter 4, osmometry data in Chapter 6, and is part of the swelling model in Chapter 7. Due to the relatively low amine content of the polymer used, even considering the worst case estimate of ΔpK_{Long} , the maximum error on i is expected to be less than 4% in Chapter 6 osmometry experiments.

2.6.3 Membrane Osmometry Monte Carlo Simulation

The purpose of this simulation is to answer three questions, namely: 1) what error tolerance should be placed on pressure during instrument selection or design, 2) how many compositions must be tested for good resolution on parameter estimates, and 3) what experimental concentration ranges should be used? To address these, simulation inputs are compared to outputs and the effect of random experimental error observed.

To improve the simulation performance four simplifications are made, namely: 1) ion activity effects are neglected, 2) salt effect on polymer solvent interaction are ignored, 3)

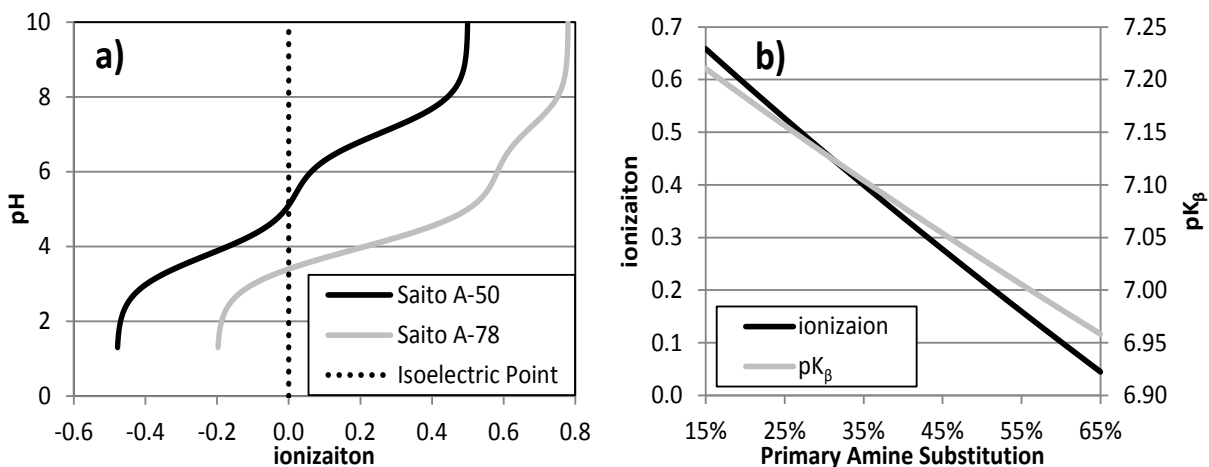


Figure 2.4: Ionization Model Results: a) simulation of [56] to validate model; b) N-succinyl-chitosan ionization and pK'_β as a function of primary amine substitution, polymer degree of deacetylation is 85%.

PBS is be approximated by an equivalent ionic strength NaCl solution with the same pH, and 4) polymer ionization is handled using the Henderson-Hasselbalch equation with a single estimate for each apparent pK_a rather than more complex Katchalsky model. These are not expected to bias the results. As 1) equates to removing the osmotic coefficient from both inputs and outputs this simplification has no effect. Making assumption 2) is the conventional approach (see Section 2.5). Given 1), the largest effect of the PBS \approx NaCl approximation is via solution density during unit conversions. Comparing NaCl data from the CRC Handbook [1] to the approach outlined in Section 2.4.8, solution densities were found to be almost identical over the entire range studied. Finally, the largest effect on polymer apparent pK_a is expected to come from changes in polymer degree of substitution. As the nature of the polymer was not varied in any given simulation, this effect is absent and the average value should provide adequate results.

With the above simplifications, simulated osmometry results were generated using the full, nonlinear equations. These results were validated as far as possible using an example in Hiemenz [42, pp. 589-553]. For the Monte Carlo simulation, uniform random error was introduced into the pressure signal and apparent ionization $\beta \approx i f_\xi$, number average molecular weight M_n , and the Flory-Huggins interaction parameter χ were estimated using the linearised model.

This simulation was used with the PVA parameter estimates discussed in Chapter 5 to plan the osmometry validation experiments. Parameter estimates found in Chapter 1 were used initially to plan oxidised-alginate and N-succinyl-chitosan osmometry experiments. As better estimates became available these were used to refine the approach. The experimental results for 21% amine substitution N-succinyl-chitosan were used to generate the final

analysis which is presented here.

Figures 2.5 and 2.6 address the interaction between experimental design and error tolerance. Noting the similarity between the osmometry approach used here and the Zim plots used for light scattering experiments [42], square designs were considered with 3, 4 or 5 salt and polymer concentrations. As expected, the total number of replicates was more important than experimental design; however even the effect of replicates paled in comparison to the effect of base variability. Adherence to the ASTM precision recommendation of 0.1 mm H₂O [45] resulted in error under 2% for all parameters. The specifications of the trans-

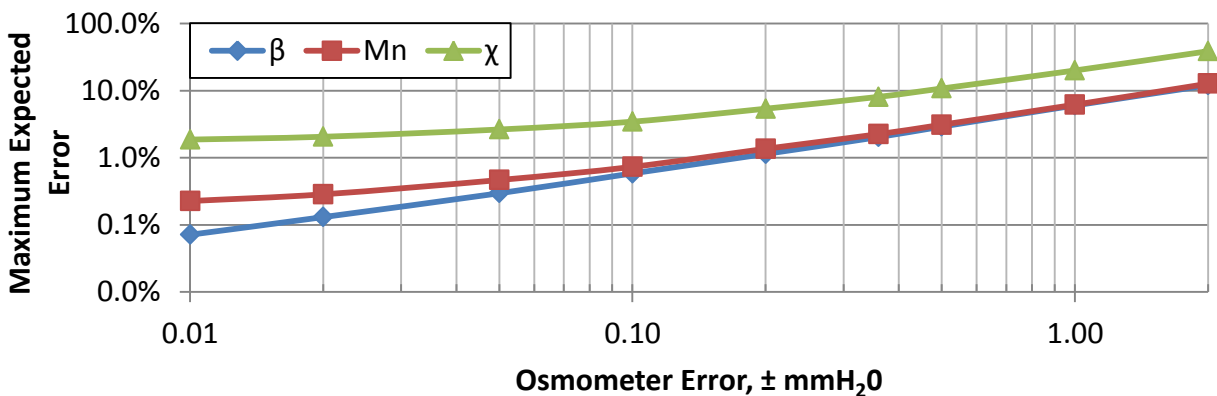


Figure 2.5: Osmometer Statistical Design Selection: Square grid statistical designs in salt and polymer concentration. Error is upper-bound of a 95% confidence interval calculated on 50,000 model runs. Model predictions superimpose for 3x3 design with 5 replicates, 4x4 design with 3 replicates and 5x5 design with 2 replicates, all of which require approximately the same number of individual tests.

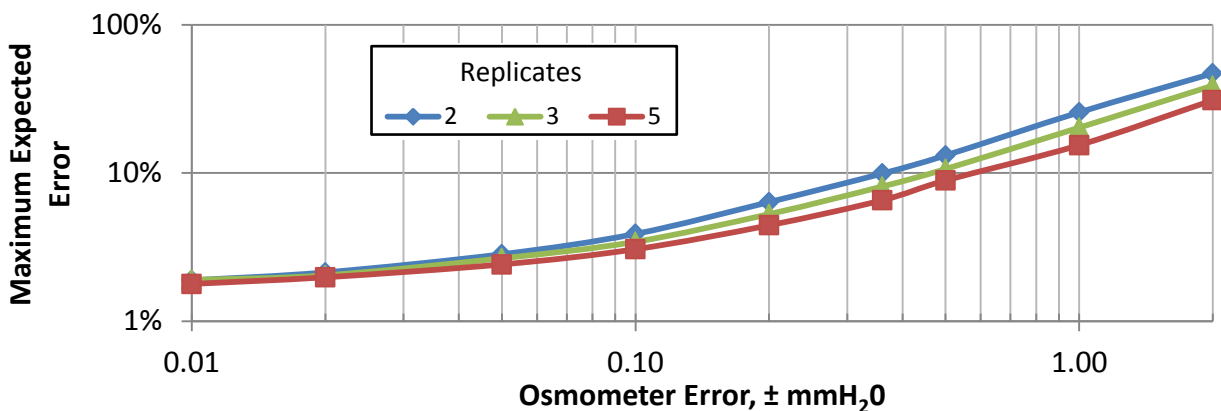


Figure 2.6: Effect of Replicates on Osmometer Resolution: 4x4 design, Error in χ , Error is upper-bound of a 95% confidence interval calculated on 50,000 model runs.

ducer used during osmometry experiments results in a worst case error of ± 0.36 mm H₂O. This still results in parameter estimation error less than 9% for χ and less than 3% for the other parameters. A 4x4 design with 3 replicates was selected based on a balance between solution preparation effort and linearity checking capabilities.

Examining Figures 2.7 and 2.8 it is concluded that the ideal concentration ranges for both polymer and salt are dominated by an interaction. Extrapolation error in determining M_n is only low at low polymer concentration or very high ionic strength. For this reason the maximum polymer concentration used with salt solutions was ~ 0.5 w/w% and the initial ionic strength range was 0.16 to 1.6 (approximately 1x to 10x that of blood). Later experiments used a range of 0.07 to 0.16 to avoid salting out effects. This can be seen to have similar error. As expected from analysis conducted during the model derivation the results plot as linear up to the instrument limit.

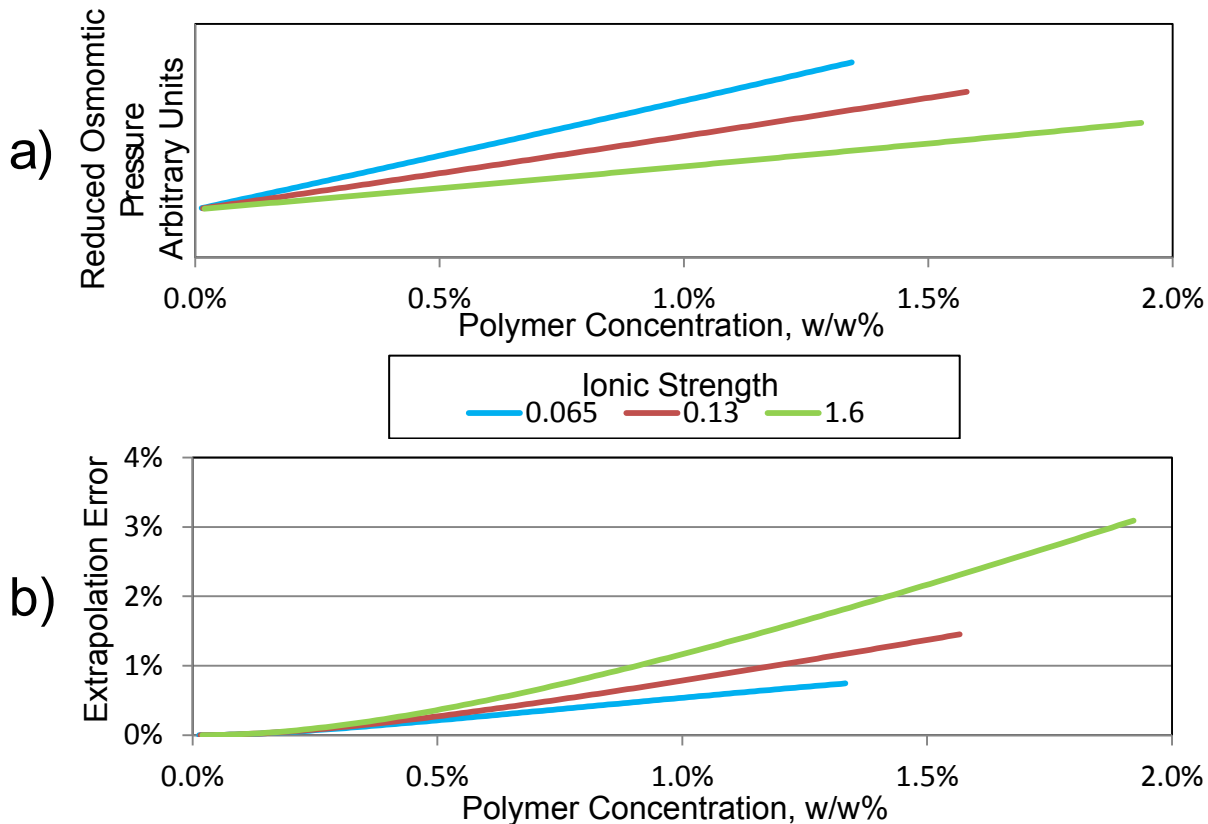


Figure 2.7: Osmometer Polymer Concentration Selection; a) Model Predictions showing reduced ionic pressure is expected to be almost linear with respect to polymer concentration up to the osmometer operation pressure limit; b) Expected error in intercept value when extrapolating from abscissa value to zero polymer concentration

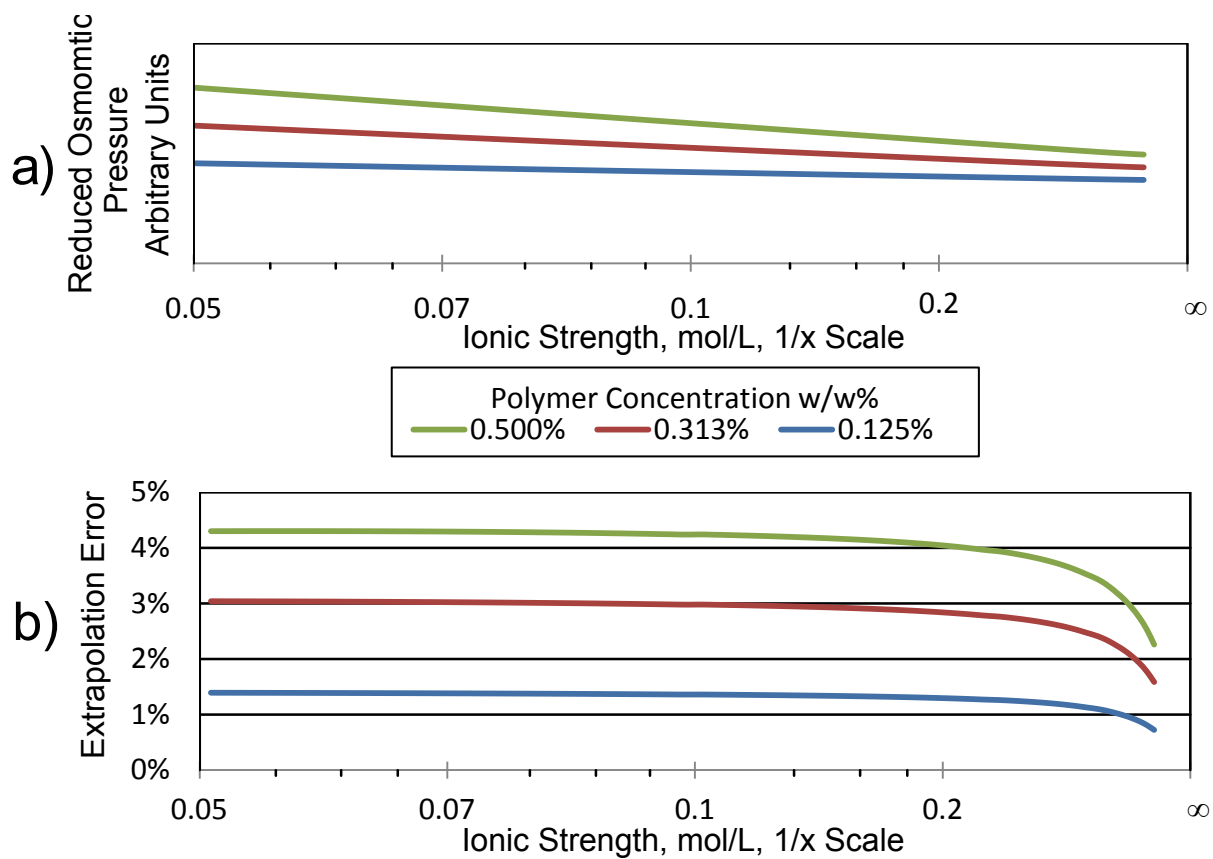


Figure 2.8: Osmometer Ionic Strength Range Selection; a) Model predictions showing reduced ionic pressure is expected to be almost linear with respect to $(\text{Ionic Strength})^{-1}$; b) Expected error in intercept value when extrapolating from abscissa value to infinite ionic strength.

2.7 Concluding Remarks

Models for polyelectrolyte gel equilibrium swelling are well established. Quantitative agreement was obtained by Chan [14] and her approach should be used as a template. The most significant difference between Chan's model and this work is the need to use a more sophisticated model for polymer ionization (Katchalsky rather than Henderson-Hasselbalch) due to the expectation of interaction effects between N-succinyl-chitosan degree of substitution and the amine apparent ionization constant.

Models for gel elasticity are well known (the theory of rubber elasticity). There is some inconsistency regarding usage of the 'affine' and 'phantom' branches with the latter recommended for gels. Improved models for hybrid gels are recommended, a topic that is discussed further in Chapter 7.

The models for membrane osmometry are the least well developed/documentated. Using well known components and following the approach taken for gels, a model was assembled and linearised into a form suitable for the analysis of experimental data. This model makes three assumptions, namely 1) solutions are dilute with respect to both polymer and total salt volume fractions, 2) ion activity coefficients and the solvent osmotic coefficient are identical in the sample and reference compartments, and 3) the effect of non 1:1 type ions is negligible. Based on simulation results the first two assumptions are shown to be reasonable. An approximate approach to check the third via nonlinear regression is provided.

Using the models discussed, a Monte Carlo simulation of an osmometry experiment was conducted to provide guidance as to what error tolerance should be placed on pressure measurement, how many compositions must be tested for good resolution on parameter estimates, and what experimental concentration ranges should be used. Error of ± 0.36 mm H₂O was deemed acceptable for pressure, 16 compositions in a 4x4 grid were found to provide a good resolution on parameter estimates, and polymer concentration below 0.5 w/w% was found necessary to limit M_n extrapolation error at a physiologically significant ionic strength.

Using parameters available in the literature and existing models it was possible to simulate phosphate buffer reference solutions and polymer ionization. The results of these simulations will be used to support experimental work in Chapters 4, 6 and 7.

Chapter 3

Polymer Modification

Synthesis of N-Succinyl-Chitosan and Oxidised-Alginate

3.1 Overview

To form the new hydrogel, oxidised-alginate and N-succinyl-chitosan are required. This chapter describes the work undertaken to synthesise these gel precursors from commercially available alginate and chitosan. The primary objective of this research work was to produce high purity oxidised-alginate and N-succinyl-chitosan with controlled modification extent, and known counterion species. Three types of characterization studies were conducted, namely: 1) H-NMR to determine modification extent, 2) TGA to determine sodium salt substitution, and 3) vacuum drying to characterise bound water content.

The primary contributions described in this chapter are the quantitative approaches used to characterise the products and observation of a reproducible log-linear relationship between reagent inputs and the product N-succinyl-chitosan substitution. Though peripheral to the overall project, the TGA analysis also produced statistically significant data demonstrating a small increase in chitosan moisture affinity and thermal stability with increasing N-succinyl substitution. The details of the modification procedures are not novel and are provided primarily to allow this work to be reproduced. Details of the H-NMR analysis have been published by the author in reference [31].

3.2 Background

3.2.1 Chitosan Succinylation

N-succinyl-chitosan (Figure 3.1c) is formed by the ring opening reaction between succinic anhydride and the chitosan amine (Figure 3.1a). The reaction is carried out in

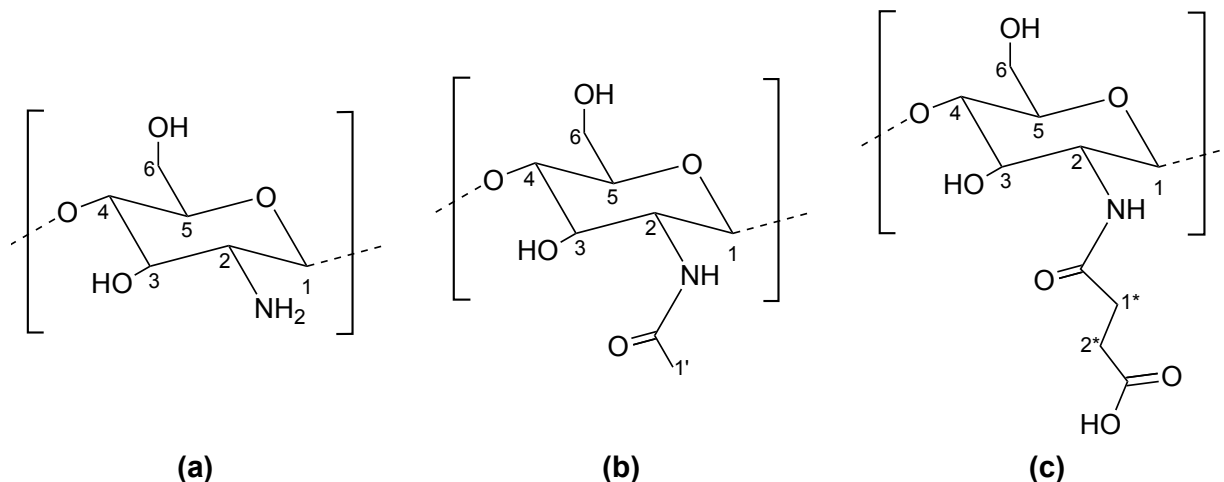


Figure 3.1: Chitosan Chemical Structure: a) glucose-amine; b) acetylated; c) succinylated. Numbers beside carbons give H-NMR labeling convention.

solution. The common procedure uses aqueous acetic acid to dissolve the polymer and some simple alcohol as a diluent [24, 28, 148]. An alternative report [149] used dimethyl sulfoxide as the reaction solvent. This is interesting as it avoids the presence of water which is implicated via a side reaction in the typical low conversion of succinic anhydride into polymer pendent groups [24, 28, 148]. Unfortunately the author was unable to reproduce the behaviour described in the report [149]. For this reason a more common procedure proposed by Yamaguchi et. al. [24] was applied, and hence it was necessary to quantify modification extent by H-NMR.

An advantage of following Yamaguchi is that he conducted the most comprehensive series of experiments and quantified modification by three independent methods [24]. When the tabulated data is plotted with the aid of a modern computer, a log-linear relationship is observed. Yamaguchi does not comment on the relationship and may have been unaware of it. As far as the author knows, it is not reported elsewhere in the open literature. Provided the observed relationship is reproducible it is hypothesised here that it could be used as a calibration curve eliminating the need for H-NMR analysis of every batch synthesised.

Purification was via membrane dialysis and freeze drying, again following Yamaguchi [24]. Based on our reading of his procedure and Donnan equilibrium considerations [140], the purified product is expected to consist of the modified polymer with succinylated units mixed between sodium and acid salt forms. Our reasons for confidence in this statement are discussed later. TGA analysis to quantify the fractional sodium substitution is discussed in a following section.

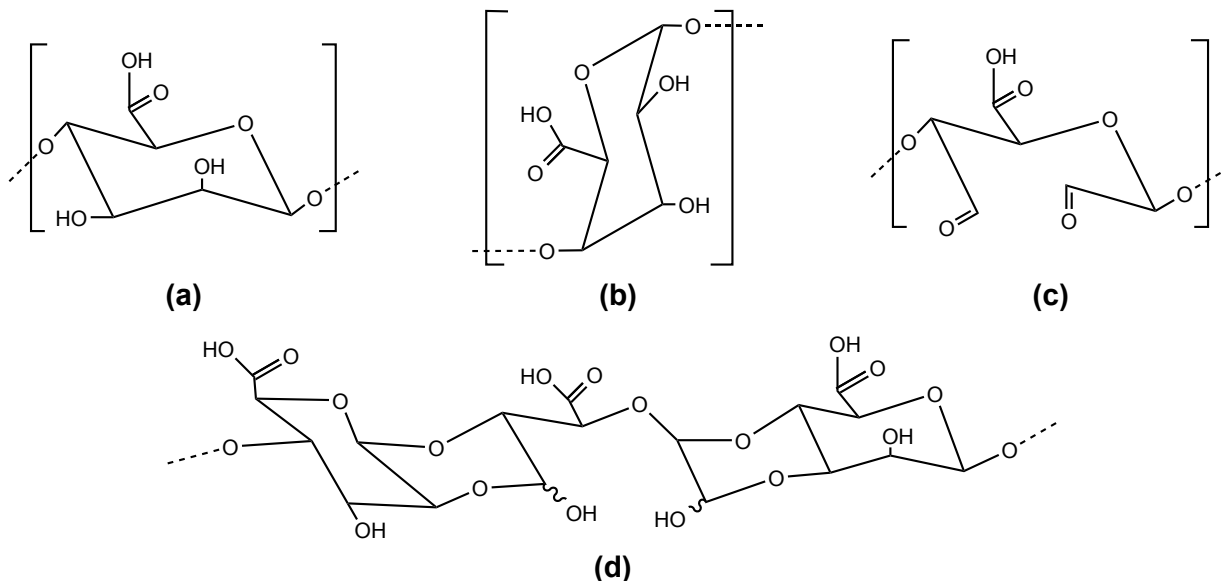


Figure 3.2: Alginic acid Structure; a) β -D-mannuronic acid (M), b) α -L-guluronic acid (G), c) oxidised M form, d) hemiacetal formed with neighbours. Adapted from [21].

3.2.2 Alginic Acid Oxidation

Oxidised-alginic acid is produced by the selective periodate oxidation of the alcohols on carbon 2 and 3 of both M and G units (Figure 3.2a and b). This breaks the intervening carbon bond and forms two aldehydes (Figure 3.2c). Painter demonstrates that these form hemiacetals with the alcohols on neighbouring units (Figure 3.2d) protecting these from further oxidation [21]. This results in a limiting oxidation extent of 45%. Provided side reactions are protected against, the addition of further periodate above this limit has no effect. Below the limit oxidation is nearly quantitative with added periodate [23]. The known relationship between reagent inputs and product oxidation makes characterization of oxidation unnecessary provided the approach taken is similar to that used in an established procedure.

Many published procedures exist for alginic acid oxidation e.g. [21, 23, 88]. Following Painter, n-propanol is used here to prevent side reactions. Low temperatures are used throughout processing to limit the rate of hydrothermal depolymerization of the oxidised product [21, 88]. The purification approach of Gomez was used initially [23], however concerns about residual contaminants, particularly the sodium chloride used to aid precipitation prompted the use of membrane dialysis as a final step.

3.2.3 Characterization by H-NMR

Nuclear magnetic resonance (NMR) is used in this work to quantify the extent of substitution for N-succinyl-chitosan. At the same time, a secondary objective was to evaluate the potential of the technique for quantifying alginate oxidation. An excellent introduction to NMR can be found in [150]. A brief overview is as follows:

NMR characterises materials based on the electron shielding around isotopes with an unbalanced nucleus spin state (e.g. ^1H). These act like small magnets. The presence of an external magnetic field creates an energy difference between two possible configurations. Orbiting electrons are affected by local chemical bonds, shielding the nucleus by varying amounts and resulting in slightly different energy levels. Radio waves at the resonant frequency can be absorbed to bias the population towards the high energy state. When the perturbation is removed, energy is emitted in the form of a radio signal as the system returns to equilibrium. This signal is called the free induction decay (FID) and provides the basis for NMR analysis. The frequencies emitted are related to the chemical structures present. The signal strength at a given frequency is proportional to the number of atoms with a particular chemical environment. Quantitative analysis relies on the integration of peak areas on a frequency plot. Good peak frequency separation is necessary for unambiguous integration and analysis.

To allow data sets from different instruments to be directly compared, frequency is reported as a ppm shift from an agreed upon reference compound. For the common ^1H hydrogen isotope, the zero reference is tetramethylsilane [150]. Deuterium also interacts, but due to its increased mass has a very different frequency response from ^1H . Use of deuterated solvents limits solvent interference with sample signals. When D_2O is used, labile hydrogens on alcohol, amine and carboxyl groups exchange with solvent deuterium eliminating the ^1H signal from these groups and producing DHO. The DHO peak has a documented temperature dependence [151] that can be used to shift it away from regions of interest and as an internal frequency calibration as an alternative to using the reference compound.

^1H -NMR of highly oxidised-alginate was not previously successful [23]. A jumble of overlapping peaks overlays the analysis region for normal alginate. This is likely due to complex form of the oxidised polymer (Figure 3.2d). For this reason the expected outcome of alginate analysis is qualitative confirmation of modification extent.

^1H -NMR of chitosan exhibits the potential to produce quantitative data. Expected peak assignments based on literature reference are as found in Tables 3.1 and 3.2. Unmodified chitosan exhibits four clear peak groupings [152–156]. Noting that C1 is proportional to the number of repeat units present, the acetyl substitution can be calculated using $\text{P1}/(3\text{P5})$ and amine substitution by $\text{P3}/\text{P5}$ or $1-\text{P1}/(3\text{P5})$ [156] Two new peaks appear in N-succinyl-chitosan which are well separated from those already present [90, 148, 157–159]. Due to the similarity between acetylated and succinylated repeat units, the significance

of the P5 and P3 peaks is expected to be unaltered. Calculations for amine using P3 and acetyl using P1 are expected to be identical to those for normal chitosan. Succinyl substitution may be calculated from $P3/(4P5)$. The alternative amine approach can be modified to $1-P1/(3P5)-P2/(4P5)$. In the knowledge of the author prior to our own report [31] this quantitative analysis was not reported in the open literature.

3.2.4 Salt Substitution by TGA

Thermal gravimetric analysis (TGA) is used here to quantify the sodium salt substitution of the modified polymers after purification. After purification by membrane dialysis, an unknown proportion of polymer repeat units are in their sodium salt and acid salt forms. A large mass difference exists between the two forms introducing unreasonable uncertainty into molar concentration calculations. TGA involves heating a sample situated on a sensitive balance and observing mass loss as a function of temperature. We expect polymer

Table 3.1: Chitosan $^1\text{H-NMR}$ Spectrum Description

Spectrum Area	Chitosan ppm	N-Succinyl-Chitosan ppm	Description
P1	2.0-2.1 ^a , 2.4 ^b	1.9-2.1[157–159]	sharp peak
P2	—	2.3-2.6[90, 148, 157–159]	two peaks
P3	3.1-3.3 ^a , 3.5 ^b	2.6-3.0[90, 148, 158, 159]	broad peak ^c
P4	3.4-4.0 ^a , 4.0-4.2 ^b	3.4-4.0[90, 158]	many peaks
P5	4.8-5.0 ^a , 4.9-5.2 ^b	4.4-4.7[90, 159]	two or three peaks ^d

^a [152, 154–156]; ^b [153]

^c Width and position affected by pH

^d Provide basis for an alternative analysis. With sufficient resolution an individual peak is observed for each repeat unit type (see Figure 3.1) [90, 156]

Table 3.2: Chitosan $^1\text{H-NMR}$ Peak Assignment

Spectrum Area	Protons	Assignment ^{a,b}
P1	3	methyl protons on acetal group
P2	4	succinyl backbone protons
P3	1	ring proton 2, glucosamine only [90, 153, 156, 158, 159]
P4	Varies	ring protons other than P3 and P5
P5	1	ring proton 1, all unit types[90, 153, 156]

^a Unless otherwise stated references are as in Table 3.1

^b See Figure 3.1 for structure numbering scheme

sodium content to be quantifiable using the mass of inorganic ash remaining after thermal decomposition in an oxidizing environment. As a byproduct of this analysis the thermal decomposition and drying temperatures of the modified polymers can be evaluated.

The residue from alginate decomposition has been identified as nearly pure sodium carbonate [160]. Oxidised-alginate and N-succinyl-chitosan are not as well studied, however, based on the behaviour of other polysaccharides and simple carboxylic acids, sodium carbonate and graphitic char are the only two high temperature products expected. Char can be minimised by use of an oxidizing environment. The relative purity of the sodium carbonate residue can be evaluated based on the color of the ash. Nearly pure carbonate is white to cream. Carbonaceous char is black. Provided the right color ash is obtained, sodium substitution can be calculated based on the mass residual ash at the end of the experiment.

According to [160] at heating rates up to 20 °C/min the TGA trace for alginate shows two well separated processes. Below ~ 100 °C water is driven off. A shoulder of stability exists for the dry polymer followed by thermal decomposition starting at 170 °C. Decomposition is complete above 610 °C leaving sodium carbonate ash. Provided N-succinyl-chitosan and oxidised-alginate exhibit similar behaviour, the shoulder can be used as the dry sample mass eliminating the need for special handling prior to testing.

3.2.5 Moisture Content via Vacuum Drying

To quantify polymer moisture content, small scale experiments were conducted where samples are weighed before and after drying using a vacuum oven. This allows accurate mass based molar concentration calculations (residual moisture may exceed 10 w/w%) and avoids the difficulty inherent with completely drying all material used.

Complete removal of water from hygroscopic polymers can be difficult even in a freeze dryer or desiccator [161]. Though vacuum helps aid the process, large surface areas and elevated temperatures are necessary for efficient removal of trace moisture [161–163]. A significant risk exists that polymer properties may be compromised by thermal decomposition, particularly for oxidised-alginate [44, 88]. Even when samples are only used to quantify moisture content, use of the lowest possible drying temperature is recommended to avoid interference from thermal decomposition [164, 165]. ASTM guidelines suggest samples dried at elevated temperatures should be cooled briefly in a desiccator before weighing to avoid interference from convection currents and atmospheric gas adsorption onto weighing boat surfaces [164].

The exact nature of each polymer affects its optimum drying temperature. Evidence exists showing water can be completely removed from PVA via vacuum drying at 60 °C for 30 h [162]. Extrapolation of alginate TGA data to zero heating rate indicates that an isothermal temperature of 76 ± 5 °C may be sufficient [160]. Examination of bound

water data for a series of other polymers [162] implicates the carboxylic acid moiety as the limiting functional group in both oxidised-alginate and N-succinyl-chitosan, meaning their minimum drying temperatures are expected to be similar. Preliminary tests are necessary and evidence from our own TGA work is useful, to validate the procedure used here for the modified polymers.

3.3 Materials and Methods

3.3.1 Materials

Specific materials used listed in alphabetic order: Acetic acid (99.9%, Fisher Scientific A38 Lot 508074), alginate sodium salt from brown algae (M/G ratio \sim 1.56, M_w 80-120 kg/mol, Sigma A2033 Lot 098K1388), acetone (University of Waterloo Chem. Stores, wash grade), chitosan (75-85% deacetylated, M_v 50-190 kg/mol, Aldrich 448869 Lot 61496MJ), deionised water (University of Waterloo Chem. stores), dialysis tubing (MWCO 12,400, Sigma-Aldrich D0655 Lot 3110), ethanol (University of Waterloo Chem. Stores), ethylene glycol (Fisher Scientific E178 Lot 092701), N-propanol (Fisher Scientific A414 Lot 090199), sodium chloride (EMD Chemicals SX0420 Lot 49133928), sodium hydroxide (EMD Chemicals 5X0590 Lot 45043), sodium periodate (Sigma-Aldrich S1878 Lot MKBB5683), and succinic anhydride (Aldrich 239690 Lot 07422BJ).

3.3.2 Chitosan Succinylation

Nine batches of N-succinyl-chitosan were made as listed in Table 3.3. Each was assigned a code from C0 to C8 in the order of production. C0 was the prototype batch. It differed from subsequent batches in the amount of acetic acid used (100 ml), procedure used to dissolve polymer (ethanol added before fully dissolved, 4 h time requirement) and the temperature used (40 °C). The procedure for batches C1 to C8 is as follows:

Volumetric measurements were made using a Corning #3022-250 ml graduated cylinder. Stock solutions of sodium hydroxide (20 w/w%) and acetic acid (5 w/w%) were prepared using deionised water and a Mettler PC 2000 balance. Polymer and succinic anhydride were weighed using a Satorius CP 1245 laboratory balance and the mass recorded to the nearest 0.1 mg. Temperature control and stirring were provided by a Corning PC-4200 hotplate with immersion probe. The probe entered the reaction flask through a single hole stopper. Other than when reagents were added, the flask was kept plugged to limit evaporation from the reaction bath.

For each batch, approximately 2.00 g of chitosan was weighed and added to 80 ml of 5% acetic acid in a 250 ml Erlenmeyer flask. The mixture was stirred for 30 min at 60 °C and

Table 3.3: Chitosan Properties by Batch

Chitosan Batch	Primary Amine (R-NH ₂) substitution%		Moisture Content w/w%		Sodium Salt (R-COONa) substitution%
	Raw NMR	Fit	Vacuum	TGA	
C0	29	22	—	—	—
C1	46	48	10	14	19
C2	28	34	13	15	25
C3	23	27	11	14	23
C4	57	52	5	16	11
C5	—	52	—	17	—
C6	—	21	6	—	—
C7	23	21	5	16	26
C8	36	41	6	13	26

600 rpm until the chitosan was completely dissolved. 120 ml of ethanol was then added and the mixture allowed to return to temperature before proceeding. A predetermined amount of succinic anhydride was weighed, dissolved in 40 ml of acetone and added to the reaction mixture without interrupting stirring. Stirring was increased to between 600 and 800 rpm and the mixture was left to react at temperature for 24 h.

Membrane dialysis was used to purify the product. Dialysis tubing was prepared by washing in sequence with tap water, hot deionised water under stirring for 3 h, and cold deionised water. The reaction mixture was diluted using deionised water to a total volume of 400 ml and its pH adjusted to ~ 10 with 20% sodium hydroxide (pH paper used to check adjustment). A magenta precipitate formed at this point for some formulations. Solution and precipitate were divided approximately evenly between several lengths of tubing and immersed in 4 L of deionised water under stirring at room temperature. The water was replaced 7 times with a minimum time interval of 4 h between changes for a theoretical dilution of ten million to one. Precipitate was observed to dissolve sometime before the first water change and is therefore unlikely to have seriously affected the quality of purification. Product was recovered by freeze drying. Batches C0 to C3 were bottled within 24 h of recovery. Batches C4 to C8 were held in a desiccator at room temperature for no less than one month before bottling. Long term storage of samples was at less than 4 °C.

3.3.3 Alginate Oxidation

Six batches of oxidised-alginate were prepared as listed in Table 3.4. Each was assigned a code from A0 to A5 in the order of production. A0 was the prototype batch. It was prepared at room temperature without n-propanol and used without purification by dialysis.

All subsequent batches used the following procedure:

Polymer and periodate were weighed using a Satorius CP 1245 laboratory balance and the mass recorded to the nearest 0.1 mg. The reaction flask was immersed up to the neck in an ice bath to maintain constant low temperature. Bath temperature rose as high as 10 °C on a couple runs when all ice melted overnight, but otherwise was stable at around 4 °C. The flask rested on bottom of bath allowing controlled stirring using a Corning PC-4200 hotplate. A single hole stopper fitted with a valve allowed the air to be evacuated from the flask during the reaction, limiting contact with atmospheric oxygen.

Sodium alginate (2 ± 0.01 g) and n-propanol (9 ± 0.1 g) were mixed with deionised water in a 250 ml flask to make $225\text{ ml} \pm 5\%$ total. The flask was sealed, evacuated and placed in the ice bath and the mixture stirred at 200 rpm in the dark until the alginate was completely dissolved (3-5 h). Sodium periodate was weighed out and dissolved in 30 ml deionised water. Stirring was turned off before releasing the vacuum and not resumed until after the periodate was added and the flask again evacuated. The reaction was allowed to proceed for 24 h for limit oxidation or 48 h for stoichiometric oxidation. Ethylene glycol (1-2 ml) was then added and the mixture stirred for 0.5 h to neutralize any remaining periodate.

All batches were purified using at least one precipitation step. The exact amounts of NaCl and solvent varied slightly for the first few batches. The best results in terms of filtration efficiency were obtained by adding 6.5 g of NaCl to the reaction mixture and then pouring this into 750 ml of stirred ethanol. This produced a coarse precipitate suitable for vacuum filtration, but may have trapped impurities in the precipitate particles. Up to batch A4, the polymer was redissolved and re-precipitated once with ethanol and once with acetone before a final rinse with pure ethanol. By batch A5 concerns about residual salt had prompted the use of membrane dialysis for final purification and therefore, this

Table 3.4: Alginate Properties by Batch

Alginate Batch	Oxidised Groups REF Structure substitution%	Sodium Salt (R-COONa) substitution%	Periodate Used mol ratio repeat units
AC	—	—	—
A0	45 ^a	—	3.5
A1	45 ^a	—	16.3
A2	<35 ^b	46	0.35
A3	45 ^a	48	2.5
A4	<25 ^b	47	0.25
A5	45 ^a	46	16.3

^a Assumed based on Painter et al. [21]

^b Maximum given mol ratio periodate

batch was only precipitated once prior to dialysis.

Dialysis tubing was prepared by washing in sequence with tap water, hot deionised water under stirring for 3 h and cold deionised water. Product from the previous purification was dissolved in deionized water (400 mL, ice bath). The solution was divided approximately evenly between several lengths of tubing and immersed in 4 L of fridge temperature deionized water ($< 4\text{ }^{\circ}\text{C}$). The setup was stored unstirred in a dark fridge. The water was replaced 7 times with minimum interval between changes of 12 h. Product was recovered by freeze drying, held in a desiccator at room temperature for no less than one month and then stored in sealed containers at less than $4\text{ }^{\circ}\text{C}$.

3.3.4 Characterization by H-NMR

N-succinyl-chitosan, oxidized-alginate, or unmodified alginate were dissolved in D2O to form 1 w/w% solutions. Unmodified chitosan was dissolved in D2O/DCl at a pH of 1. The acid solution was mixed using D2O and 37% hydrochloric acid, introducing normal hydrogen at a concentration of 0.2 mol/L. This resulted in a more pronounced DHO peak in the NMR spectra but did not otherwise interfere with analysis. 0.45 μm syringe filters were used to remove undissolved contaminants during injection into NMR tubes. Spectra were taken on a Bruker Avance 500 at $90\text{ }^{\circ}\text{C}$ following the ASTM recommended pulse programs for the respective unmodified polymers [156, 166]. Using the data published in [151] as a calibration curve, the position of the DHO peak (4.13 ppm at $90\text{ }^{\circ}\text{C}$) was used as an internal reference.

MestReNova v9.0.1-12354 was used with the default settings to convert the FID into frequency domain signals. As curvature was not very pronounced a polynomial of order three or less could be used to fit the baseline. The baseline corrected spectra can be found in Figures 3.3 and 3.4. Oxidized-alginate proved too difficult to analyse quantitatively. Calculations using chitosan peak areas were carried out following the approach outlined in Section 3.2.3. Linear regression analysis was conducted using Microsoft Excel 2010. The statistical functions used were validated against Montgomery [167].

3.3.5 Salt Substitution by TGA

Alumina pans were prepared by boiling in $\sim 8\text{ M}$ nitric acid and rinsing with deionized water. Pans were dried by baking for 2 h at $100\text{ }^{\circ}\text{C}$. Just prior to use, any trace contamination was burnt off using a Bunsen burner.

Polymer samples were removed from low temperature storage in their sealed containers and allowed to equilibrate at room temperature. Samples were weighed out ($7\pm 1.5\text{ mg}$) and the remainder sealed immediately and returned to storage. Individual 20 ml glass vials were used to store and transport the samples. Prior to testing, a clean glass rod was used

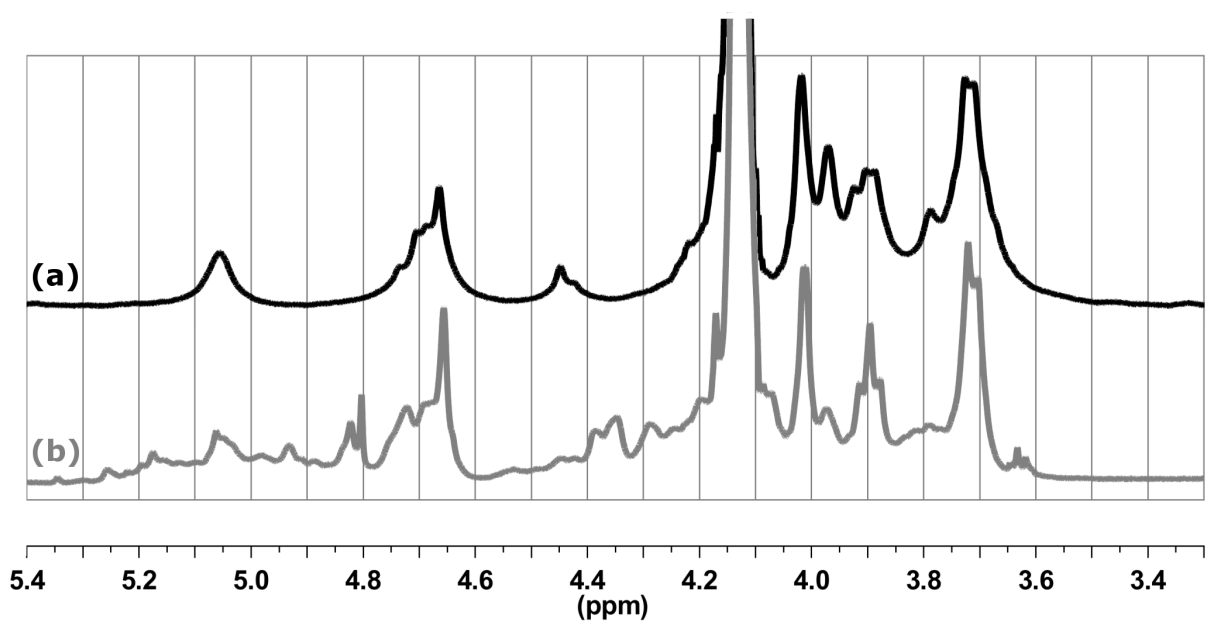


Figure 3.3: Alginic acid NMR Results: a) Control, b) Limit Oxidized, batch A0

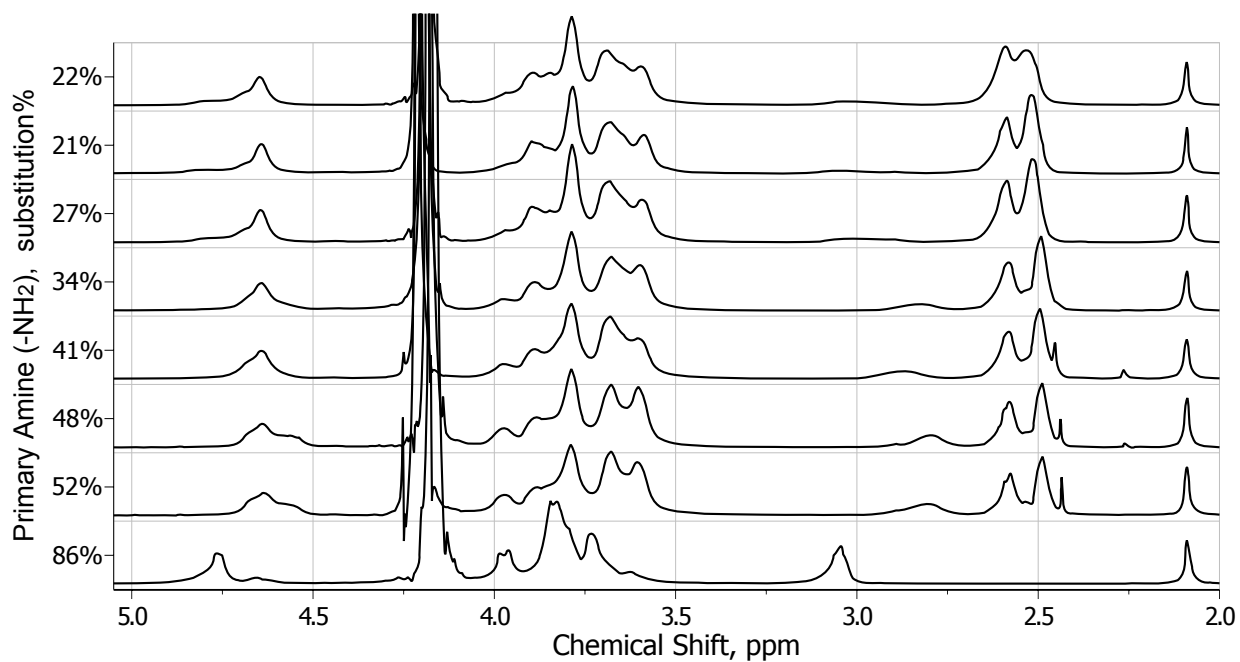


Figure 3.4: Chitosan NMR Results: Free amine per fit in Table 3.3, 86% free amine is the unmodified control.

to compress each sample against the bottom of the vial forming a thin disk with similar dimensions to the TGA pans.

Tests were conducted in a TA Q500 TGA. After preliminary experiments a two stage procedure was adopted. In the first stage, samples were ramped from room temperature to ~ 600 °C under 100 ml/min nitrogen purge at a heating rate of 20 °C/min. As can be seen in Figure 3.5, this provided good separation between the end of moisture loss and the beginning of thermal decomposition. For the second stage, the sample was equilibrated at 550 °C, the purge gas switched to air and the temperature ramped to 800 °C. Although some variability existed in the kinetics, all samples reached their final plateau mass well before the test end. The residue was in the form of a fused pellet with a faint cream colouration.

TA Universal Analysis 4.7A was used to analyse the data. Salt substitution was calculated using dry mass, residual mass, and average repeat unit molecular weight. For alginate the assumed conversion in Table 3.4 was used in this calculation. For N-succinyl-chitosan the NMR fit estimate in Table 3.3 was used.

The maximum moisture loss rate and thermal decomposition onset temperatures were also determined. To evaluate the effect of polymer modification on these parameters a linear regression analysis was conducted in Microsoft Excel 2010. The statistical functions used were validated against Montgomery [167].

3.3.6 Moisture Content via Vacuum Drying

To determine the optimum drying temperature, preliminary experiments were conducted on alginate batch AC and chitosan batch C6. It was predicted that these would

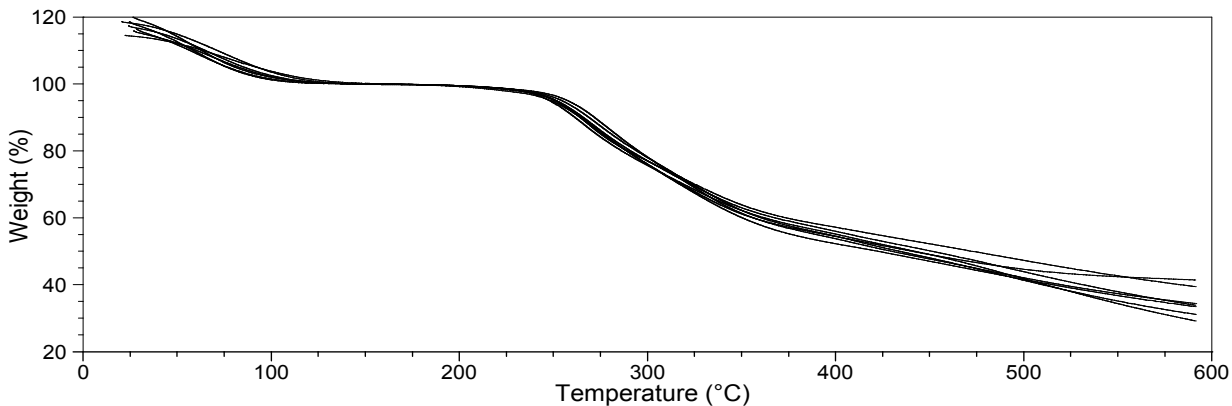


Figure 3.5: Chitosan TGA Results: All compositions tested shown superimposed; First stage data only (Purge Gas is Dry Nitrogen); Data is normalized with respect to the dry polymer mass.

be the most hygroscopic and would require the most aggressive drying. Samples were held isothermally under vacuum and periodically removed and weighed. The minimum time between weighings was 4 h. When a static mass was obtained over three successive determinations, the oven temperature was raised and the procedure repeated. Raising the temperature above 80 °C resulted in no further mass loss. In a follow up experiment samples were stored under vacuum for three days at 80 °C. The masses were found to stabilize within the first 24 h.

The precise procedure followed for subsequent quantitative determinations is as follows:

20 ml glass vials were cleaned by ultrasonication in deionized water. Vials were rinsed with both DI water and acetone after which they were only handled with gloves or tongs. The vials were placed under vacuum, heated at the test temperature for 24 h and stored in a desiccator until use.

Polymer samples were removed from low temperature storage in their sealed containers and allowed to equilibrate at room temperature. The vacuum oven was preheated to 80 °C. 90 ± 10 mg of polymer was weighed into the speciality prepared glass vials, and both vial and sample masses recorded to the nearest 0.1 mg. The vial was covered with dried laboratory wipe held in place by an elastic band. The covered vial was immediately loaded into the oven and placed under vacuum (~ 30 inHg).

To purge the chamber of released water, the vacuum was cycled a minimum of three times over the 24 h drying time. Following ASTM D570 [164] the sample was placed in a desiccator while still at temperature and allowed to cool before weighing.

3.4 Results and Discussion

3.4.1 Polymer Modification

Modified polymer yield was hard to quantify due to known losses during purification. Generally amounts greater than 1.5 g were recovered per batch.

Oxidized-alginate estimated degree of substitution can be found in Table 3.4. As the synthesis procedure closely mirrors those of other authors [21, 23] the results should be very similar, particularly for batches A1 and A5. These almost exactly follow the limit oxidation procedure of Painter and Larson [21]. Qualitative confirmation of successful oxidation is provided by the agreement between the oxidized-alginate NMR spectrum presented here (Figure 3.3) and that of Gomez et al. [23].

N-succinyl-chitosan NMR shows clear trends in the raw data 3.4. Polymer modification was observed to have no statistically significant effect on acetylation (log-linear trend p-value 0.17, average substitution 13 ± 1.3 mol%). Regardless of analysis method a log-linear

trend exists for free amine and succinyl substitution versus mole fraction succinic anhydride (Figure 3.6). The lowest probability of significance based on measured data is 99.8%.

Comparing the two approaches suggests systematic error exists for at least one approach. The 95% confidence prediction interval on the NMR A fit is ± 21 mol% meaning the difference between NMR A and B is not statistically significant when the NMR data is taken in isolation. Good agreement between NMR A and Yamaguchi et al. [24] suggests that it is the more reliable estimate. Uncertainty on the combined fit predictions (Equation 3.1) is reduced to ± 12 mol% establishing that the difference between the combined fit and NMR B is statistically significant at a 95% level. Here y is the desired free amine substitution in molar fraction repeat units and x is the succinic anhydride used in moles per mole polymer repeat units. As it provides the least uncertainty, Equation 3.1, is used to estimate free amine for each sample in remainder of this thesis. NMR A raw results and fit line values can be found in Table 3.3.

$$y = -0.18\ln(x) + 0.51 \quad (3.1)$$

An interference with the succinyl peak is likely the source of the systematic discrepancy between NMR A and B. Agreement between Yamaguchi and NMR A rules out problems with the amine peak and the consistency of the acetyl peak suggests it is not at fault.

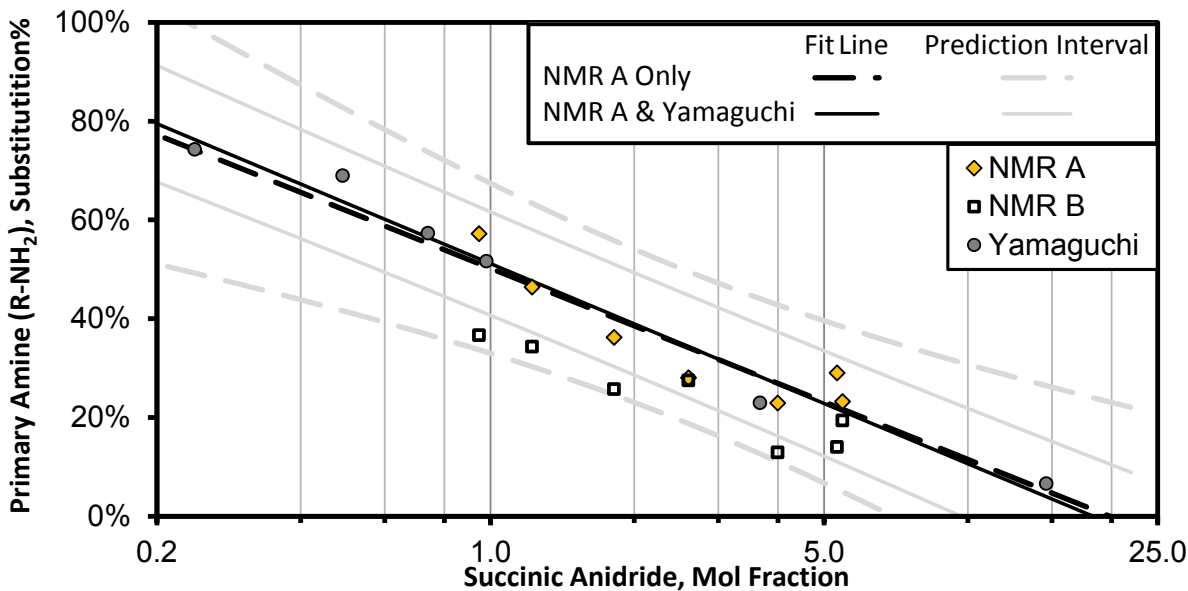


Figure 3.6: Chitosan N-Succinylation Calibration Curve: NMR A analysis based on amine peak; NMR B analysis based on succinyl and acetal peaks; Yamaguchi from [24]; Black curves show fits to data, light grey curves bracketing fit show respective prediction error.

Four possible interferences with the succinyl peak are considered, namely: 1) integration error due to insufficient NMR pulse program delay; 2) integration error from unknown organic contamination; 3) partial O-succinylation [154]; and 4) succinic acid contamination due to salt formation with the chitosan amine. A check of pulse program adequacy was conducted by the NMR technician and the area of minor peak / shoulder observed in the succinyl region is insufficient to explain the discrepancy. This leaves two options that can not be ruled out or differentiated between: O-succinylation and amine/succinic acid salt contamination. The potential error both introduce into gravimetric calculations is about the same. Extra mass equivalent to 6 to 14% additional succinyl substitution may be present. This results in a 3 to 7% error in repeat unit average molecular weight calculations. The error is larger at higher amine substitutions giving some support to the salt hypothesis.

3.4.2 Salt Substitution

The purified alginate is known to contain some quantity of insoluble impurities precluding precise gravimetric calculations. The salt substitutions in Table 3.4 ignore these impurities and are therefore approximate. Workarounds for this issue are discussed in later chapters.

N-succinyl-chitosan sodium content as a percentage of the sample dry mass was determined very precisely. This reduces the overall uncertainty of chitosan gravimetric calculations by as much as 6%. The sodium substitutions provided in Table 3.3 assume purified samples consist of polymer, sodium counterions and absorbed water. Error introduced by the amine substitution uncertainty is $\pm 5\%$, while the maximum possible error stemming from assuming no amine/succinic salt formation varies from 3 to 7%. These errors do not propagate into further calculations provided internally consistent estimates of sample composition and polymer structure are used.

The decision to ignore amine/succinic salt formation can be justified based on the chitosan purification procedure. Sodium hydroxide is added to raise the pH to 10 just prior to membrane dialysis. Under this condition all succinyl groups are negatively charged and amines are uncharged. Donnan equilibrium dictates that negatively charged succinic acid and acetic acid are preferentially transferred to the external compartment [140]. Positively charged sodium is preferentially retained. Any possibility of amine salt formation occurs at the end of dialysis after contaminant concentrations have dropped to very low levels. The pH after dialysis is between 6 and 7 indicating the sodium concentration is less than stoichiometric. Under the final condition some of the amines are charged however the polymer charge is still predominantly negative. This is expected to repel negative counterions, and any amine salt formation is expected to be with acid groups on adjacent repeat units.

3.4.3 Moisture Content

Competing estimates of moisture content are obtained by TGA and vacuum drying (Tables 3.3 and 3.4). Vacuum drying is believed to be more accurate due to the better control of polymer atmospheric contact during sample preparation. Vacuum results show the expected correlation with time spent in desiccator prior to bottling. Similarity between observed moisture levels across all TGA tests suggests that samples reached equilibrium with the environment prior to test start.

The hypothesis that vacuum drying was incomplete can be rejected based on the validation experiments conducted, and the TGA data seen in Figure 3.7. Examining the temperature at which maximum moisture loss rate occurred, it can be seen that validation was conducted using samples with the strongest water binding. This temperature can be taken as an upper-bound at which a finite equilibrium moisture content is possible. In all cases maximum moisture loss rate occurs below the 80 °C drying temperature selected during validation.

No statistically significant trend with substitution was found for alginate (p-value 0.46). The temperature for maximum drying rate is 71 ± 4.5 °C. The chitosan trend with substitution is significant at a 97% level. The 20 °C difference between extreme compositions is expected to be of practical significance.

3.4.4 Polymer Stability

The degradation onset temperature by TGA provides insight into polymer stability (Figure 3.7). The linear trend for chitosan is significant at a 98.5% level. This may not be of practical significance as the change between extreme values is only 10 °C. The alginate

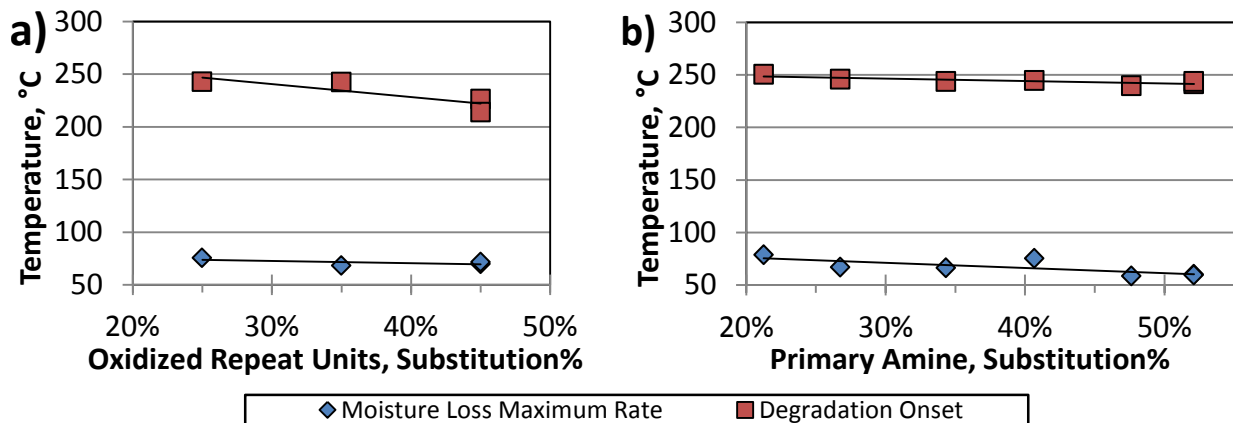


Figure 3.7: Modification effect on Moisture Removal and Degradation Temperatures: a) Alginate; b) Chitosan

change is 30 °C and the trend is in good agreement with predictions from the literature [44, 88] however the statistical evidence is weak (p-value of 0.17).

3.5 Concluding Remarks

Oxidized-alginates and N-succinyl-chitosans were successfully synthesized. Alginate degree of substitution is not verified but uncertainty is expected to be small, particularly for batches A1 and A5 which were used for subsequent experiments. The purity of alginate will be discussed in the following chapters. N-succinyl-chitosan substitution was quantified with maximum uncertainty of 12%. This translates into a 5% error when estimating repeat unit molar mass. Chitosan purity was questioned based on NMR result discrepancy. Ignoring this discrepancy results in no more than 7% error in molar concentration calculations. Chitosan moisture and sodium content were determined with high degree of precision eliminating these factors as significant contributions to overall error.

Chapter 4

N-Succinyl-Chitosan Solution Rheology

4.1 Overview

This chapter describes the approach taken to determine what N-succinyl-chitosan solution concentrations have reasonable handling characteristics. Based on literature guidelines an apparent viscosity of 0.2 Pa·s was selected as the upper bound for the “injectable” viscosity range [73]. The difficulty experienced in handling the 5 w/w% N-succinyl chitosan solutions used in our initial work indicates that they probably exceeded this guideline. N-succinyl-chitosan belongs to a class of polymers called polyampholytes which have both positively and negatively charged groups on the chain [20]. Structure property relationships for these polymers indicate that viscosity could rise and solubility decrease as amine substitution moves from the 21% used in the initial work, to the 52% substitution prepared. As higher concentrations generally result in stiffer gels, handling considerations provide an important constraint on what formulations are practical.

In addition to information on usable solution concentrations, this chapter provides insights into N-succinyl-chitosan chain morphology in solution based on comparison to published scaling relationships [46]. In the knowledge of the author neither the handling characteristics nor morphology analysis of N-succinyl-chitosan solutions under physiological conditions are published elsewhere in the open literature.

4.2 Background

4.2.1 Polymer Solution Rheology

For all polymer solutions, viscosity depends on three factors: temperature, molecular weight and concentration. This dependence is understood in dilute solutions using simple models. The polymers are modelled as rigid, non-interacting particles suspended in the solvent [42, pp 583-597]. From the model, viscosity is expected to depend on solvent properties, the number of particles, and the particle size. Solvent viscosity is temperature dependent so the solution viscosity will be as well. The number of particles is dependent on polymer concentration. Size is dependent on molecular weight and polymer solubility, which is often a function of temperature. According to the theory, reduced viscosity (η_{red} , Equation 4.1) provides a linear relationship with concentration. Here η is solution viscosity, η_o is solvent viscosity and c_2 is the polymer concentration [42].

$$\eta_{\text{red}} = \frac{1}{c_2} \left(\frac{\eta}{\eta_o} - 1 \right) \approx m c_2 + b \quad (4.1)$$

In concentrated solutions polymers begin to interact, resulting in a transition from *dilute* to *entangled* regimes [20, 26, 42, 46, 128]. Polyelectrolytes interact through charge even at very low concentrations, but mainly repel one another, extending the concentration range before entangled behavior sets in. Fuoss's law (Equation 4.2) is an empirical relationship that provides a good fit to viscosity data over this wide semidilute regime [26, pp 635-637][46]. Here A and B are fit constants which depend on the nature and charge of the polymer.

$$\eta_{\text{red}} = \frac{A}{1 + B c_2^{1/2}} \quad (4.2)$$

More recent polyelectrolyte theory results in scaling relationships with the form given in Equation 4.3 [46]. Here net charge f joins concentration as a predictor variable and relative viscosity η_r replaces reduced viscosity as the response variable. As will be seen in chapter 6, net charge is inversely proportional to amine substitution for all compositions of interest in this work.

$$\eta_r = \frac{\eta}{\eta_o} \propto f^b c_2^e \quad (4.3)$$

The size of neutral polymers in solution is primarily affected by solvent affinity. Polyelectrolyte size is also affected by polymer net charge and salt screening, while polyampholyte size is affected by internal charge attractions. The physics of this in the semidilute regime is the subject of several recent reviews [20, 46, 125]. As N-succinyl-chitosan is a polyampholyte this is the most relevant branch of theory. Four morphologies are possible namely: 1) the fully extended form (if net charge dominates), 2) collapsed globule (if attraction dominates), 3) a random coil (if salt screening dominates), and 4) a bead necklace

morphology (if a balance exists between net charge, screening and attraction) [20, 46]. All else being equal, solution viscosity is higher for more extended forms (e.g. coil > necklace > globule).

Away from the isoelectric point, polyampholyte net charge tends to dominate resulting in similar behaviour to polyelectrolytes, potentially allowing polyelectrolyte scaling relationships to be used [46]. Near the isoelectric point, all polyampholyte effects are close to balance making behavior prediction difficult [125]. Polymers tend to collapse into compact globules resulting in a viscosity minimum; however they also tend to aggregate, and if affinity for the solvent is low, precipitate [20, 125]

So far an implicit Newtonian fluid assumption has prevailed by ignoring flow effects on polymer morphology in solution. The viscosity of Newtonian fluids has a simple definition as the proportionality constant between shear stress, τ , and shear rate, $\dot{\gamma}$ (Equation 4.4) [168]. Polymer chains often deform or untangle under shear resulting in non-Newtonian shear thinning [128, pp 23-25,135-140]. Under such a circumstance the nature of the flow field is important and different viscosities may be measured depending on the experimental method. For non-Newtonian fluids a phenomenological approach is often taken where apparent viscosity is reported as a function of shear rate under specific experimental circumstances.

$$\tau = \eta \dot{\gamma} \quad (4.4)$$

To make the measured viscosity relevant to the larger project it is necessary to define under what circumstances it will be measured. Temperature, concentration and shear rate must all be defined as all may be important.

4.2.2 Injectability Evaluation

Evaluation of formulation injectability is a developing field [73, 83]. In the knowledge of the author no globally accepted threshold exists for apparent viscosity. In this work 0.2 Pa·s is used based on the guidelines provided by Martens et. al. [73].

Shear rates are not well defined in works on injectability [73, 83] however a bounding envelope of 1000 s⁻¹ to 10,000 s⁻¹ can be defined based on the equipment used. This guideline is in line with volumes and advice found in [169]. Due to the possibility of shear thinning and start-up resistance, lower shear rates may also be of interest.

The guidelines for temperature are much more clear. Two key temperatures exist namely: 1) Body temperature 37 °C and 2) the standard lab environment 25 °C.

4.2.3 Instrument Selection and Operating Principals

A good summary of instrument types for polymer blends is provided by [128, pp 135-140]. This is applicable to polymer solutions due to similar physics [128, pp 135-140].

Oscillatory approaches used for polymer melts are not a good measurement option as the “Cox Merz rule” used to extrapolate results is “not applicable to dilute solutions, crosslinked systems or gelled systems” [170]. This leaves the three common steady state instrument designs as possible alternatives, namely: 1) cone plate, 2) Couette flow, and 3) capillary. The capillary design was selected for reasons discussed below.

In rotational designs, fluid is sheared between two surfaces such as the angle between the cone and plate or gap between concentric cylinders (Couette flow). Typically the cone or inner cylinder rotates. Shear rate is defined by gap geometry and the rotation rate. Measured torque allows estimation of shear stress. Designs are limited in maximum shear rate due to momentum effects at high radial velocities. These break down the standard stress estimation assumptions. The limitation is particularly severe at low viscosity (more desirable formulations). Samples are also not easily recoverable from rotational designs. They are generally smeared over large surfaces and may be contaminated with silicone oil (if used to prevent evaporation) or have their concentration change due to atmospheric contact (if oil is not used).

Looking at rotational designs in more detail, cone and plate is the preferred geometry due to the uniformity of the shear field [171]. Using the correlation provided by Felwell and Hellums [172] at reasonable cone angles and allowing a 5% deviation from uniformity, shear rate is limited to less than 100 s^{-1} for $0.02 \text{ Pa}\cdot\text{s}$ and may not exceed 850 s^{-1} at $0.2 \text{ Pa}\cdot\text{s}$. Couette flow faces similar problems. The limitation is due to Taylor instability with the onset of turbulent flow at $\text{Ta}_{\text{crit}} \approx 1700$ in Equation 4.5 [168, p 277]. The form of this relationship explains why obtainable shear rates are highly correlated with viscosity resulting in a narrow operational window for any given instrument configuration. Looking at the Brookfield lineup the best option model DV2T is due to its highest max speed [173, 174]). Even so it can only operate up to 960 s^{-1} at $0.2 \text{ Pa}\cdot\text{s}$ viscosity [173].

$$\text{Ta}_{\text{crit}} = \frac{r_i x^3 \Omega_i^2 \rho^2}{\eta^2} \quad (4.5)$$

The capillary rheometer design has different operating principals, relaxing shear rate limitations. Fluid is forced through a tube of known radius r and length L at a known flow rate Q . Shear is developed due to wall friction. Stresses are estimated from the pressure drop Δp along the tube. The primary disadvantage is a non-uniform shear rate in the radial direction. A distinct advantage for non-Newtonian fluids is the direct applicability of the flow geometry to the target application. Comparability with existing injectability literature is also an asset [73, 83]. Practical advantages of easy sample recovery and simple instrument design make experimental planning easier.

Assuming a Newtonian fluid and fully developed laminar flow, viscosity can be estimated from capillary rheometer results using the Poiseuille equation (Equation 4.7) [42, 168]. The corresponding average shear rate is given by Equation 4.6 [168, p. 274]. A laminar flow assumption is accurate below a critical Reynolds number of $Re_D \approx 2300$, Equation

4.8 [175, p. 467]. Flow is fully developed beyond the hydrodynamic entry length L_e given by Equation 4.9 [168, pp. 348-349][175]. For non-Newtonian fluids the Rabinowitsch-Mooney equation (not shown) gives a similar form to Equation 4.7 [176]. This allows a smooth transition to be made from a phenomenological apparent viscosity approach to a precise rheological description, provided data is collected under a sufficient range of conditions [176].

$$\dot{\gamma}_{\text{ave}} = \frac{4Q}{\pi r^3} \quad (4.6)$$

$$Q = \frac{\pi r^4 \Delta p}{8\eta L} \quad (4.7)$$

$$Re_D = \frac{2\rho Q}{\pi r \eta} \quad (4.8)$$

$$L_e \approx 0.12 r Re_D \quad (4.9)$$

Due to end effects, the pressure difference across a capillarity is never solely due to fully developed laminar flow. The conventional solution is to conduct series of experiments using capillaries of differing lengths but identical in all other respects. Provided all lengths have a region of fully developed flow, the regression model Equation 4.10 allows end effects to be eliminated.

$$\Delta p = \frac{8\eta Q}{\pi r^4} L + \text{end effect} \quad (4.10)$$

4.3 Experimental

4.3.1 Experiment Design

For all experiments, the solvent is phosphate buffered saline (PBS) at a pH of 7.4. This was to provide a simulated physiological environment. Six N-succinyl-chitosan amine substitution levels are available (22, 27, 34, 41, 48, 52%). 52% was not usable due to limited solubility. The remainder were run as a bisection search to cover as much of the field as possible within the time available for this study. In the end there was time for all five polymers. For each polymer a three factor experiment was planned in temperature, shear rate and concentration. A statistical design consisting of only *star* or *axial* points was selected to minimise the number of tests (see [167, pp 428-433]). The details of this design can be found in Table 4.1.

Temperatures of interest are approximately body temperature and the standard lab environment of 25 °C. Controller capabilities made 40 °C more practical than precisely body temperature. Provided reduced viscosity gives a good fit, interpolation to body temperature is possible, and only minimal uncertainty is introduced by using the higher temperature (see Equation 4.1).

Table 4.1: Rheometry Study Statistical Design: Star design with center point and three branches

Factor	Number of Levels	Center Point	Full Range
1) Concentration, w/w%	3 ^a	2	1,2,3,5 ^b
2) Average Shear Rate, s ⁻¹	2	470	47,470
3) Temperature, °C	2	40	25,40

^a 34% and 41% amine N-succinyl-chitosan only studied at two concentrations.

^b 2 and 3 w/w% with additional point at 1 or 5 w/w%.

The intended shear rates were 100 and 1000 s⁻¹. The upper is representative of those used by [73, 83] while the lower was selected to provide information on shear thinning and the potential for start-up resistance. Due to the received capillaries deviating from the 20 gauge standard, the achieved shear rates were 47 and 470 s⁻¹.

A concentration range of 1 to 5 w/w% N-succinyl-chitosan was chosen. For each N-succinyl-chitosan level, preliminary tests were conducted to pick the minimum concentration in Table 4.1 with a viscosity exceeding the target. Subsequent concentrations were prepared by dilution, necessitating that concentration levels be run from highest to lowest.

4.3.2 Capillary Rheometer Description

A capillary rheometer was built by the author to run these experiments (Figure 4.1). For a full design description see Appendix A. A system overview is as follows:

Flow rate control is provided by Kent Scientific GenieTouch syringe pump. This device can output a maximum force of 350 N, has a maximum carriage travel speed of 2.1 mm/s and has position detection to the nearest 0.2 mm [177]. To achieve higher flow rates and allow the sample syringe to be immersed in a water bath a hydraulic linkage system was constructed. Component sizes and pressure limits are listed in Table 4.2. With this system, volume accuracy is ± 100 μ L assuming no backlash. Steady state flow rate accuracy is likely much greater based on multiple position measurements.

Temperature control at 40 ± 0.5 °C was provided by a water bath controlled by a Corning PC-4200 hotplate with immersion probe. The rheometer systems all provide a watertight seal, however a plastic bag was used as secondary containment. For 25 ± 1 °C test the lab environment was sufficient.

Pressure measurements were made using an Omega MMG500USBHB6L0T8A9CE transducer. Thermal zero drift is $\pm 0.5\%$ FS, rated accuracy is $\pm 0.08\%$ FS BSL and linearity is $\pm 0.03\%$ FS. By recording a static baseline before experiment start and subtracting this

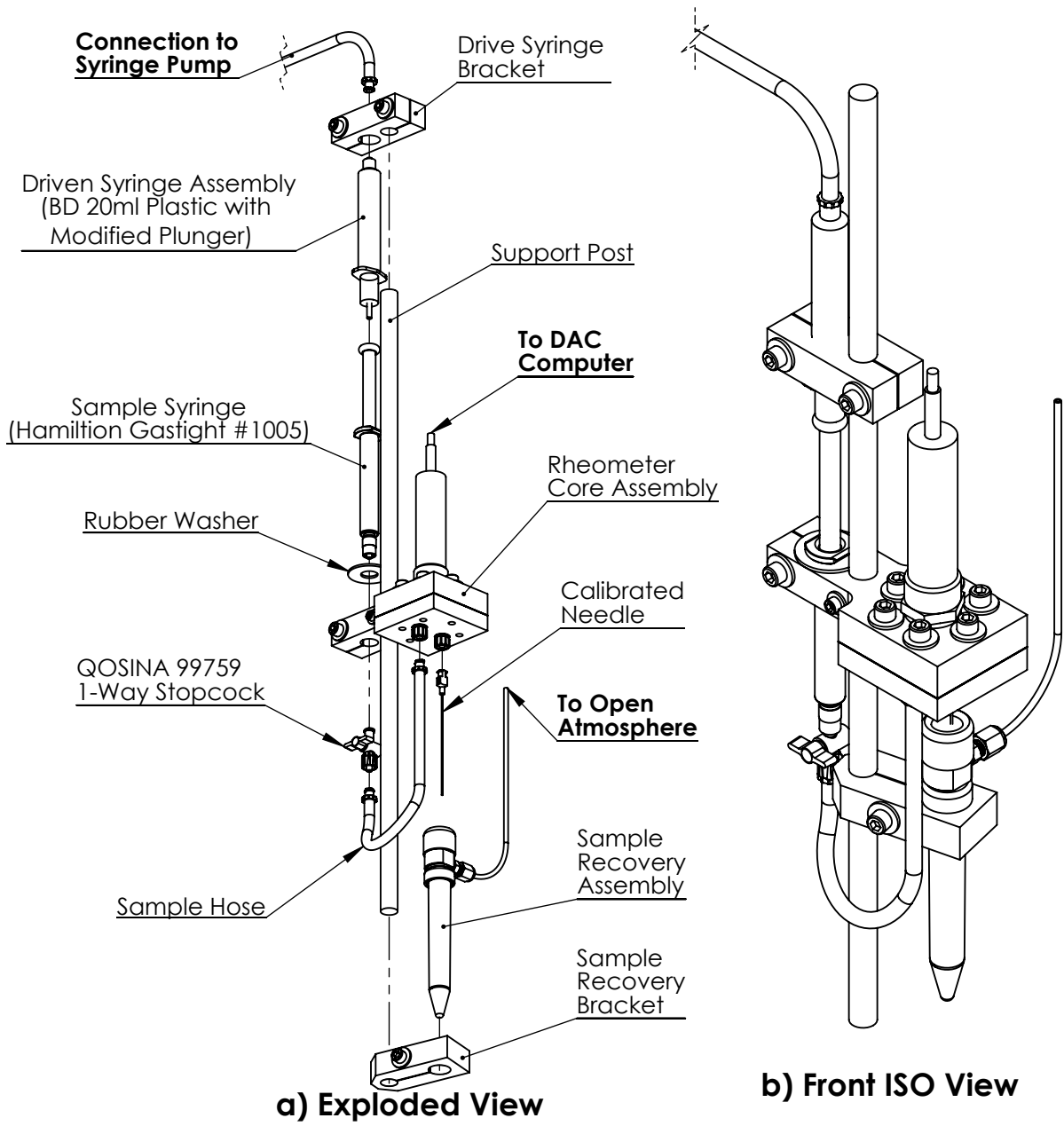


Figure 4.1: Capillary Rheometer Schematic

Table 4.2: Pressurised Rheometer Components

Component Description	Pressure Limit kPa	Syringe Barrel ID mm
Transducer	3500 ^a	—
Tubing	1200	—
Sample Syringe	1400	10.30
Drive Syringe BD 20ml Plastic	860	19.13
Driven Syringe BD 10ml Plastic	860	14.50
Lure Fittings	860	—

^a Transducer Measurement Rage, Damage Overpressure Limit 13,800 kPa

from the steady state pressure during the experiment the accuracy and thermal errors could be eliminated. As can be seen in Figure 4.2 the transducer was mounted in the core block above a PTFE membrane and the intervening space filled with silicone oil to transmit pressure. The large sample flow channel under the membrane limits pressure measurement error due to the Bernoulli effect.

Hypodermic needles were used as capillaries (Dana Medical 20 gauge #1101-192 Lot 02235326). The needles were cut and the tips ground flat, providing lengths between ~ 10 and 140 mm at 10 mm increments. Lengths were measured with a precision of ± 0.01 mm. The standard internal diameter for 20 gauge needles is 0.603 ± 0.019 mm. Lot variability is expected to be well under that implied by the manufacturing tolerance. To quantify this variability an optical microscope was used to measure the diameter of 5 needles. Based on these measurements the internal diameter was 0.776 ± 0.003 mm, where the error bars represent a 95% confidence interval. This means that even though the needles were not

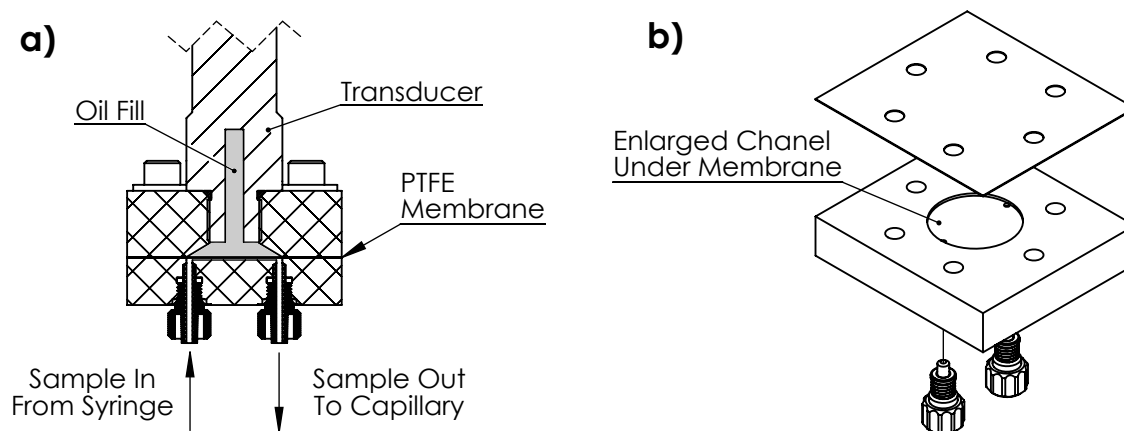


Figure 4.2: Capillary Rheometer Core Detail: a) Section view showing internal flow; b) Exploded view showing sample side only

labelled as such they were the thin wall variant. This was not discovered until after the experiments had been run which meant that there was no alternative but to use the results with the correct but lower than target shear rate. A check for error due to needle deformation showed no cause for concern. The maximum recorded pressure resulted in stresses less than 10% of the yield strength. Under the same circumstances radial elastic strains were approximately 400 times smaller than the diameter uncertainty. After diameter measurement the shear rate uncertainty contribution from capillary geometry is $\pm 1.2\%$.

For sample recovery the calibrated needle passed through a septa followed by a vented fitting and into a 15 ml centrifuge vial. A snorkel tube attached to the fitting provided the zero pressure reference for the system. The large diameter difference between tube and capillary as well as the viscosity difference between air and the sample prevented any appreciable pressure difference across this tube during an experiment.

4.3.3 Assumption and Safety Checks

Five check calculations are necessary to set up an experiment, namely: 1) laminar flow assumption check, 2) hydrodynamic entry length estimation, 3) pressure signal to noise ratio, 4) obtainable drive speed, and 5) system pressure safety factor.

Calculations for laminar flow and hydrodynamic entry length were already introduced in Section 4.2.3. These considerations were never limiting for any experiment.

Transducer linearity (min resolution 1 kPa) is the limiting factor for signal to noise ratio. When both viscosity and shear rate are low, signal resolution defines the minimum capillary length. Calibration experiments with water were conducted at a shear rate of 4700 s^{-1} to allow good signal resolution in the capillary length range available. The increased viscosity of all other solutions prevented the minimum capillary length from exceeding the practical lower limit of 40 mm.

The syringe pump has a maximum drive speed of 2.1 mm/s [177]. With the system setup as described, this limits the maximum shear rate to 4700 s^{-1} .

Pressure safety is the most important calculation both to prevent damage to the rheometer and to protect the operator. As can be seen from Table 4.2, the limiting components are the sample lure fittings. Though the hydraulic system has the same limit, pressures are always lower in the hydraulic loop due to the smaller sample syringe diameter. This design provides contingency for an overpressure event as the failure of a sample fitting is unlikely to be dangerous. Even so a check was conducted before each experiment to ensure the 860 kPa limit would not be exceeded at the maximum needle length selected. In a few cases this placed restrictions on the available options.

4.3.4 Experimental Methods and Data Analysis

Before each experiment all safety and assumption checks were run and the results were used to pick capillary lengths. Each experiment used a minimum of four evenly spaced lengths. At least six rheometer runs were used for each viscosity determination. Using the longest and shortest capillaries two replicates were run for increased precision. One replicate was run at each intermediate point to check linearity. Run order was randomised with the restriction that replicates of the same length were not grouped too closely within the set.

When the sample viscosity was unknown, a rough comparison between the flow characteristics of the sample and calibration materials was made. This provided an upper-bound estimate for viscosity. Based on this estimate, a single point experiment using the minimum capillary length was conducted. Ignoring end effects and using Equation 4.7, a sufficiently precise viscosity estimate could be obtained to plan the full experiment.

The full procedure for setting up a rheometer run can be found in Appendix A. Before starting an experiment, temperature equilibration was verified using a thermocouple attached to the sample syringe and the temperature recorded. Tests were conducted at 40 ± 0.5 °C or 25 ± 1 °C. Electronic pressure data was recorded at a sampling rate of 10 Hz.

To determine Δp for each run, the data was plotted and an average was calculated using all steady state points. Bubbles in the sample sometimes caused transient pressure fluctuations resulting in several steady state regions. Due to the vertical orientation of the capillary it was necessary to correct the transducer reading for static pressure head. For this purpose solution density estimates to two significant digits could be obtained by using the density of PBS at a given temperature. This was initially estimated using data for NaCl solutions of equivalent ionic strength [1] and the values later confirmed using a more precise PBS model [143]. Only the contribution from needle length was considered in the head correction as any other offset is captured in the end effects during the regression procedure.

The equations for viscosity analysis are provided in Section 4.2.3. When points exhibited larger than usual deviation from the regression line, outlier analysis was conducted using the r-student statistic [167, pp. 397-399][178]. Several times the results of this analysis pointed out problems with specific capillaries. In these cases the problem was corrected and the points in question were repeated. In a few cases no cause could be determined for a clear statistical outlier. Under such circumstances 4 to 6 additional points were collected to provide a larger data pool. In the absence of a known cause, the probability criterion for point exclusion was set at 99%.

For polymer samples a calibration multiplier was applied to the final results based on the appropriate fit equation in Figure 4.3. 95% confidence intervals were constructed for each analysis result using the arithmetic sum of the analysis uncertainty and the calibration prediction interval.

DI water for calibration was obtained from University of Waterloo chem stores. Water density and viscosity for calibration calculations came from the CRC Handbook [1]. The glycerol for calibration was EMD Lot 52172243, min 99.5%. Its density was estimated by linear interpolation of data provided by the Glycerine Producers Association [179]. Glycerol viscosity was estimated using Segur et al. [180] with the recommended interpolation functions (linear for temperature and logarithmic for concentration). Glycerol viscosity is a strong function of water content in the high purity range. A purity assay was conducted according to ASTM E928 Method B [181] which returns molar concentration. On the assumption that the primary impurity is water, glycerol purity was estimated at 99.98 ± 0.0002 w/w%.

4.3.5 Chitosan Solution Preparation

N-succinyl-chitosan (Table 3.3, C1 to C4, C6 or C8) was weighed into a centrifuge vial (Corning #430791 or #430829; Satorius CP 1245 Balance). Vial and sample weights were recorded to the nearest 0.1 mg. Solutions at the maximum polymer concentration were prepared using PBS, (Sigma D1408, diluted to 1x). Error during PBS addition was maintained below 0.1% target mass. The target was calculated on a dry polymer basis meaning the PBS was slightly diluted by the water carried on the polymer. No correction was made at this time for salt substitution.

To dissolve the polymer, the tube was heated to 60 °C by partial immersion of the closed vial in a water bath (200 ml beaker with acrylic tube holder, Corning PC-4200 hotplate, immersion probe in bath). To accelerate the process the vial was periodically removed from the bath and mixed vigorously using a vortex mixer (Corning #6775). If a

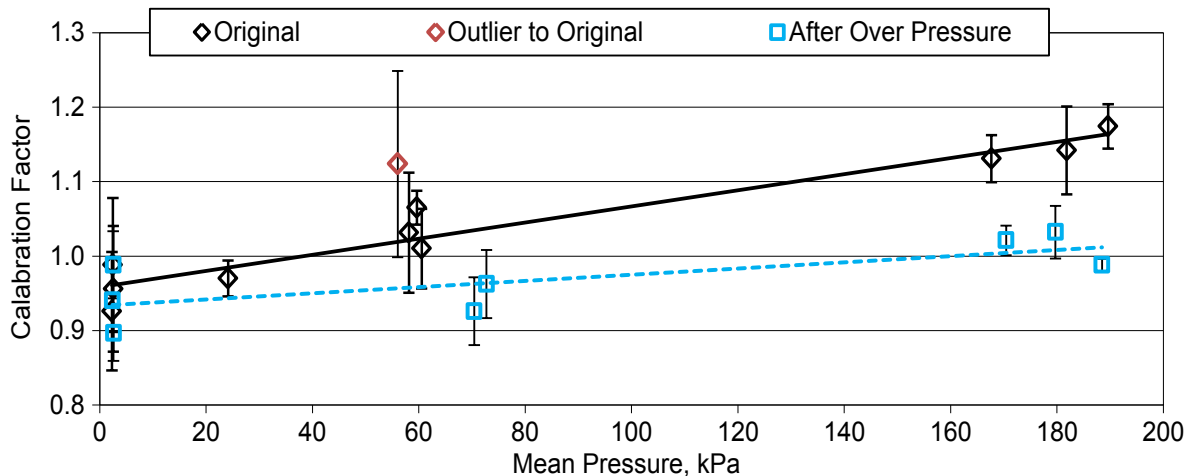


Figure 4.3: Capillary Rheometer Calibration, Black: First Calibration; Blue: Calibration after over-pressure event; Red: Outlier Point Caused by Contamination

homogeneous solution was not established after a reasonable time period (4-24 h), PBS was added to attempt the next lowest concentration. This was continued until a homogeneous solution at one of the target concentrations was obtained or the concentration options were exhausted. In marginal cases rough pH adjustment was investigated to aid solubility before the solution was completely homogeneous.

After the polymer dissolved, the bath was equilibrated at 40 °C and solutions adjusted to pH 7.4±0.01 using sodium hydroxide in deionised water. pH was measured using an Omega PHH222 meter calibrated using standard buffers (carbonate pH 10; VWR BDH5072 and phosphate pH 7; VWR BDH4046). Sodium hydroxide concentration was controlled to limit PBS dilution while still allowing precise adjustment. After adjustment the pH probe was rinsed into the solution using DI water to prevent polymer loss.

After pH adjustment the temperature was returned to 60 °C and excess water from polymer and pH adjustment driven off with forced air (room air, oil free pump; Welch 2534B-01). During this process a polymer rich skin formed on the solution surface. To prevent polymer loss, skin formation was monitored and the skin stirred down periodically using the vortex mixer. The process was continued until the vial mass dropped below the target. The mass was returned to within 0.1% of the target by final adjustment with DI water.

Lower concentrations were prepared by dilution of the initial solution with pH adjusted PBS. During the preparation procedure no contact with the vial contents was made by any instrument other than the pH probe. When it was necessary to pull the solution or condensation down off the vial walls this was done by centrifuging (7830 rpm, 5 min; Eppendorf 5430). Masses were measured using a Satorius CP 1245 laboratory balance.

Solutions were sealed and stored at less than 4 °C when not in use.

4.4 Results and Discussion

Apparent viscosity results can be found in Figure 4.4. The solid lines in the figure represent Equation 4.11. Coefficients are statistically significant (maximum p-value 10^{-9} , Table 4.3). The model fit excludes two regions where regime changes may exist, namely: 1) 47 s^{-1} shear rate above 34% amine substitution, and 2) 48% amine substitution below 2 w/w%. Use of relative viscosity accounts for the temperature dependence of all compositions.

$$\eta = \eta_o \exp(a) f^b c_2^c \quad (4.11)$$

Although the form of Equation 4.11 is the same as is used for polyelectrolyte scaling theories, the exponents are quite different meaning significant differences exist in the underlying physics [46]. This is somewhat contrary to expectations [20, 46, 125] but the discrepancy may be due to the high concentrations and shear rates used in this study. The

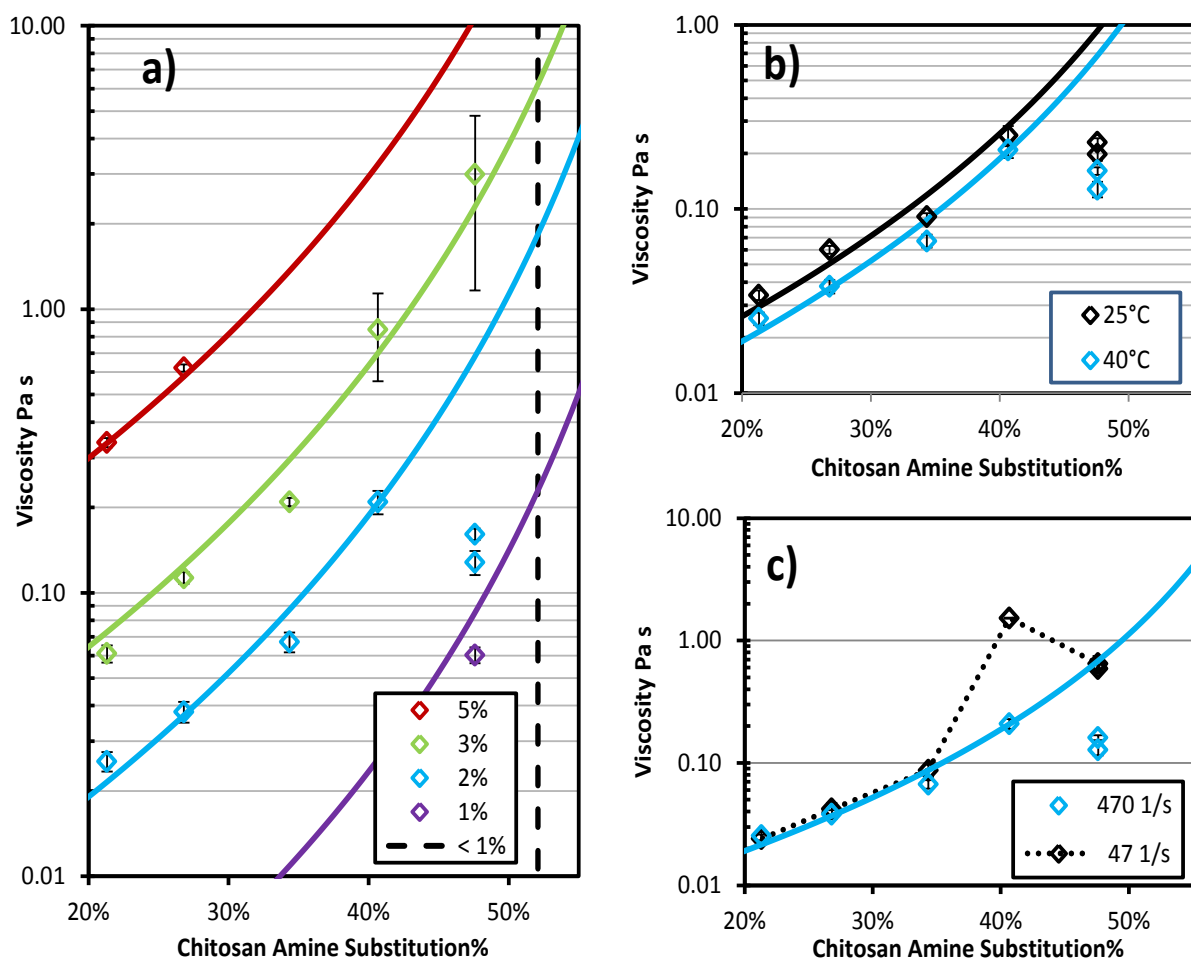


Figure 4.4: N-Succinyl-Chitosan Apparent Viscosity: a) Concentration effect, b) Temperature effect, c) Shear rate effect; Solid lines are contours from model (Equation 4.11) using the parameter values found in Table 4.3; Dotted line in c) is provided as a guide to the eye.

Table 4.3: Viscosity Model Parameters and Regression Coefficients

Description	Symbol	Value
Water Viscosity, 40 °C	η_o	6.53×10^{-4} Pa·s [1]
Water Viscosity, 25 °C	η_o	8.92×10^{-4} Pa·s [1]
Front Factor	a	13.0 ± 0.3 ***
Concentration Scaling	b	4.1 ± 0.1 **
Charge Scaling	c	3.0 ± 0.1 **

* $\exp(a)$ has units of $(w/w\%)^{-1}$

** $\pm x$ represents 95% confidence interval

deviation of the 2 w/w% line from the regression fit is in good qualitative agreement with the viscosity behaviour typical of polyampholytes as they approach their isoelectric point [20].

A hypothesis for the divergent behaviour of 48% amine N-succinyl-chitosan solutions is that inter-chain interactions stabilise polymer morphology at 3 w/w% but result in aggregation and chain collapse at 2 w/w%. This is consistent with: 1) what is known about polyampholyte phase separation behaviour, 2) observations made during long term storage, and 3) the behaviour of adjacent compositions. Nearly charge-balanced polyampholytes are known to sort themselves by charge, forming long range ordered structures [47], or aggregates that minimise the collective charge of the group [20, 47, 125]. During long term storage 3 w/w% solutions of 48% amine chitosan are stable but 2 w/w% solutions eventually form a precipitate. One step closer to the isoelectric point at 52% amine substitution solutions take the form of a polymer rich gel and a <1 w/w% dilute phase. In the other direction, at 41% amine substitution, the start of non-Newtonian behaviour occurs indicating the onset of morphological instability and/or inter-chain interactions. The presence of non-Newtonian behaviour indicates that shear rate may play a role in the agreement observed across the 3 w/w% range and suggests more study into dynamic effects on polyampholyte morphology might provide interesting results.

In the overall study plan the purpose of this experiment was to estimate what solution concentrations provide the upper bound 0.2 Pa·s viscosity. Good model agreement at low substitution allows interpolation up to 34% amine substitution. Table 4.4 lists concentration estimates from Equation 4.11. The actual concentration used in Chapter 7 experiments was selected using a preliminary analysis and is slightly different. Recalculation of the viscosity using the final approach shows deviation from the target value; however the concentrations selected seem reasonable given the range of viscosities observed and the imprecise nature of the target. Regardless of the interpolation approach taken, above 34% amine, non-Newtonian and complex phase behaviour make viscosity estimation much more difficult. As indicated in the table, the concentration of 2 w/w% was selected

for further experiments in the high amine range based on experimental results.

Table 4.4: Chitosan Solution Concentrations for Target Viscosity

Chitosan Amine substitution%	Concentration, w/w%		Viscosity Used, Pa·s	
	Eq. 4.11	Used	Eq. 4.11	Experimental
21	4.2	4.2	0.20	—
27	3.5	3.8	0.25	—
34	2.6	3.0	0.29	0.21
41	—	2.0	—	0.21
48	—	2.0	—	0.15

Chapter 5

Membrane Osmometer: Design and Validation

5.1 Overview

A membrane osmometer is necessary to characterise oxidised-alginate and N-succinyl-chitosan for swelling prediction. These experiments are described in Chapter 6. As the instrument is not available commercially, it was necessary to design and build a membrane osmometer in-house. The effort required multiple iterations before a fully operational and reliable instrument was developed. The manual osmometer design described in textbooks and used for teaching (e.g. [42, 182]) was found to be inadequate when compared to a sophisticated design developed later [183]. The final design has thermal stability and measurement precision in compliance with ASTM D3750 [45]. Instrument performance was validated using Poly(vinyl alcohol) for which published property estimates exist.

5.2 Background

5.2.1 Alternatives to In-House Fabrication

A commercial membrane osmometer was not available and obtaining access to an instrument at another institution was ruled out. This left no alternative other than to building one in-house. The large scope of experimental work needed in this study requires months of instrument time. A specialised instrument was required to provide sufficient sensitivity while resisting damage from concentrated chlorides. The risk of damage took on increasing significance as it became more apparent that new instruments and even replacement parts were completely unavailable.

Commercial membrane osmometers were once relatively common. The development of alternative molecular weight measurement techniques in the late 1980's resulted in reduced need for membrane osmometry [184]. This led to the withdrawal of the ASTM Standard in 1991 [45]. The Fisher web page listed an inexpensive manual instrument during the initial stages of experiment planning (2011), however it was discontinued by the time inquiries were made regarding purchase. Two suppliers of automatic devices confirmed that their instruments were discontinued (Wescor, Model 4420; UIC, Models 230 and 231), with the latter also noting that they had stopped carrying replacement parts. A third instrument supplier (Gonotec, Osmomat-090) has no Canadian distributor and did not respond to repeated attempts at contact. No other commercial instruments with sufficient resolution were found.

5.2.2 Design Constraints and Criteria

Four key constraints must be met by any instrument design, namely: 1) cost, 2) pressure resolution, 3) thermal stability, and 4) solvent resistance. Cost was a very significant constraint for the first design iteration. More resources were provided after the first design failed and it became apparent that larger factors of safety should be used if osmometry was to be successful. Pressure measurement resolution better than 0.1 mm solvent column is recommended by ASTM D3750 [45]. Monte Carlo simulations indicate total scatter below ± 0.4 mm H₂O is sufficient for estimation error of less than 10% for the worst parameter and less than 5% for the majority of parameters (see Section 2.6.3). Thermal control is necessary for baseline stability [183]. Recommendations range between ± 0.05 °C and ± 0.005 °C [26, 45, 183, 185]. Thermal baseline fluctuation is strongly dependent on membrane hydraulic conductivity which in turn is dependent on expected molecular weight (see Section 5.4.4). Minimizing corrosion is the main challenge in choosing solvent-contacting materials. To undertake the experiments in Chapter 6 phosphate buffered saline with up to ten times the usual chloride content was used. Titanium, most plastics and glass are all resistant, surgical stainless steel is marginal while aluminium and carbon steel are not usable.

Osmometer design criteria are: 1) fast response time, 2) low sample volume, and 3) easy manufacturability. Fast response time is important because of the potential for alginate degradation [44, 88]. Sample volume should be minimised as limited material is available for experiments. Ease of manufacturability is important if both cost and solvent resistance constraints are to be met because materials that can handle chlorides are often hard to work with.

5.2.3 Membrane Osmometer Design Review

Osmometer designs can be classified according to the sensing and operational approaches used. Pressure sensing is accomplished by use of a transducer or by measurement

of differential fluid heights. The height method is the oldest and simplest; however instrument speed is limited by the practical cross sectional area of the measurement capillary [183, 185]. The transducer approach allows for use of a rigid cell. Measurement speed is increased by eliminating the capillary volume.

Osmometer operation may be classified as active or passive [183]. Under the active approach, equilibration kinetics are observed at a series of operating points. Interpolation of these results provides an estimate of the equilibrium level. This technique assumes no polymer diffuses across the membrane, and does not provide a means for checking this assumption. Operation in passive mode captures the whole equilibration curve. The shape of this curve provides a check that low molecular weight polymer is not leaking across the membrane [45, 183].

Osmometry as a field is old, dating back to late 1800's [183]. The manual designs covered by the most recent operation guidelines, [45][42, p. 549], date to the 1940's and use the capillary sensing approach [186–189]. Though widely used historically and well understood these are very slow in the passive mode. Equilibrium times under passive operation range from “several days”[187] to “a couple hours” [185, 189]. Under active operation performance is much more reasonable. With the “Fuoss-Mead” manual design recommended by ASTM D3750 a “consistent reading” is possible in as little as 3 min [45, 186]. Typical sample volumes are on the order of a few milliliters.

Design innovations reported by Hansen in 1969 [183] appear to be the basis for most instruments developed after 1970 [184, 190–192]. This includes the automatic commercial devices noted above. The key innovations were pressure measurement on the reference side and use of a transducer allowing for a sealed and rigid reference chamber. If the chamber contents are practically incompressible, very small fluid flows can result in large pressure changes and fast response times. The limiting factor is the least rigid component, generally the membrane. Use of a curved membrane support on the reference side allows the membrane to be very rigid. With this design the passive equilibration curve can be captured in as little as five minutes [192]. The use of micro-liter sample volumes are also possible [191, 192].

Temperature control is important at elevated temperatures for both types of instruments [26, 45, 183]. Under standard laboratory conditions, insulation or a sufficiently stable room temperature is sufficient [183, 186, 192, 193]. At other temperatures immersion baths are typically used [183, 185, 187–189].

The decision to pursue a “Fuoss-Mead” design was made based on the following factors: Performance is similar between “Fuoss-Mead” and “Hansen” type osmometer designs, with the exception of error checking ability [186, 192]. Manual instruments are less costly, (no transducer, lower precision components), and more typical of in-house builds [182, 188]. If error checking becomes necessary the “Fuoss-Mead” design can be run in static mode similar to the best performing manual designs [185, 186]. A switch to a “Hansen” type

design occurred later when the slow speed of error checking with manual designs became a serious challenge.

5.3 Initial Design - Fuoss-Mead Variant

5.3.1 Introduction

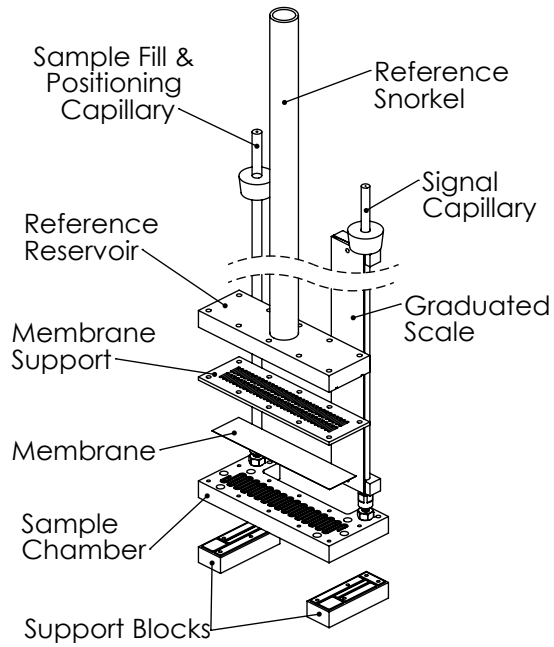
Documented success with very simple designs, [182, 188], and cost as a key constraint led to the decision to build a manual type instrument. Design constraints are as listed in Section 5.2.2. The basic operating principles are similar to designs by Fuoss and Mead [186] and to a lesser extent Zimm and Myerson [185]. The goal was to use active operation for fast measurement, and passive mode for trouble shooting and validation.

5.3.2 Design Description

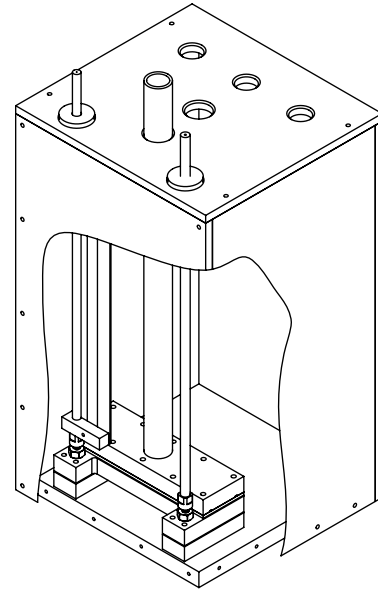
Figure 5.1 provides a design schematic. Engineering drawings can be found in Appendix B. One challenge of the “Fuoss-Mead” design is the existence of dead volume in the sample chamber [186]. Several rinses might be necessary during sample changes to prevent cross contamination and eliminate bubbles. To minimise this risk, a convoluted sample chamber with minimal dead volume was adopted (Figure 5.1d). The channel is narrow (~ 1.6 mm) providing a similar membrane span to Fuoss (2 mm [186]). The shallow depth of the channel allows a large membrane area with a small sample volume (~ 3.5 ml).

To allow for pressure adjustment a positioning system similar to that of [185] was attached to the fill capillary (not shown in figure). The system consisted of a compression fitting at the top of the capillary, a long hypodermic needle closely matching the capillary internal diameter, and a stopcock to close the needle. For active operation, the needle could be moved up or down in the fill capillary changing the sample chamber internal volume and allowing precise adjustment of the system operating point. The compression fitting both sealed the top of the fill capillary and locked the needle in place at any position. The stopcock allowed sample injection during changes.

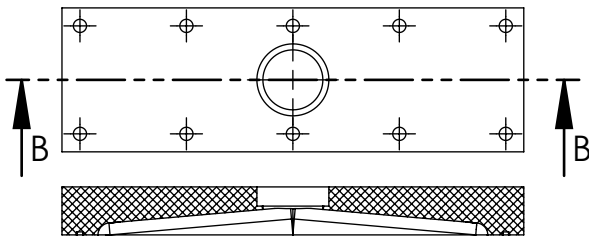
To keep costs low the design uses: an existing hotplate as the immersion bath controller, inexpensive dialysis tubing as the membrane, and an existing digital camera to measure pressure by capillary height. For effective heat transfer the water bath bottom was made from a piece of copper plate. Because the bottom is not ferromagnetic, this also allowed a magnetic stir bar to be used for bath circulation. Tubing width and water bath dimensions constrain the active membrane area. Despite this, performance was predicted to be adequate. The design’s active membrane area of 980 mm^2 is bracketed by those of Fuoss (4000 mm^2 [186]) and (Zimm 300 mm^2 [185]). Scaling should be linear with membrane



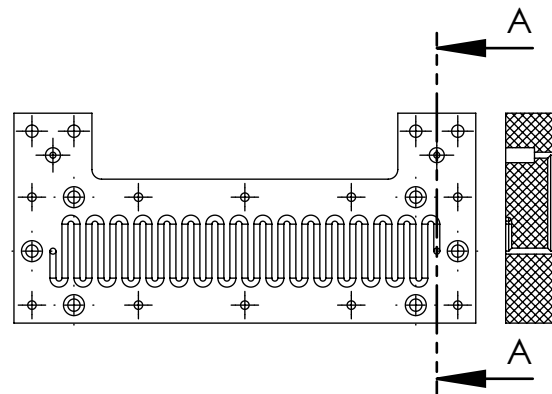
a) Primary Component Exploded View



b) Osmometer in Bath Cut Away View



c) Reference Reservoir Detail



d) Sample Chamber Detail

Figure 5.1: Osmometer Initial Design: needle and compression fitting for sample loading and position setting not shown in figure.

area resulting in an expected active cycle time of ~ 15 minutes based on Fuouss's 3 minute number and a passive cycle time of 30 to 60 minutes based on Zimm's 1 to 2 h result [185, 186].

For precise pressure measurement a graduated scale was placed in the water bath immediately behind the measurement capillary. This minimises parallax and refraction errors. A consistent zero reference was established by use of a large diameter glass snorkel tube and an angled ceiling in the reference reservoir (Figure 5.1c). These allow bubbles to be cleared minimizing the effect of thermal fluctuations. The camera was mounted on a tripod allowing the meniscus to be vertically centred in the frame while maintaining a consistent focal length. Time-stamped photographs showing reference and signal levels provide a record of readings. Image analysis allows the scale to be read to the 0.1 mm precision recommended by the standard [45].

Aside from the replaceable stainless steel positioning needle all parts are made from chloride resistant materials. Major machined parts are made from polycarbonate. In addition to chloride resistance, polycarbonate was selected due to its transparency and easy machinability. Transparency allowed bubble elimination to be verified improving performance. Easy machinability helped keep costs low. To seal joints between primary components an initial iteration used neoprene gaskets. The final version uses in situ gaskets cast from silicone rubber in grooves machined for this purpose. (These are visible on the upper surface of the support blocks in Figure 5.1, but are hidden on the underside of the membrane support and reference reservoir.) Parts were masked with several layers of tape during gasket casting to provide the compression necessary for a good seal during assembly.

Capillary fittings were made from titanium to ensure chloride resistance and a strong external thread. The fittings were designed as small turned components. This made them relatively inexpensive and easy to manufacture despite their material's reputation. The turned fittings allowed both capillary tubes to be simple cylinders. All the tubes including the reference snorkel were cut from lengths stocked by the campus glass blower. They were attached using epoxy for strength and a water tight seal.

In this design, the capillary fittings and the sample chamber (Figure 5.1d) require a trained machinist, glass tubes must be cut and flame polished by the campus glass blower but all other parts are simple enough to be made by the author in the University of Waterloo student shop.

5.3.3 Performance

This initial instrument design failed to achieve acceptable baseline stability. Although the column height could be measured within 0.1 mm optically, 2 to 20 mm swings in level combined with long response time (hours to days) prevented any experimental results from being gathered. Subsequent investigation with improved designs places much of the

blame on the membrane used (Sigma-Alrich D0655, Table 5.1) and insufficient temperature control (Figure 5.4).

Six other factors may have contributed to the failure of this design, namely: 1) aqueous solution sticking in the measurement capillary as noted by [185]; 2) lack of secondary leak protection making a small leak from water bath difficult to rule out; 3) manual data logging making troubleshooting very difficult and time consuming; 4) the base plate connection contributing to pressure swings via differential thermal expansion; 5) use of lower modulus plastic rather than steel for membrane supports [186], and 6) excessive gasket bolt spacing. For the latter, Shigley recommends less than 6 nominal diameters between bolt centres in full gasket joints[194]. In this design the bolt spacing is greater than 9 nominal diameters. The move to non-load-bearing gaskets partially mitigated this difficulty however bolt load still may not have been sufficiently uniform for good membrane clamping. These factors were considered during the transducer design and should be considered for future manual designs.

5.4 Transducer Osmometer Design - Hansen Variant

5.4.1 Introduction

Robustness, automated data collection, and error checking were given higher priority after the difficulties experienced with the first iteration. The Hansen type instrument was selected due to its superior performance statistics [183]. The Hansen design allows automated collection of the full equilibration curve in as little as 5 min and with sample volumes as low as 5 μ L [192]. Relaxation of cost and solvent resistance constraints allowed purchase of the required pressure transducer.

Three principal challenges had to be addressed while implementing the design, namely: 1) modifying published core designs to work with available pressure traducers; 2) adding capacity for thermal control; and 3) trouble shooting the membrane and membrane clamp area to overcome pressurization problems during assembly.

5.4.2 Core Design

The osmometer core assembly is shown in Figure 5.2. Machined components are made from polycarbonate. Membranes and gaskets are prepared as needed using tool steel punches. Appendix C.2 provides detailed design drawings. Punch design details and guide templates can be found in Appendix C.6.

Core operating principals are credited to Hansen [183] but membrane support geometry is as provided by Aukland [192]. The critical area is shown in Figure 5.2c. All void space

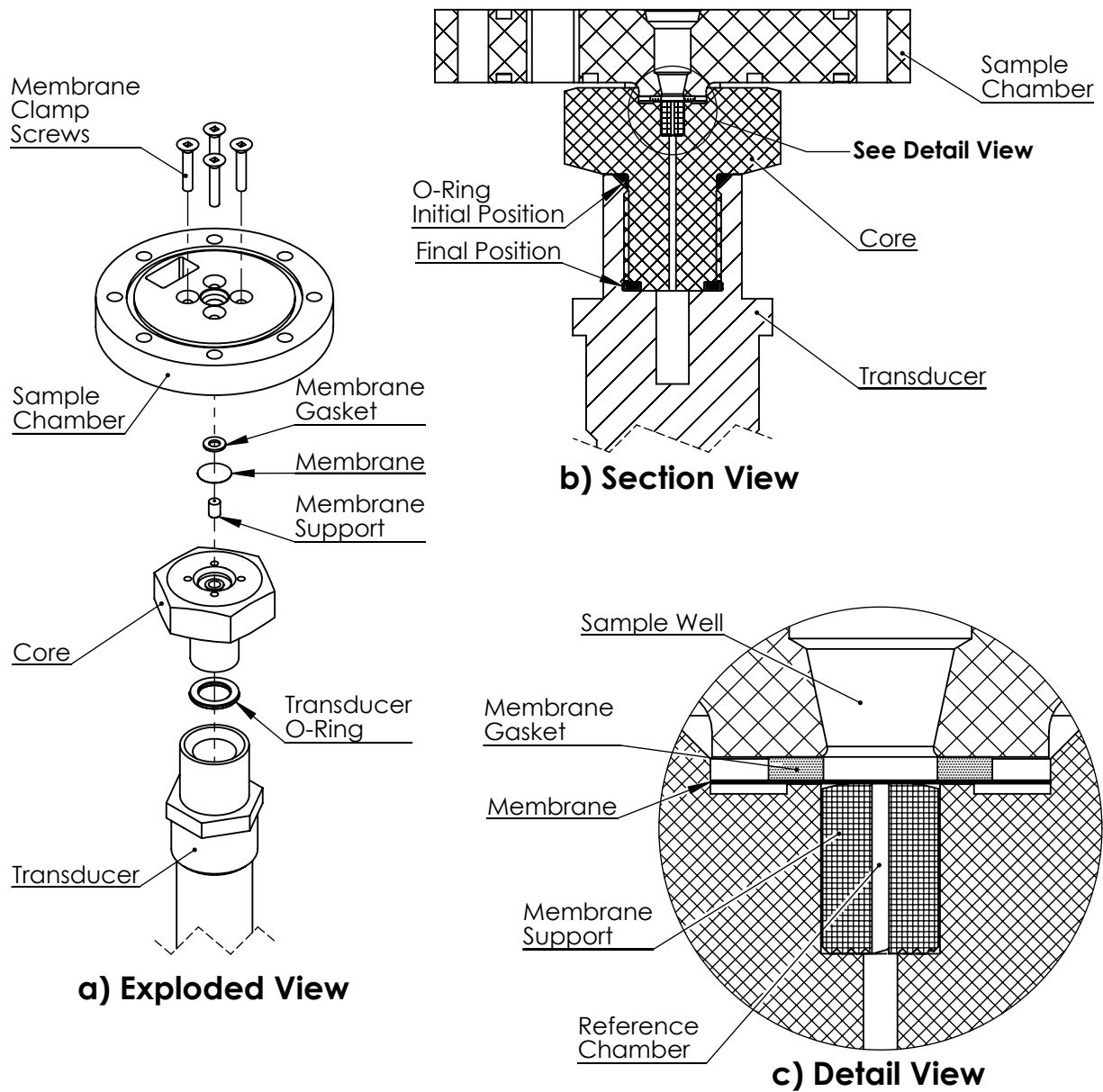


Figure 5.2: Transducer Osmometer Core Design (modified from [192]); Note: a) and b) rectangular slot for transducer cord in sample chamber; Note: c) inset membrane clamp face on osmometer core allowing it to be submerged in reference fluid during membrane installation

below the membrane is part of the reference chamber, including the thin fluid film between the membrane support and the membrane. Polymer cannot cross the membrane and draws solvent into the sample well. The resultant pressure difference compresses the membrane against the support. Provided the pressure does not crush the membrane, the fluid film behind the membrane is unaffected allowing the whole area to be active. If the reference chamber is free of gas bubbles the equilibrium volume change is small. Sample dilution can therefore be ignored and equilibrium is rapid.

It is noted that the performance of the instrument could be severely affected by the formation of gas bubbles which expand under vacuum conditions increasing the flow volume. The reference solvent must therefore be degassed before use (see Section 5.5.2) and special procedures are necessary to fill the core with gas free solvent. To facilitate this, the membrane clamp area is at the bottom of a shallow dish allowing it to be flooded with degassed solvent during membrane installation.

Leakage at the membrane joint can be prevented by crushing the membrane along the clamp line or completely sealing the surrounding cavity. Auckland [192] calls for crushing the membrane. With the use of an inexpensive dialysis membrane, our design geometry was over-constrained which prevented sufficient clamping pressure from being developed (Figure 5.2b). Although this could have been addressed by redesigning the part, several gasket approaches were tried instead. A steel spacer compressed the membrane but did not seal against the sample chamber. O-Rings sealed the cavity but deformed inward resulting pressure buildup under the membrane. To achieve adequate mechanical support, clamp screws had to be tightened in stages to avoid damaging the transducer. With the dialysis membrane this took approximately 1 week. Success was achieved by making two changes in conjunction: faster membranes were obtained (see Section 5.4.4) and a composite gasket material was adopted (McMaster Carr 9470K26). This combination resulted in a good seal and reduced tightening time to ~ 45 min.

A modular transducer from Omega instruments (MMV10WUSBK6MF0T9A10CE) provided the best compromise between price, design robustness, and instrument performance. This is a vacuum-range gauge-pressure transducer with a full scale reading of 2.5 kPa, accuracy of $\pm 0.14\%$ FS, and up to $\pm 0.07\%$ FS BSL linearity. Although not necessarily up to the ASTM standard (error is as high as ± 0.36 mm of water column) this was the best off the shelf transducer available in a package that can tolerate chlorides (all wetted parts 316L stainless steel). Experiment simulation results (Section 2.6.3) indicate that the pressure range is excellent (5x factor of safety) and that the error level is tolerable (error less than 10% for the most affected parameter).

Auckland partially disassembled a pressure transducer to allow direct access to the sensing membrane and minimal reference chamber volume [192]. This was not an option with the available transducers. Pressure is transmitted to the sensing chip via a fragile stainless steel membrane which is located after the fitting at the bottom of a blind hole (see Figure 5.2b). This protective well is responsible for most of the reference chamber volume.

Use of a female fitting allowed additional volume to be limited to the small diameter connecting channel in the core. The initial o-ring location is at a feature specifically designed for this purpose. Slow pressure equilibrium along the thread introduced virtual leaks that degraded instrument response time [195]. Sealing against the turned floor of the fitting eliminated this difficulty. As the transducer connection is not as convenient as Auckland's, a slightly greater instrument response time is anticipated [192].

The outer hole pattern and large o-ring grooves on sample chamber provide mechanical support and the interface between the core assembly and the thermal control system (Figure 5.2a). The square slot in the sample chamber is to allow the transducer USB cable to loop around and exit the instrument via the top of the assembly.

5.4.3 Thermal Isolation and Stability

There were two major thermal control design iterations. The first had the osmometer sample chamber at the top of the water bath and largely uninsulated from the room (Figure 5.3). The second iteration used a thermal isolation spacer to break the connection with the environment (Figure 5.5). The necessity of a thermal break was determined in commissioning experiments using the first thermal design which showed an unacceptably high noise level (Figure 5.4). The fact that the derivative of pressure correlates with temperature rather than the derivative of temperature indicates the core had an external temperature reference.

At the same time it was noted that thermal stability was inadequate for the hotplate based water bath (± 0.2 °C compared to ASTM recommendation of ± 0.05 °C [45]) To address this, a circulating bath controller was purchased (Fisher ISO Temp 4100) and a new bath enclosure was built to provide a flow pattern that promotes good mixing (Figure 5.5c) [196]. Achieved temperature stability was better than ± 0.01 °C based on the bath controller display.

Figure 5.5b provides a design schematic for the thermal isolation spacer. Engineering drawings can be found in Appendix C.4. A brief description is as follows:

At the core end of the spacer, a heavy copper flange and plug provide rapid thermal conduction inward, resulting in a limited thermal gradient in the radial direction. Plug surfaces are angled to maximise the contact area and limit contact resistance. Above the conducting plug, an insulating plug made from expanded polypropylene minimised thermal conduction to the environment. Both plugs are removable without disturbing the instrument core. To lift them out simultaneously, a low thermal conductivity nylon handle is provided.

Mechanical support is provided by the thin copper spacer tube. This is sized for rapid conduction radially from the bath and poor conduction laterally to the environment. The

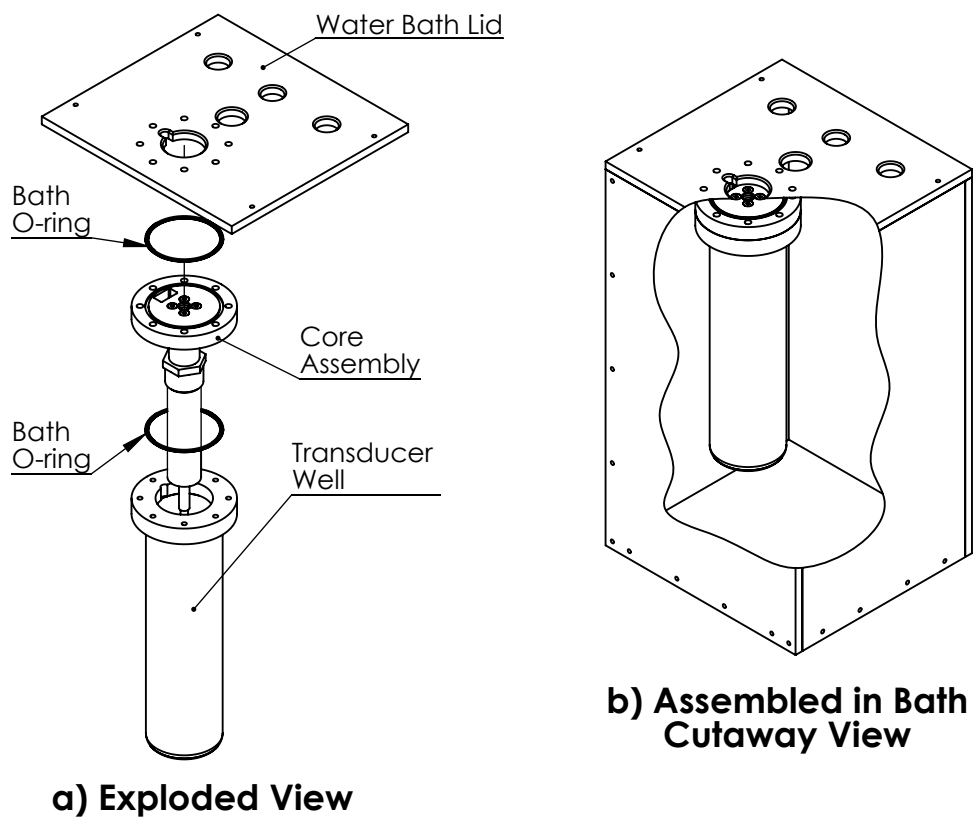


Figure 5.3: Initial Transducer Osmometer Temperature Control

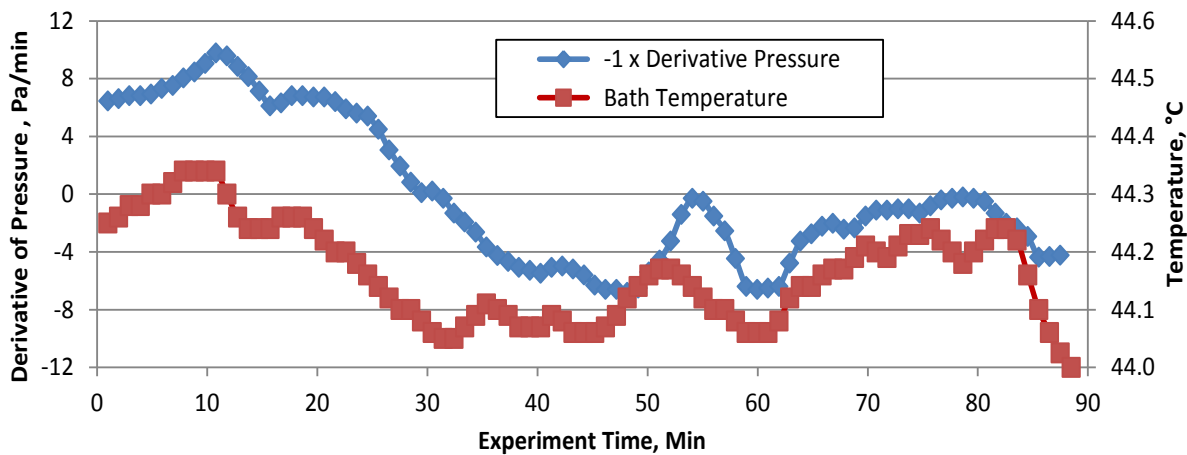


Figure 5.4: Osmometer Temperature Effect: Typical scan of inadequate water bath temperature control.

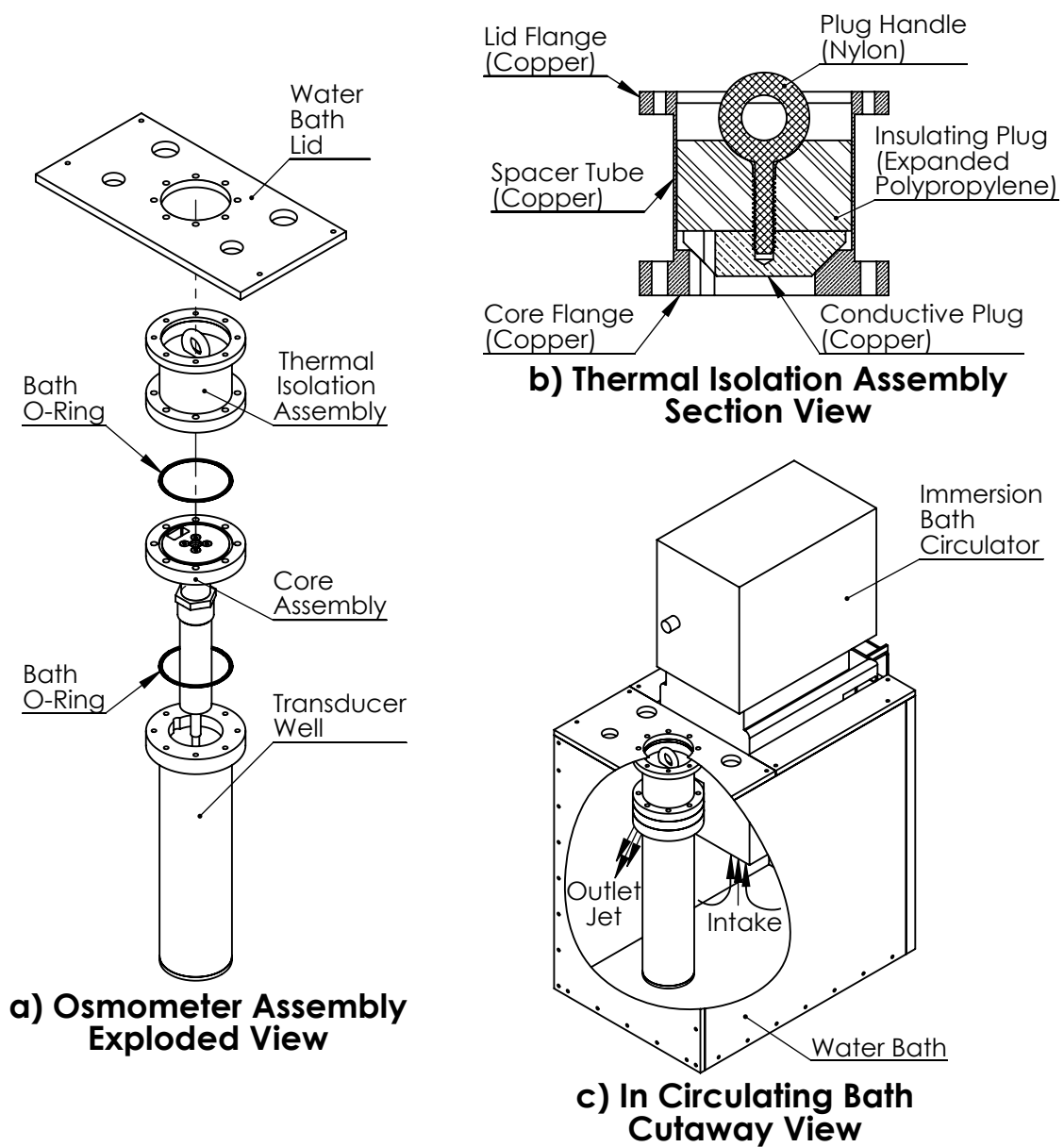


Figure 5.5: Improved Isolation and Temperature Control: a) Osmometer Assembly Exploded View; b) Thermal Isolation Assembly Section View: Note transducer cord slot in left hand side of conductive plug and core flange; c) Osmometer in Circulating Bath Cutaway View

spacer is sized so the lower edge of the insulating plug is always below the bath low water line.

Flanges are soldered to the spacer tube to establish a strong watertight connection. To allow for this and to avoid problems with differential thermal expansion, the lid flange was also made from copper. An o-ring seal was used at the core end. The lid flange is above the water line. This joint is exposed to condensation on the underside of the lid, however the seal provided by contact between the smooth component surfaces proved adequate.

A first order estimate indicates that the thermal gradient between the bath and the center of the conductive plug should be less than 0.01 °C. The calculation is based on a resistance network model between the 40 °C bath and a 25 °C room. Conduction from the bath to the center line, including contact resistance is modelled using a 1D axisymmetric approximation. From here the nylon bolt and insulating plug are modelled as two 1D resistors in parallel. Conduction in the spacer tube is neglected.

The core flange and conductive plug are slotted and there is a slit cut in the insulating plug to allow the transducer cord out and provide pressure equalization with the room.

5.4.4 Membrane Hydraulic Conductivity

In the absence of a membrane, the improved thermal control resulted in good pressure stability. This indicated that external environmental effects were no longer a concern. For most of the development period inexpensive dialysis membranes were used (Sigma-Aldrich D0655, Table 5.1). With this membrane installed the overall performance was still unacceptable indicating that membrane hydraulic conductivity might be too low. Of particular concern was the need to tighten membrane clamp screws over a 1 week time period to avoid over pressure damage to the transducer.

To characterise the dialysis membrane, a device similar to a crude manual osmometer was fabricated (see [188]). The membrane clamp was made using a modified centrifuge vial and a graduated pipette was used for the capillary. Pure water was used in both compartments and tests were conducted under laboratory conditions. By adjusting the capillary to well above the reference level and recording the flow volume at set intervals the membrane hydraulic conductivity could be estimated. As can be seen in Table 5.1 it is very low.

Observed baseline stability is in good agreement with the calculation results in Table 5.1. Hourly fluctuations in the 2 to 10 mm range were common with the dialysis membrane. A three day stability study with Millipore PLTK membrane resulted in a baseline standard error of less than 0.13 mm H₂O from all causes.

Table 5.1: Estimated Influence of Temperature Stability on Osmometer Baseline

Membrane Type	NMWL Cutoff kDa	Hydraulic Conductivity LMH/psi	Baseline Fluctuation in mm H ₂ O with Temperature Stability ^{a b}		
			±0.2 °C	±0.05 °C	±0.01 °C
Millipore PLTK	30 ^c	25 ^c	0.4	0.09	0.02
Millipore PLGC	10 ^c	7.5 ^c	1	0.3	0.06
Millipore PLBC	3 ^c	1.0 ^c	9	2	0.4
Sigma-Aldrich D0655	12.4 ^c	0.2-0.02 ^d	40-200	10-60	2-10
Impermeable	—	—	500	100	20

^a 0.06 µL/100mmHg [192] cell rigidity estimate used

^b Membrane conductivity effect assumes 10 min temperature swing

^c Manufacturers Specification

^d Experimentally determined. Range is based on three tests. Average is closer to lower bound.

5.4.5 Final Cost and Performance

Total development costs likely exceeded \$5000, however the total cost of the primary components in the final design is less than \$3500. Primary component cost from most to least expensive is as follows: circulating bath controller (\$1,075), machined core components (\$740), pressure transducer (\$690.00), thermal spacer (\$525) and micropipette (\$260.00). Note that this does not include the water bath enclosure which was built by the author for material cost, but does include the micropipette (necessary for sample loading) which may already exist in many labs. Operation costs are minimal (membrane cost is about \$4 per instrument setup.)

Stability of ±1.0 Pa or ±0.10 mm H₂O was achieved in an unperturbed baseline test. (6 readings per min for 3 days; ten minute smoothing window; Millipore PLTK membrane with 50 µL DI water for sample and silicone oil cover to prevent evaporation.) The system time constant is estimated at 9.6 min based on autocorrelation analysis of the same data set. This was in good agreement with the pressure response time during screw tightening. Baseline repeatability is ±0.25 mm (upper bound 95% confidence interval based on a commissioning trial and some Chapter 6 experiments; 12 different days data >100 points). Baseline error was calculated using sets of three sequential points. To closely mirror the data reduction approach adopted in actual experiments, baseline error is calculated using the center point value minus the average of the two adjacent points. Comparing the stability and repeatability figures, sample loading is highlighted as the current limiting factor for this instrument.

5.5 Setup and Operating Procedure

5.5.1 Setup

Figure 5.6 provides the setup time-line. A detailed procedure can be found in Appendix C.8. The minimum turnaround time is approximately 3.25 h with two people. 4 h is more typical for a single person. Summary of key points:

1. **Parts Cleaning:** Between uses, parts were rinsed with deionised water and then ultrasonicated three times with a complete water change each time. Before their first use, parts were ultrasonicated in DI water with soap to remove any residual grease. The transducer could not be ultrasonicated and was merely rinsed. As it does not contact the polymer solution this was sufficient to prevent contamination cross talk between experiments.
2. **Membrane Preparation:** Three 9.5 mm diameter disks were punched from each 25 mm purchased disk. Punched disks were cleaned according to the manufacturer’s instructions and stored in 10% ethanol at fridge temperature until required for use. Membranes to be used immediately received a 10 min rinse in 10% ethanol to standardise the assembly starting point. In the lead-up to assembly membranes were rinsed for 10 min with reference solution and briefly with degassed reference solution.
3. **Degas:** See Section 5.5.2

ID	Task Name	Duration, min	Time, hours				
			1	2	3	4	Overnight
1	Membrane Rinse	75					
2	Osmometer Tear Down	15					
3	Cleaning	40					
4	Degas Reference Solution	40					
5	Assembly	30					
6	Thermal Equilibrium	45					
7	Clamp Screw Tightening	45					
8	Stability Shake Down	Overnight					

Figure 5.6: Osmometer Setup Timeline

4. Assembly: A detailed procedure was developed to insure the core remains free of bubbles (see Appendix C.8). During assembly, care was taken to ensure membrane clamp faces were parallel for uniform gasket pressure. Membrane screws were tightened lightly to hold components in place without establishing a seal.
5. Thermal Equilibrium: To avoid over-pressurization it was necessary to allow the core reference solution to expand to its working volume before screw tightening.
6. Screw Tightening: Membrane clamp screws were tightened in four even stages using a torque wrench. Core pressure was allowed to dissipate between stages. The baseline shifted systematically as a seal was established. The final screw torque was selected such that the baseline level was not noticeably changed between the third and final torque stages. The final torque was between 10 and 15 N·cm and with the precise value depending on the membrane.
7. Stability Shake Down: An overnight period was necessary to reach mechanical (gasket creep) and chemical (dissolved gas) equilibrium.

5.5.2 Solution Degas

A review of degassing theory was conducted to determine the correct conditions. The application meets the requirements for use of a simplified form of Henry's Law per Eq 11 in [197]. Water vapour pressure was estimated using the Antoine equation with parameters from [198]. The air pressure history for the lab location was obtained from the University of Waterloo Weather Station [199]. Air solubility in water was taken from Battino et al. [200]. Note that the equation provided in the reference has a unit conversion or typographic error. (Does not match the associated table.) Fortunately for our work, a regression fit using the same functional form as the original provided a good match to the table.

The key result of the review is that a complete degas requires the partial pressure of air at the liquid interface to be zero. Temperatures were selected to place the water partial pressure above the maximum vacuum pressure achievable by the pump (Welch Model # 2534B-01, Max vacuum pressure 27.2" Hg). 60 °C was calculated for pure water. This was raised to 62 °C for salt solutions due to the boiling point elevation effect.

Special valved lids were developed to allow reference solutions to be degassed inside 50 ml centrifuge tubes (Corning #430829, see Appendix C.7). Tubes were filled to the 35 ml line and evacuated. Note that the pump used is an oil free device intended for vacuum filtration. Although it cannot draw a strong vacuum, it can handle significant volumes of solvent vapour unlike high vacuum oil-seal pumps.

Tubes were suspended in a water bath at the desired degassing temperature. A bath to hold three tubes was prepared using a 600ml beaker with an acrylic tube holder. Circulation (1000 rpm stir) and temperature control were provided by a Corning PC-4200 hotplate with

immersion probe. The total time from a cold start to equilibration at the set temperature was about 30 minutes.

After temperature was reached, tubes were reattached to the vacuum pump while still suspended in the bath. By carefully feathering the tube valve under maximum vacuum, it was possible to purge the air space with solvent vapour and establish a vigorous boil within the sealed tubes without losing any liquid. This pump down procedure was repeated a second time after 5 min of boiling. Boiling in the sealed tubes was maintained by a coolant loop effect where vapour condensed on the valve assembly lowering the internal pressure and allowing more solvent to boil off at the bottom of the tube. Obtaining this state proved an internal check of success as very small amounts of entrapped air are sufficient to poison coolant loops.

Tubes were weighed on a laboratory balance before and after the degas procedure (Satorius CP 1245). Any mass change was within the measurement error indicating any concentration error in salt solutions stemming from this procedure is negligible.

In this procedure centrifuge tubes were used at above their rated temperature range. Collapse was a problem with freshly purchased tubes. Tubes that had been stored for a while or vacuum dried for a number of hours at 80 °C were noticeably more rigid and resistant to collapse. Tubes were scratched with a nylon scrub pad prior to cleaning to provide a preferred bubble nucleation location at the tube tip allowing rising bubbles to agitate / purge the full solvent column.

5.5.3 Operation

To keep dissolved gas content similar to that of the osmometer core, reference and sample solutions were equilibrated at the water bath temperature prior to loading into the osmometer. Extra ports in the bath lid were included for this purpose. Samples were loaded using an Eppendorf Research plus 10-100 μ L Micro-pipette. Sample volume was standardised at 50 μ L. Based on cell geometry and pipette precision, the fill level is theoretically repeatable to ± 0.01 mm. Even if samples were not precisely at bath temperature, the thermal expansion error is not expected to be significant (~ 0.02 mm for worst case room temperature to 40 °C).

Wait times between procedure steps were set to allow two statistically independent estimates of the equilibrium level assuming time series error can be modelled as a Markov chain. With 30 kDa membranes the wait period was 30 min based on the system time constant determined by auto-correlation analysis. For 3 kDa membranes 50 min was required based on the time required to obtain a stable reading.

A typical day's procedure is as follows:

1. Start-up

- (a) Check membrane clamp screw torque, rinse cell with reference solution, adjust to working level and wait for equilibration.
 - (b) (Repeat 2x): Load reference solution and wait for reading.
2. Sample Runs (Repeat 4 to 6 times)
 - (a) Load sample and wait for reading.
 - (b) Load reference solution and wait for reading.
 3. Shutdown: Rinse cell and top up with reference solution

5.6 Design Validation

5.6.1 Overview

Poly(vinyl alcohol), PVA, is a well-studied water soluble polymer. It is not a polyelectrolyte, allowing pure water to be used as the solvent and the classical model given by Equation 2.17 to be used for analysis [42]. The required parameters for this model are number average molecular weight (M_n), polymer partial specific volume (\bar{v}), and the Flory-Huggins interaction parameter ($\chi_{1,2}$).

Due to its nature, molecular weight must be characterised for the specific sample. This was accomplished using gel permeation chromatography (GPC). Literature estimates are available for \bar{v} and $\chi_{1,2}$ but temperature and concentration must be known for precise estimates. For validation, an experimental temperature 40 °C was selected to closely match the requirements of Chapter 6. Four polymer concentrations between 0.25 and 1 w/w% were selected using the Section 2.6.3 Monte Carlo simulation. Property estimates for the simulation came from the same references as the final converged values in Table 5.2.

These can be compared to the experimental results to validate instrument performance.

Table 5.2: Polyvinyl Alcohol Model Parameters

Symbol	Value	Units	Description
M_n	77-85 ^a	kDa	Number Average Molecular Weight
\bar{v}	0.755-0.756 ^b [201, 202]	cm ³ /g	Partial Specific Volume
$\chi_{1,2}$	0.486 ^c [203]	—	Polymer-Solvent Interaction Parameter

^a Range represents results from two analysis approaches

^b Obtained by interpolation of literature data. Low value ignores temperature, High value represents extrapolated effect of temperature.

^c Obtained by extrapolation of literature data to concentration range used.

5.6.2 PVA Property Estimates

The PVA used was Aldrich 563900-5006, 99.9% hydrolysed, batch 10708CH, weight average molecular weight $M_w = 130$ kDa. Note that M_w is provided but M_n is needed for osmometry validation. PVA is prepared by hydrolysis of poly(vinyl acetate) [204] which is prepared by addition polymerization of the vinyl acetate monomer. Though reasonably accurate conversions between M_w and M_n exist for condensation polymers via the “most probable molecular weight distribution” this is not the case for addition polymers [26, p. 334].

To characterise M_n , a GPC experiment was conducted by Marzieh Riahi of Dr. Neil McManus’s Lab (Chemical Engineering, University of Waterloo). The sample was prepared by dissolving 1 mg/ml dry polymer in a buffer solution at 90 °C. The buffer solution was provided by Ms. Riahi and consisted of 0.2 M NaNO_3 with 0.01 M $\text{NaH}_2\text{PO}_4/\text{Na}_2\text{HPO}_4$ adjusted to pH 7. This solution was also used as the GPC mobile phase at a flow rate of 0.5 ml/min. The instrument was an Agilent PL-GPC 50 equipped with three detectors: 1) refractive index, 2) viscosity, and 3) dual angle light scattering (45° and 90°). Two Agilent PL1149-6800 columns were used in series. Column range of applicability is quoted by the manufacturer as 6-10,000 kDa. Results are as stated in Table 5.2.

For PVA, \bar{v} may be function of temperature, degree of hydrolysis and molecular weight [201, 202, 205]. Due to identical degree of hydrolysis, the estimates provided by two of the authors are a very good match for the material used here [201, 202]. Data for 4 molecular weights and 2 temperatures is provided. Though this is insufficient for strong conclusions, the temperature effect appears to be very small across a 25 to 40 °C range. Molecular weight has a greater effect which is well modelled by an exponential function. Interpolation with respect to molecular weight results in the Table 5.2 estimates.

$\chi_{1,2}$ is a function of temperature and polymer volume fraction for the water / PVA pair [203]. The concentration dependence is weak and highly linear at the low end of the range. In the experiment average polymer volume fraction is $4.7 \cdot 10^{-3}$ (estimated using \bar{v} and Equation 2.66). The $\chi_{1,2}$ value in Table 5.2 was obtained by extrapolating the 40 °C line in [203] Fig. 2 into the concentration range used in the current experiment.

5.6.3 Experimental Method

To make a 1.000 w/w% master solution PVA was weighed in 15 ml centrifuge vials and dissolved in deionised water at 90 °C (Satorius CP 1245 Balance; Corning #430829 vials). This was diluted on a mass basis to make 0.253, 0.503, and 0.755 w/w% samples. These were tested in the osmometer using Millipore PLTK 30 kDa membrane per Section 5.5. Volume fractions were calculated from the known properties of PVA solutions in water [201, 202].

To test for systematic error, two sample ordering schemes were used. Some days' samples were run in sequential order from low to high concentration per ASTM D3750 [45]. On other days' sample order was randomised.

5.6.4 Validation Results

No statistically significant effect was found regarding run order (min p-value 0.19, lowest concentration). This shows the precautions taken to avoid series sample loading effects are adequate. The full data set was used for parameter estimation.

Osmometer data is compared to the regression fit in Figure 5.7. From the fit M_n is 83.9 ± 0.9 kDa and $\chi_{1,2}$ is 0.495 ± 0.001 (error bars represent 95% confidence interval). This is in good agreement with the values found in Table 5.2. $\chi_{1,2}$ is within 1% of the literature value, while M_n is bracketed by the experimental estimates.

5.7 Concluding Remarks

A transducer based membrane osmometer has been successfully designed and built to conduct the set of experiments needed for this research study. PVA validation results

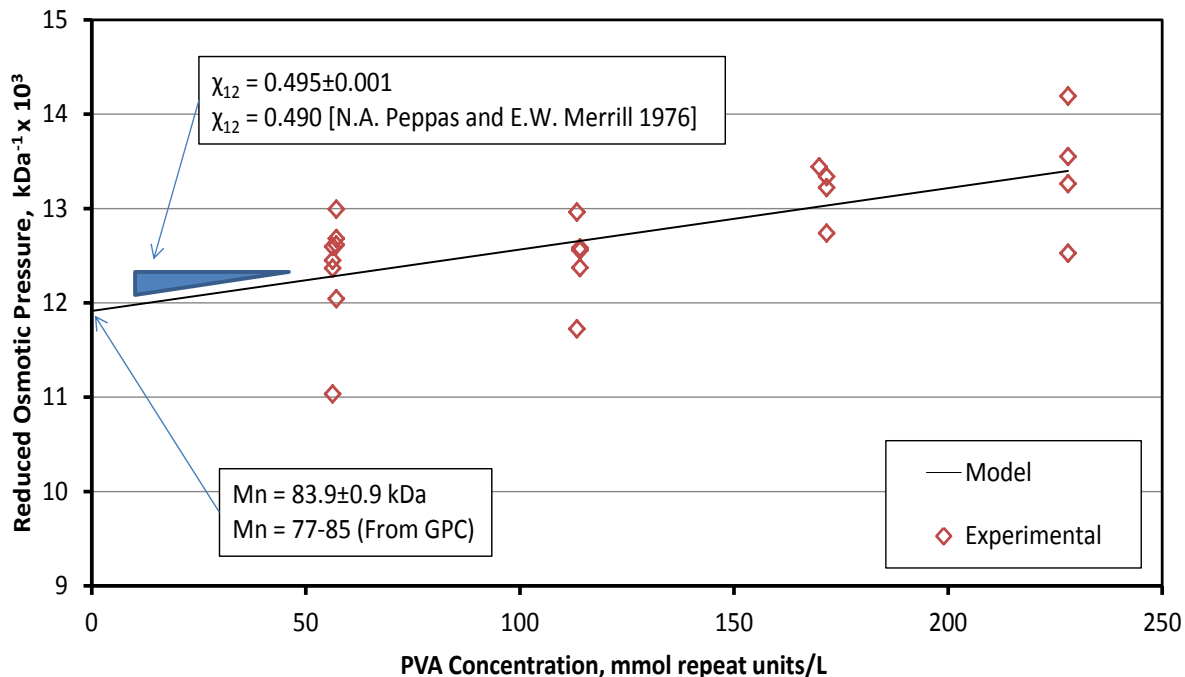


Figure 5.7: PVA Osmometry Results; All experimental data points shown.

are within 1% of the target values. Thermal stability and measurement precision are in compliance with ASTM D3750 [45]. Baseline repeatability of ± 0.25 mm H₂O is better than the 1 mm pressure repeatability quoted by the standard.

The final design is a Hanson type instrument [183] incorporating the membrane clamp geometry of Auckland [192]. It was modified by the author to work at elevated temperatures and with modern pressure transducers. For good performance a fast membrane, degassed solvent, and good thermal control are essential. In hindsight, the initial design could not meet the objectives because of poor membrane performance and thermal control. It is believed that the fundamental design approach was suitable.

Chapter 6

Membrane Osmometry Experiments

6.1 Overview

As was discussed in Chapter 2, membrane osmometry uses the equilibrium pressure signal across a semi-permeable membrane to examine up to four polymer / solution properties, namely: 1) polymer number average molecular weight, 2) polymer/solvent mixing affinity, 3) whether salt affects polymer / solvent mixing, and 4) polymer counterion activity. The first two are applicable to all polymers, 3) requires the presence of added salt, and 4) is specific to polyelectrolytes. All are required in Chapter 7 to model hydrogel swelling under simulated physiological conditions.

Oxidised-alginate properties were not evaluated due to degradation within the time scale of the experiment; however the findings for N-succinyl-chitosan were significant. The osmometer results confirm that the counterion effect is dominant, mixing effects are small, and the salt / mixing interaction is completely negligible. The most significant finding is that counterion activity is approximately half what is predicted by Manning-Oosawa theory.

6.2 Theory Background

6.2.1 Why Membrane Osmometry?

The theoretical basis for membrane osmometry is described in Chapter 2. Similarity between swelling and membrane osmometry allows for the same theoretical principles to be used. There are other techniques for measuring each individual property but only membrane osmometry can characterise all of them under simulated physiological conditions. Possible alternative methods are light scattering and other colligative techniques (freezing point and vapour pressure). Light scattering characterises average molecular weight and

polymer / solvent mixing affinity, however neither quantity is in a form that can be directly applied to swelling experiments [42]. Both of the other osmotic techniques have potential to gather the same data set, however signal to noise is low because added salt (necessary for physiologically representative results) contributes as strongly as the polymer [26, 42]. Only membrane osmometry has the potential to get all required parameters at high resolution from a single experiment.

6.2.2 Osmometry Theory

Figure 6.1 shows the system model used for membrane osmometry. At equilibrium any component that can cross the membrane must have equal chemical potential in both compartments. Though concentrations are unable to equalise, the osmotic pressure provides a counter potential preventing further net flow across the membrane. In this system the solvent makes a useful probe for analysing thermodynamic quantities. Assuming the sample contains a polyelectrolyte, Equation 6.1 provides the equilibrium chemical-potential balance for the solvent. (Originally provided as Equation 2.2 and restated here for convenience.)

$$\Delta\mu_{1,ionic}^{sample} - \Delta\mu_{1,ionic}^{reference} = \Delta\mu_{1,polymer\ mixing} + \Delta\mu_{1,salt\ interaction} + \Delta\mu_{1,osmotic\ pressure} \quad (6.1)$$

In Chapter 2, there is a detailed discussion of how the four terms in Equation 6.1 are evaluated using a different branches of polymer solution theory. Briefly: the ionic term is modelled using Gibbs-Donnan equilibrium theory (Section 2.4.7), mixing and salt interactions use Flory-Huggins theory (Section 2.4.2), and the osmotic pressure effect uses the van't Hoff equation (Section 2.4.1). In Section 2.5, linearised models were derived and

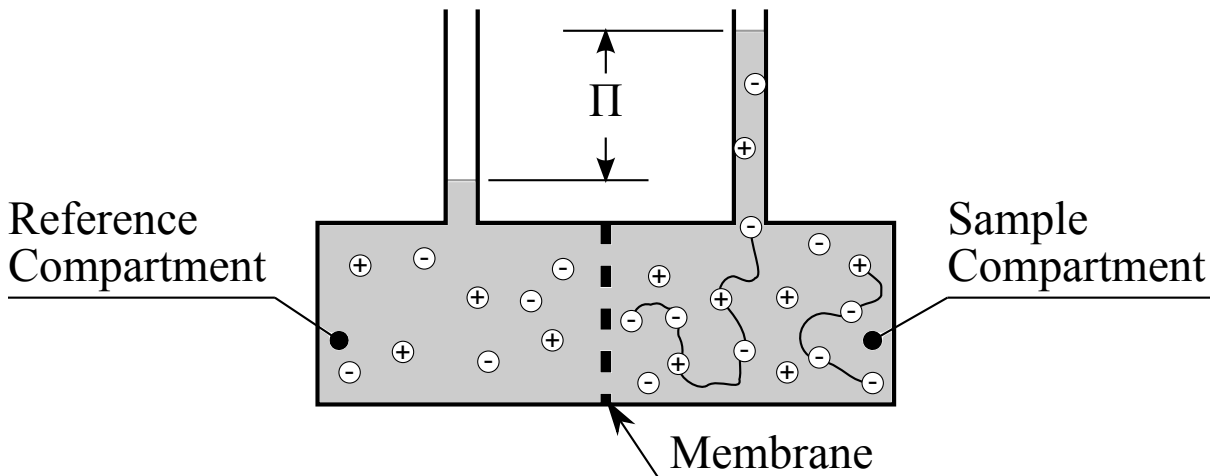


Figure 6.1: Membrane Osmometry System Model

simplified into the form of Equation 6.2. This allows least squares regression to be used for parameter estimation. Parameter groupings for this model are summarised in Table 6.1. The significance of individual parameters and their role in the regression analysis can be found in Table 6.2. It is noted that precise interpretation of β_1 requires a good estimate of polymer partial molar volume $\bar{V}_{r,3}$ but that an order of magnitude estimate suffices for interpretation with respect to solvent quality [26].

$$y = \beta_0 + \beta_1 x_1 + \beta_2 x_2 + \beta_3^* x_3^* \quad (6.2)$$

The linear model derivation requires three key assumptions, namely: 1) solutions are dilute with respect to both polymer and total salt content, 2) ion activity coefficients and the solvent osmotic coefficient are identical in sample and reference compartments, and 3) the effect of non 1:1 type ions is negligible. 1) pertains to the Flory Huggins

Table 6.1: Osmometry Regression Model, Linearised Terms for Equation 6.2

Description ^a	Symbol ^b	Parameter Grouping
Reduced Osmotic Pressure	y	$-\frac{\Pi}{RT \rho_3^*}$
Polymer Mixing	β_0	$\frac{1}{X_n M_{r,3}}$
	β_1	$A_2 \text{ or } \left(\frac{1}{2} - \chi_{13}\right) \frac{\bar{V}_{r,3}^2}{\bar{V}_1 M_{r,3}^2}$
	x_1	ρ_3^*
Salt Interaction	β_2	$-\left[(1 - \chi_{13}) \frac{\bar{V}_{r,3} \bar{V}_2}{\bar{V}_1 M_{r,3}} - \chi_{23} \frac{\bar{V}_2^2}{\bar{V}_1 X_n M_{r,3}} \right]$
	x_2	c_2
Ionic (Donnan Equilibrium)	β_3^*	$-\frac{(\gamma_f i f_\xi)^2 M_1}{2 \bar{V}_1}$
	x_3^*	$\frac{\phi^* m_{r,3}^2}{\rho_3^* \sum_i m_i^*} \approx \frac{\phi^*}{M_{r,3}} \frac{\rho_3^*}{c_2}$

^a Denotes which term in Equation 6.1 the parameter group originates in.

^b Equivalent term in regression model (Equation 6.2)

Table 6.2: Planned Model Inputs and Outputs

Symbol	Description	Variable Type ^a	Source
γ_f	Average Counterion Activity Coefficient	constant or result	Section 2.4.5
Π	Osmotic Pressure	response variable	—
ρ_3^*	Polymer, Mass per Volume Conc.	predictor variable	—
χ_{13}	Polymer Solvent Interaction Parameter	result	—
χ_{23}	Polymer Salt Interaction Parameter ^b	result	—
ϕ^*	Osmotic Coefficient in Reference Soln.	predictor variable	Section 2.4.4
A_2	Osmotic Second Virial Coefficient	result	—
c_2	Salt, Molar Conc. ^b	predictor variable	—
f_ξ	Manning Fraction	constant or result	Section 2.4.5
i	Polymer Repeat Unit, Average Charge	constant or result	Section 2.4.6
M_1	Solvent, Molar Mass	constant	[1]
$M_{r,3}$	Polymer Repeat Unit, Average Molar Mass	constant	Chapter 3
m_i^*	i th Ionic Species, Molal Conc. in Reference Soln.	predictor variable	—
$m_{r,3}$	Average Polymer Repeat Unit, Molal Conc.	predictor variable	—
R	Molar Gas Constant	constant	[1]
T	Absolute Temperature	predictor variable	—
\bar{V}_1	Solvent, Partial Molar Volume in Reference	constant	Section 2.4.8
\bar{V}_2	Salt, Partial Molar Volume ^b	constant	Section 2.4.8
$\bar{V}_{r,3}$	Polymer Repeat Unit, Average Partial Molar Volume	constant	Table 1.2 ^c
X_n	Polymer, Degree of Polymerization	result	—

^a Denotes assumed role in regression fit.

^b Uses three component approximation: 1) solvent, 2) all salts, and 3) polymer

^c Osmometry solution preparation provides an order of magnitude estimate, however measurement precision is not sufficient for a good estimate of $\bar{V}_{r,3}$.

linearization (Section 2.5.1) and the associated error is given by Equation 2.77. 2) can be checked by substituting the experimentally determined ($\gamma_f i f_\xi$) value into Equation 2.64, using Equation 2.61 to estimate the maximum concentration change for each species and comparing this to the calculated coefficient values using the Pitzer model (Section 2.4.4). 3) requires solution of the nonlinear model by use of the iterative approach described in Section 2.5.2 and comparison to the linear result to see if a significant effect exists. 1) and 2) were checked at the time of theory derivation in Chapter 2. That 3) is reasonable will be checked here during the final data analysis.

6.3 Osmometer Experiments

6.3.1 Experimental Design

Design iterations were based on feedback between theory, instrument design and experimental practice. The plan outlined in Table 6.3 represents the final iteration of this process. The instrument was finalised in Chapter 5 leaving two key questions that needed answers: 1) what reagent concentrations should be used, and 2) what is the minimal statistical design for good resolution on parameter estimates?

The first is partially addressed by the Monte Carlo simulation in Chapter 2. Strong interaction was observed between polymer and salt. Error rises with polymer concentration and drops rapidly as ionic strength approaches 10x physiological. Polymer concentration no greater than 0.5 w/w% is required for molecular weight error less than 5% at physiological ionic strength. Salt concentration should be as high as possible while still maintaining polymer solubility.

Table 6.3: Osmometry Study Statistical Design

Factor	Levels	Range
1) Polymer Concentration, w/w%	4	0.125 to 0.500
2) Relative Ionic Strength ^{a b}	3 ^c	0.5 to 1
	4 ^d	1 to 10

^a 1x taken as ~ 0.155 mol/kg which is a good average value for human blood [75]

^b Ionic strength range used depends on polymer solubility.

^c The low statistical leverage available in the low range did not justify use of more than three ionic strength levels. Levels are uniformly distributed.

^d The high range uses an approximately logarithmic progression (1, 2, 5, 10) for better resolution at physiological ionic strength and a more uniform progression in physical effect.

The desire to draw conclusions at physiological ionic strength requires 1x physiological strength to be in the experimental range. For highly soluble polymers, it was possible to work between 1x and 10x. For samples which were barely soluble at 1x, it was necessary to work between 0.5x and 1x. Ionic strength was adjusted by changing the NaCl concentration leaving buffering capacity constant across solutions. The lower bound ionic strength was picked to keep NaCl as the majority salt (4x other salts down from 10x at physiological).

Minimum polymer concentration was addressed by theory. The experimental objective is to extrapolate from low concentrations where the linearised model works best to the higher concentrations found in gels. Oosawa reports two regimes for counterion activity, namely: 1) a lower regime where concentration effects are significant, and 2) an upper regime where counterion activity is nearly independent of concentration. The transition occurs around an apparent volume fraction of approximately 0.04 (very roughly 0.001 mol-repeat-units/L) [108]. Based on these values, a minimum polymer concentration of 0.125 w/w% provides a 2x factor of safety in this work.

The constraints on statistical design are well addressed by the Monte Carlo simulation in Chapter 2. With the concentration ranges selected above, there is little difference in the experimental error expected from 3x3, 4x4 and 5x5 statistical designs provided the total number of replicates is similar. The final choice is a compromise between error checking and practicality. Linearity assumptions are best checked at 5x5 but preparation of the 25 required compositions is time consuming. Dropping to 4x4 still allows a reasonable check of linearity while reducing the number of required compositions to 16.

6.3.2 Materials

The specific materials used are listed in alphabetic order: deionised water (University of Waterloo Chem. stores); Dulbecco's phosphate buffered saline without calcium or magnesium, 10x concentrate (Sigma D1408); oxidised-alginate (A5, Table 3.4); N-succinyl-chitosan (C7 and C2, Table 3.3); pH 10, standard carbonate buffer (VWR BDH5072); pH 7, standard phosphate buffer (VWR BDH4046); potassium chloride (EMD Chemicals PX1405); potassium phosphate, monobasic (EMD Chemicals PX1565); sodium chloride (EMD Chemicals SX0420); sodium hydroxide, 20 w/w% solution (As prepared in Chapter 3); sodium phosphate, dibasic, heptahydrate (EMD Chemicals SX0715).

6.3.3 Buffer Solutions

The standard for 1x ionic strength was Dulbecco's phosphate buffered saline (PBS) with calcium and magnesium omitted [144]. Ionic strength was adjusted by varying the NaCl concentration. When possible, solutions were prepared using purchased concentrate. For ionic strengths below 1x, solutions were prepared from salts.

Buffer solutions were prepared by mass. Weights over 120 g were measured using a Mettler PC 2000 Balance. Weights under 120 g were measured using a Satorius CP 1245 Balance. Weight was recorded to the full precision of the device used. Concentrations on the molar and molal scales were calculated at test temperature using [1, 143].

Solutions were adjusted to $\text{pH } 7.4 \pm 0.01$ at $40\text{ }^\circ\text{C}$ using sodium hydroxide in deionised water. Temperature was controlled using a Corning PC-4200 hotplate with immersion probe. pH was measured using an Omega PHH222 meter calibrated using standard buffers. During initial preparation a small amount of the required water was omitted. Solutions were adjusted to their final mass by adding DI water after pH adjustment. Maximum deviation of buffer salts from the target concentration was approximately 0.2%. Ionic strength precision was better than 0.5% at a given level but accuracy relative to the targets was only about 6%. This low accuracy came from use of approximate calculations for solution preparation. This is not expected to have any effect on the final result as only imprecision contributes to analysis error.

6.3.4 Oxidised-Alginate Solution Preparation

Limit-oxidised-alginate was weighed into a centrifuge vial (Corning #430829) and 1x PBS added to make a $\sim 5\text{ w/w}\%$ solution. This was pH adjusted as with buffer solutions and centrifuged at 7830 rpm for 20 min (Eppendorf 5430) to drop a fine particulate. The clear supernatant was withdrawn using a pipette and transferred to another vial.

Polymer concentration in the supernatant was estimated using a variant on the Chapter 3 vacuum drying procedure. 20 ml glass vials were prepared as in Chapter 3. $\sim 2\text{ g}$ of supernatant and an equal mass of 1x PBS were weighed into separate vials and the masses recorded. The vials were covered with laboratory wipe and held on top of a hotplate at $\sim 80\text{ }^\circ\text{C}$ until the visible liquid had been driven off. They were then vacuum dried and weighed using the same procedure as Chapter 3.

Polymer weight fraction was calculated by subtracting the salt mass fraction determined from the buffer solution from the solids mass fraction determined for the polymer solution. Polymer molar concentration was calculated assuming complete polymer dissociation after the pH adjustment meaning that all acid repeat units are in their sodium salt form. This is reasonable given the pH was greater than 7 and the polymer pK_a is less than 4 [55]. In this experiment solution mass was selected with balance precision in mind to keep concentration uncertainty below 0.5%.

For use in osmometry standardised solutions were diluted to $2.00\text{ w/w}\%$ using 1x PBS to allow for more precise weighing during final sample preparation.

6.3.5 N-Succinyl-Chitosan Solution Preparation

For osmometry N-succinyl-chitosans with 21 and 34% amine substitution were used. Following the procedure outlined in Section 4.3.5, 2.00 w/w% solutions in 1x PBS were prepared. To obtain final ionic strengths of 2x, 5x and 10x, these were diluted to 1.00 w/w% polymer using buffers of the appropriate NaCl concentration. After overnight storage the 34% amine chitosan precipitated in all but 1x PBS. This prompted use of 0.50x and 0.75x solutions prepared by a similar procedure and using 0.50x PBS for the initial step.

6.3.6 Final Sample Preparation

To prepare samples of known volumetric concentration, polymer solutions of known mass concentration were weighed into volumetric flasks and diluted with PBS of matching ionic strength. Procedure guidelines found in ASTM D3750 were followed [45]. Temperature during final volume adjustment was 40 ± 0.5 °C. 5 ml class A volumetric flasks were used and temperature corrections were applied per ASTM E542 [206]. After preparation, samples were sealed in 15 ml centrifuge vials (Corning #430791) and stored at less than 4 °C when not in use.

Flask mass, stock solution mass, and final mass were recorded for each dilution allowing precise calculation of both molal and molar concentrations. Though approximate, mass concentrations closely conform to those found in Table 6.3. Theoretically \bar{v} could be obtained from these measurements, however the dilute solutions used and the error associated with 5 ml flasks ($\pm 0.4\%$ [207]) limit expected precision to less than one significant digit.

6.3.7 Membrane Osmometry

Samples were tested according to the procedures outlined in Chapter 5. Test temperature was 40.00 ± 0.01 °C. For alginate, 30, 10 and 3 kDa membranes were all tried however repeatable results were not obtained and baseline drift indicative of polymer leakage was observed. The decision to discontinue experiments is discussed in more detail later. For chitosan, error checking indicated 30 kDa membrane might not be sufficient. Good results were obtained with 10 kDa membranes. Results were analysed using the approach outlined in Section 6.2.2.

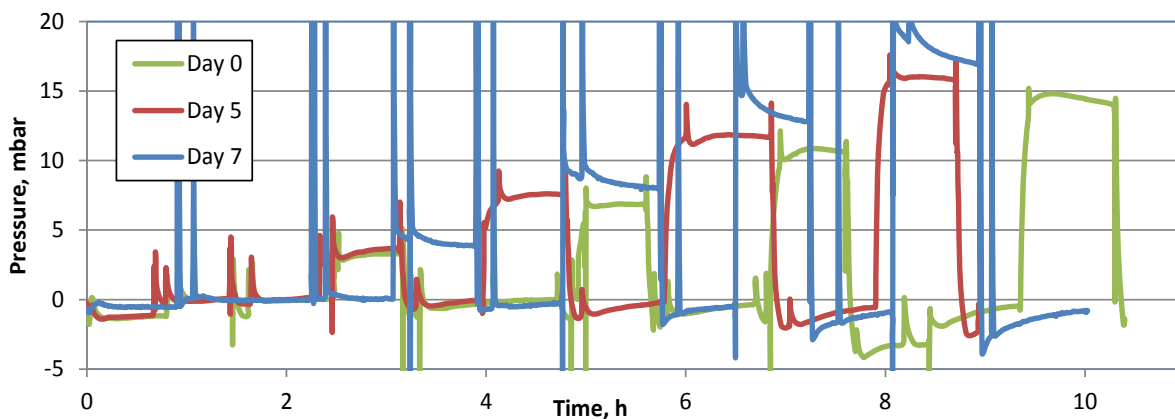


Figure 6.2: Alginate Degradation Time Series: Raw osmometer data from three full day experiments, zero pressure is baseline level before any samples have been loaded.

6.4 Results and Discussion

6.4.1 Oxidised-Alginate

Oxidised-alginate experiments were halted due to polymer degradation during sample thermal / dissolved gas equilibration. Figure 6.2 shows data from three replicates of the same experiment using independent instrument setups. All used 3kDa membrane and samples were drawn from the same vials. Pressure spikes are sample loading and unloading. Plateaus alternate between PBS baseline and sample osmotic pressure. Samples were loaded in sequence from low to high concentration. Similar height plateaus at similar times in the experiment are from the same concentration sample. The increase in sample plateau height at constant concentration across the three replicates is indicative of sample molecular weight decrease due to degradation. The decrease in baseline level throughout the day indicates sample diffusion through the membrane and polymer build-up in the reference compartment. If it were not for this baseline drift it might have been feasible to split samples into multiple vials to avoid repeated exposure to the pretest thermal equilibration. With the baseline drift, the only solution is a lower cutoff membrane, which according to analysis conducted in the previous chapter is unlikely to be practical (see Table 5.1).

6.4.2 N-Succinyl-Chitosan

Very promising results were obtained for N-succinyl-chitosan where there was good agreement between the 21% and 34% amine substitutions. Figures 6.4 and 6.3 compare the final regression fit to experimental data. In both cases the 1:1 salt approximation holds

and linearization error is negligible. Disagreement between experimentally determined $\gamma_f i f_\xi$ and theory was such that analysis was limited to the x_3^* approach. The largest effect is ionization (1000x molecular weight), followed by polymer solvent interaction (100x molecular weight). Molecular weight is the smallest statistically significant effect (largest p-value for M_n still $\sim 10^{-7}$). The salt / mixing interaction effect was not statistically significant for either polymer (p-values of 0.23 and 0.17 for 21 and 34% amine respectively). On this basis, it is safe to rule out a practically significant salt effect; however this does not mean a real but small salt interaction effect does not exist. The coefficients obtained had the correct sign and a consistent magnitude suggesting that the experiment may have been under powered with regard to this effect. Based on the initial regression results and on the assumption that the salt interaction effect is negligible it was omitted in the final analysis. Final analysis results are presented in Table 6.4. The difference between 21% and 34% amine substitution chitosan is statistically significant for all parameters derived from osmometry data.

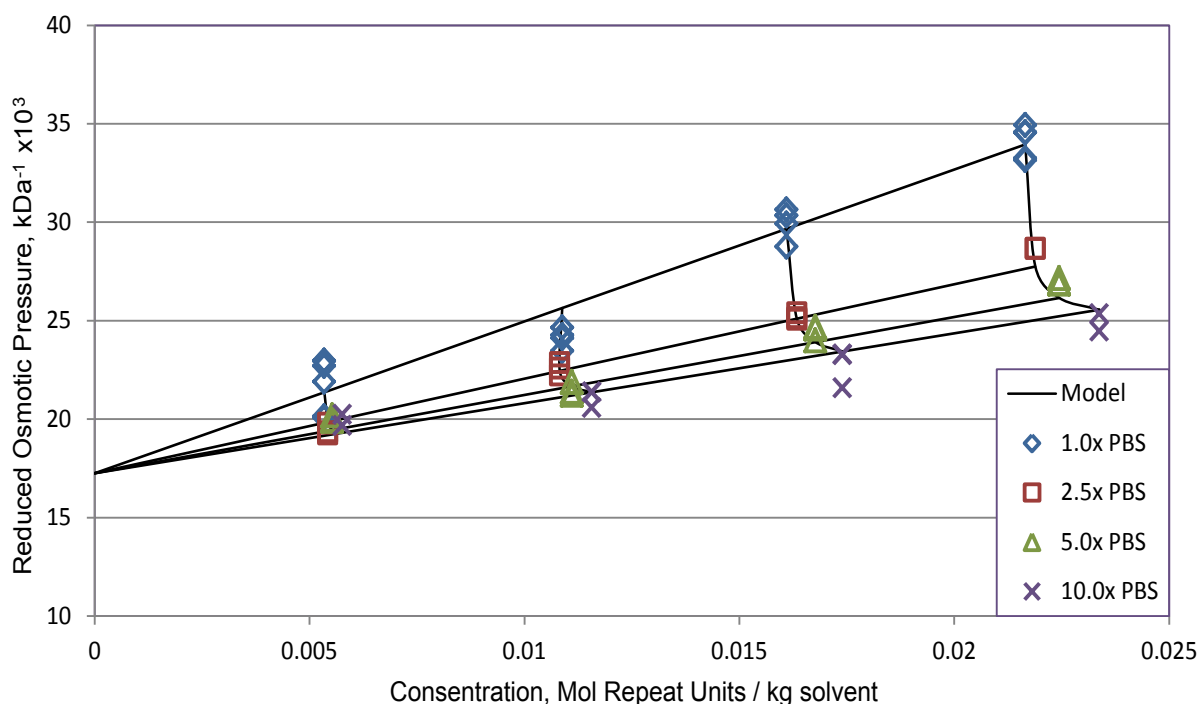


Figure 6.3: Chitosan Osmometry Results: 21% Amine Substitution Polymer; reference solution ionic strength is quoted relative to that of phosphate buffered saline; all experimental data points are shown.

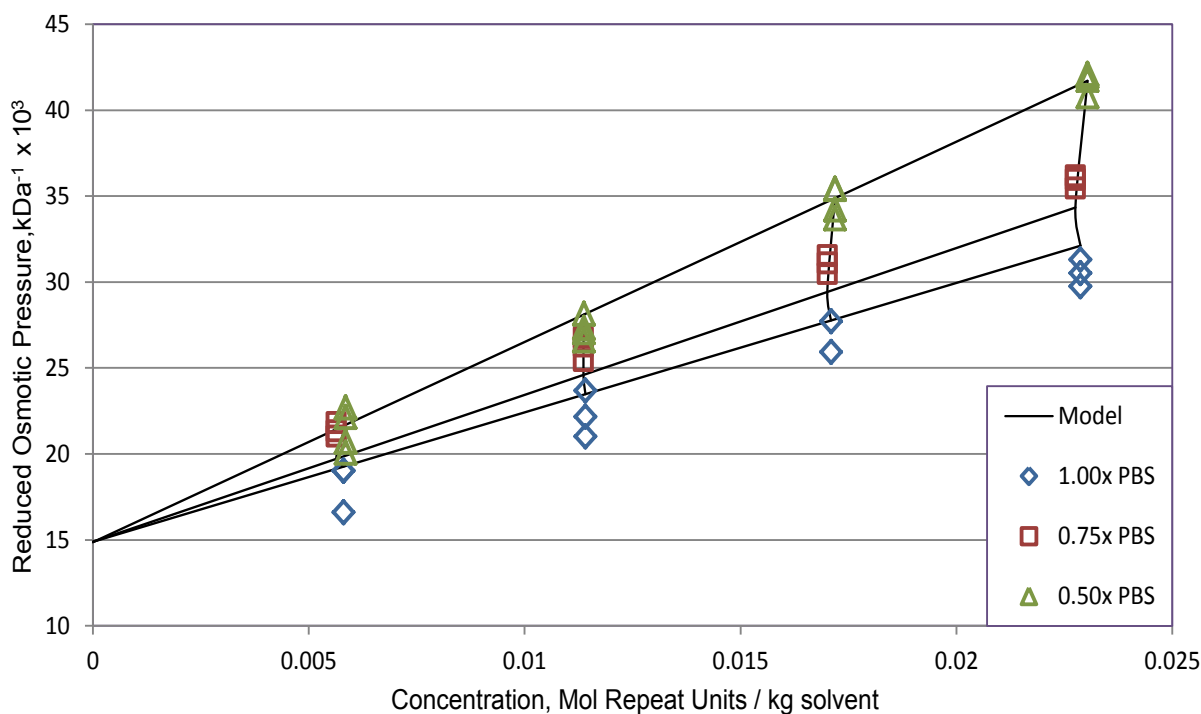


Figure 6.4: Chitosan Osmometry Results: 34% Amine Substitution Polymer; reference solution ionic strength is quoted relative to that of phosphate buffered saline; all experimental data points are shown.

Table 6.4: Chitosan Osmometry Results

Parameter	Primary Amine Substitution		Notes
	21%	34%	
M_n , kDa	58.0 ± 0.3	67.2 ± 0.8	^a
X_n , repeat units	250 ± 1	307 ± 4	^a
A_2 , mol L/g ²	0.00138 ± 0.00003	0.00167 ± 0.00009	^{a,b}
$\gamma_f i f_\xi$	0.26 ± 0.03	0.23 ± 0.04	^a
	0.59	0.40	^c
\bar{v} , cm ³ /mol	1.3 ± 0.7	1.8 ± 0.6	^d

^a From Osmometry, difference statistically significant at a 95% level, considering simultaneous confidence intervals.

$${}^b A_2 = \left(\frac{1}{2} - \chi_{13}\right) \frac{\bar{V}_{r,3}^2}{\bar{V}_1 M_{r,3}^2}$$

^c Values calculated using theory in Chapter 2

^d From solution density data. Low resolution is as expected. Not used in the remainder of this work.

Molecular Weight

Chitosan with 34% amine substitution is estimated to have a greater molecular weight than that with 21%. When degree of polymerization is considered, the difference is even larger. This is contrary to expectations, as both modified polymers were produced from the same lot of chitosan. The chitosan with 21% amine substitution is more highly modified. This should increase molecular weight, but is not expected to significantly influence degree of polymerization. The difference is of small practical significance, however its statistical significance is sufficient that some thought be given to its probable cause.

Four hypotheses are considered regarding the molecular weight difference, namely: 1) experimental error due to membrane leakage affecting the two polymers differently, 2) stability differences during handling / storage, 3) greater uncertainty extrapolating to infinite ionic strength in the lower ionic strength experiment, and 4) charge mediated aggregation behaviour raising molecular weight estimates for the less charged polymer. Hypothesis 1) is ruled out, however the other three are found to have merit. Hypothesis 1) is rejected on the basis that leakage raises the molecular weight estimate. The 34% amine polymer carries a lower net charge giving it a more globular form in solution and making it less likely to leak. Hypothesis 2) is supported by TGA data from Chapter 3. This indicates 21% amine polymer is more stable in the dry state. Unfortunately this does not provide any information on stability in solution and does not rule out the other possible clauses. Hypothesis 3) is supported by the observation that molecular weight estimates are much more similar if the salt interaction term is considered real. Only the lower salt experiment with the 34% amine polymer is significantly affected. This raises the possibility that very accurate estimates of molecular weight may require: a) the estimation of a real salt interaction term or, b) the higher salt content and greater salt level separation of the 21% amine experiment. Further study of this phenomenon is recommended. Regarding hypothesis 4), nearly charge-balanced polyampholytes are known to form aggregates which have lower net charge than any of their constituents [20, 125]. It would therefore be plausible that more aggregation would occur in the 34% amine polymer with its lower net charge.

Although there is some uncertainty regarding the molecular weight values obtained, in the broader scope of this work they are only required for calculation of dangling end correction terms in the swelling simulation. The uncertainty observed here will not significantly affect these estimates.

Mixing Effects

For both polymers the second virial coefficient (A_2) is very small. Regardless of which estimates are used for \bar{v} the Flory Huggins interaction parameter (χ_{12}) is very close to 0.5. This is contrary to expectations when compared to the literature value in Table 1.2. The

discrepancy is explained by noting that the Table 1.2 value was obtained using only the enthalpic contribution [54]. It has been known for some time that the entropic contribution dominates [59]. Small values for A_2 imply that the experiment was conducted very close to what are known as theta conditions. Under theta conditions chain dimensions are unaffected by interaction with the solvent. Solvent affinity follows the expected trend. A small positive interaction is observed which is greater for the 34% amine polymer which bears fewer hydrophobic C-H₂ groups. For both polymers A_2 is sufficiently small as to have little practical significance in the swelling simulation.

Ionic Effects

The apparent ionization parameter ($\gamma_f i f_\xi$) is approximately 50% lower than is expected from theoretical calculations for both chitosans. Though counterion condensation is not expected for either polymer (net charge is too low) and activity coefficients calculated by Manning method (Equation 2.49) are close to 1, polymer counterion activity does not match the predicted disassociation from Katchalsky theory (see 2.6.2). Uncertainty in the amine ionization calculation could potentially account for the discrepancy in the 34% amine polymer, but it cannot explain the discrepancy in the 21% amine experiment. Better theory is required to account for electrostatic effects. Two improvements are recommended. The low screening distance (κ^{-1}) in the salt solutions studied suggests that using an average ionization value for the entire polymer may be inappropriate. If sub-chains capable of ion condensation exist it might explain the current results. This could be tested by using the Monte Carlo method to evaluate the sub-chain probability distribution. Manning-Oosawa theory has also been shown to give inadequate results at elevated salt concentrations and use of a more advanced theory is recommended [136, 137]. For swelling simulations in Chapter 7 the experimentally determined $\gamma_f i f_\xi$ values will be used.

6.5 Concluding Remarks

Oxidised-alginate degradation is too rapid under experimental conditions for the characterization approach adopted here to be successful. Characterization by methods other than membrane osmometry is recommended.

N-succinyl-chitosan was successfully characterised. The excellent fit of the model derived in Chapter 2 to the results obtained here demonstrates that the adopted approach works. The 1:1 salt approximation proved valid for phosphate buffered saline, and the salt effect on polymer water interaction was shown to be negligible. Contrary to initial expectations, even though statistical significance was obtained, the polymer solvent interaction is also too small to be of practical significance. The most significant finding is that the apparent parameter ($\gamma_f i f_\xi$) from the Donnan term is approximately half the size predicted

by Manning-Oosawa theory using whole molecule average charge. The experimental value will be used for swelling simulation in Chapter 7. Future investigation is recommended using sub-chain charges or one of the more advanced theories recently put forward (see [136, 137]).

Chapter 7

Gel Characterization: Equilibrium Swelling and Submersion Compression

7.1 Overview

There are three primary objectives for the gel experiments, namely: 1) to determine if a gel composition with modulus greater than 10 kPa can be prepared; 2) to test the swelling model described in Chapter 2; and 3) to test the hybrid gel model derived in this chapter.

In seeking the optimum gel modulus, four formulation factors might be considered, namely: 1) overall polymer concentration, 2) polymer blend ratio, 3) alginate oxidation extent, and 4) N-succinyl-chitosan degree of substitution. To keep the project scope manageable, only the maximum alginate oxidation extent was used and the overall polymer concentration was limited to the maximum for an injectable viscosity at any given N-succinyl-chitosan degree of substitution. With these limitations the full range of practical blend ratios and N-succinyl-chitosan amine substitutions were studied.

To make efficient use of limited time and material, the two types of experiments were run in tandem, compression tests were limited to unswollen samples, and polymer leaching during gel swelling was not quantified. These limitations allowed the primary study to be run in approximately 7 weeks.

The implications of these limitations are discussed in more detail in Section 7.2.2. They prioritise tests to validate theoretical principles rather than those to determine gel suitability. Our primary goal is to develop a predictive capability to facilitate further development, allowing future formulations to be more precisely tailored to the specific needs of their target application.

This chapter brings together themes from many of the previous chapters. Literature guidelines from Chapter 1 and the swelling model from Chapter 2 have already been discussed. The materials used here were prepared and characterised in Chapter 3. Maximum chitosan concentration is dictated by the rheology results in Chapter 4. Finally several model terms for swelling predictions come directly from the Osmometry experiments in Chapter 6.

7.2 Background

7.2.1 N-Succinyl-Chitosan / Oxidised-Alginate Hybrid Gels

Up to this point, polymers have been handled in solution. In Chapter 3 chitosan was functionalized for solubility at a known pH (Figure 7.1, Step 1a). Alginate was functionalised to act as a polymeric crosslinker for chitosan (Figure 7.1, Step 1b). In Chapters 4 and 6 solutions of known concentration were prepared (Figure 7.1, Step 2). Now the solutions are mixed and a hybrid network formed via the Schiff base reaction between the amine group in chitosan and the aldehyde groups formed during alginate oxidation [2, 34] (Figure 7.1, Step 3). The formation reaction imposes a connectivity constraint on the network such that chitosan chains can only join to alginate and vice versa (Figure 7.2c). This has implications for the network stiffness as seen in Section 7.3.1 below.

Chitosan modification imparts solubility but consumes some of the amine groups required for crosslinking. An optimum modification is plausible where the interaction between concentration and crosslinkability results in a maximum crosslink density and therefore stiffness. The effect on swelling is more difficult to predict. Swelling is reduced by higher gel stiffness, and increased by polymer solubility and charge. The last two are minimised in the least modified polymer while the stiffness is expected to be maximised at mid-range. Swelling behaviour depends on the relative magnitudes of the effects and therefore can not be predicted.

Further uncertainty in stiffness prediction is introduced when varied alginate / chitosan blend ratios are considered. Three interrelated factors may influence results: 1) assuming the same overall number of crosslinks are formed, the relative lengths of the two chain types are fixed by the blend ratio, 2) the inherent stiffness of alginate and chitosan network chains may differ resulting in different overall network stiffness even if number of crosslinks is kept constant, and 3) the overall crosslinkability is expected to be influenced by the reactive group concentrations which is affected by blend ratio.

Assuming random crosslinking in the hybrid gel, relative chain lengths are directly proportional to the blend ratio. A 1:1 blend ratio is expected to produce a unimodal length distribution, while short chains are always the minor constituent of unbalanced blends. Literature predicts that a bimodal length distribution (Figure 7.2b) will result in

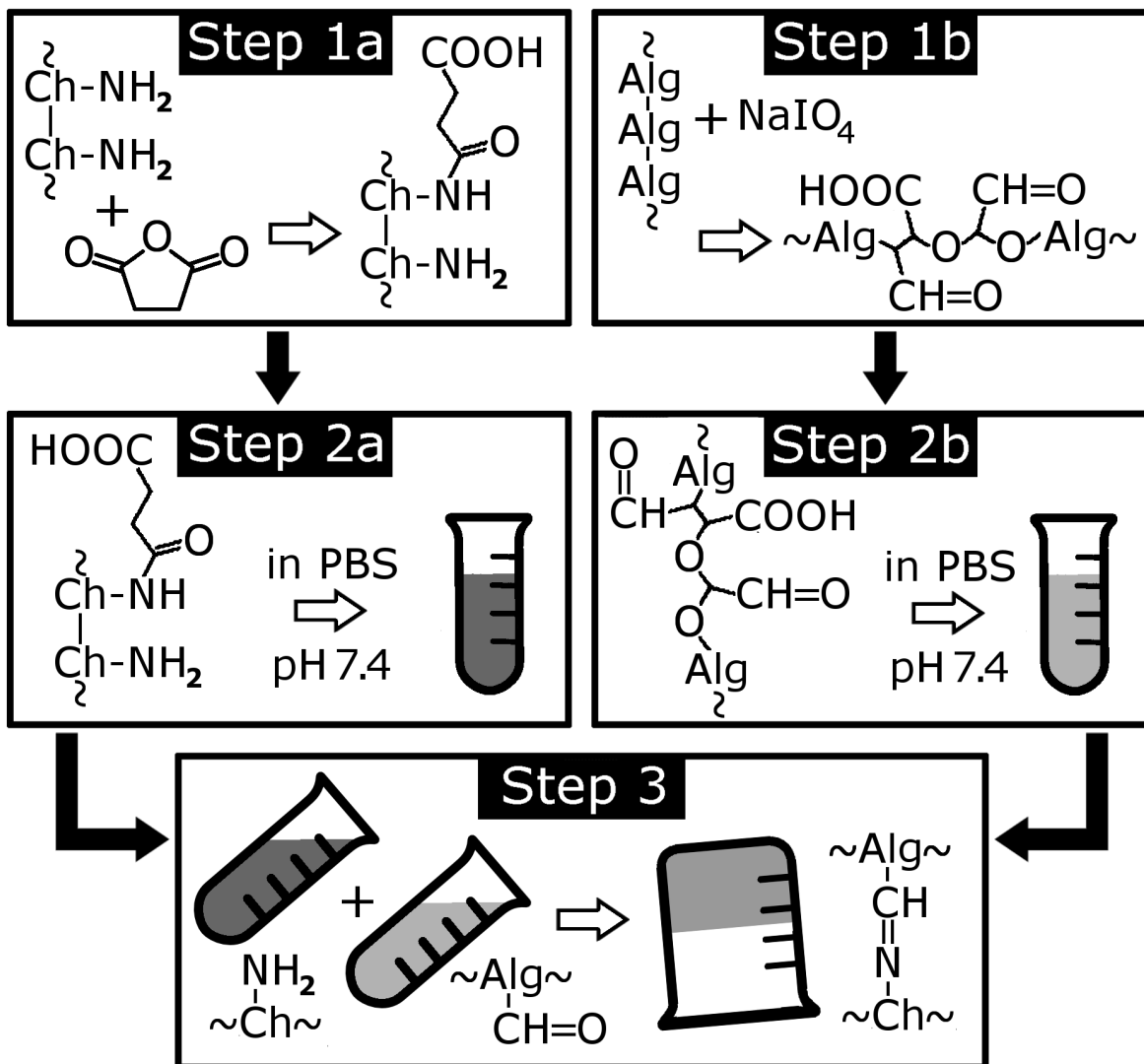


Figure 7.1: Gel Formation Summary

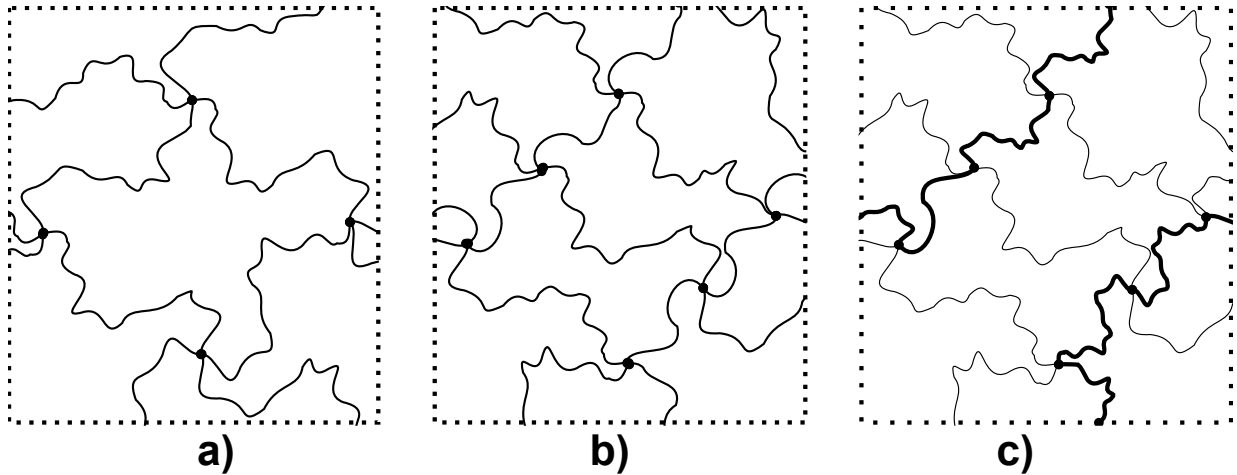


Figure 7.2: Network Structure Schematic: a) Homogeneous Network, b) Bi-modal Network, c) Hybrid Network. Dots represent crosslinking locations.

the highest stiffness and toughness if chain stiffness is equal [25]. A reasonable hypothesis is that highest overall stiffness/toughness will be obtained by having lowest inherent stiffness chains as the minor constituent. This allows the force redistribution efficiency gains of a bimodal network while allowing the maximum overall network stiffness.

The N-succinyl-chitosan / oxidised-alginate inherent chain stiffness ratio is hard to predict. Both polymers are polysaccharides meaning their inherent stiffnesses should be similar at the outset. Alginate is more highly charged under experimental conditions, while oxidation results in greater backbone flexibility. Charge can increase initial elongation increasing stiffness but backbone flexibility allows for a more coiled form, decreasing stiffness. Chitosan maintains the inherent stiffness of polysaccharides, and adds positive self interactions from amine / acid groups. However under experimental conditions, charge interactions are screened by salt at distances not much larger than an individual monomer and therefore may not be very significant at the length scale of a polymer chain. Relative to a typical polysaccharide there is a possibility of decreased alginate chain stiffness and increased chitosan stiffness, making higher chitosan stiffness the most reasonable hypothesis.

According to the theory of rubber elasticity, crosslink density is expected to have a large effect on gel stiffness. Two possible measures of crosslinkability exist, namely: 1) the limiting reactive group concentration, and 2) the product of the two reactive group concentrations. 1) assumes a significant fraction of groups react. 2) assumes steric hindrance halts the reaction almost immediately, making crosslink formation dependent on the interaction probability between two reactive groups.

7.2.2 Project Scope and Limitations

Chitosan solution viscosity limits the concentrations that can be used to form gels. As discussed in Chapter 4, the guidelines for injectable solutions place a 0.2 Pa·s upper bound on viscosity. The concentration at which this is achieved varies by chitosan. Formulation stiffness is expected to scale with concentration allowing its maximum to be captured by the approach adopted; however the swelling driving force also scales with concentration making determination of maximum swelling resistance uncertain. Despite unequal concentrations, the success of the stiffness model derived in Section 7.3.1 provides insight into how stiffness scales with concentration, allowing comparisons to be made across the entire range of compositions. As the swelling model was less successful such comparisons are more difficult in the swelling data set.

As the primary objectives were to develop the proof of concept for a new hybrid hydrogel and the validation of predictive models for this class of materials, three additional simplifying limitations were placed on experiments, namely: 1) as cast rather than samples were used for compression testing rather than samples at swelling equilibrium, 2) polymer leaching was not characterised during swelling, and 3) cure times were standardised at 24h. The implications of these limitations are discussed briefly below. Further experiments with swollen compression samples and characterization of polymer leaching during swelling would be a reasonable extension of the experiments conducted here.

For accurate compression results, well defined sample geometry is required. To enable comparisons with theory, well defined polymer concentrations must be used. Unswollen compression samples preserve ‘as moulded’ geometry and concentration. This readily allows comparisons to theory; however the results need to be combined with swelling experiments to draw conclusions about final swollen properties. With unknown mass loss during swelling, however, this is somewhat difficult.

The priority in the swelling experiment was to determine the equilibrium ratio for comparison to theory. The requirements for equilibrium level verification could cause breakdown of the specimens needed for accurate leaching estimation. Several similar readings are required to verify equilibrium. During initial experiments, samples started to degrade around the time equilibrium could be verified. To obtain accurate leaching results, polymer content before and after swelling must be determined accurately. This is usually accomplished via a de-swelling experiment. De-swelling experiments are however not practical as the gel samples would grow mould when stored for extended periods. Although freeze drying might have been an option, a dedicated freeze dryer was not available, preventing samples from being handled on the same schedule as swelling tests. Freezer space for batch processing was also not readily available. Given the procedural logistics, the low quality of swelling samples by the end of testing did not justify further efforts to capture leaching data. Samples were therefore discarded at the end of each swelling experiment.

Preliminary experiments showed an increase in gel stiffness for up to 12 days after

initial cure [31]. As the change in stiffness over this time period was moderate and the time involved in waiting would greatly complicate experimental planning, it was decided to limit cure to 24h for all samples. Due to the potential for ongoing cure, timing was kept fairly precise in the final study. This should give a good comparison between compositions provided all reach a similar percentage of their ultimate cure within the 24h period. Otherwise the effects of differing cure rates will show up as compositional differences in the results.

7.2.3 Theory for Gel Stiffness

Three models were initially considered for gels stiffness in uniaxial compression tests, namely: 1) the theory of rubber elasticity, Equation 7.1; 2) Hooke's law, Equation 7.2; and 3) the two parameter Mooney-Rivlin model, Equation 7.3. As the theory of rubber elasticity provides the best fit to preliminary data, it is the model with the strongest theoretical justification. It is also the model used to provide the elasticity term in swelling simulations. Detailed discussion has already been provided in Chapter 2. The other two models are provided here for comparison purposes. Hooke's model, the simplest possible, provides a good check if complexity inherent the theory of rubber elasticity is warranted. The Mooney-Rivlin model has been shown equivalent to the general constrained chain form of rubber elasticity theory [25]. As such it serves as a check if the simple model has the appropriate form. In the equations, σ is the principal stress, (ν_e/V_o) is the effective network chain density, k is the Boltzmann constant, T is the absolute temperature, λ is the stretch ratio, ε is the logarithmic strain, ϕ_n is the network functionality and the remaining terms (E , E' , C_1 and C_2) are empirically derived fit parameters.

$$\sigma = C k_B T \frac{\nu_e}{V_o} \left(\lambda - \frac{1}{\lambda^2} \right) = \frac{1}{3} E' \left(\lambda - \frac{1}{\lambda^2} \right), \quad C = \begin{cases} 1 & \text{afine} \\ 1 - \frac{2}{\phi_n} & \text{phantom} \end{cases} \quad (7.1)$$

$$\sigma = E \varepsilon = E \ln(\lambda) \quad (7.2)$$

$$\sigma = 2 \left(C_1 - \frac{C_2}{\lambda} \right) \left(\lambda - \frac{1}{\lambda^2} \right) \quad (7.3)$$

Examining 7.1 with a scaling analysis in mind, it is observed that the two result in identical forms for the uniaxial case. The differences in 'C' are buried inside the fit constant, E' , and is therefore irrelevant. It is only when Equation 7.1 is used to estimate the actual network chain density that theoretical considerations become an issue.

It is noted that Equation 7.1 is formulated for only one type of chain in the polymer network [25] (Figure 7.2a). Analysis in Section 7.3.1 shows that, provided some changes are made to the front factor definition, the scaling form is still relevant to the hybrid gels

studied here, where chain lengths and types may vary but network connectivity constraints require two chains of each type in any given loop (Figure 7.2c). Although models for mono-modal and multi-modal networks are well known [25], to the best of the author’s knowledge, a model for hybrid networks as described here does not exist in the open literature.

7.2.4 Theory of Gel Swelling

Detailed information on swelling in polyelectrolyte gels can be found in Chapter 2. The reader is directed to Section 2.2 where existing thermodynamic models for predicting swelling equilibrium are reviewed. Three key contributions were identified, namely: 1) elastic potential, 2) solution mixing, and 3) ionic interactions. The last two provide the driving force for gel swelling, while the elastic term provides a countering potential. The ionic term is expected to be the most significant of the two driving terms. To model it precisely three additional topics must be considered, namely 1) electrolyte solution non-ideality, 2) counterion condensation, and 3) weak electrolyte ionization. The modelling approach adopted here is discussed further in Section 7.4.

Although the focus here is on equilibrium swelling, the kinetics of swelling are relevant to determining if equilibrium has been reached. Whether Fickian diffusion or poroelasticity approaches are used, the ‘disturbance’ due to the advancing solvent front is expected to travel a uniform linear distance in square root time [208, 209]. As such, it can be more easily observed that equilibrium has been established, by plotting data versus normalised time $t_{\text{normalised}}$ (Equation 7.4). This is also in accordance with the recommendations of ASTM D570 [164]. Here t is the time since experiment start and x is the minimum sample dimension.

$$t_{\text{normalised}} = t^{1/2}/x \tag{7.4}$$

7.3 Model Derivations

7.3.1 Hybrid Gel Elasticity

The hybrid network model presented here is derived from the theory of rubber elasticity and the connectivity constraint that dictates there must be alternating alginate / chitosan chains in the network. This allows the average loop stiffness to be derived based on inherent chain stiffness and relative chain lengths. A mathematical relationship exists between number of loops and crosslink density allowing these two parameters to be substituted for one another without greatly altering the rubber elasticity model’s functional form [25]. A regression relationship is derived based on the hybrid network model to allow this theory to be tested. The derivation is as follows:

The Helmholtz free energy (ΔF) of an individual Gaussian chain is given by Equation 7.5 where k_B is the Boltzmann constant, T is the absolute temperature, $\langle r^2 \rangle_0$ is the end to end distance of the ‘free chains as unperturbed by excluded-volume effects’ and r is the end to end distance of a perturbed chain [110, p 13].

$$\Delta F = \frac{3 k_B T}{2 \langle r^2 \rangle_0} r^2 = \frac{1}{2} K r^2 \quad (7.5)$$

The force due to deformation of an individual chain takes the form [110, pp 13-15]:

$$f = \frac{3 k_B T}{\langle r^2 \rangle_0} \Delta r = K \Delta r \quad (7.6)$$

Noting that the hybrid polymer network must consist of alternating alginate and chitosan strands, a typical load bearing segment (chain or loop) must conform to the following relationships determined by analogy to linear springs in series. Here r_i are chain lengths as in 7.5, f_i is the force which must be the same for all sub units and K_i are stiffness as in equations 7.5 and 7.6.

$$r_{\text{segment}} = r_A + r_C \quad (7.7)$$

$$f_{\text{segment}} = f_A = f_C \quad (7.8)$$

$$K_{\text{segment}}^{-1} = K_A^{-1} + K_C^{-1} \quad (7.9)$$

Substituting the parameter group in Equation 7.6 for K_i in Equation 7.9, adding polymer specific correction factors E'_A and E'_C to account for the fact that alginate and chitosan may well have different length / statistical segment relationships based on differing chemistry, and also noting a similar averaged correction factor should exist for the overall segment results in:

$$\frac{\langle r_{\text{segment}}^2 \rangle_0}{3 k_B T E'_{\text{segment}}} = \frac{\langle r_A^2 \rangle_0}{3 k_B T E'_A} + \frac{\langle r_C^2 \rangle_0}{3 k_B T E'_C} \quad (7.10)$$

Dividing through by segment length and multiplying by the reciprocal of the number of crosslinks / loops in the network allows the rubber elasticity modulus to be introduced on the left hand side:

$$\frac{1}{E'_{\text{experimental}}} = \frac{1}{3 E'_{\text{segment}} \nu k_B T} = \frac{1}{3 \nu k_B T} \left[\frac{\langle r_A^2 \rangle_0}{\langle r_{\text{segment}}^2 \rangle_0} E_A'^{-1} + \frac{\langle r_C^2 \rangle_0}{\langle r_{\text{segment}}^2 \rangle_0} E_C'^{-1} \right] \quad (7.11)$$

Defining $B = (\beta_B \nu)^{-1}$ and including the thermal energy dependence and proportionality constant into the sub chain constants ($E_i = 3 \beta_B^{-1} \nu k_B T E'_i$) provides a general regression relationship (Equation 7.12) for testing the relationship between various predictors of crosslink formation B and elastic modulus data E' .

$$\frac{1}{E'_{\text{experimental}}} = B \left[\frac{\langle r_A^2 \rangle_0}{\langle r_{\text{segment}}^2 \rangle_0} E_A^{-1} + \frac{\langle r_C^2 \rangle_0}{\langle r_{\text{segment}}^2 \rangle_0} E_C^{-1} \right] \quad (7.12)$$

Returning to the connectivity relationship Equation 7.7, and defining,

$$A = \left(1 + \frac{\langle r_C \rangle_0}{\langle r_A \rangle_0} \right)^{-1} \quad (7.13)$$

it can be shown that:

$$\frac{\langle r_C^2 \rangle_0}{\langle r_{\text{segment}}^2 \rangle_0} = (1 - A)^2 \quad (7.14)$$

$$\frac{\langle r_A^2 \rangle_0}{\langle r_{\text{segment}}^2 \rangle_0} = A^2 \quad (7.15)$$

This results in the final form for the regression relationship:

$$\frac{1}{E'_{\text{experimental}}} = B A^2 E_A^{-1} + B (1 - A)^2 E_C^{-1} \quad (7.16)$$

Here $E'_{\text{experimental}}$ is the fit constant from the scaling approach to rubber elasticity theory, $B = (\beta_B \nu)^{-1}$ is a predictor for the number of crosslinks ν , A is the average chain length ratio and E_i is the chain stiffness estimator which is expected to depend on temperature. The ratio between E_A and E_C is expected to be more informative than the values themselves as the form of the model will tend to inject any crosslinking variation not well fit by B into the E_i terms.

7.3.2 Network Functionality for Crosslinking Estimation

An estimate of crosslink density ($\frac{\nu_e}{V_o}$) is useful as a diagnostic tool to test polymer reaction efficiency and to check if the ionic term of the swelling model should be corrected for the number of chitosan amine groups consumed by the gel formation reaction. The theory of rubber elasticity can provide such an estimate via Equation 7.1. However, three difficulties arise from this approach, namely: 1) only mechanically effective chains are included in crosslinking estimates from stiffness measurements; 2) Equation 7.1 assumes a single type of chain and as such neglects the effects of hybrid gel topography discussed above; and 3) for consistency the ‘phantom’ version should be used, requiring an estimate of network functionality ϕ_n .

A first order approach is adopted here, using hybrid gel topography to provide an estimate of network functionality which is consistent with the ‘phantom’ version of Equation 7.1 so that an estimate of crosslink density can be made. Equations 7.17 and 7.18 assume negligible free ends (reasonable for polymer-polymer crosslinking [25]) and that one type of polymer chain dominates stiffness (reasonable provided the combined effects of chain length and inherent stiffness make one chain type significantly stiffer than the other).

Equation 7.17 provides the number of repeat units between crosslinks for either polymer ($n_{ave,j}$), where N_A is the Avogadro constant, $c_{r,j}$ is the molar concentration polymer repeat units at the time of the uniaxial test, and $X_{n,j}$ is the polymer degree of polymerization. Although either polymer may be used, crosslinks are double counted if both polymers are mechanically significant. Equation 7.18 implements connectivity constraints. The functionality is 4 for side–side links, 3 for end to side links and 2 for end–end links. Equation 7.18 first calculates x which assumes only end links from polymer 1 to 2 and then corrects this assumption based on the number of side links formed on polymer 1. The equations are symmetrical such that the same result is obtained regardless of which polymer is 1 or 2. The MAX and MIN operators address the situation where on average there may be less than one crosslink per chain.

$$n_{ave,j} = 1 + \frac{V_o N_A c_{r,j}}{\nu_e X_{n,j}} \quad (7.17)$$

$$\begin{aligned} \phi_{n,ave} &= [(x + 1) \text{MAX}(n_1 - 2, 0) + x \text{MIN}(n_1, 2)] / n_1 \\ x &= [3 \text{MAX}(n_2 - 2, 0) + 2 \text{MIN}(n_2, 2)] / n_2 \end{aligned} \quad (7.18)$$

7.4 Simulation: Swelling Equilibrium

The present simulation uses the swelling theory presented in Chapter 2 to predict the outcome of the experiments described below so that a comparison can be made between theory and experiment. The simulation is based around the chemical potential balance presented in Equation 7.19. Here it is formulated as a test function for the numerical solution such that $Error = 0$ at swelling equilibrium. Equations 7.21 to 7.22 provide estimates of each term as a function of the swelling ratio Q . Starting with the unswollen condition ($Q = 1$) the system is solved numerically by incrementally raising Q and checking the sign of the error term. When the sign reverses it indicates the equilibrium point has been exceeded; Q is then decreased by one increment, a smaller step size selected and the process continued until the desired degree of precision is obtained. Provided the initial increment is not overly large and the correct solution does not involve de–swelling, this simulates an actual swelling experiment. For this reason even though the possibility of multiple roots exists, the solution obtained is expected to be the physically significant one.

$$Error = \Delta\mu_{1,elastic} + \Delta\mu_{1,mixing} - \Delta\mu_{1,ionic}^{gel} + \Delta\mu_{1,ionic}^{surroundings} \quad (7.19)$$

$$\Delta\mu_{1,elastic} = \begin{cases} \frac{1}{3} E' N_A^{-1} \left(Q^{-1/3} - \frac{4}{\phi_n} Q^{-1} \right) & \text{afine} \\ \frac{1}{3} E' N_A^{-1} Q^{-1/3} & \text{phantom} \end{cases} \quad (7.20)$$

$$\Delta\mu_{1,mixing} = Q^{-2} \sum_{j=Alginate}^{Chitosan} A_{2,j} \rho_{o,j}^{*2} \quad (7.21)$$

$$\Delta\mu_{1,ionic}^{gel} - \Delta\mu_{1,ionic}^{surroundings} = M_1 RT \phi^* \sum_i (f_D^{z_i} - 1) m_i^* \quad (7.22)$$

$$f_D = \frac{-b + \sqrt{b^2 + 4ac}}{2a}$$

$$a = \sum_i m_i^{*(+1)} \quad b = Q^{-1} \sum_{j=Alginate}^{Chitosan} \gamma_{f,j} f_{\xi,j} i_j m_{r,j,0} \quad c = \sum_i m_i^{*(-1)}$$

The elastic term (Equation 7.20) uses the theory of rubber elasticity. The form presented here is a restatement of Equation 2.12 using the scaling analysis described in Section 7.2.3. The recommended ‘phantom’ model was used for the simulation allowing the modulus from compression tests (E') to be used without any ambiguity caused by unknown crosslink functionality (ϕ_n) [25]. Here N_A is the Avogadro constant.

The mixing term is not very significant. Both the second virial coefficient (A_2) and the initial weight per volume polymer concentration (ρ_o^*) are small for both polymers. For this reason Equation 7.21 assumes that polymer-polymer interaction effects on polymer-solvent mixing are negligible. The common assumption of infinite network molecular weight is also made. N-succinyl-chitosan parameters for mixing were determined by membrane osmometry in Chapter 6 for two chitosans. As polymer-solvent specific interactions are expected to scale with polymer modification extent the values obtained were linearly interpolated / extrapolated to provide estimates for all chitosans studied. Parameters for alginate come from Chan [14] and can be found in Table 1.2.

The ionic term provides the most significant driving force for swelling. It is evaluated using Equation 7.22 which assumes: 1) Equation 7.23 is valid when applying the volumetric parameter Q to molal initial repeat unit concentration $m_{r,0}$; 2) osmotic and ion activity coefficients are equal in both the gel and reference phase; and 3) the salt solution consists exclusively of 1:1 type salts. Low polymer content and minimal density differences make 1) reasonable, 2) introduces a maximum error of approximately 3%, and 3) is mitigated by use of the iterative procedure described in Section 2.5.2 to account for the non-linearity introduced by the presence of 1:2 phosphate ions.

$$\rho_{s,o} \left(1 + \sum_{j=2}^n m_{j,o} M_j \right)^{-1} \approx \rho_s \left(1 + \sum_{j=2}^n m_j M_j \right)^{-1} \quad (7.23)$$

The reference solution osmotic coefficient (ϕ^*) and salt concentrations (m_i^*) are evaluated via the reference solution simulation (see Section 2.6.1). Polymer ionization i and

Manning fraction f_ξ are evaluated using the ionization simulation (see Section 2.6.2). Based on the results of Chapter 6 the counterion activity γ_f is used as an empirical correction factor representing the ratio between measured and calculated $\gamma_f i f_\xi$ values in Table 6.4. γ_f values are expected to scale with polymer net charge based on the assumption that the difference between theory and experiment is due to a charge interaction effect. Linear interpolation / extrapolation based on experimental values for 21% and 34% amine chitosan, respectively, resulted in estimates of 0.44 to 0.74 for for 21% to 48% amine substitution. Two estimates for alginate γ_f were considered, namely $\gamma_f \approx 0.4$ from Chan [14] and $\gamma_f \approx 1.0$ from ion condensation theory (see Section 2.4.5).

For the simulation, chitosan amine substitution was roughly corrected for reactive groups lost to crosslinking using the approach described in Section 7.3.2. To solve the system, non-linear Gauss-Seidel was employed with a relaxation factor of 0.5 on average network functionality. Even so, the singularity obtained as functionality approaches 2 made the solution somewhat unstable. The unknown alginate molecular weight was addressed by substituting a wide range of values. A bounding box of 15 to 400 was established for alginate number average degree of polymerization based on membrane leakage during osmometry and polymeric raw material prior to modification. Alginate molecular weight was not found to be influential in this range. The calculation indicates a significant fraction of amines may have been lost to crosslinking, with amine substitution reduced in some cases by as much as 17%.

7.5 Experimental

7.5.1 Preliminary Experiments

Preliminary experiments consisted of a compression study and a series of swelling trials. These served both to show proof of concept that gels can be formed and to validate experimental methodologies. Additional information regarding the significance of blend ratio and cure time was also gathered. Overall polymer concentration was maintained at ~ 5 w/w% throughout preliminary experiments. Limit oxidised-alginate (Table 3.4, A1 and A5) and $\sim 21\%$ amine substitution chitosan and (Table 3.3, C0 and C6) were used.

Initially same size samples used for both tests (10 mm diameter, 5 mm thick disk). For compression specimens, this is in accordance with the aspect ratio recommendations of ASTM D1621 and the maximum specimen height recommended by ASTM D5024 [210, 211]. For swelling 0.79 mm thick disks were ultimately adopted, allowing equilibrium to be rapidly obtained and eliminating interference from sample degradation.

The compression study was published as [31] and produced five key findings, namely: 1) gels can be formed, 2) repeatable results are obtained using the Section 7.5.5 approach, 3) only three samples can be reasonably tested in an 8 hour day, 4) sample modulus continues

to evolve over an 8 to 12 day time period, and 5) maximum stiffness was obtained with 2 parts chitosan to 1 part alginate. All blend ratios had an excess of chitosan leaving uncertainty if the effect was due to unbalanced blend ratio (chain length hypothesis) or inherent chitosan chain stiffness / crosslinking efficiency.

Swelling samples for the preliminary study used a 1:1 blend ratio. Two measurement approaches were considered to quantify sample dimensional changes, namely: 1) optical approach where sample dimensions are measured from digital photos, and 2) a gravimetric approach where volume change is assumed to be proportional to mass uptake. 1) avoids disturbing fragile samples, however the diffuse edges of highly swollen samples and low resolution of the available digital camera limited dimensional resolution to ± 0.2 mm (approximately ± 20 mg). Improved handling techniques (see Section 7.5.5 below) allowed 2) to be used with very soft samples. Measurement precision was that of a Satorius CP 1245 laboratory balance (± 0.2 mg). This equates to a dimensional accuracy of approximately ± 0.002 mm which is in accordance with the recommendations of ASTM D570 [164].

7.5.2 Combined Study Plan

As per the chapter scope (Section 7.2.2), overall polymer concentrations were selected based on rheology results (Table 4.4) and ultimately only a single alginate oxidation was studied. This reduced the plan to a two factor experiment in blend ratio and chitosan amine substitution. Each factor had 5 levels for 25 compositions total (Tables 7.1 and 7.2). A minimum of 2 compression replicates were tested per composition. Approximately twice this number of swelling samples were tested. To allow for potential failed experiments, the testing schedule called for approximately 60 sample preparation cycles. The total period for conducting this set of experiments to completion was approximately 7 weeks.

The day-to-day experimental testing was conducted by a co-op student over a regular 40 hour work week (see Table 7.3). Compression tests were the limiting factor, with a maximum of three samples tested per day. Two swelling samples per composition could be tested in the allotted time for a total of six samples in a given day. As samples must

Table 7.1: Polymer Concentration used with each Chitosan

Chitosan Amine, substitution%	21	27	34	41	48
Concentration, w/w%	4.2	3.8	3.0	2.0	2.0

Table 7.2: Blend Ratio Study Block

Ratio, Chitosan : Alginate	2:1	1:1	1:2	1:4	1:9
Block	1	1	2	2	3

be prepared 23 h in advance to address concerns over continued cure, testing was limited to 4 days or 12 slots per week.

Given the unknown direction of experiments, chitosan:alginate blend ratio was divided into three blocks. All chitosans were tested in each block. Sample order was randomised within a block with the restriction that one replicate of each composition must be run before the first extra sample slot.

Block 1) 1:1 and 1:2 blend ratios were tested to address which side of 1:1 should be pursued. The finding was that 1:1 is clearly superior and the 2:1 side of range should be pursued.

Block 2) 2:1 and 4:1 blend ratios tested. The finding was that 4:1 is superior to 2:1 which differed from the preliminary result. Further experiments were necessary to test the hypothesis that limited crosslinkability would eventually end this behaviour.

Block 3) 9:1 blend ratio. The crosslinkability limit was reached at this blend ratio and hence, the experiment was halted.

7.5.3 Materials

Specific materials used listed in alphabetic order: deionised water (University of Waterloo Chem. stores); Dulbecco's phosphate buffered saline without calcium or magnesium, 10x concentrate (Sigma D1408); oxidised-alginate (A5, Table 3.4); N-succinyl-chitosan (C1 to C3, C7 and C8, Table 3.3); pH 10, standard carbonate buffer (VWR BDH5072); pH 7, standard phosphate buffer (VWR BDH4046); silicone oil (University of Waterloo Chem. Stores, heating bath grade); silicone vacuum grease (DOW Corning High Vacuum Grease); sodium hydroxide, 20 w/w% solution (as prepared in Chapter 3).

7.5.4 Sample Preparation

Chitosan solutions were prepared as in Section 4.3.5. Alginate solutions with matching concentrations were prepared as in Section 6.3.4. Gels were formed by mixing chitosan and alginate solutions in the desired ratio. To obtain consistent results four key approaches were adopted, namely: 1) solutions were measured by mass, 2) the time between the start of mixing and the end of moulding was limited to ~ 3 min, 3) samples were moulded under vacuum, and 4) samples were cured in the mould for 23-24 h at atmospheric pressure and 40 °C. This resulted in bubble-free gel samples with known composition, geometry and history. The detailed procedure is as follows:

Mould Design: For initial samples vacuum tight moulds were used. Later moulds were merely water resistant and placed inside a vacuum chamber for moulding. Moulds were made by sandwiching an acrylic or PTFE template layer (Figure 7.3b) between two 1/4"

Table 7.3: Typical Gel Experiment Schedule

Time	Compression	Swelling	Sample Molding	Other
08:30 ^a	—	Day 0-2: $\sqrt{t} = 9.2$	—	—
08:40 ^a	—	Day 0-1: $\sqrt{t} = 9.7$	—	—
09:00	Day 1-1: Startup	—	—	—
09:05 ^a	—	Day 1-1: Unmolding	—	—
09:15 ^a	Day 1-1: Unmoldiing	—	—	—
09:20	—	Day 1-1: $\sqrt{t} = 1.0$	—	—
09:30	—	—	—	30 min
10:00	—	—	Day 2-1: Prep	—
10:10	—	Day 1-1: $\sqrt{t} = 2.1$	—	—
10:20 ^a	—	—	Day 2-1: Timed	—
10:40	—	—	—	10 min
10:50	Day 1-1: Cleanup	—	—	—
11:10	—	—	—	20 min
11:30	Day 1-2 Startup	—	—	—
11:35 ^a	—	Day 1-2: Unmolding	—	—
11:45 ^a	Day 1-2: Unmoldiing	—	—	—
11:50	—	Day 1-2: $\sqrt{t} = 1.0$	—	—
12:00	—	Day 1-1: $\sqrt{t} = 3.4$	—	—
12:10	—	—	—	20 min
12:30	—	—	Day 2-2: Prep	—
12:40	—	Day 1-2: $\sqrt{t} = 2.1$	—	—
12:50 ^a	—	—	Day 2-2: Timed	—
13:10	—	—	—	10 min
13:20	Day 1-2: Cleanup	—	—	—
13:40	—	—	—	20 min

^a Supervised or done by the author^b.

^b Unmarked work suitable for an independent co-op student.

Table 7.3: Typical Gel Experiment Schedule (continued)

Time	Compression	Swelling	Sample Molding	Other
14:00	Day 1-3 Startup	—	—	—
14:05 ^a	—	Day 1-3: Unmolding	—	—
14:15 ^a	Day 1-3: Unmolding	—	—	—
14:20	—	Day 1-3: $\sqrt{t} = 1.0$	—	—
14:30	—	Day 1-2: $\sqrt{t} = 3.5$	—	—
14:40	—	Day 1-1: $\sqrt{t} = 4.7$	—	—
14:50	—	—	—	10 min
15:00	—	—	Day 2-3: Prep	—
15:10	—	Day 1-3: $\sqrt{t} = 2.1$	—	—
15:20 ^a	—	—	Day 2-3: Timed	—
15:40	—	—	—	10 min
15:50	Day 1-3: Cleanup	—	—	—
16:00	—	—	—	20 min
16:20	—	Day 1-3: $\sqrt{t} = 3.0$	—	—
16:30	—	Day 1-2: $\sqrt{t} = 4.5$	—	—
16:40	—	Day 1-1: $\sqrt{t} = 5.5$	—	—
16:50	—	Day 1-3: $\sqrt{t} = 3.3$	—	—
17:00	—	—	—	40 min
17:40 ^a	—	Day 1-3: $\sqrt{t} = 3.8$	—	—

^a Supervised or Done by Author^b^b Unmarked work suitable for independent co-op student

polycarbonate shells. Sample thickness and diameter were set by the template, the rigid shells insured flat sample ends. The small second cavity provided a space for bubbles to pop during moulding. To prevent sample leakage and aid sample removal a thin layer of vacuum grease was applied to the shells prior to mould assembly. The vacuum chamber (Figure 7.3a) consisted of a crystallizing dish with a house made lid. The neoprene gasket seals around edges, while the quick connect allows rapid switching of the vacuum line between degassing and moulding. An imperfect seal was acceptable due to active vacuum generation (Welch 2534B-01 oil free filtration pump).

Moulding preparation: Chitosan solutions were weighed out in advance into 15 ml centrifuge vials which were sealed and stored in the fridge at <4 °C until required. The solution was removed from the fridge 10 min in advance to warm to room temperature, mixed under vacuum to draw out dissolved gasses, centrifuged to drive condensation down from sides of tube and vortex mixed again to ensure homogeneity. Alginate solutions were removed from refrigeration and vortex mixed vigorously to mix in condensation and maintain constant concentration.

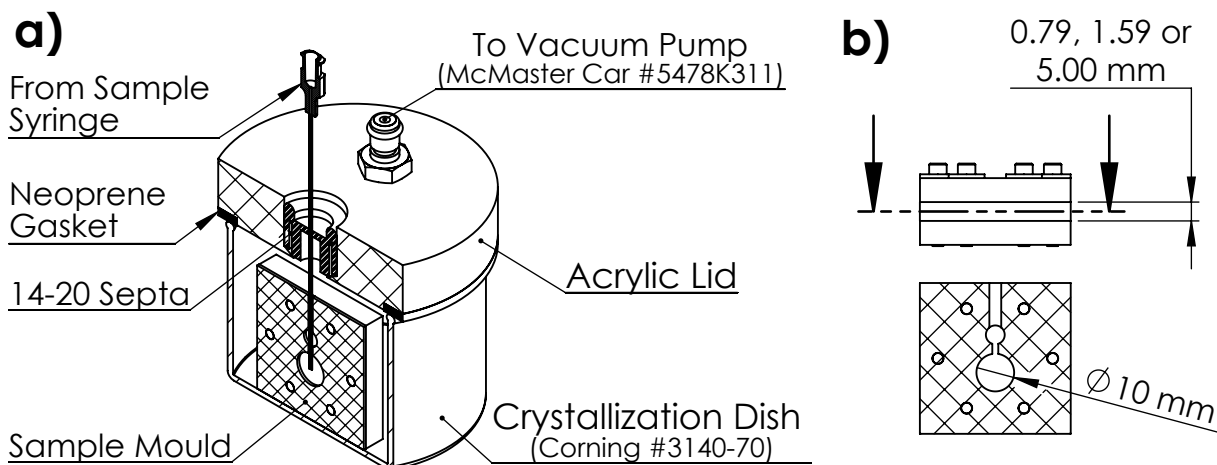


Figure 7.3: Swelling and Compression Sample Moulding: a) Vacuum Chamber Details, b) Mould Geometry

Timed Section: The target amount ($\pm 5\%$) of alginate solution was added to the pre-weighed chitosan solution (~ 15 s). The tube was vortex mixed under vacuum (~ 30 s). The sample was drawn into a syringe and injected into the mould under vacuum (~ 120 s). Some compositions were centrifuged briefly after vortex mixing or during moulding of the first few samples to pull sample material down off the tube sides. The total time between the start of alginate addition and the end of moulding never exceeded 3 min.

Cure: Moulds were sealed with ‘Tuck Tape’ (secondary containment against water) and bundled in plastic bags before placing in a water bath at $40\text{ }^{\circ}\text{C}$ for 24 ± 0.2 h (preliminary experiments) or 23 ± 0.1 h (final experiments). Experiments were scheduled such that samples were unmolded and used a precise time interval after preparation (see Table 7.3).

7.5.5 Compression Methodology

Tests were conducted at $37\pm 0.5\text{ }^{\circ}\text{C}$ under silicone oil using the immersion-compression clamp of a TA DMAQ800. A 1 h thermal soak prior to test start was used to ensure minimal temperature gradients. A pseudo-strain-controlled mode was selected, and a deformation rate of 0.1 mm/min was used. Deformation was measured using the crosshead displacement which was calibrated for instrument compliance. The small buoyancy force produced by the oil was corrected for by running tests without samples and subtracting the resultant baseline from the force results. Tests proceeded until the 18 N load limit of the instrument was reached or the sample height was reduced to 1 mm through failure or otherwise.

For all data sets rubber elasticity theory and Hooke’s law were fit to the data using Equation 7.1 over the first 46% logarithmic strain. The two parameter Mooney-Rivlin

model was fit to preliminary data, however it did not provide any improvement over rubber elasticity theory and therefore was not used for the final analysis.

7.5.6 Swelling Methodology

The swelling medium was Dulbecco's phosphate buffered saline with calcium and magnesium omitted [144]. This was prepared as in Section 6.3.3. For swelling, samples were immersed in $>50x$ their volume of PBS and held at 40 ± 1 °C. Fresh media was used after each weighing. Weighing were conducted on a schedule constructed to give evenly spaced points on a square root time scale (see Table 7.3). Temperature control was established by partly immersing sample bottles in a circulating bath equipped with an insulating lid. A spacer disk served to maintain bottle separation and orientation for good thermal control. Twice as many bottles as samples were placed in the bath at any given time, allowing samples to be transferred to fresh bottles without significant temperature change during weighing.

To achieve the desired precision a specialised weighing procedure was developed. In each weighing a fresh PBS bottle was removed from the water bath, shaken to mix condensation back into the bulk solution and then dried using laboratory wipes on its exterior and on the inside of its lid and neck. The laboratory balance was tared to the mass of the prepared bottle. For the first weighing, samples were removed from their moulds, trimmed of any 'flash' and dropped into the tared PBS. After taring the bottle was only uncovered for the amount of time necessary to drop in the sample, and the change in mass after sample addition was recorded as the sample mass.

For subsequent weighings polyester batting normally used for vacuum bagging was used as a sample handling tool. To recover the sample from its bottle the PBS was poured through a piece of batting to capture the gel with minimal stresses. The gel was flipped onto fresh batting twice to remove surface moisture and then drooped into a tared PBS bottle for re-weighing. In trial experiments with dummy samples this procedure was repeatable within the precision of the weigh scale (Satorius CP 1245 laboratory balance ± 0.2 mg).

7.6 Results and Discussion

7.6.1 Stress Strain Curves

Figure 7.4 shows a typical stress strain curve from the preliminary compression tests. As can be seen, at high strains the theory of rubber elasticity provided a better fit for the data than Hooke's law. The agreement at low strains allows $E' \approx E$, which is convenient for comparison to other authors. With a single adjustable parameter the theory of rubber

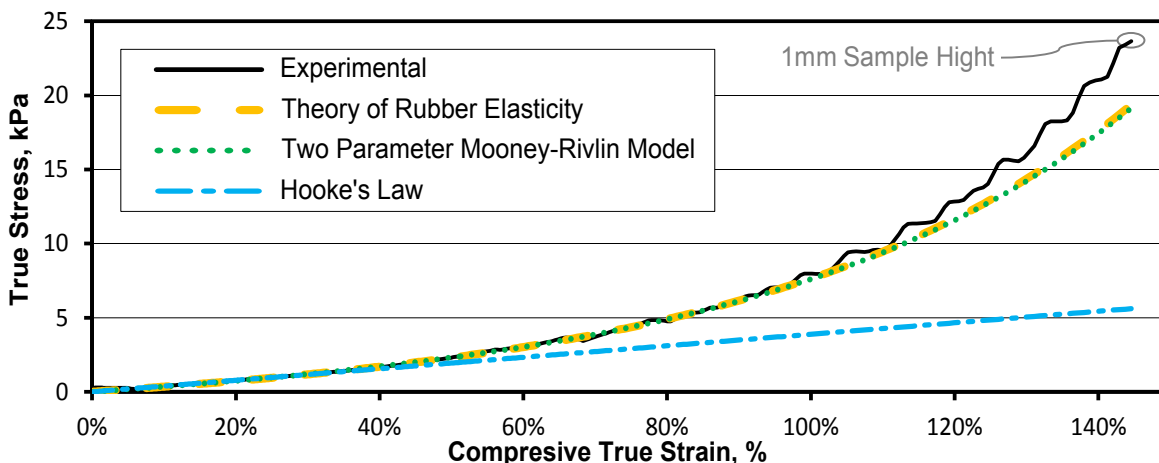


Figure 7.4: Uniaxial Model Comparison: 21% amine chitosan in 1:1 ratio with limit oxidized alginate

elasticity performed comparably to the Mooney-Rivlin model. Further analysis indicates that the Mooney-Rivlin model is unsuitable for the system because of instability in C_2 . The confidence interval for this coefficient contained zero, indicating that the reduced model, which is identical to the theory of rubber elasticity, is the correct form. This provides strong empirical support for the use of rubber elasticity theory, which until this point had been favoured on purely theoretical grounds. The full modulus data set is provided in Figure 7.5. Due to varying polymer concentration across amine substitutions modulus results are best interpreted via the hybrid-gel stiffness model in the next section.

To compare the shape of the stress strain curves across the full experiment, the stress magnitude was normalised using E' , Figure 7.6. In all cases, rubber elasticity theory provides a good fit to greater than 50% logarithmic strain. The disagreement at higher strains is likely due to the onset of chain inextensibility, although it could also be an artefact of the compression test methodology. The fact that the onset of disagreement correlates with polymer modification extent rather than blend stiffness suggests that it is a blend property rather than an experiment artefact. Further insight into chain inextensibility requires use of a more sophisticated model. Several are available for networks containing a single chain type [14, 16, 19, 25, 26]; but none of these are formulated for a hybrid system. For future studies involving deformation of swollen samples, investigation of limited chain extensibility is recommended. In this work the maximum logarithmic strain observed during equilibrium swelling was 45% meaning the simple theory should be adequate (Equation 7.1).

Although the strain range is much larger, the shapes of the stress strain curves in Figure 7.6 are reminiscent of those observed for cardiac muscle tissue, where the upturn is often described in terms of a secondary modulus [7]. A correlation appears to exist

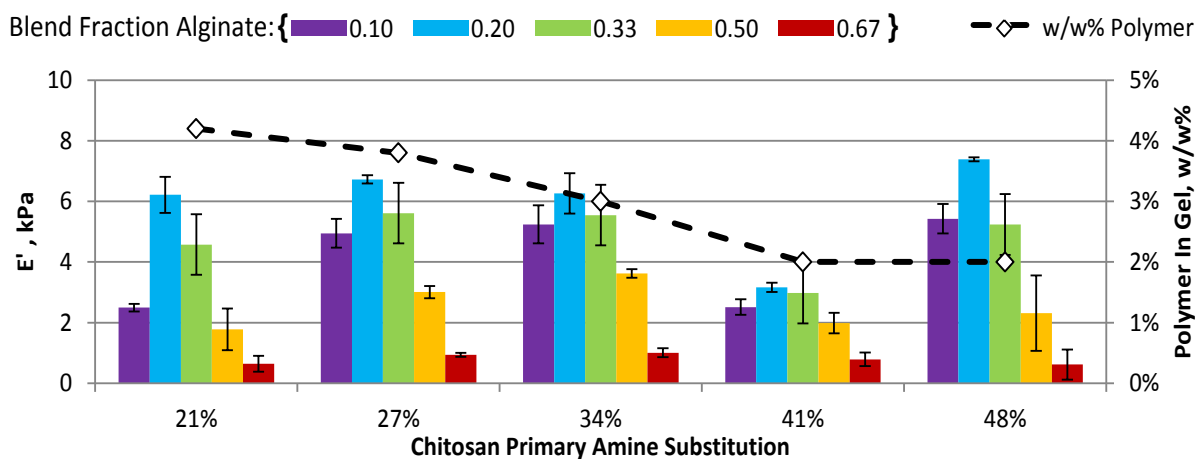


Figure 7.5: Elastic Modulus Results: Note rubber elastic modulus E' is approximately equivalent to Young's modulus E at zero deformation; Polymer concentration was kept constant for each amine substitution and varied across substitutions as indicated by closed diamonds, dotted line provides a guide to the eye; Error bars represent range where two replicates were tested or standard deviation in cases with more than two replicates.

between the primary and secondary modulus for any given amine substitution; however, the proportionality is different across the range of chitosans studied. This is more obvious when all the data is superimposed as in Figure 7.7. Other than the 0.1 alginate fraction, shape is only weakly affected by blend ratio. This is interesting because the zero deformation modulus varies most strongly with blend ratio across a wide range of compositions (Figure 7.5). For cardiac tissue engineering, a means for decoupling elastic curve shape from the material modulus has been desired to allow scaffold stress strain response to be more closely tailored to that of the natural tissue [7]. It appears hybrid gels may provide such a mechanism.

7.6.2 Hybrid Gel Stiffness Model

Figures 7.8 and 7.9 compare the hybrid gel stiffness model (Equation 7.16) to E' data obtained by fitting Equation 7.1 to experimental stress strain results. In formulating the predictive variables it was assumed that the gel network contains the same molar ratio polymers as the blend, making the length ratio in A equal to the molar blend ratio. The crosslinking explanatory variable B could be limiting group concentration, or the product of reactive group concentrations. The latter assumes the initial reaction rate is the most significant factor dictating the final number of crosslinks formed.

A good model fit is obtained for 4 out of the five chitosan substitutions. For the product model, global fit coefficients are statistically significant at 98%, but individual

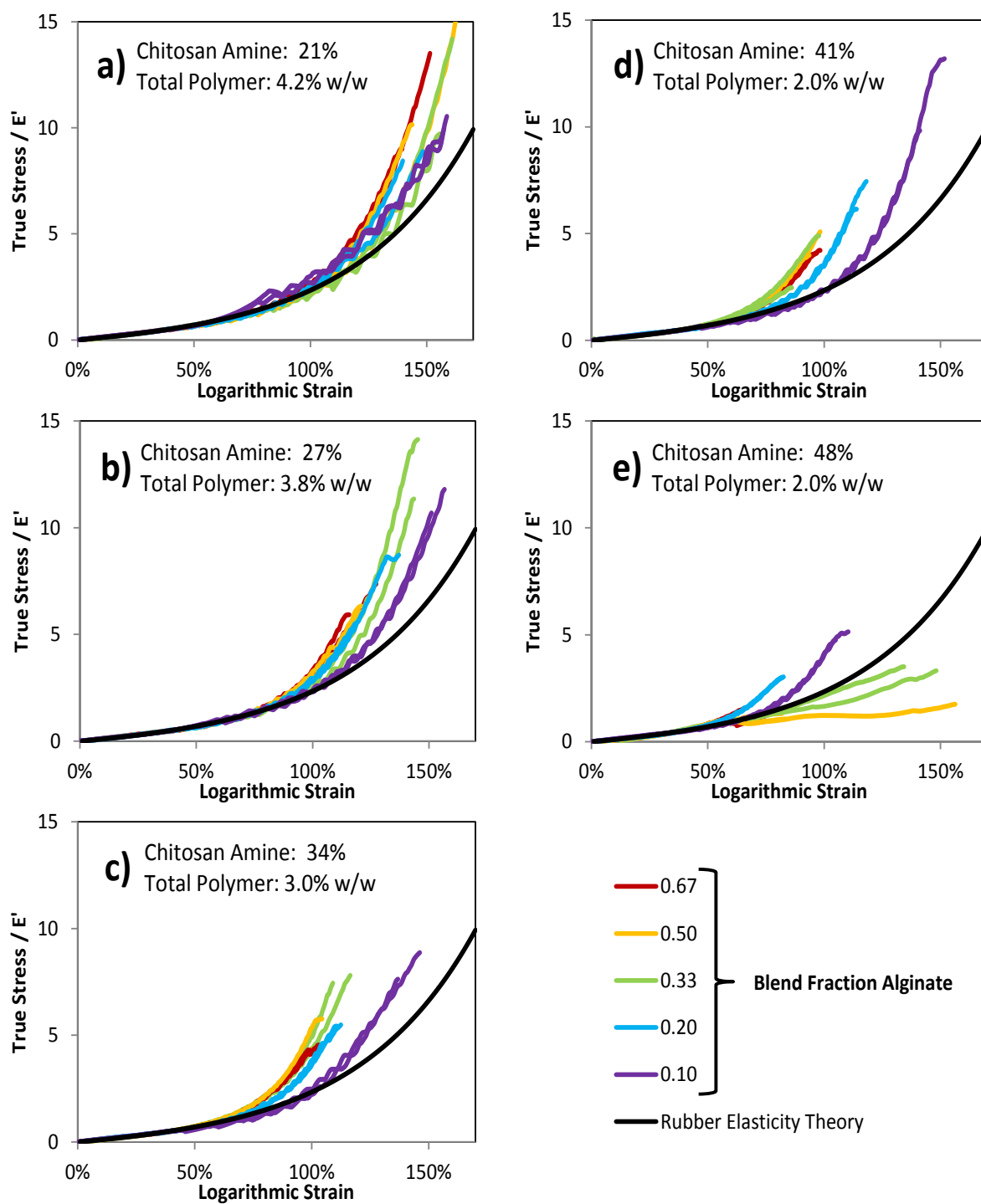


Figure 7.6: Compression Curve Shape Comparison by Blend Ratio: Curves are normalised by rubber elastic modulus

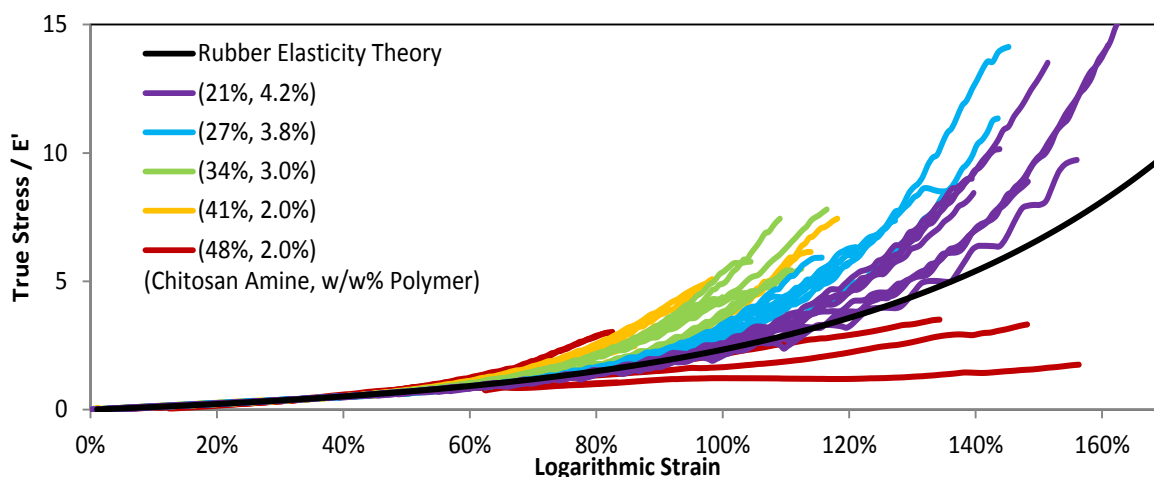


Figure 7.7: Compression Curve Shape Comparison by Chitosan Modification: Curves are normalised by rubber elastic modulus; 0.1 alginate fraction composition excluded

fit coefficients are not statistically significant (p-values around 0.2). The assumption fits subsets of data well, but cannot simultaneously provide a good fit for the full data set (e.g. both 1:2 and 4:1). Using the limiting reactant approach on the data sets shown in Figure 7.8, global and individual model coefficients are all statistically significant at better than a 97% level. It can therefore be concluded that the limiting reactant assumption is the correct approach.

The model indicates that chitosan is on average 16x stiffer than alginate. From the individual fits, (Figure 7.10), the stiffness ratio is found to vary with chitosan substitution (21% amine < 27% amine < 34% amine, minimum probability of significance 96%). When examining the fit for individual parameters in Figure 7.11, the trend is primarily a result of E_c so it is reasonable to attribute it to polymer modification. While the exact mechanism for this is uncertain, possible causes include: concentration effects, crosslinking efficiency and therefore chain length effects, or charge interaction effects. Whatever the mechanism it only appears to operate below 34% amine. A strong indication exists that the 41% amine stiffness ratio is lower than that of 34% amine chitosan (p-value 0.07).

Looking at Figure 7.9 it is apparent that neither crosslinking predictor provides a good fit to 48% amine substitution chitosan. The model assumes polymer behaviour is constant across blend ratios which appears to be inaccurate for the 48% amine gels. Focusing on the more interesting high modulus gels, statistically significant fit coefficients are obtained for 48% amine chitosan. Comparing these to the other chitosans, we note that 48% chitosan has a similar stiffness ratio to adjacent compositions (Figures 7.10). The much higher individual chain stiffness in Figure 7.11 may be an artefact of the narrow focus. In particular, as the same alginate is used for all compositions, the difference observed in Figure 7.11b can only be attributed to chain length / crosslinking efficiency, which is expected to be

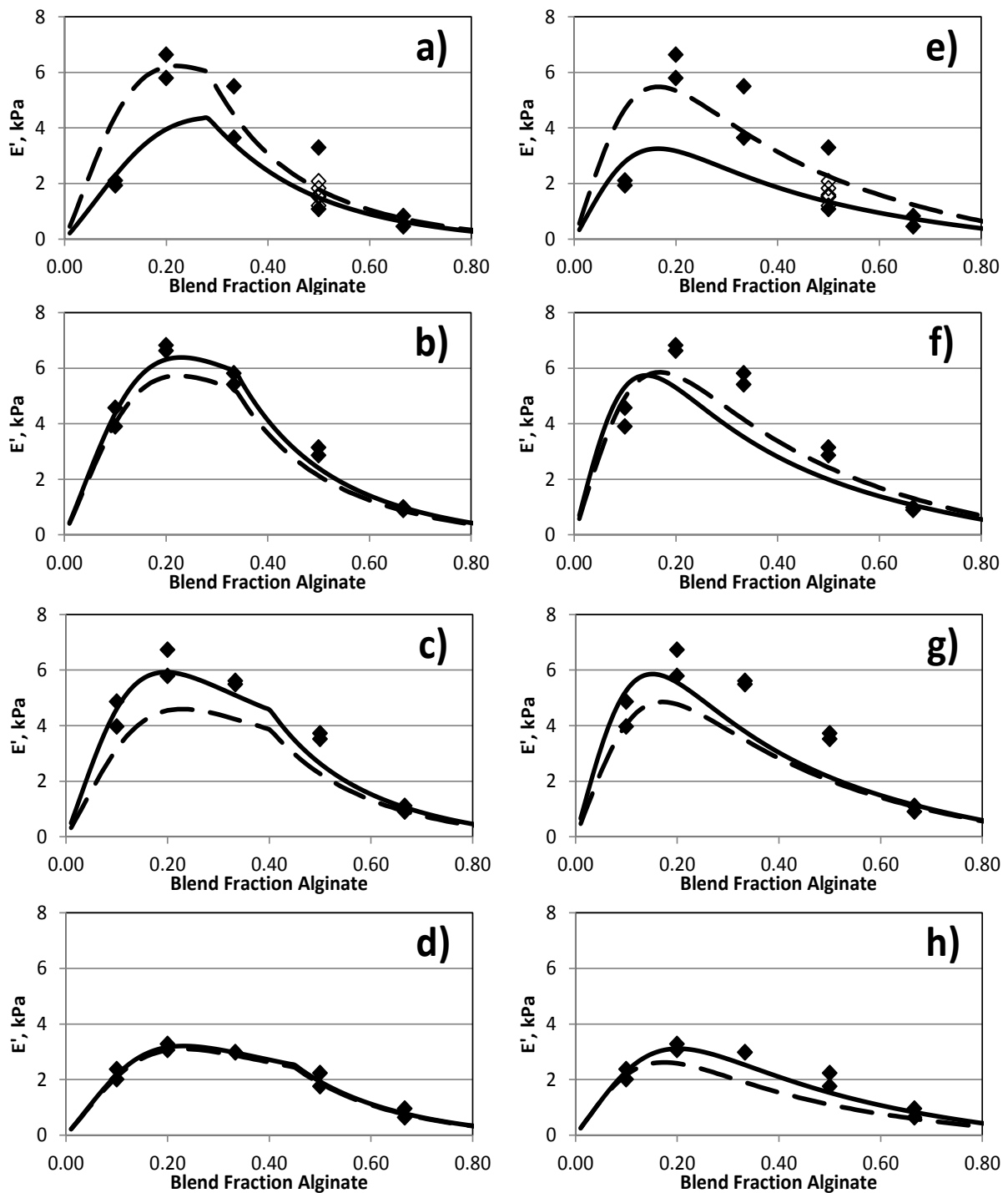


Figure 7.8: Elasticity model test: Diamonds are experimental points, a) to d) limiting reactant approach, solid line individual fit, dashed line global fit; e) to h) reactant product approach, solid line individual fit, dashed line global fit; a) and e) 4.2w/w% polymer, 21% amine chitosan; b) and f) 3.8w/w% polymer, 27% amine chitosan; c) and g) 3.0w/w% polymer, 34% amine chitosan; d) and h) 2.0w/w% polymer, 41% amine chitosan

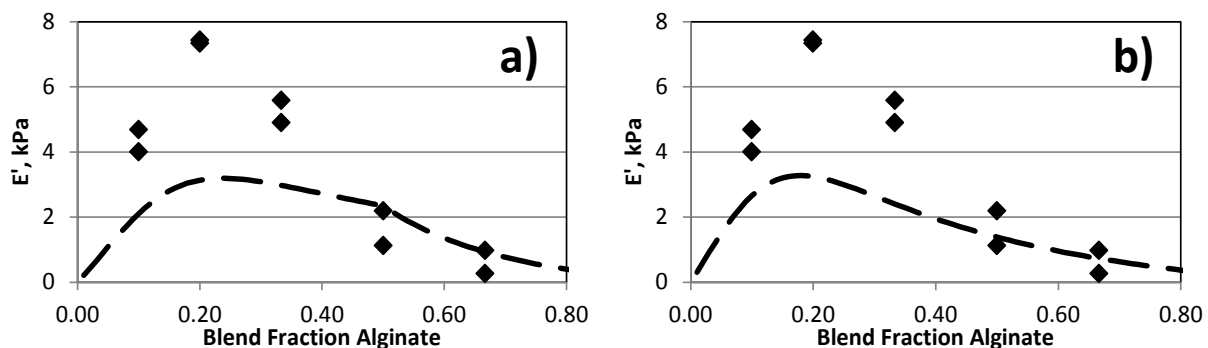


Figure 7.9: Elasticity model anomalous composition: Diamonds are experimental points; 2.0w/w% polymer, 48% amine chitosan; a) limiting reactant approach; b) reactant product approach; dashed line is respective global model fit to all other compositions

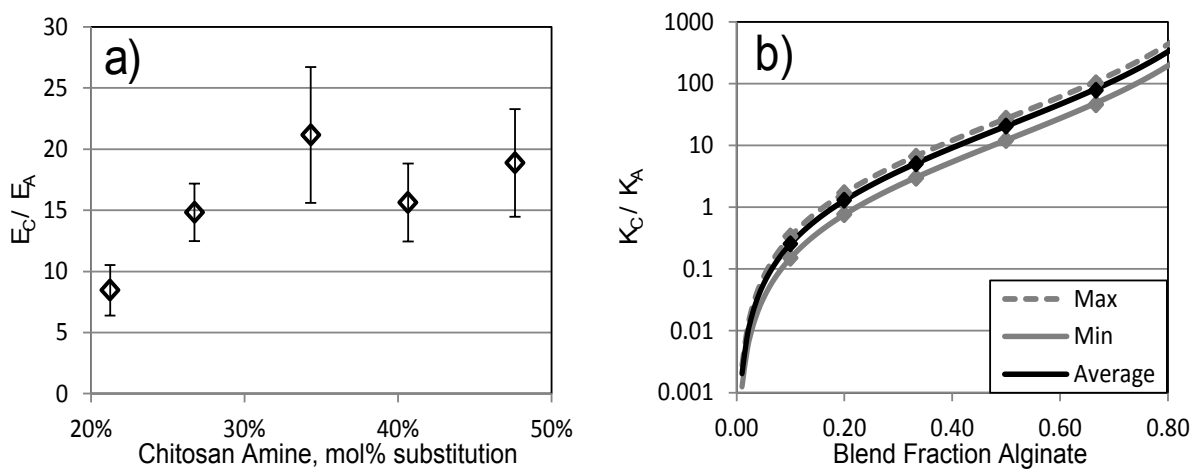


Figure 7.10: Network Chain Stiffness Ratios: a) Ratio of polymer fit parameters; error bars are a 95% confidence interval on the mean, 48% amine point excludes low modulus data; b) Chain stiffness ratios including length effects; points are experimental compositions

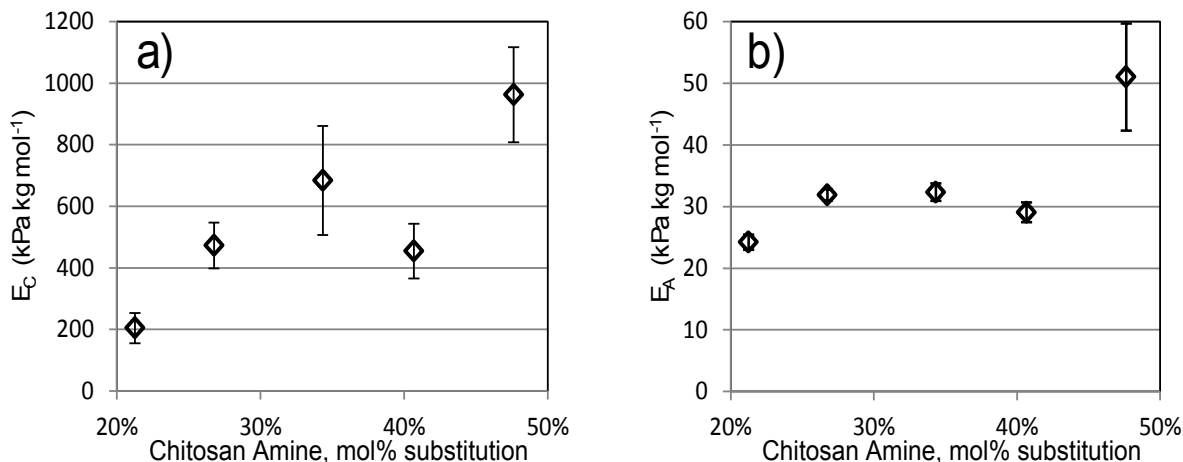


Figure 7.11: Polymer specific Elasticity Fit Constants: a) Chitosan; b) Alginate; error bars are a 95% confidence interval, 48% amine point excludes low modulus data

higher in the subset of blends included in the 48% amine fit.

When addressing the question of crosslinking efficiency, the hybrid gel effect must be considered for any accuracy. Figure 7.12a is generated using the Section 7.3.2 approach which ignores chain length and composition effects on hybrid gel stiffness. When this result is divided through by the terms in the hybrid gel model pertaining to length and stiffness effects ($A^2 E_A^{-1} + (1 - A)^2 E_C^{-1}$) the result is Figure 7.12b.

Exact values for crosslink density cannot be obtained using the derived theory because the proportionality constant for average crosslinking efficiency (β_B) is inseparable from the chain stiffness constants. This does not prevent relative comparisons across the set over which the average is taken. The good agreement between the overall fit and similar E_A results for the first four compositions allows relative comparisons to be made. Comparisons within the 48% amine chitosan set are possible but it cannot be compared to the other compositions.

Following this analysis, Figure 7.12a shows the gains in crosslinking efficiency predicted when hybrid gel physics is ignored. The gains disappear when it is included Figure 7.12b. The opposite trend is actually observed, where the best crosslinking efficiency appears to be obtained by maximizing alginate content. However, as was observed above, the stiffness losses resulting from a slightly lower rate of crosslink formation are more than offset by stiffness gains from balancing relative chain stiffness.

Examining Figure 7.10b the crossover point for individual chain stiffness coincides with the maximum blend stiffness observed in Figure 7.8, even though the maximum crosslinking potential occurs much lower (inflection point Figures 7.8a to d). Model predictions are accurate and it is concluded that the model provides a useful tool for interpreting hybrid gel stiffness results.

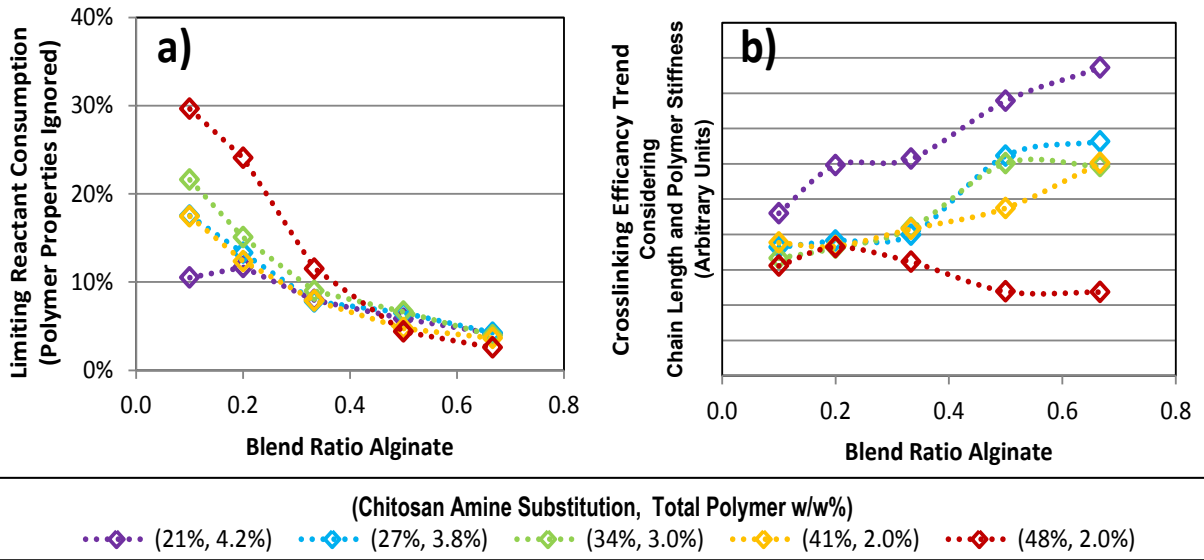


Figure 7.12: Gel Crosslinking Estimates: a) Section 7.3.2 approach ignoring relative chain stiffness and length; b) Relative efficiency scaling after stiffness and length effects are considered; dotted lines are a guide to the eye.

7.6.3 Gel Failure Analysis

Understanding failure modes was not a core objective of this study but can provide insight into network topology. The trends in Figure 7.13 shows strain to failure is influenced strongly by chitosan modification / polymer content. A weak influence by blend ratio may also exist in the low range. Lower strain to failure with increasing amine content might be attributable to decreasing network chain length as the average number of crosslinkable groups per chain is increased. The increase in failure strain as blend ratio decreases is consistent with toughness increases observed by other authors in gels of a single polymeric species but with distinct populations of chain lengths [25]. Failure patterns provide support for the chain inextensibility / secondary modulus hypothesis in explaining elastic curve deviation from standard theory of rubber elasticity.

7.6.4 Equilibrium Swelling

As can be seen in Figure 7.14, results from samples with varying dimensions initially superimpose based on the diffusion time scale (Equation 7.4). Later divergence is attributed to degradation of the polymer network. Because degradation has different time scaling it is possible to separate the two signals with the true equilibrium level observed at a time between 1 and 3 $h^{1/2} mm^{-1}$ in the 0.79 mm thick specimens.

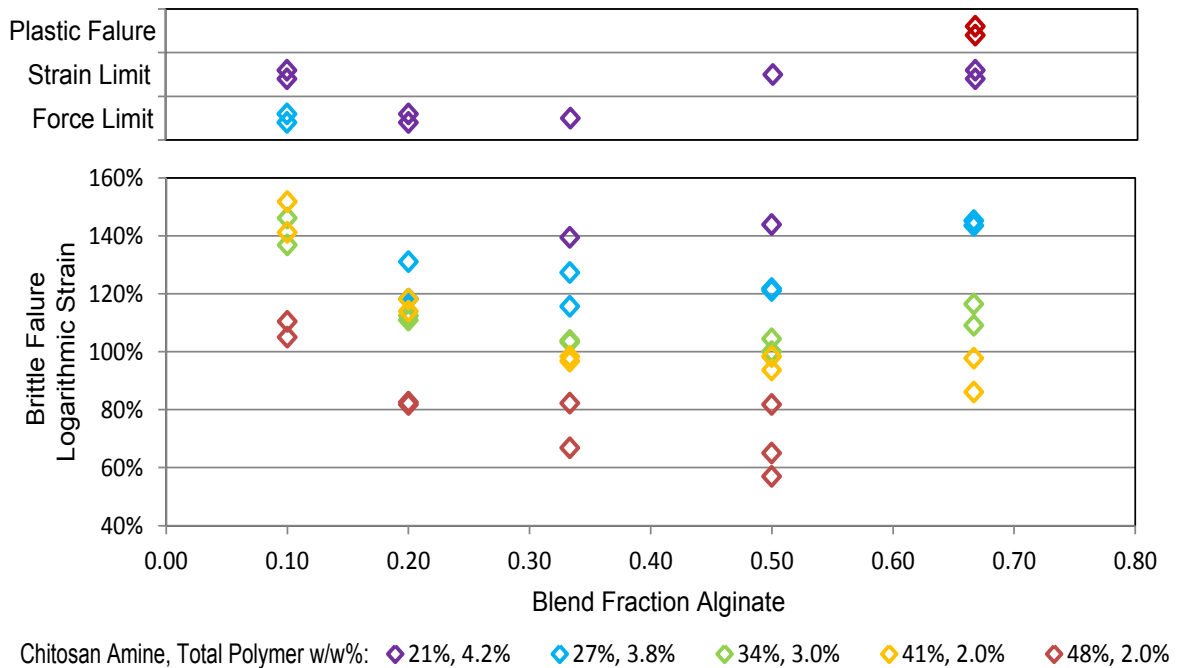


Figure 7.13: Compression Sample Failure Modes: Strain to failure plotted for clearly defined brittle failure; displacement limit samples reached 160% logarithmic strain without failure and exhibited elastic recovery; force limit samples reached 230 kPa engineering stress (18 N load) without failure; plastic failure samples exhibited permanent deformation and no obvious discontinuity in their stress strain curve

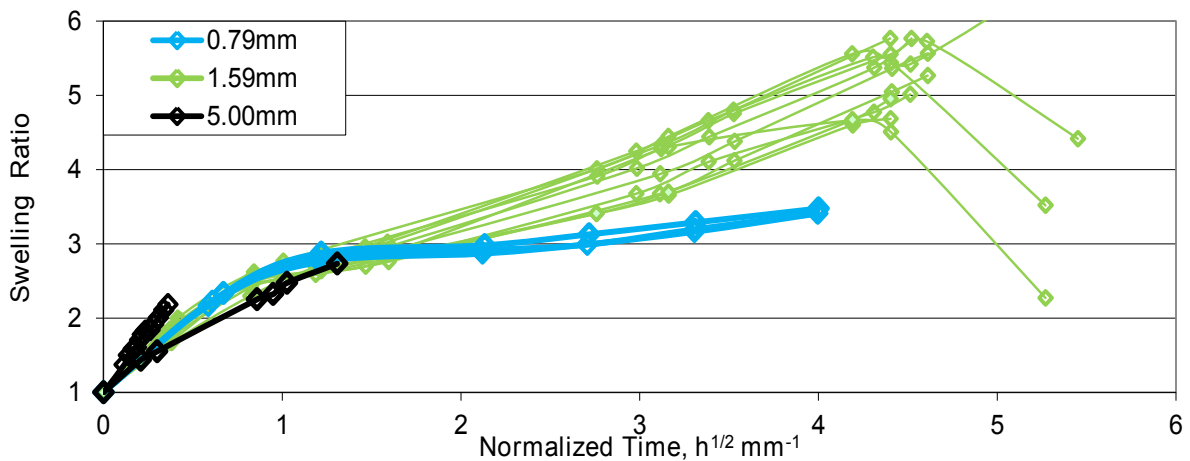


Figure 7.14: Swelling Sample Optimization: 5%, Polymer 1:1, ratio 21% amine chitosan; 10mm diameter disks with indicated thickness in phosphate buffered saline

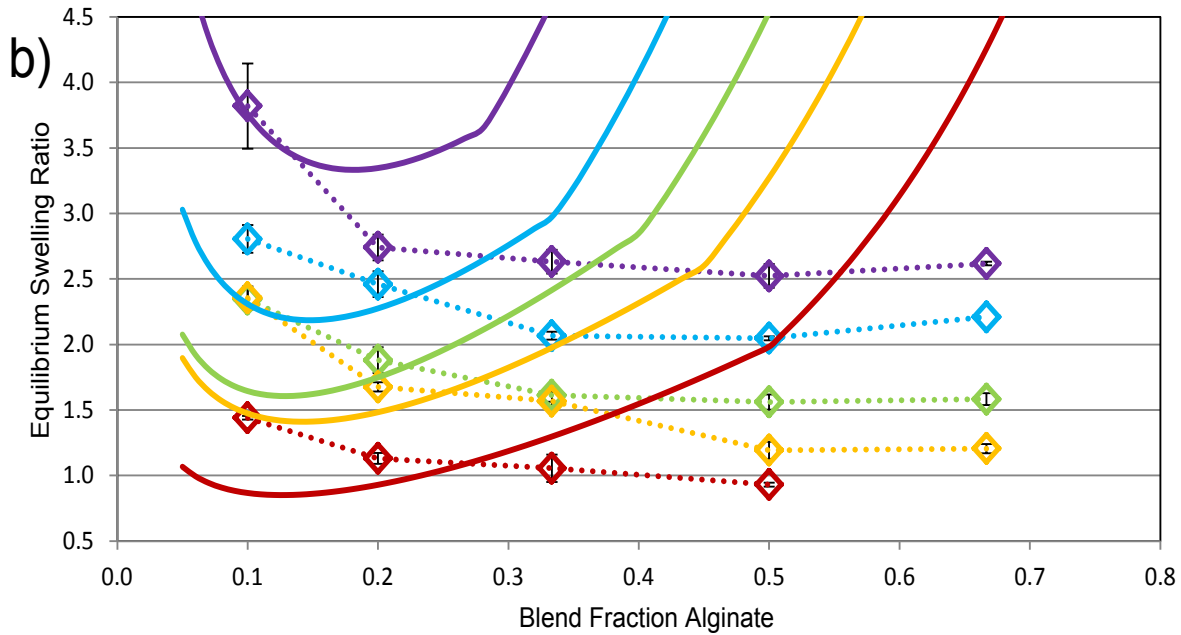
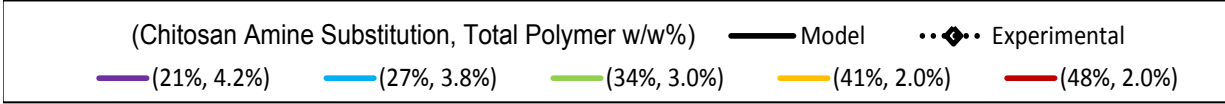
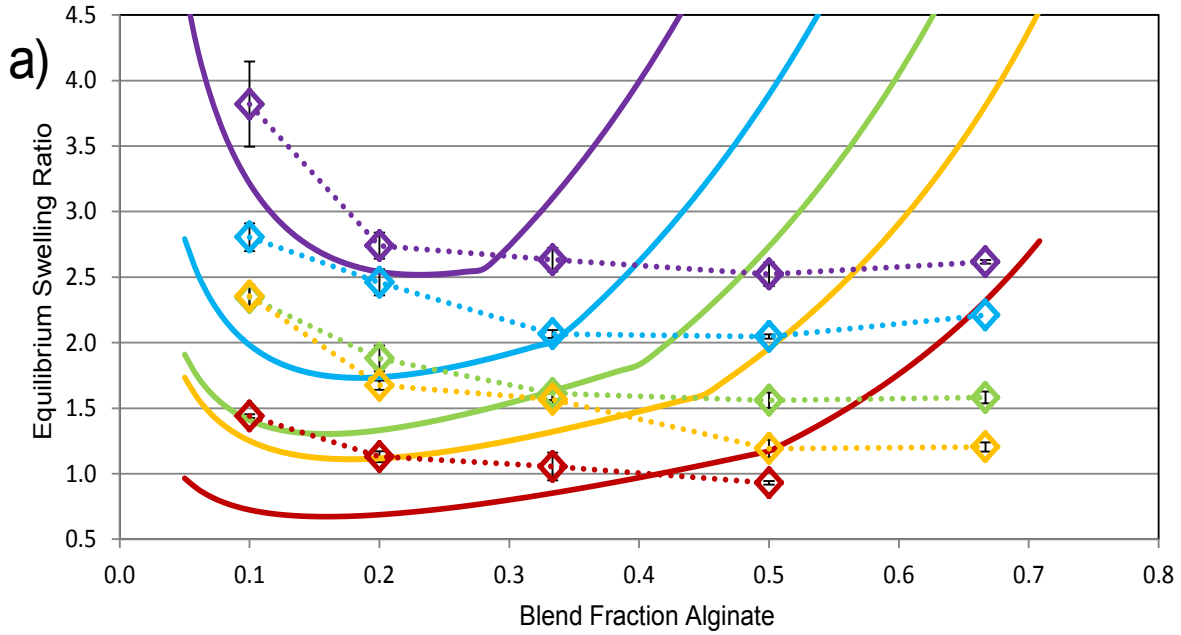


Figure 7.15: Equilibrium Swelling Ratios: a) using literature alginate ionization, $\gamma_f = 0.4$; b) using calculated alginate ionization $\gamma_f = 1$. Solid lines are model predictions; Diamonds are experimentally determined, error bars show standard deviation, dotted lines provided as a guide to the eye.

Equilibrium swelling results are compared to model predictions in Figure 7.15. Agreement is mostly qualitative although it approaches quantitative in a few cases. The most important contribution of the model is that the correct trend is observed across chitosan amine substitution. The elasticity model uses experimental data with the only possible discrepancy being the scaling resulting from gel swelling. Moving to the ‘affine’ model reduces the magnitude of the elastic term, making the model disagreement worse. As the best agreement is observed at high chitosan content there is a strong indication that the source of error lies in the alginate model terms. The only model term of any significance that pertains only to alginate is its influence on the ionic driving force.

The most plausible explanation is that all the alginate is not bonded to the network and a significant fraction is leaching out of the blend when alginate is the majority component. Alginate is the gel component implicated in the observed degradation [44, 88], making loss of some alginate reasonable; however under the current theoretical premise, practically all the alginate would have to be lost for agreement to be obtained. The weakest link in the current theory is the counterion activity / condensation model used. A constant correction factor γ_f is assumed even though the charge density of the gel changes significantly as the alginate content is increased. Comparing Figure 7.15a with 7.15b it can be observed that this term has a significant effect. Recent work using more sophisticated models has shown that the assumption of a constant γ_f is likely inaccurate [136, 137], and it is recommended that future work update the counterion condensation / activity terms to reflect the more sophisticated approach.

7.6.5 Gel Appropriateness for Tissue Engineering Application

Before swelling, the maximum stiffness obtained is below the 10 kPa target. Theory indicates swelling should decrease modulus. Therefore, none of the studied formulations are likely to be suitable for muscle tissue engineering in their current forms. More work is necessary to improve system performance. Two directions are recommended, namely: 1) use of a lower molecular weight chitosan, and 2) use of a stiffer oxidised polysaccharide. Lower molecular weight chitosan might allow higher concentrations to be used and result in higher overall stiffness despite an increase in dangling ends. The initial modulus is dominated by the low stiffness component. A stiffer oxidised polysaccharide, (a lower oxidation alginate or some other polysaccharide) might result in a significant improvement in initial stiffness. Despite failure to meet the target stiffness the ability to partially delink curve shape from initial stiffness is interesting and justifies further work on hybrid gels.

Polyelectrolyte gel stiffness scaling is a complex subject [212], even without considering hybrid gel effects. The ability to model hybrid gel swelling appears to be limited, posing a design challenge. It is possible that superimposed swelling and uniaxial deformation might activate the secondary modulus at much lower apparent deformations which could make current formulations applicable to muscle tissue engineering. A recommended extension to

the current work is to collect stiffness data on hybrid gels at varying degrees of swelling.

Some observations regarding cure and degradation kinetics were noted in this work but were not characterised to fully understand their mechanisms. Prediction of these is necessary for any practical application. Further study in these directions is also recommended.

7.7 Concluding Remarks

Rubber elasticity theory provides a good fit to low extension stress strain data for the present material. The theory, however, does not account for chain inextensibility. The ‘secondary modulus’ observed at high strains is attributed to the latter effect. The onset of disagreement and relative magnitude of the ‘secondary modulus’ is dependent on the chitosan amine substitution. Similar dependency’s observed during gel failure analysis corroborate this hypothesis. Hybrid gels provide the potential to control the elastic curve shape of tissue engineering scaffold materials. Development of a hybrid gel stiffness theory incorporating limited chain extensibility is recommended to further design efforts.

The hybrid gel stiffness model derived here provides a very good fit to modulus data below the extensibility limit. Using the model, limit-oxidised-alginate is found to be 16x less stiff than the studied N-succinyl-chitosans. Standard theory was shown to give erroneous estimates of crosslinking efficiency. Relative crosslinking efficiency for hybrid gels was determined using the new model. It is observed to be the greatest in high alginate compositions. In determining overall blend stiffness, this effect is completely offset by the lower alginate stiffness.

Gel equilibrium swelling is generally lower than theoretically predicted values. The discrepancy is attributed to inaccuracy in the alginate ion-interaction model used. Experimentally determined correction factors (see Chapter 6), allowed the current theory to provide a good description of the relative chitosan effects on swelling. In future work, the use of a more sophisticated ion-condensation theory is recommended [136, 137].

The maximum unswollen modulus was less than the 10 kPa target. This makes it unlikely than any of the studied compositions are directly applicable to muscle tissue engineering. As formulation stiffnesses are close to the target and several avenues of investigation are still open, further study is recommended. In particular, stiffness should be characterised at varying degrees of swelling, formulations with higher concentrations of lower molecular weight chitosans should be investigated, and a stiffer oxidised polysaccharide should be used (less oxidised alginate or completely different polymer).

Chapter 8

Conclusions and Recommendations

8.1 Primary Scientific Contributions

Injectable oxidised-alginate / N-succinyl-chitosan hybrid gels have been identified as a new material with promise for some biomedical applications. To facilitate their eventual adoption as useful biomaterials two initial studies were undertaken, mainly: 1) to explore compositions that meet target viscosity and stiffness ranges appropriate for common hydrogel applications, and 2) to develop and validate models to predict two hybrid-hydrogel mechanical properties, i.e. swelling and stiffness behaviour.

To allow for injectability, precursor solution viscosity was constrained to $< \sim 0.2$ Pa·s. This combined with the unexpectedly low stiffness of oxidized alginate resulted in a maximum low strain stiffness of 7 kPa in the current study. This is below the 10 to 30 kPa target range recommended for muscle tissue. Despite this, the system can be engineered further to offer potential practical use. Two key findings are interesting, namely: 1) the turbidity observed in some formulations indicates the gels were heterogeneous, and 2) the onset of high strain ‘secondary stiffness’ behaviour is correlated with chitosan modification extent rather than low strain stiffness. Unlike the homogeneous systems commonly studied, heterogeneous gels have the potential to allow both the required pore size and the desired stiffness. Controllable ‘secondary’ stiffness behaviour provides the potential for a much closer match to the non-linear elastic response of muscle tissue than is currently possible. To obtain the 10 kPa stiffness target in future investigations two approaches are recommended: 1) use of lower molecular weight N-succinyl-chitosan to see if higher polymer concentrations can be obtained at the limiting viscosity, and 2) use of less oxidized alginate or a different oxidized polysaccharide which is likely to be stiffer resulting in a greater overall contribution to gel mechanical response.

Swelling models well documented by Chan [14] were expanded to apply to hybrid systems containing polyampholytes. Our finding is that they do not readily apply to this

specific hybrid gel and currently do not produce quantitative agreement. The primary discrepancy lies in ion condensation theory. Agreement was particularly poor at high alginate content due to a lack of empirical data for alginate ion condensation. Qualitative agreement across N-succinyl-chitosan compositions was obtained by handling ion-condensation phenomenologically via osmometry experiments. Membrane osmometry models were updated paralleling the approach used in swelling and incorporating modern solution nonideality corrections. From osmometry, the simple Manning-Oosawa model for ion condensation does not accurately predict results. It is recommended that predictions from recent models (e.g. [136, 137]) be compared to experimental results to see if quantitative agreement can be obtained. It is also recommended that simpler conductivity experiments be investigated to characterise ion condensation. The hybrid gel stiffness model was found to offer remarkably good accuracy and it is recommended that it be tested against other materials and expanded to include chain inextensibility / secondary stiffness behaviour.

8.2 Other Contributions

While working on the primary questions, other findings were made that are of potential value to the field. These can be divided into two categories, namely: 1) instrument design / validation, and 2) material property characterization.

Two instruments were designed: 1) a membrane osmometer suitable for characterizing small samples of polyelectrolytes at elevated temperature and in concentrated chloride solutions, and 2) a small sample capillary rheometer for characterization of polymer solution injectability with almost 100% sample recovery. The osmometer was validated against PVA and shown to meet the performance requirements of ASTM D3750 [45]. The rheometer was calibrated using Glycerol and DI water with a typical repeatability of $\pm 4\%$. Both instrument designs are sufficiently simple and inexpensive to be built by researchers in-house. This addresses a need by the scientific community for these types of instruments that is not currently being filled by commercial sources.

In the material property characterization work: 1) N-succinylation results fit a log linear empirical correlation with respect to input reagent concentrations; 2) a small increase in chitosan moisture affinity and thermal stability is observed with increasing N-succinyl substitution; 3) anomalous phase separation and rheological behaviour is observed in N-succinyl-chitosan solutions as the solubility limit is approached; 4) polyampholyte solution rheology scales differently than that of polyelectrolytes; 5) limit-oxidised-alginate stability is too low for osmometry at 40°C; and 6) limit-oxidised-alginate is 16x less stiff than N-succinyl-chitosan.

8.3 Recommendations for Future Work

Recommendations primarily pertain to the two thesis topics. The only exception is a recommendation based on rheology results that further study be conducted into dynamic effects on polyampholyte morphology / solubility in solution.

To advance modelling efforts and support tissue scaffold design, there are four recommendations, namely: 1) characterization of alginate ion condensation by methods other than membrane osmometry; 2) modelling of chitosan ion condensation using sub-chain charges or the more sophisticated theory recently put forward [136, 137]; 3) updating swelling models to incorporate whichever ion condensation approach proves most effective; and 4) development of a hybrid gel stiffness theory incorporating limited chain extensibility affects.

The extensive yet still preliminary work to date has demonstrated that the N-succinyl-chitosan / oxidised-polysaccharide system is very promising as a practical, low cost alternative for some biomedical applications. Continued development is recommended. Characterization of pore size in gels using low solubility chitosan is recommended to see if scaling relationships are broken. Characterization of gel stiffness at varying degrees of swelling and measurement of polymer leaching during swelling are recommended to support stiffness modelling efforts. To improve gel stiffness two directions should be considered, namely: 1) use of higher concentrations of a lower molecular weight chitosan, and 2) use of a stiffer oxidised-polysaccharide.

APPENDICES

Appendix A

Rheometer Design

A.1 Overview

This document provides part design detail, assembly instructions and operating procedures for a simple capillary rheometer.

A.2 Operating Procedure

Though the broad outline was provided by the author, Mr. Alex Vasile is credited with developing many of the intricate details of the sample loading procedure. He was also responsible for producing the first electronic copy from his and the author's notes which in edited form is provided below.

0. Starting Assumptions

- (a) All equipment cleaned and dried
- (b) Syringe pump speed set for desired flow rate
- (c) Safety and assumption check calculations made to select needle lengths

1. Dip loading needle into sample, and use to coat the tip of the sample syringe plunger
2. Insert plunger into sample syringe body
3. Fill sample syringe
 - (a) Attach stopcock to sample syringe

- (b) For very viscous samples: Draw a small amount of sample into a disposable syringe and inject into the sample syringe to fill dead volume and ensure bubble free loading
 - (c) Attach loading needle to stopcock
 - (d) With the stopcock open draw $\sim 2\text{mL}$ of sample into the syringe, try to ensure that there are as few air bubbles as possible
4. Attach stopcock to sample tube and tube to rheometer core; Flush with sample
 - (a) On first run with a composition flush cell with $\sim 1\text{ml}$ of sample and discard
 - (b) On subsequent runs push out any bubbles and allow hanging drop to form to insure bubble free connection
 - (c) Ensure that the syringe still has some sample left in it, this will make it far easier to prevent air bubbles later on
 5. Cap open end of main block, close stopcock and detach sample syringe
 6. Attach sample syringe to drive syringe assembly, and fix the assembly to the rheometer
 7. Detach stopcock from hose, attach both ends of the hose to the main block in order to make a closed loop and reattach stopcock to sample syringe
 8. Using drive system, draw up as much sample as possible into the syringe
 - (a) Remember to set the empty position for the syringe in the pump menu. When doing so, set the empty position at the 0.5mL mark. This volume will be used to purge the needle of air bubbles when drawing up sample the next time.
 - (b) If large air bubbles are present close the stopcock with about 0.5ml of space left into the syringe and create a vacuum
 9. To get rid of any air bubbles detach the needle from the stopcock and flip the rheometer upside-down
 - (a) This will allow the bubbles to float up to the top of the syringe where they can be pushed out
 - (b) Once all the bubbles have settled at the top open the stopcock, the rush of air will draw back most of the sample in the syringe, thus minimizing losses
 - (c) With a lab-wipe handy, push the air out; allow a small convex meniscus to form on the stopcock
 - (d) If too little sample remains in the syringe return to step 8, otherwise continue to 10

- (e) Attach the end of the hose that is connected to the out hole in the main block to the stopcock and plug the out hole before flipping the rheometer right side up
10. Retrieve the correct calibrated needle for this run, double-checking its length with a ruler and insert it through the sample recovery septa.
11. Unplug the out hole and attach the calibrated needle to it.
12. Raise the sample recovery bracket and clamp recovery assembly.
 - (a) Ensure that the needle is centered radially in the tube and has as little bend in it as possible.
 - (b) Allow enough space at the bottom of the tube for the sample to accumulate without reaching the needle tip.
13. Record the volume of the sample in the sample syringe and in all of the tubes being used.
14. If the thermocouple is not attached to the syringe, attach it and ensure that the markings above the 3mL mark are clearly visible
15. Double check all fittings and bolts
16. If placing in water bath prepare the plastic bag, if bag is already prepared proceed to 18, if the water bath is not being used precede to 21.
 - (a) Obtain a new bag and check for leaks
 - (b) Apply a strip of thermal tape across the entire bottom seam
17. Check bag for any leaks
18. Insert rheometer into plastic bag and fix the bag to the rheometer using ~20cm of nichrome wire.
19. Insert rheometer into the water bath, wait for thermal equilibration before starting experiment
 - (a) If the water bath is already at temperature, you must wait at least 30 minutes
 - (b) If the water bath is not at temperature, or if it is the first run of the day, wait at least 60 minutes
20. Run Experiment
 - (a) Enter file name and start data acquisition on computer

- (b) Check programmed flow rate and start syringe pump
- (c) Wait for experiment stop.
- (d) Turn off data acquisition.

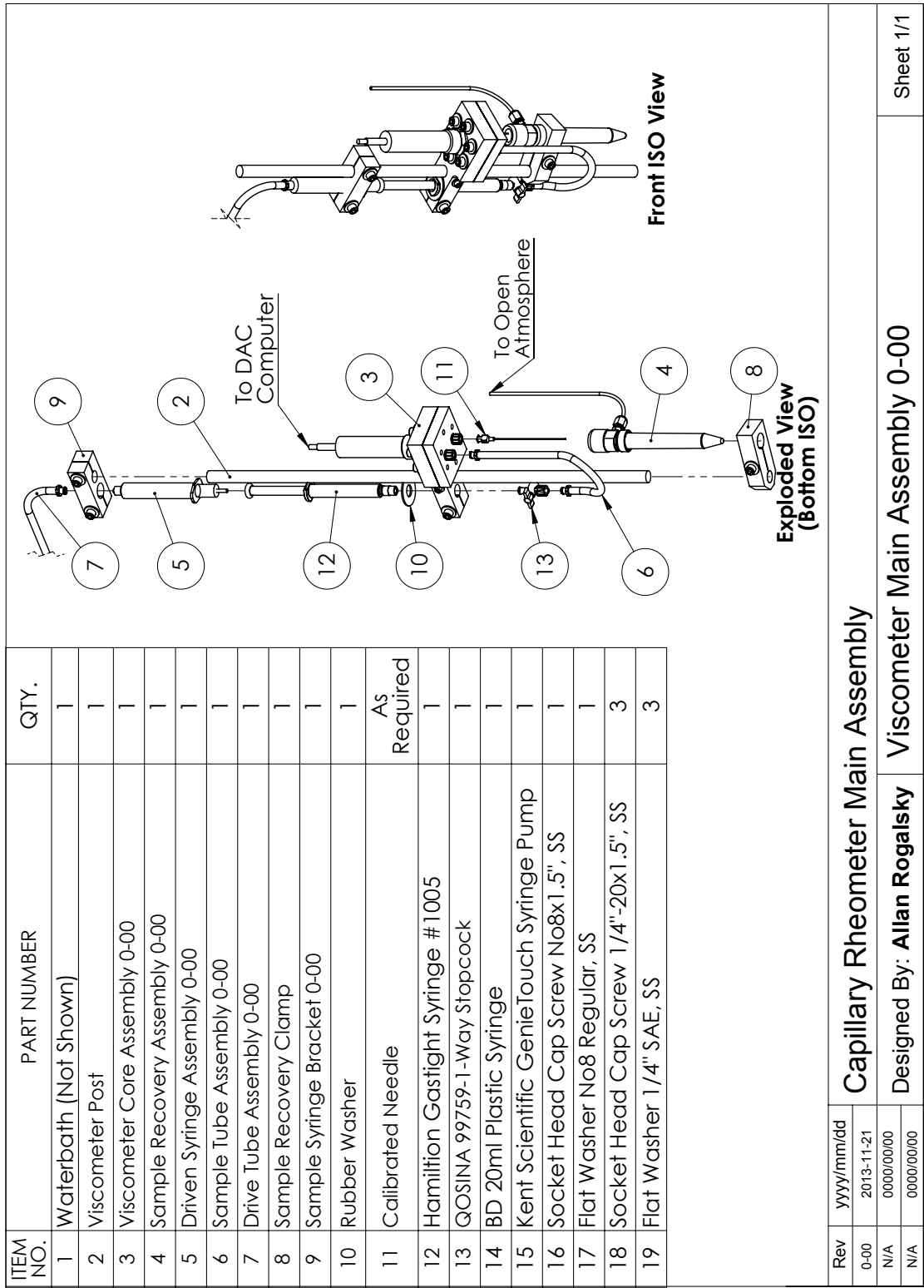
A.3 Detail Design and Assembly

A.3.1 Design Tree

Main assembly:

1. Mounting Post
2. Core Assembly
 - (a) Core
 - (b) Transducer Adapter
 - (c) Membrane
3. Sample Recovery Assembly
 - (a) Vented Septa Adapter for 15ml Centrifuge Vial
 - (b) Modified Nut for 15ml Centrifuge Vial Lid
4. Driven Syringe Assembly
 - (a) Syringe Plunger
5. Sample Hose Assembly
6. Drive Hose Assembly
7. Sample Recovery Clamp
8. Sample Syringe Bracket, Re-purposed to Hold Drive Syringe

A.3.2 Engineering Drawings



Capillary Rheometer Main Assembly

Designed By: **Allan Rogalsky** Viscometer Main Assembly 0-00

Figure A.1: Capillary Rheometer Main Assembly

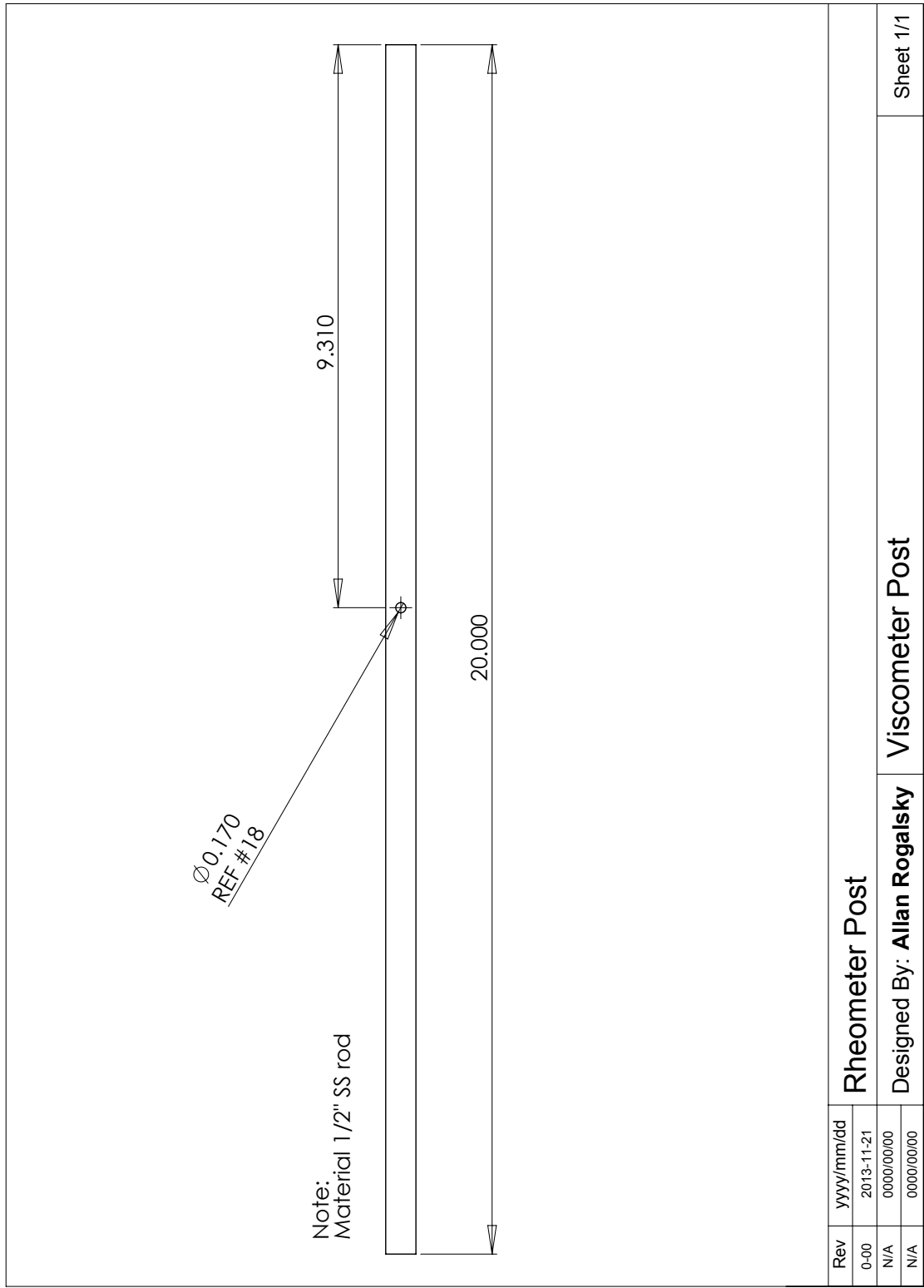


Figure A.2: Capillary Rheometer / Post

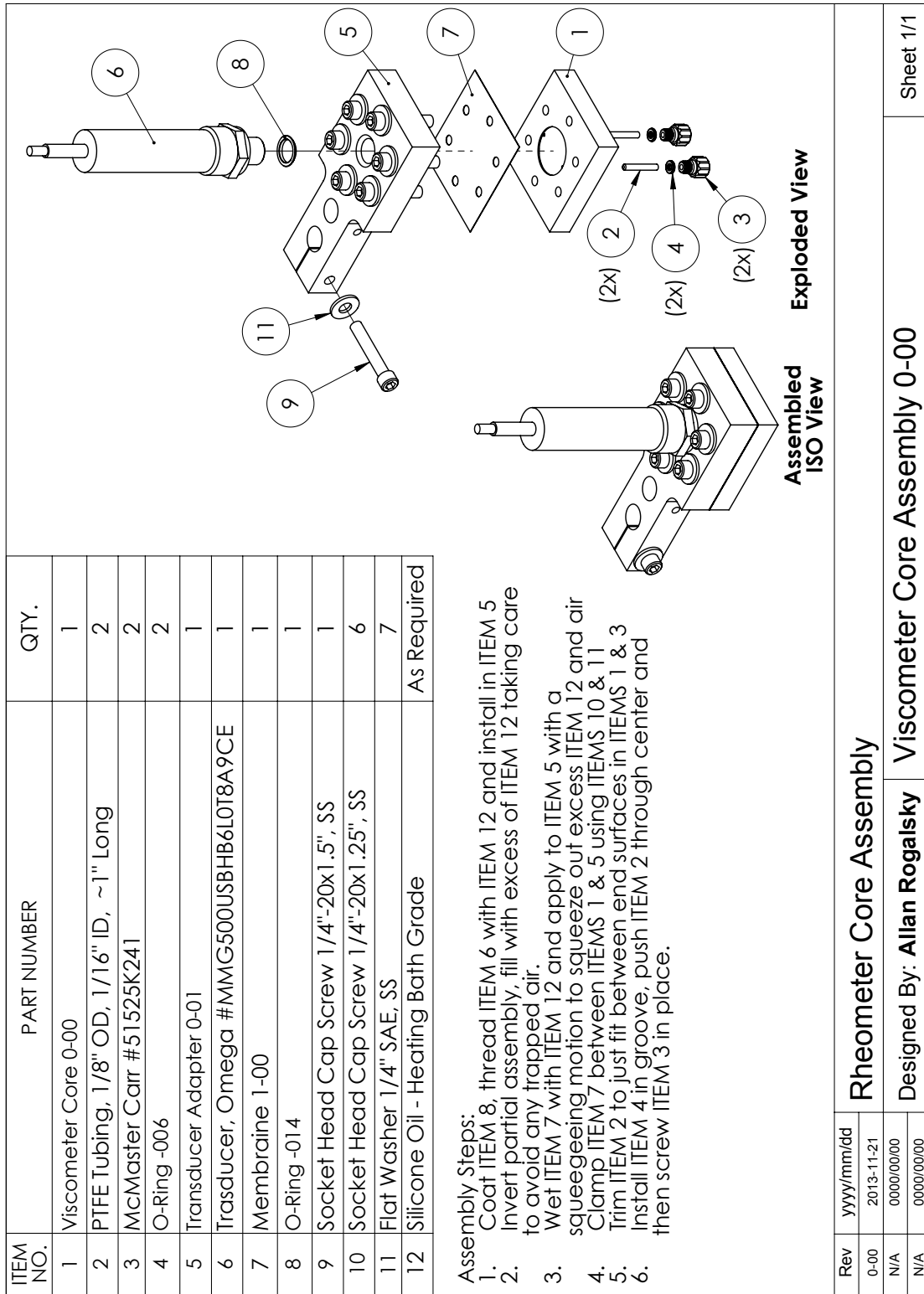


Figure A.3: Capillary Rheometer / Core Assembly

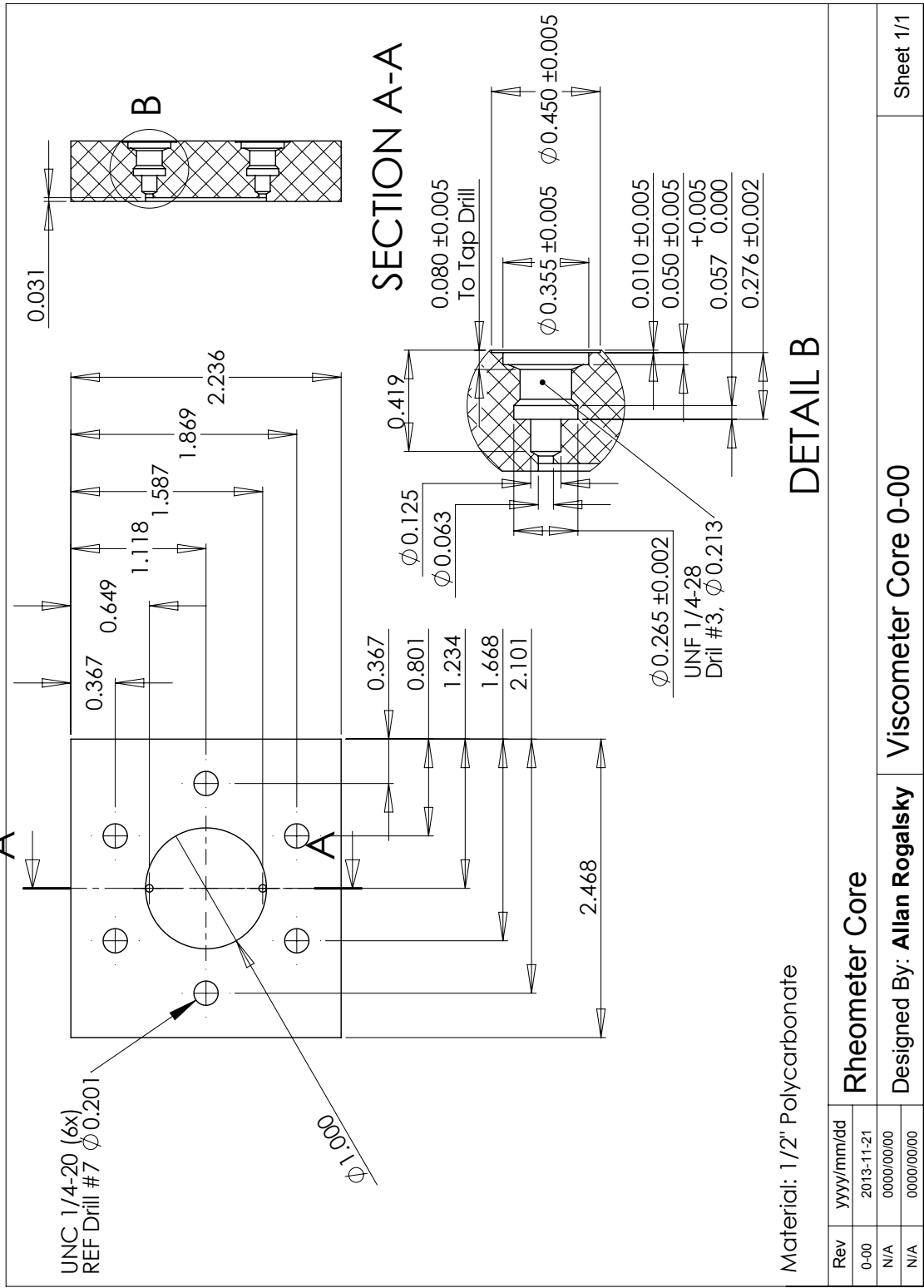


Figure A.4: Capillary Rheometer / Core Assembly / Core

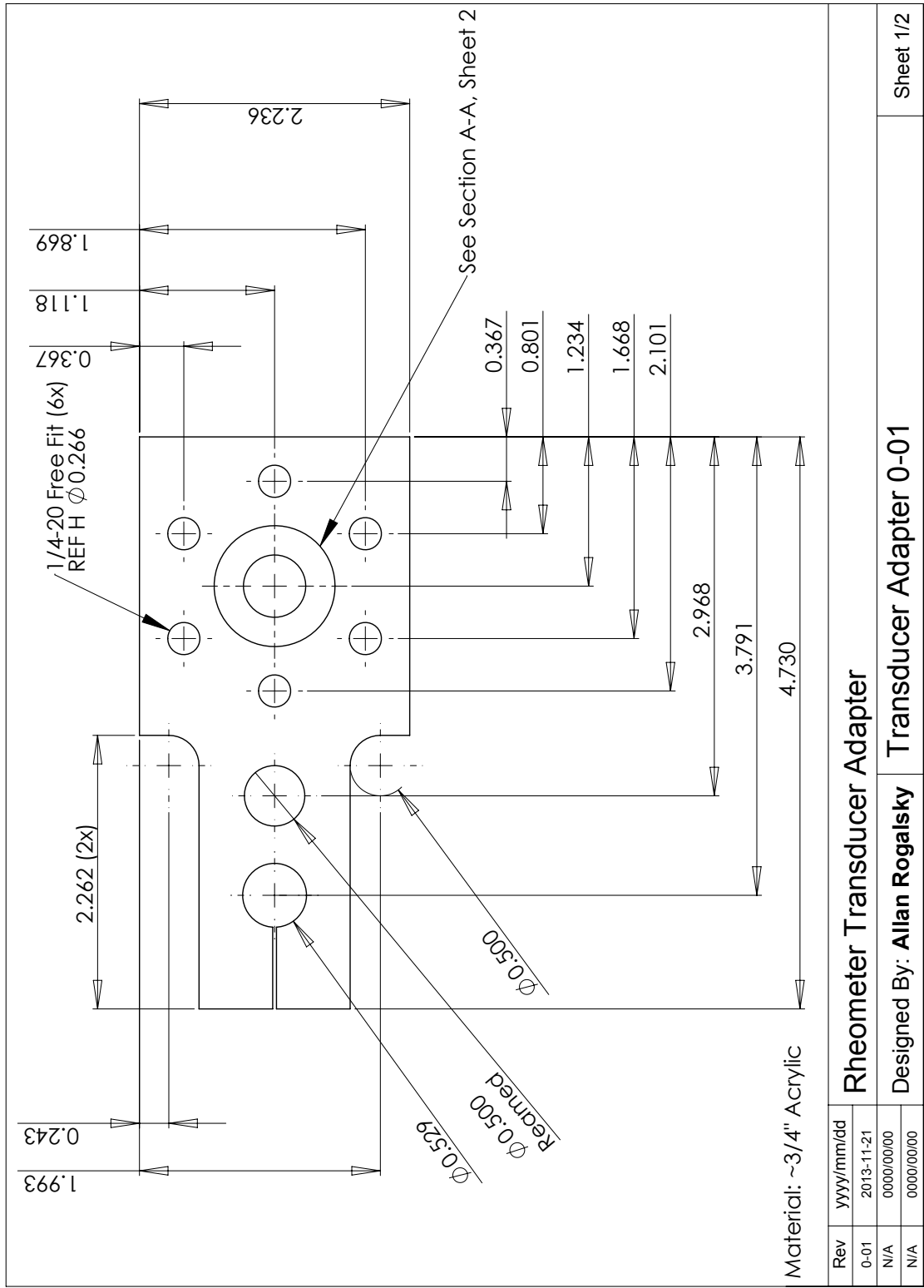
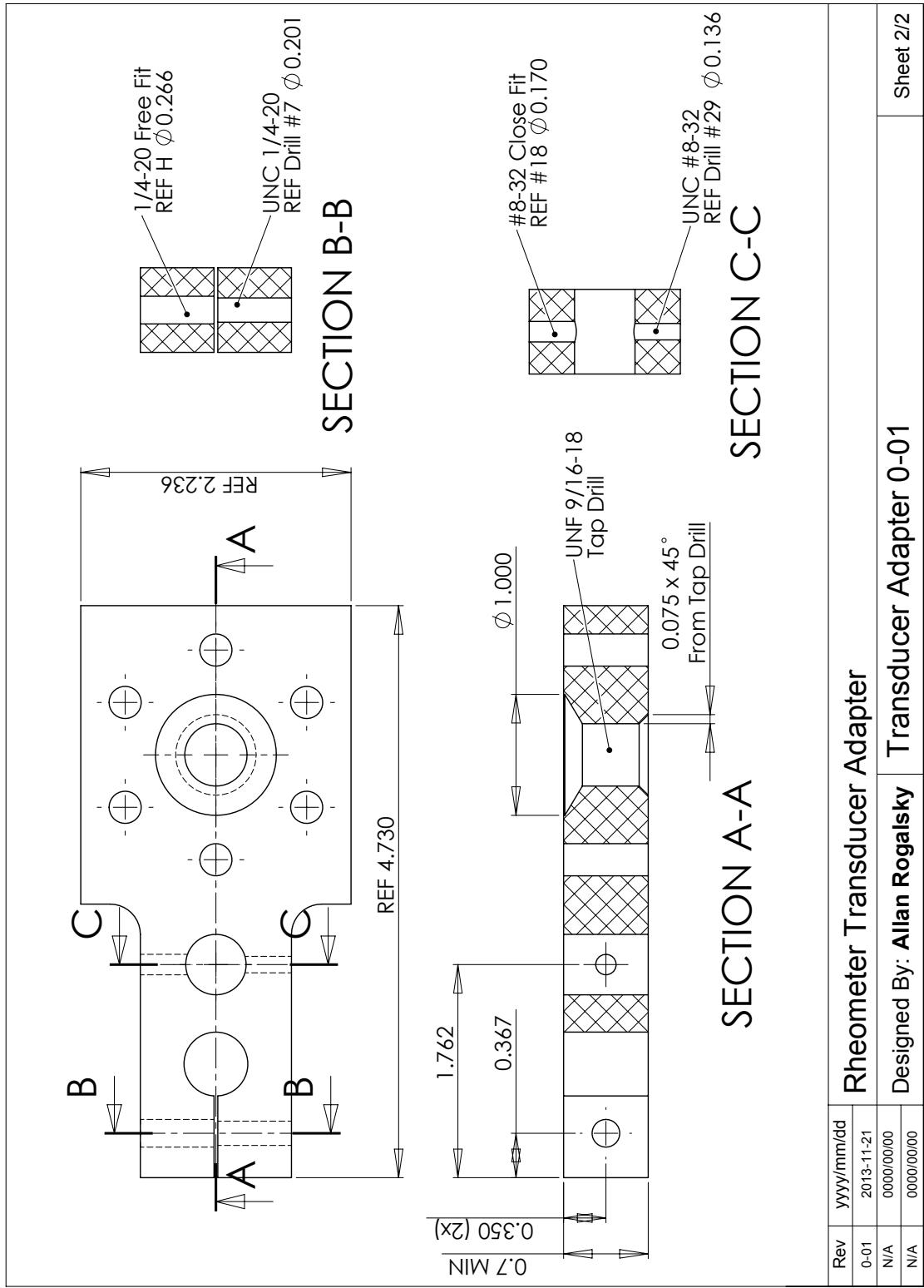


Figure A.5: Capillary Rheometer / Core Assembly / Transducer Adapter / Sheet 1

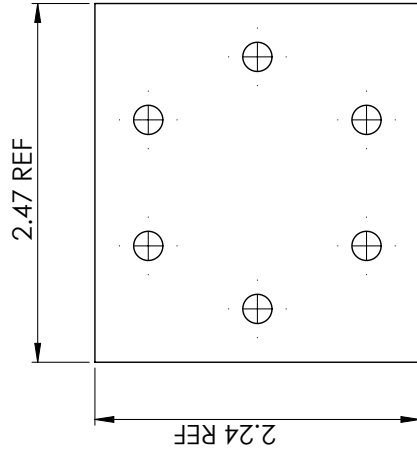


Rheometer Transducer Adapter		Transducer Adapter 0-01		Sheet 2/2
Rev	yyyy/mm/dd			
0-01	2013-11-21			
N/A	0000/00/00			
N/A	0000/00/00			

Figure A.6: Capillary Rheometer / Core Assembly / Transducer Adapter / Sheet 2

Notes:

1. Print drawing full scale and use as template to cut out part
2. Part is to match "Viscometer Core 0-00"



Material: 0.047mm PTFE Film

Rev		yyyy/mm/dd		Rheometer Membrane	
1-00		2013-11-21			
N/A		0000/00/00		Designed By:	Membrane 1-00
N/A		0000/00/00			Sheet 1/1

Figure A.7: Capillary Rheometer / Core Assembly / Membrane

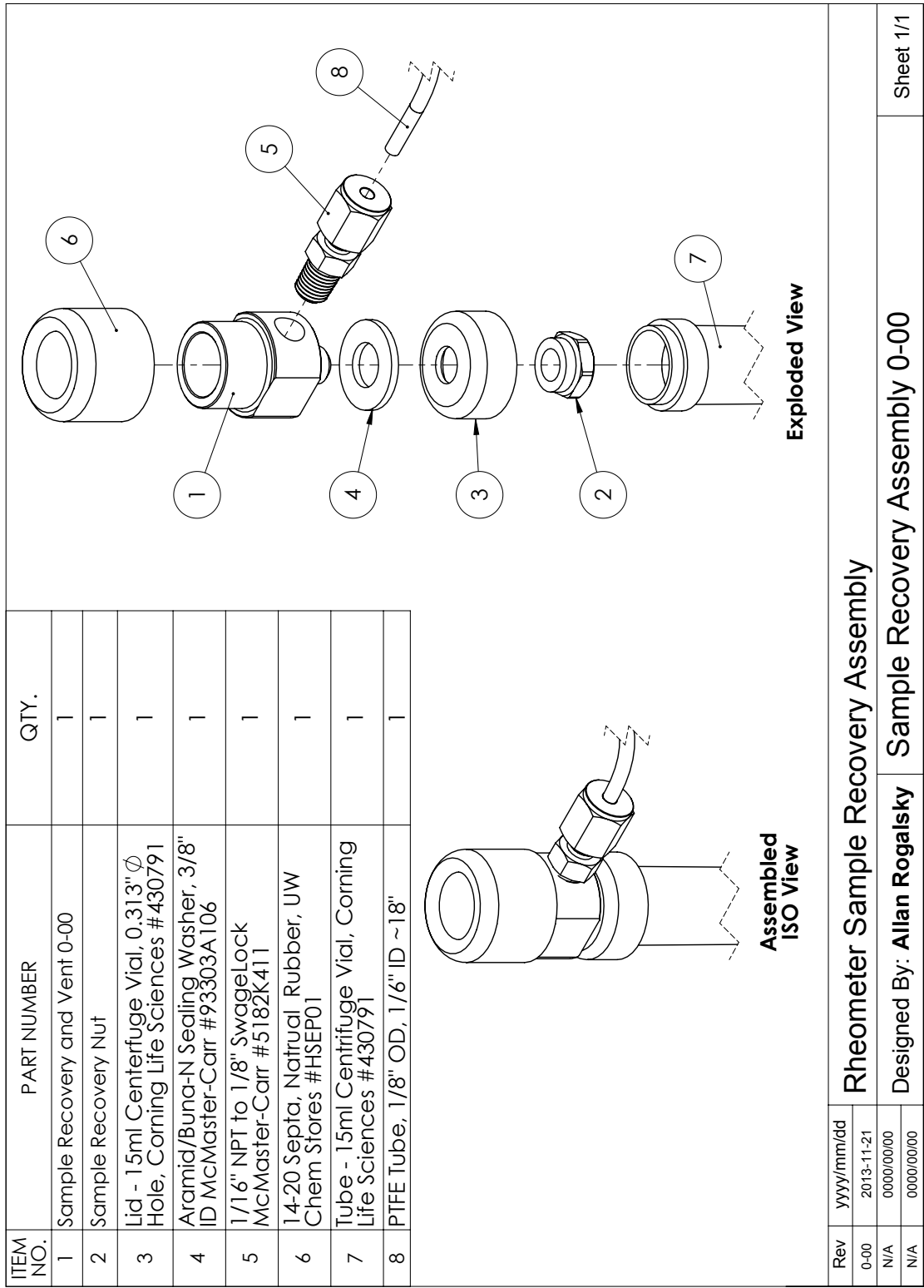


Figure A.8: Capillary Rheometer / Sample Recovery Assembly

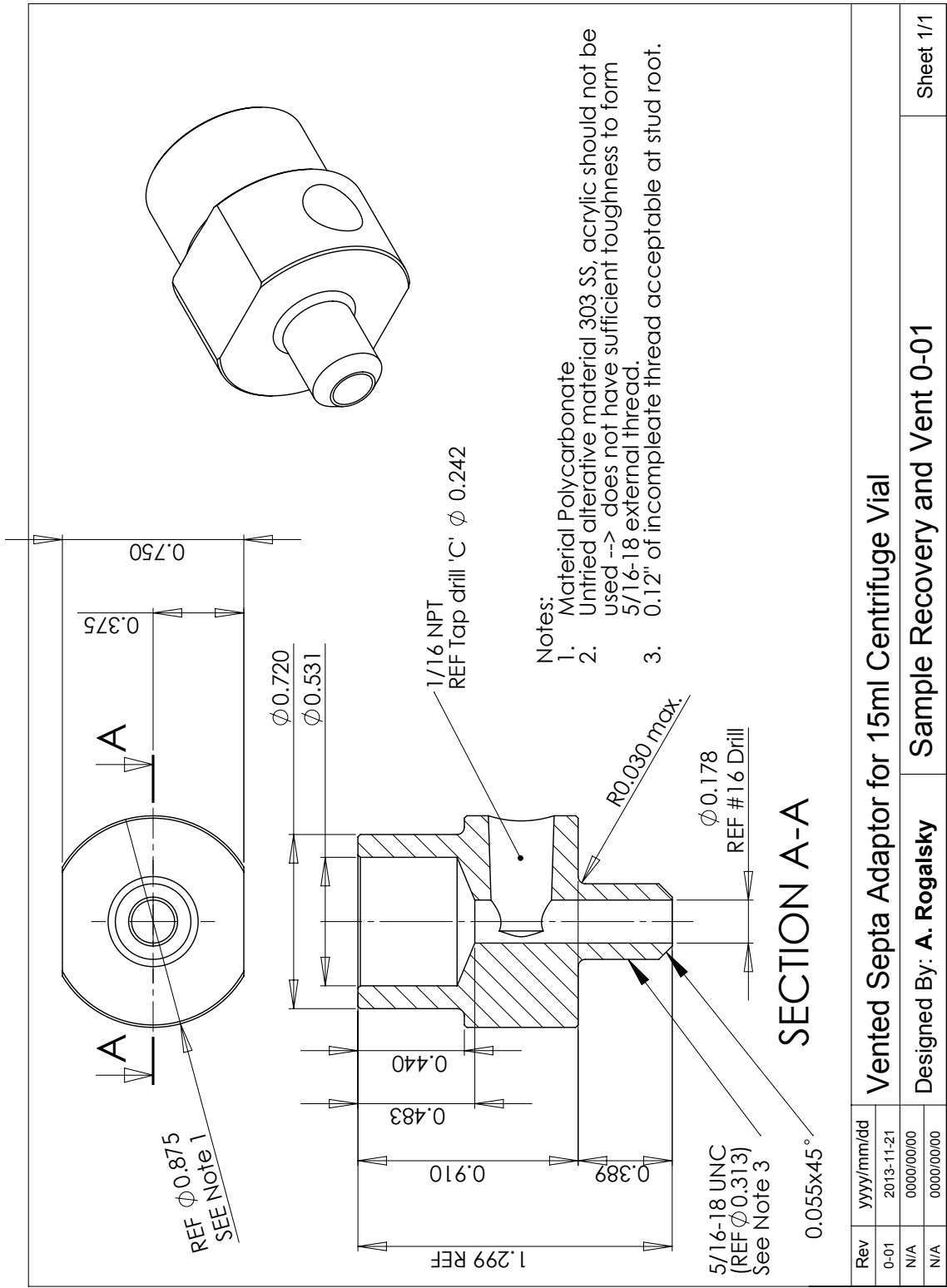


Figure A.9: Capillary Rheometer / Sample Recovery Assembly / Vented Septa Adapter for 15ml Centrifuge Vial

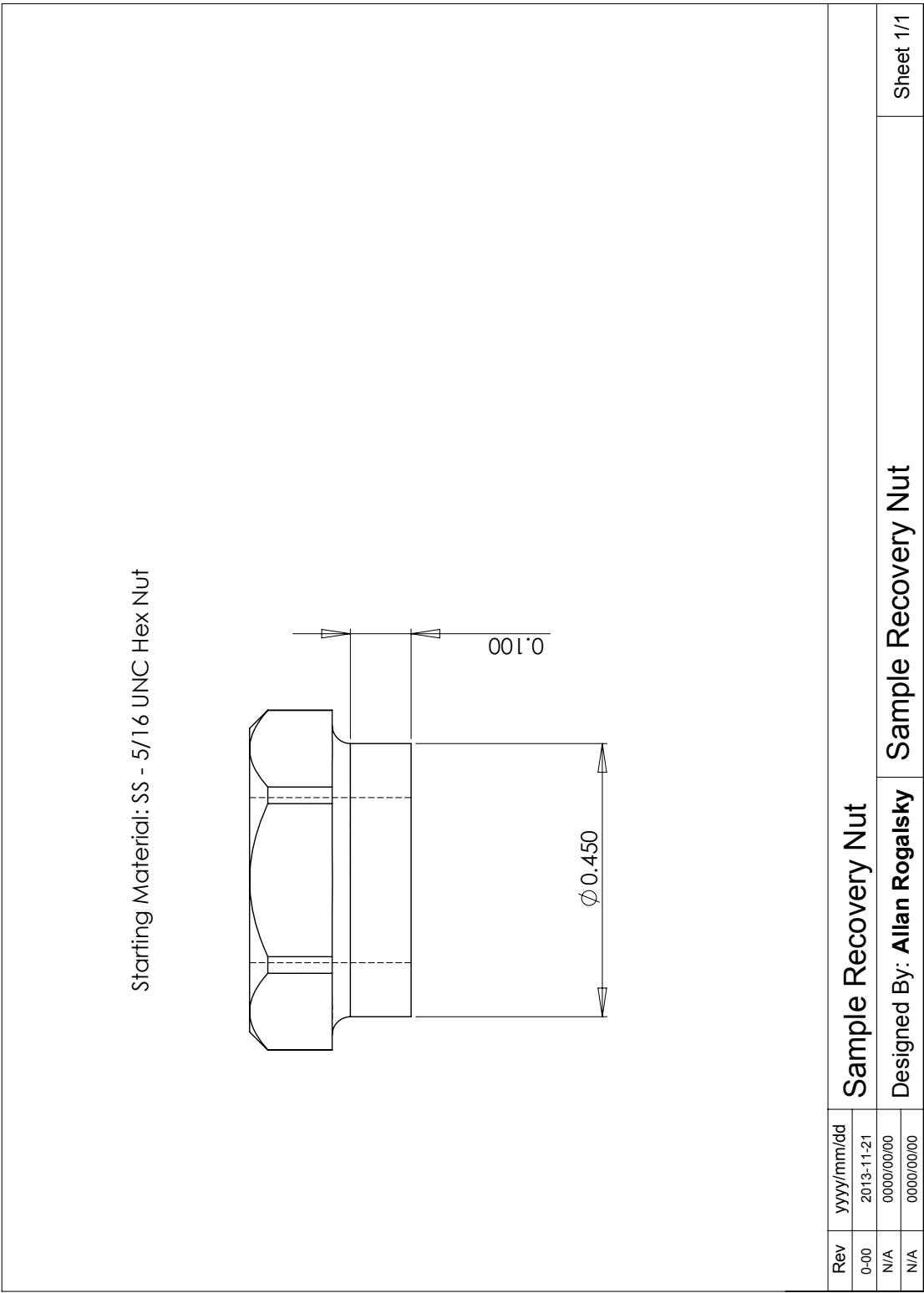


Figure A.10: Capillary Rheometer / Sample Recovery Assembly / Modified Nut for 15ml Centrifuge Vial Lid

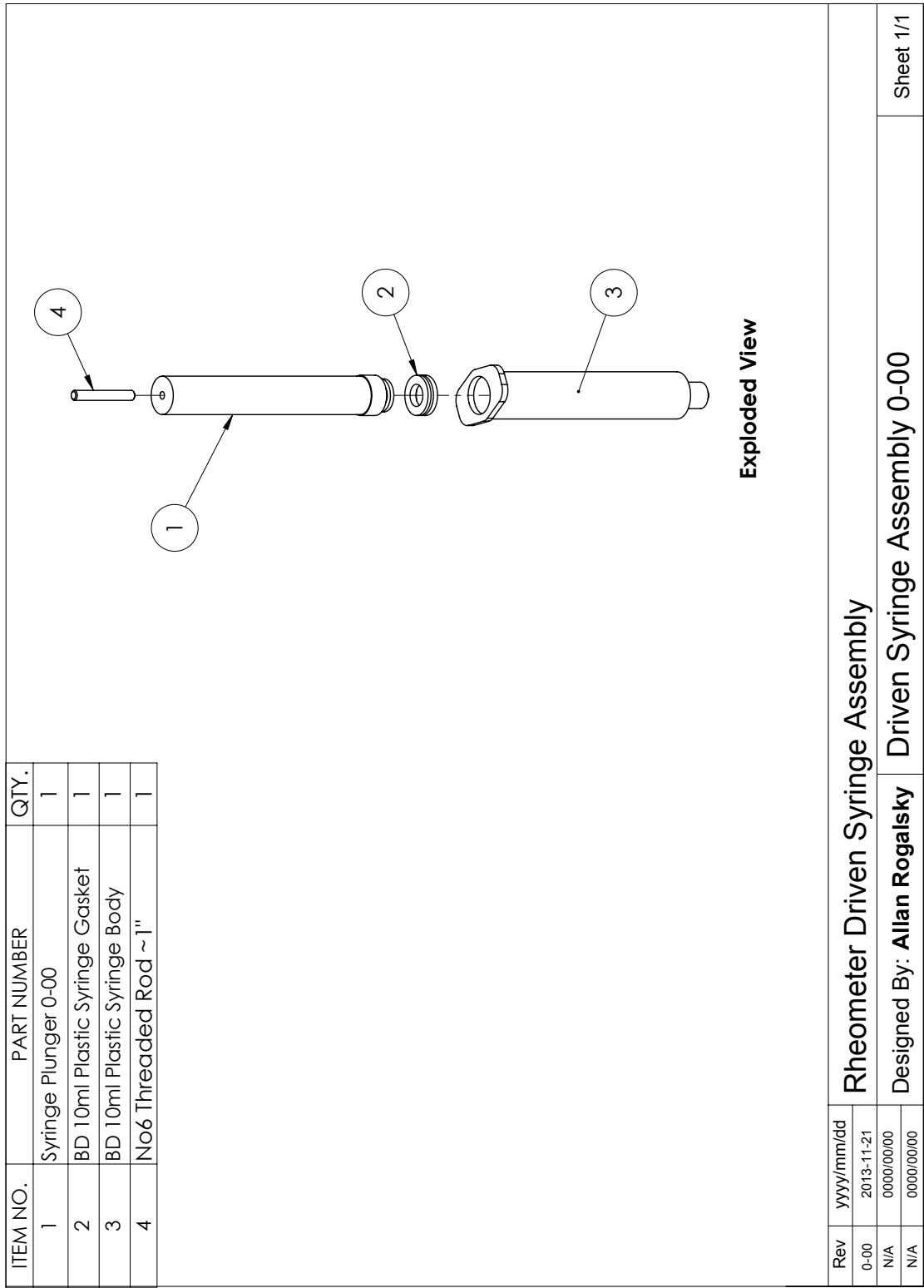


Figure A.11: Capillary Rheometer / Driven Syringe Assembly

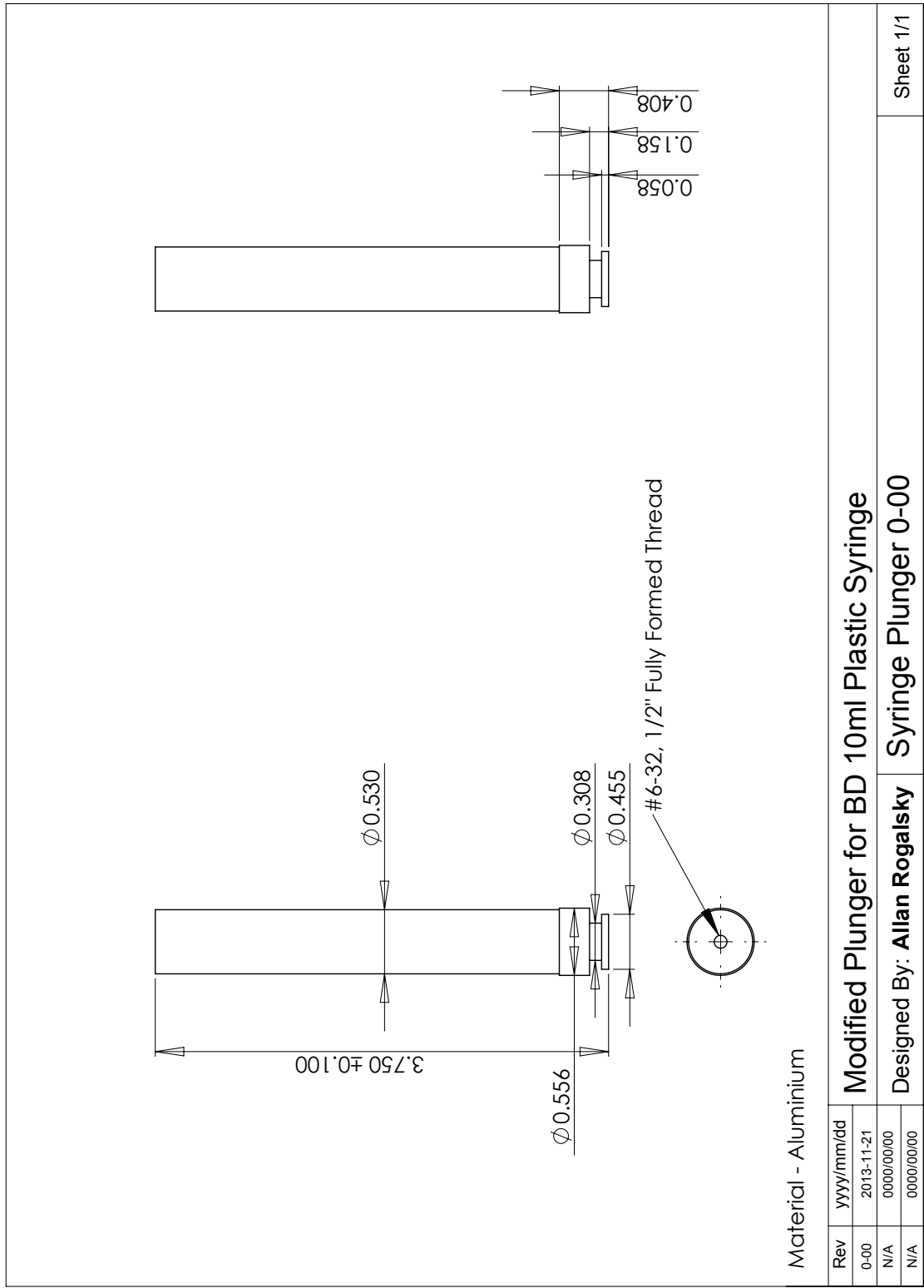


Figure A.12: Capillary Rheometer / Driven Syringe Assembly / Syringe Plunger

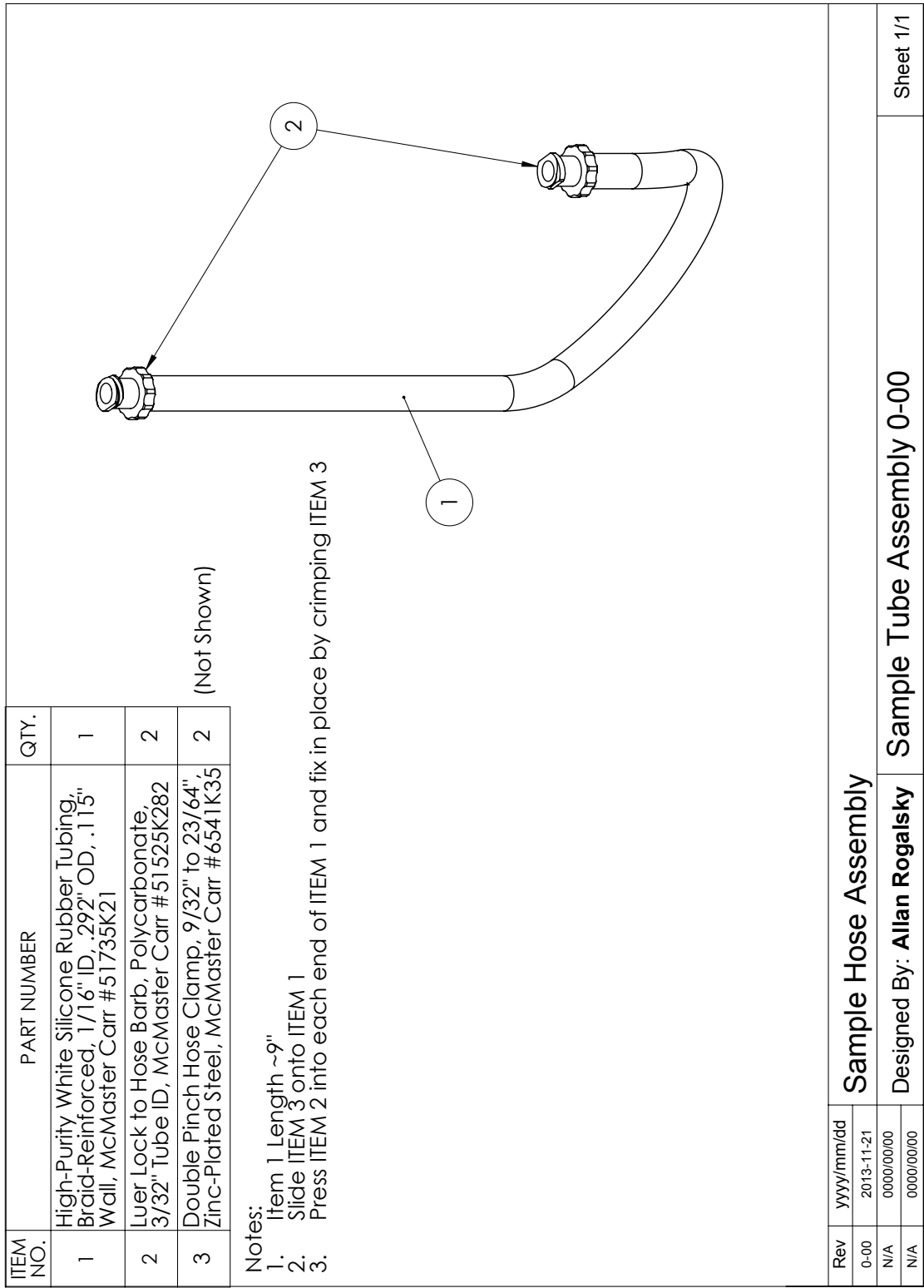


Figure A.13: Capillary Rheometer / Sample Hose Assembly

ITEM NO.	PART NUMBER	QTY.
1	High-Purity White Silicone Rubber Tubing, Braid-Reinforced, 1/16" ID, .292" OD, .115" Wall, McMaster Carr #51735K21	1
2	Luer Lock to Hose Barb, Polycarbonate, 3/32" Tube ID, McMaster Carr #51525K282	2
3	Double Pinch Hose Clamp, 9/32" to 23/64", Zinc-Plated Steel, McMaster Carr #6541K35	2

(Not Shown)

Notes:

1. Item 1 Length ~36"
2. Slide ITEM 3 onto ITEM 1
3. Press ITEM 2 into each end of ITEM 1 and fix in place by crimping ITEM 3

Rev	yyyy/mm/dd	Rheometer Drive Hose Assembly
0-00	2013-11-21	
N/A	0000/00/00	Designed By:
N/A	0000/00/00	Drive Tube Assembly 0-00

Sheet 1/1

Figure A.14: Capillary Rheometer / Drive Hose Assembly

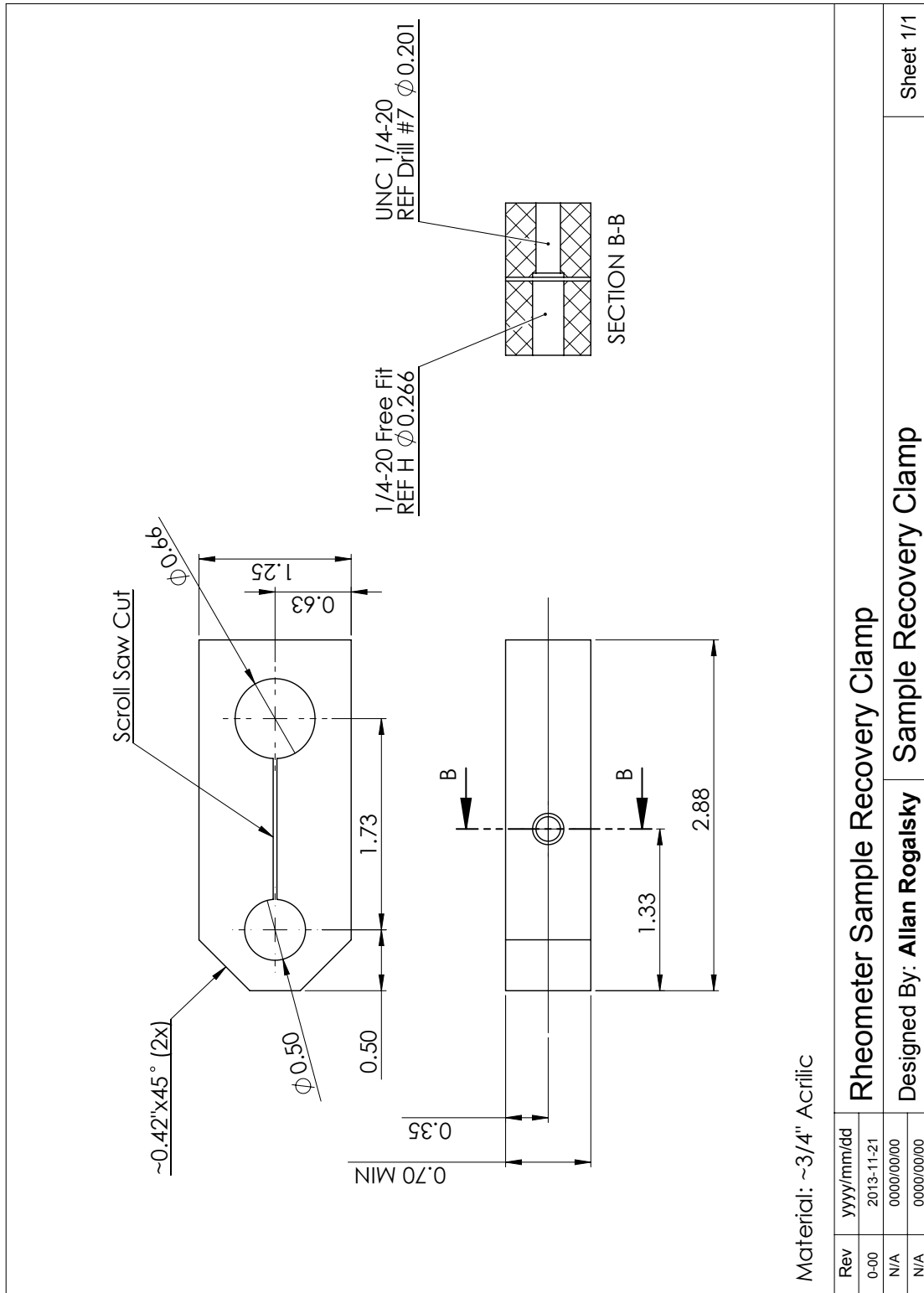


Figure A.15: Capillary Rheometer / Sample Recovery Clamp

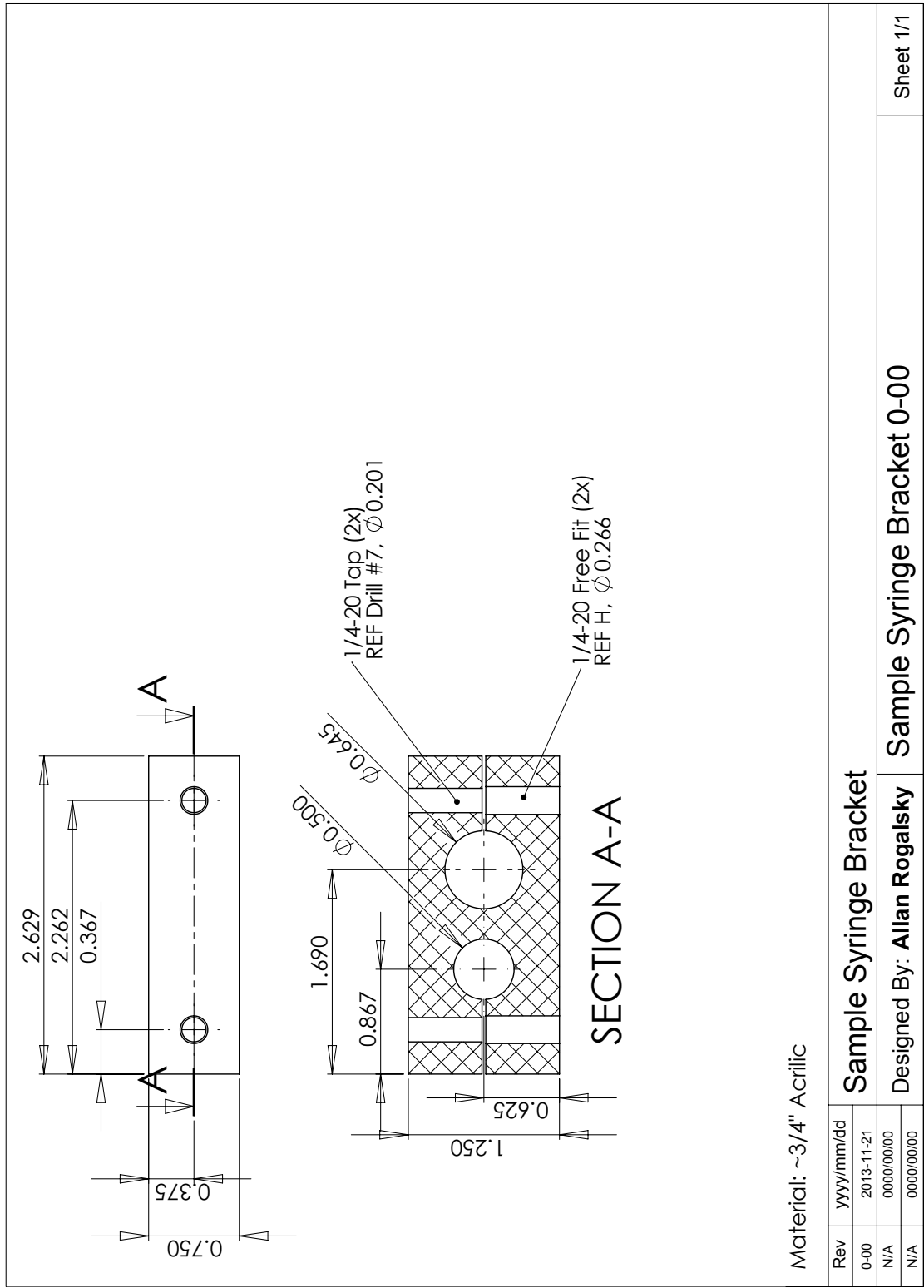


Figure A.16: Capillary Rheometer / Sample Syringe Bracket, Re-purposed to Hold Drive Syringe

Appendix B

Initial Osmometer Design - Fuoss-Mead Variant

B.1 Overview

Credit for the basic operating principals of this design goes Fuoss and Mead [186].

Engineering change tracking used. Missing design numbers represent branch iterations that never became the active design.

(Design 4-0) First viable design - sent to shop for quote.

(Design 4.2) Change of material for membrane backup disk at shop request, finalize design for water-bath - First Part Manufacture

(Design 5.2) Change Core Assembly due to issues with capillary seating (fragile silicone gasket needed mechanical support, titanium fittings added) Backup gasket added to membrane clamp area.

(Design 8.0) Change to cast silicone gaskets from neoprene gaskets - neoprene gaskets transmitted force, silicone gaskets seated in groove. Clamping force now transmitted through polycarbonate stiffening membrane clamping. Change partially necessary due to excessively wide bolt spacing. Design recommendation from Shigley is less than 6 nominal diameters [194] actual bolt spacing is greater than 9 nominal diameters. Could not easily fix because hole pattern is repeated on all parts and would require a complete re-manufacture.

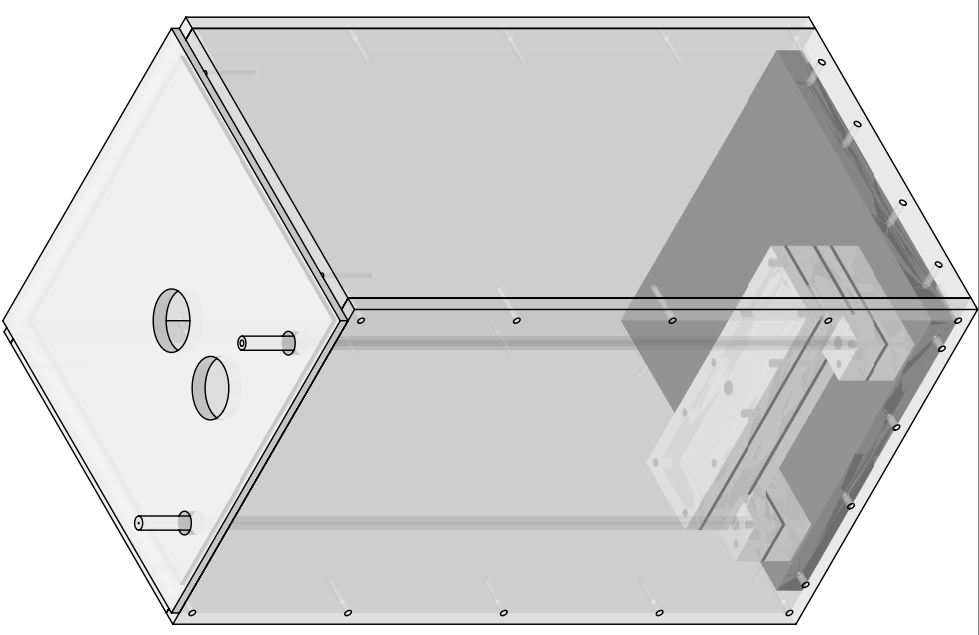
(Design 9.0) Change to solid reference reservoir and glass snorkel - Elimination of last neoprene gaskets further stiffening assembly

B.2 Design 4.0 - Drawings for Shop Quote

ITEM NO.	PART NUMBER	QTY.
1	Waterbath	1
1.1	Waterbath Base	1
1.2	WaterBath-Side	2
1.3	WaterBath-Front	2
2	Lid Design 4	1
3	Spacer Block Design 4	2
4	Spacer Gasket Design 4	2
5	Osmometer Core Design 4	1
5.1	Cap Design 4.3	1
5.2	Capillary Tube	1
5.3	Positioning Tube	1
6	Membrain Design 4	1
7	Backup Disk Design 4	1
8	Gasket Design 4.1	2
9	Reservoir Design 4.1	1
10	Reservoir Lid Design 4	1

Notes:

1. Please provide price estimate for manufacture of this assembly
2. Highlight any possible problems in manufacturing (In particular see item NO: 5)
3. Do not start manufacture until quote has been approved



Rev	yyyy/mm/dd	Design 4 Top Level Assembly
04-0	2011-09-26	
N/A	0000/00/00	
N/A	0000/00/00	

Designed By: Allan Rogalsky	Design 4 Assembly	Sheet 1/1
-----------------------------	-------------------	-----------

Figure B.1: Osmometer Top Level 4.0

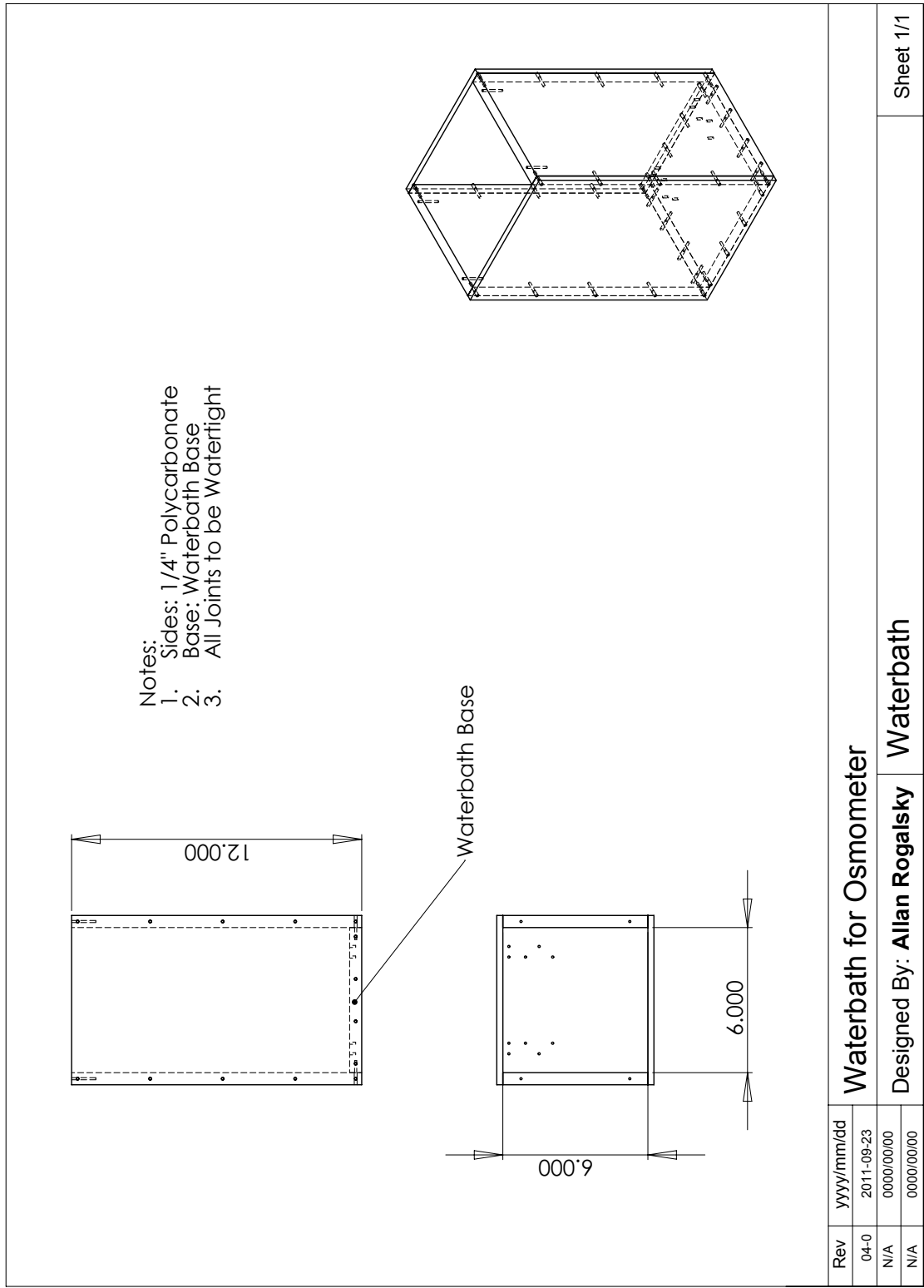


Figure B.2: Osmometer Top Level 4.0 / Waterbath Assembly

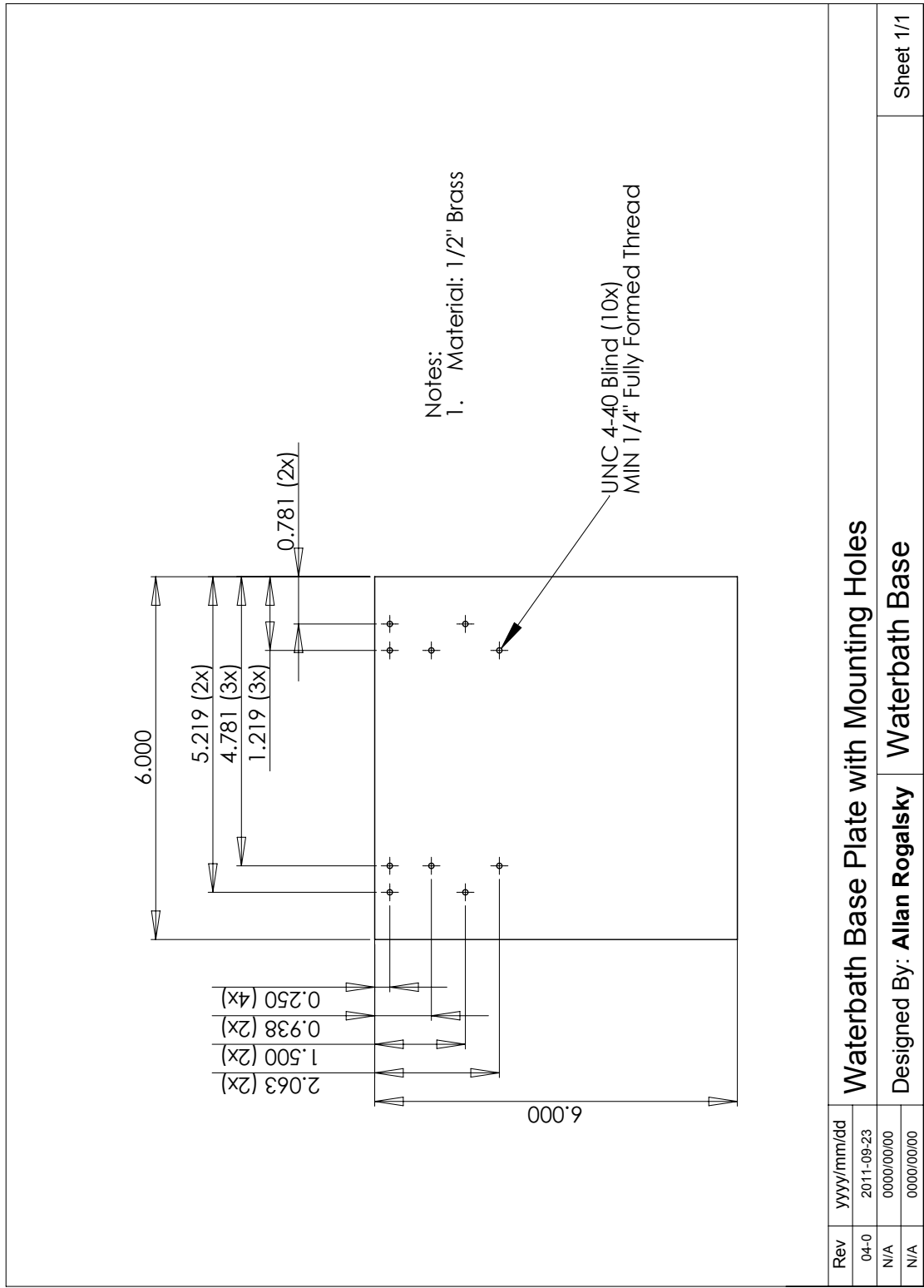


Figure B.3: Osmometer Top Level 4.0 / Waterbath Assembly / Waterbath Base

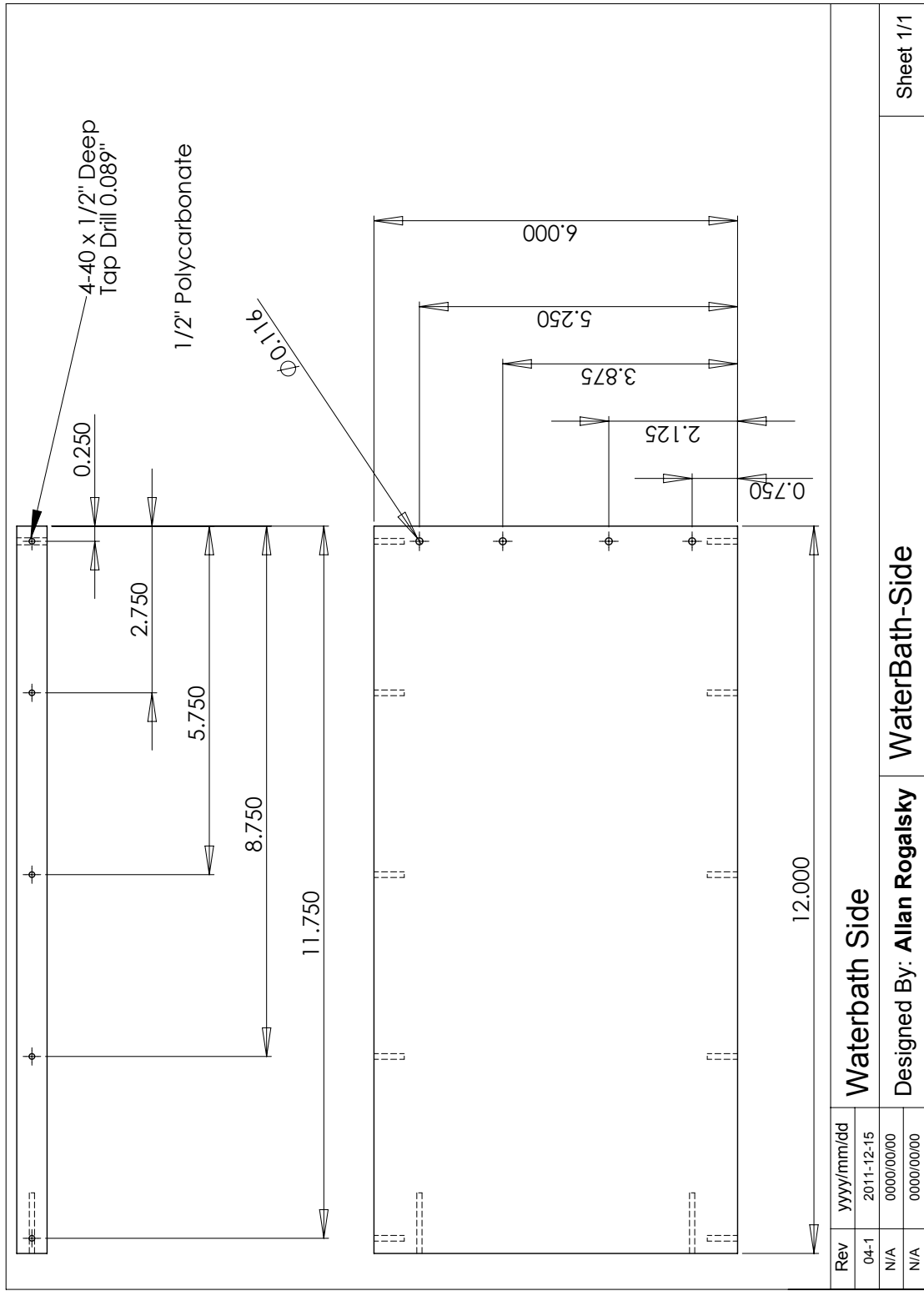


Figure B.4: Osmometer Top Level 4.0 / Waterbath Assembly / Waterbath Side

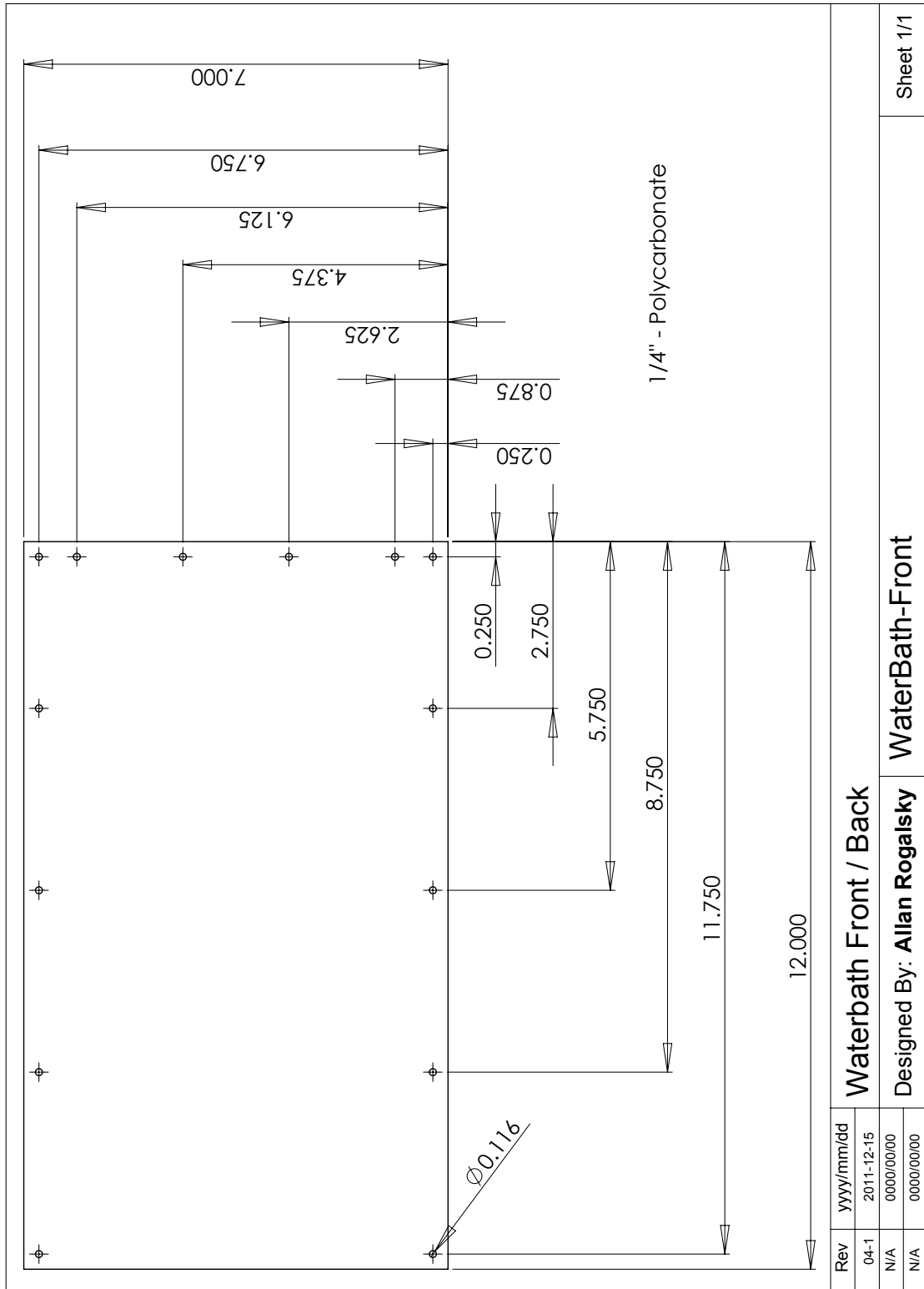


Figure B.5: Osmometer Top Level 4.0 / Waterbath Assembly / Waterbath Front

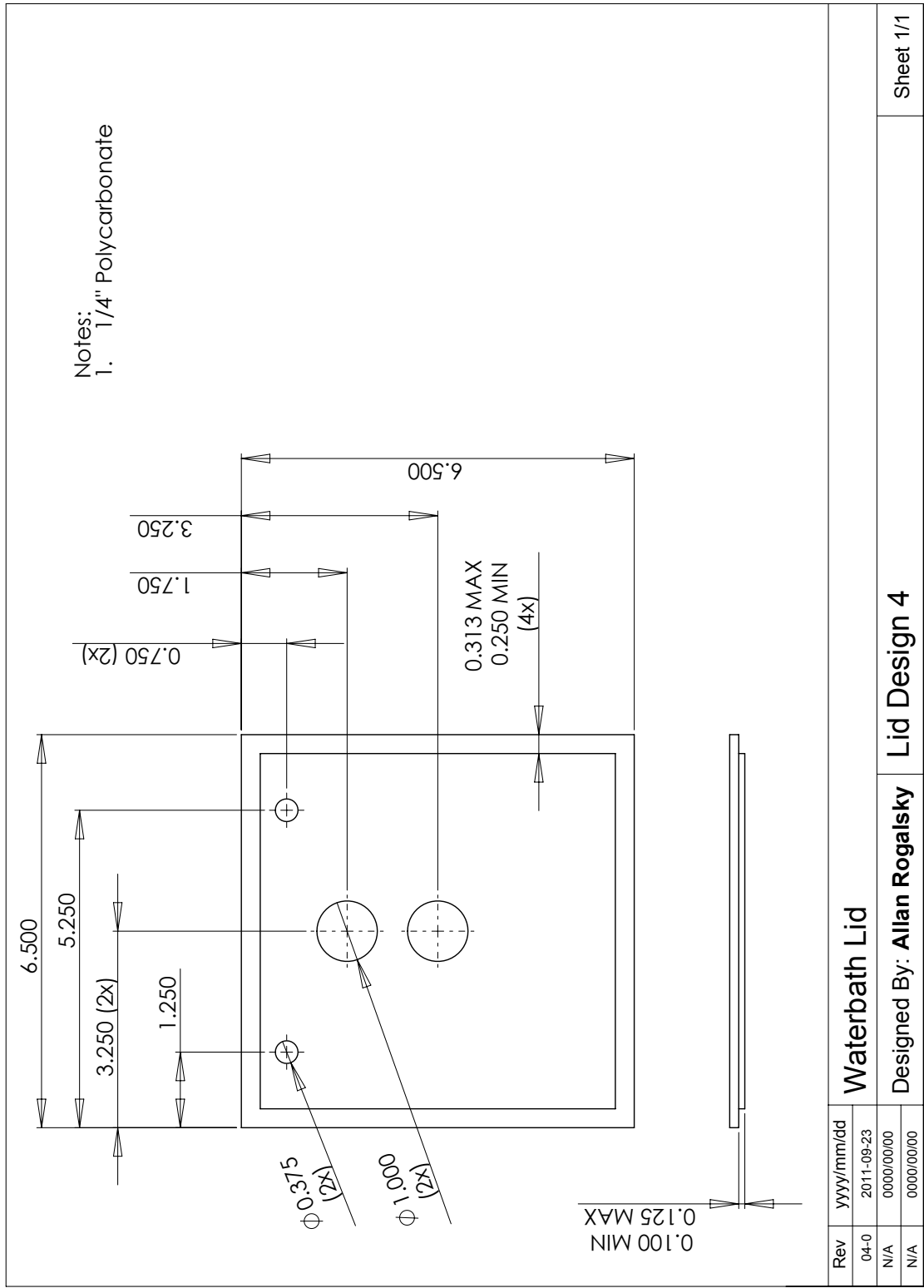


Figure B.6: Osmometer Top Level 4.0 / Waterbath Lid

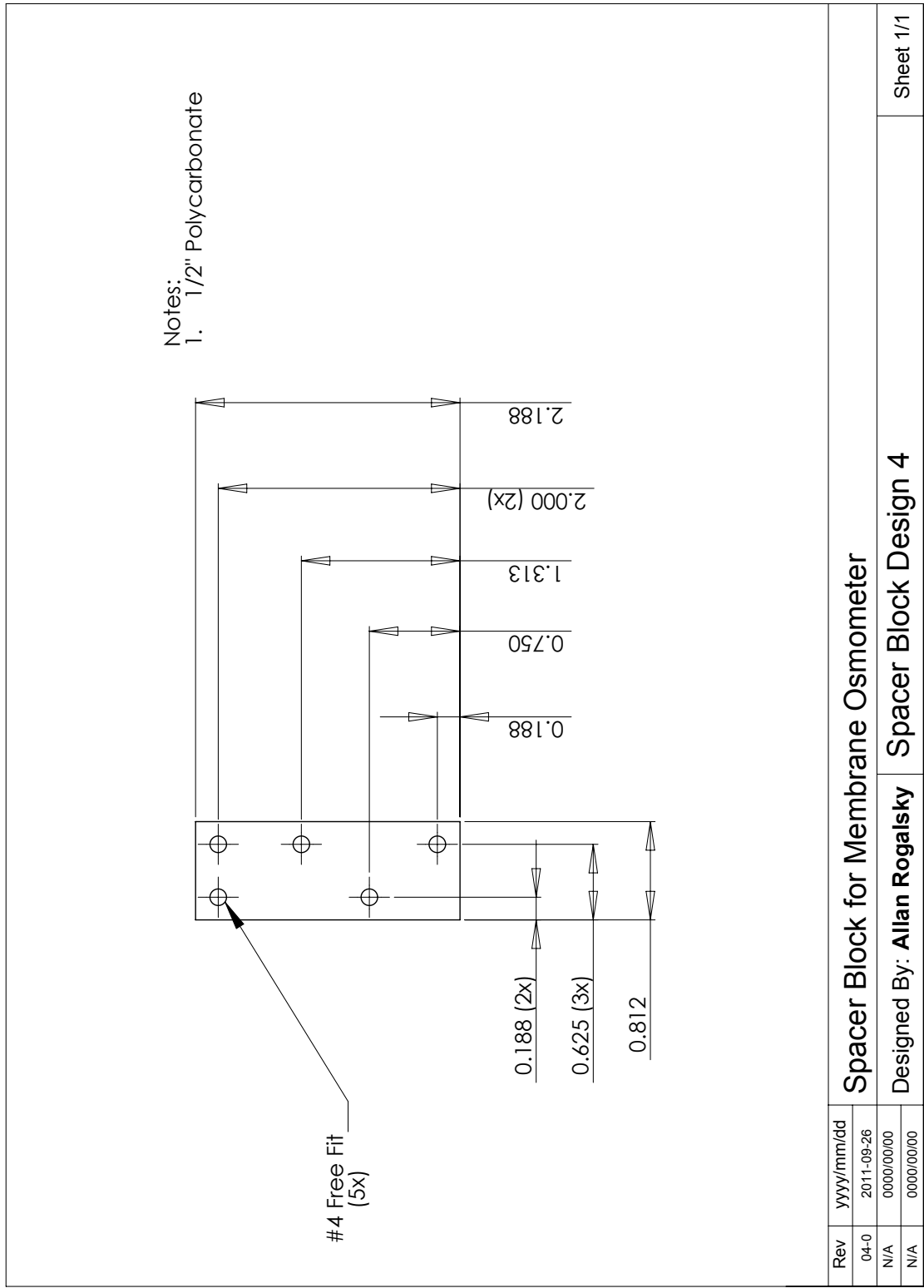


Figure B.7: Osmometer Top Level 4.0 / Spacer Block

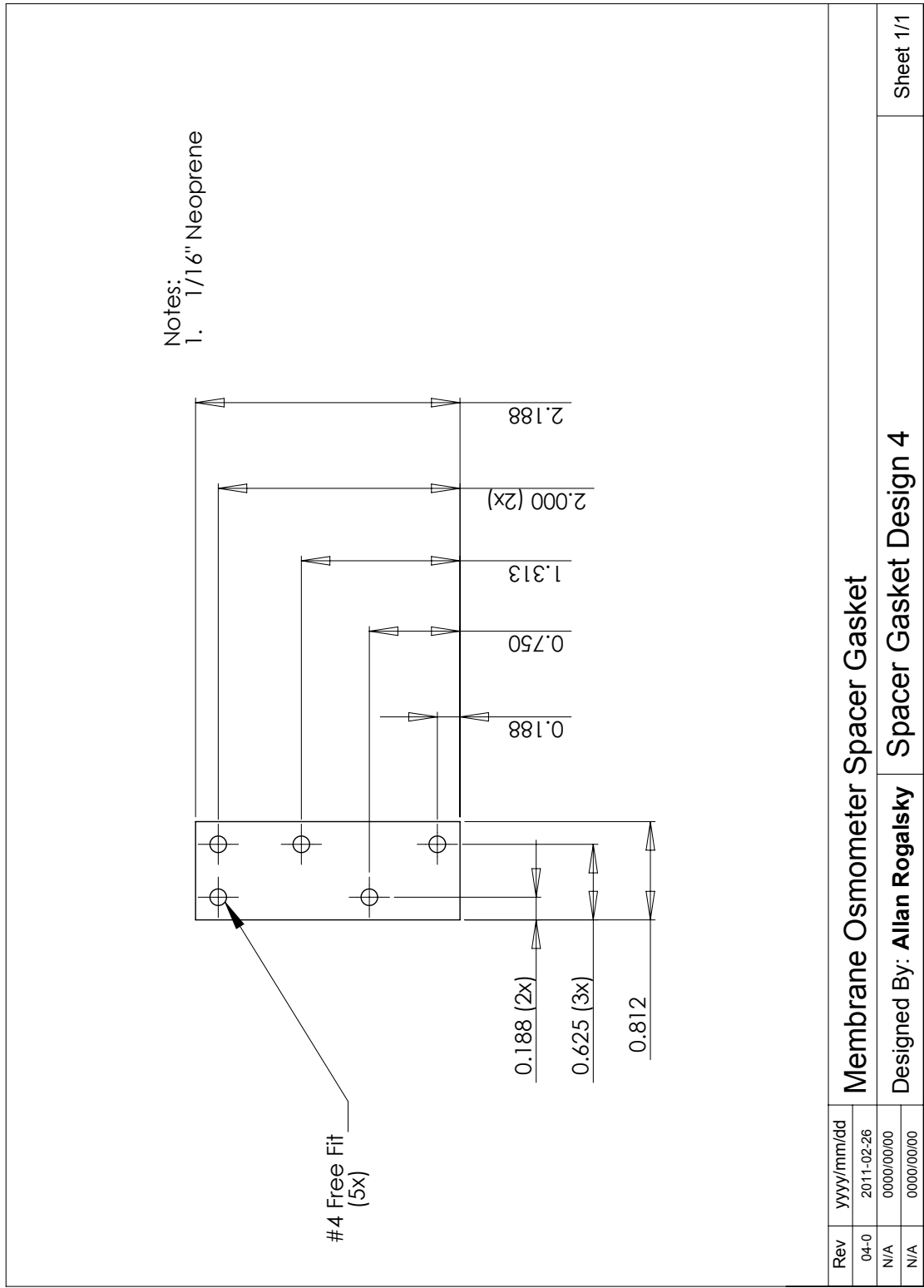


Figure B.8: Osmometer Top Level 4.0 / Spacer Gasket

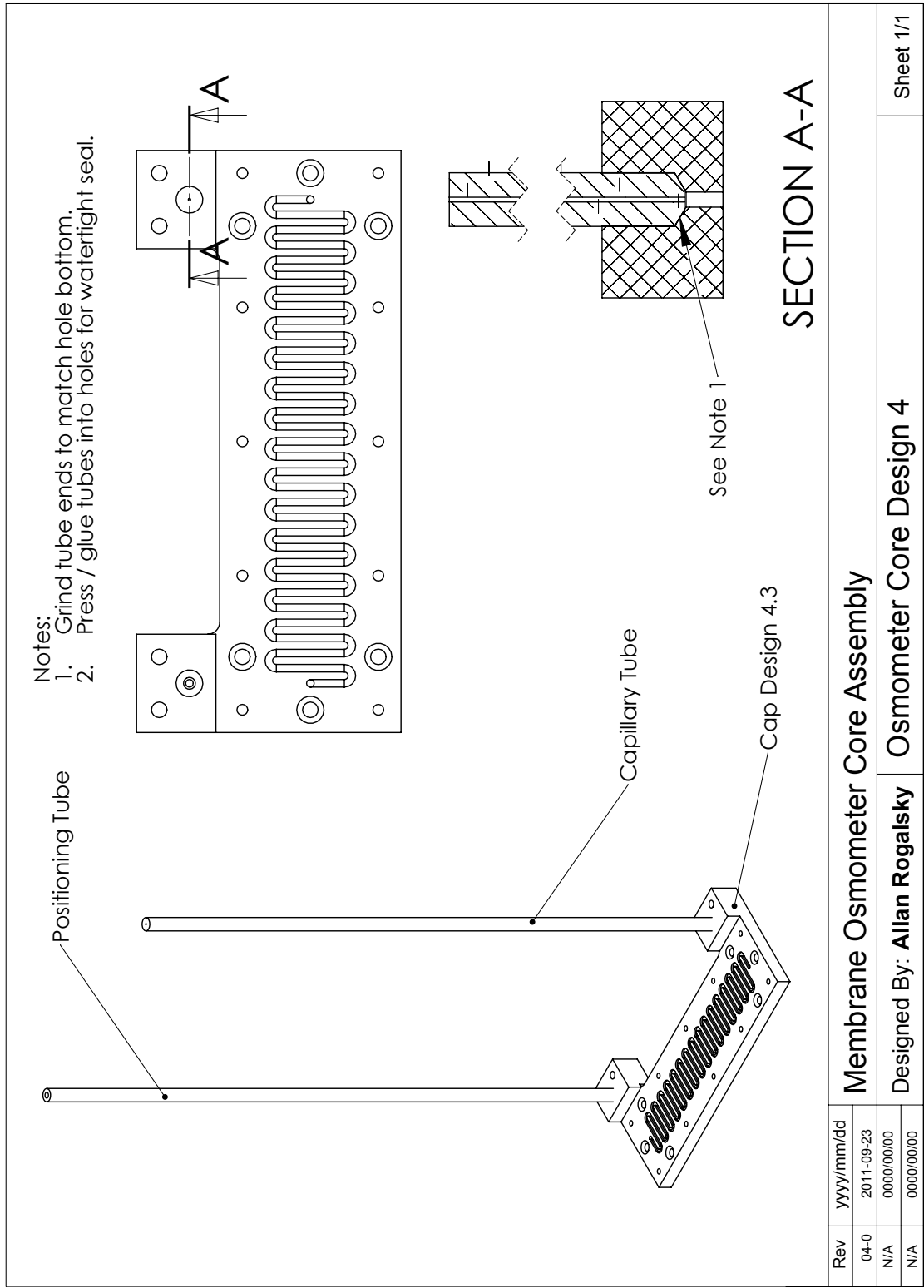


Figure B.9: Osmometer Top Level 4.0 / Core Assembly

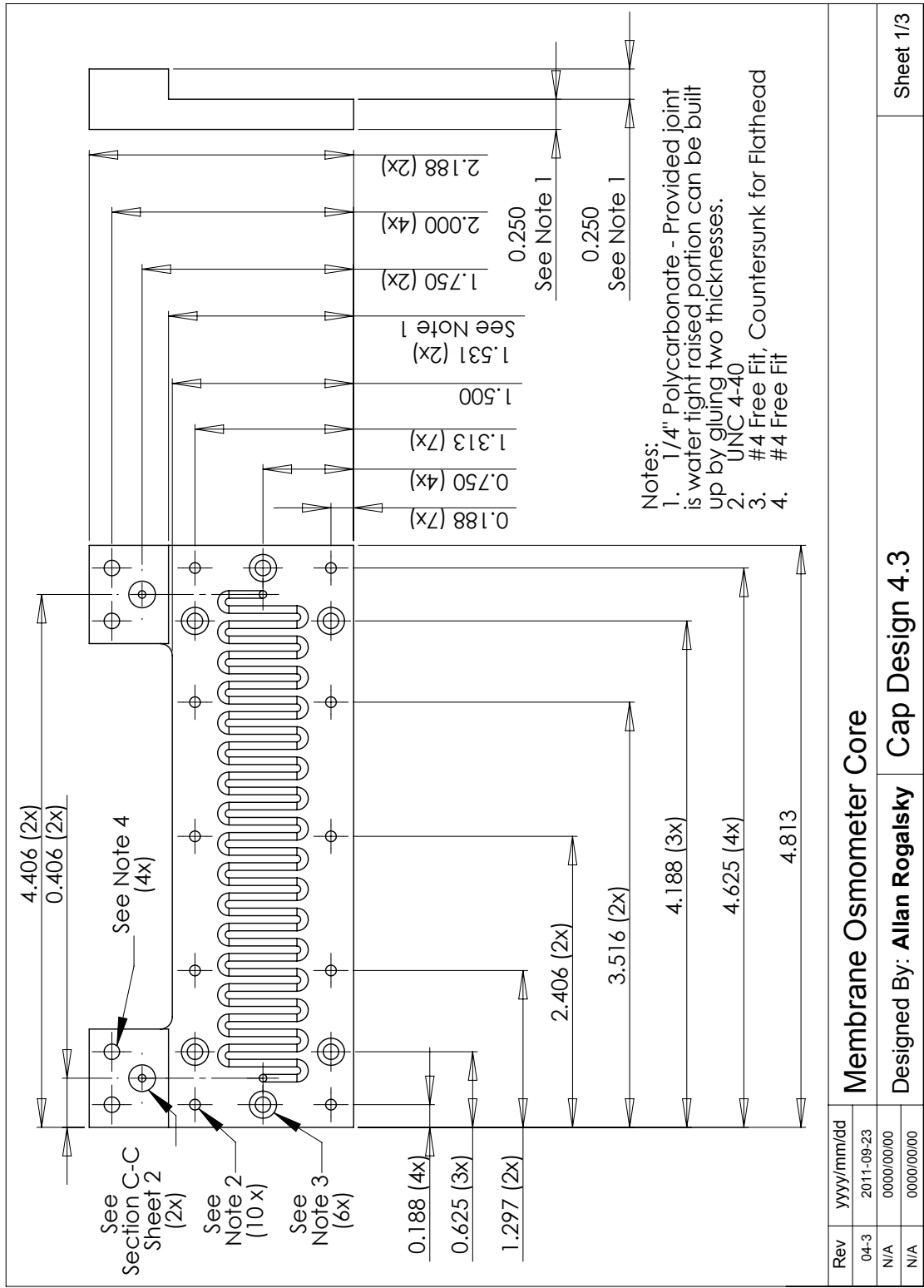


Figure B.10: Osmometer Top Level 4.0 / Core Assembly / Cap / Sheet 1

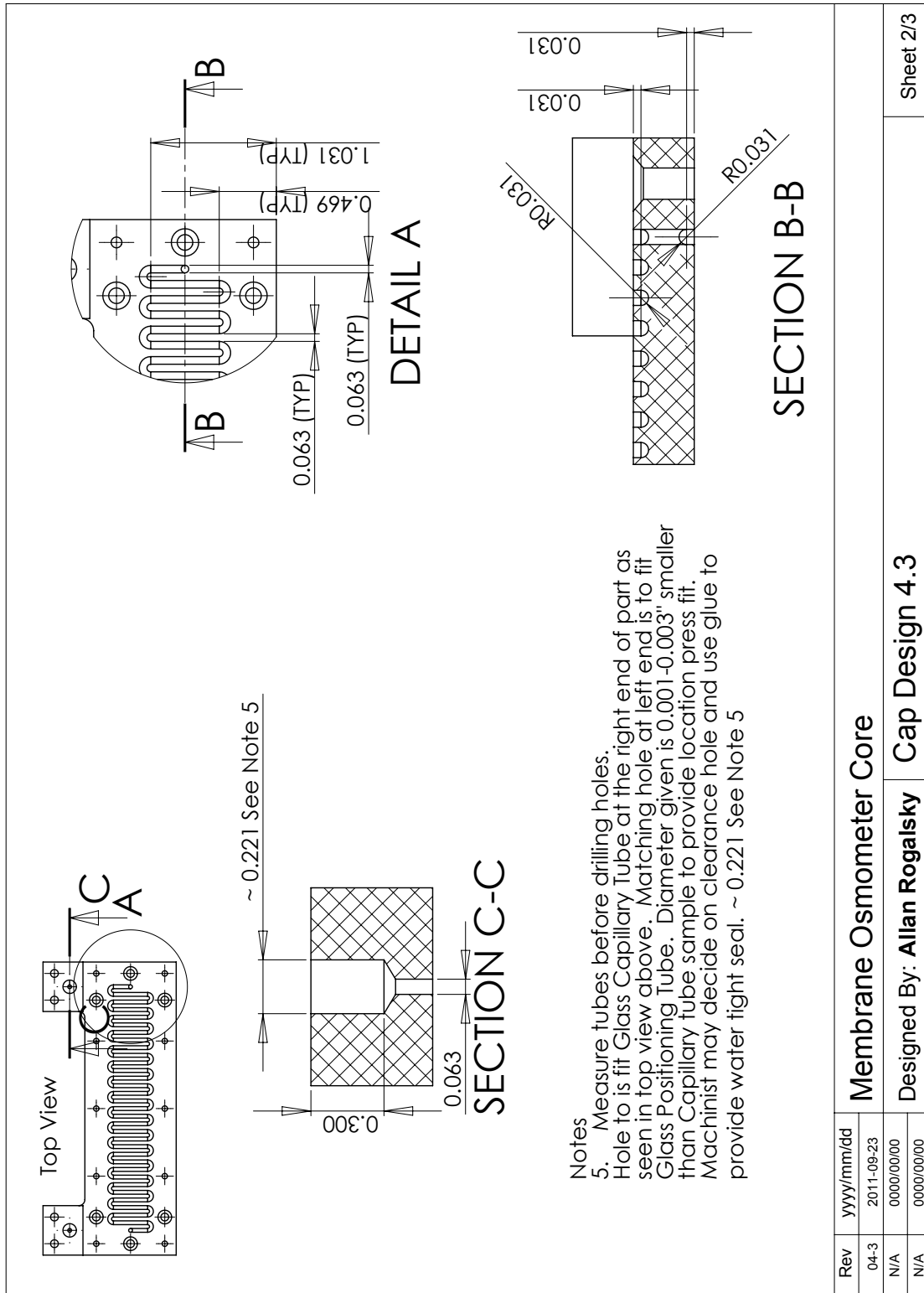


Figure B.11: Osmometer Top Level 4.0 / Core Assembly / Cap / Sheet 2

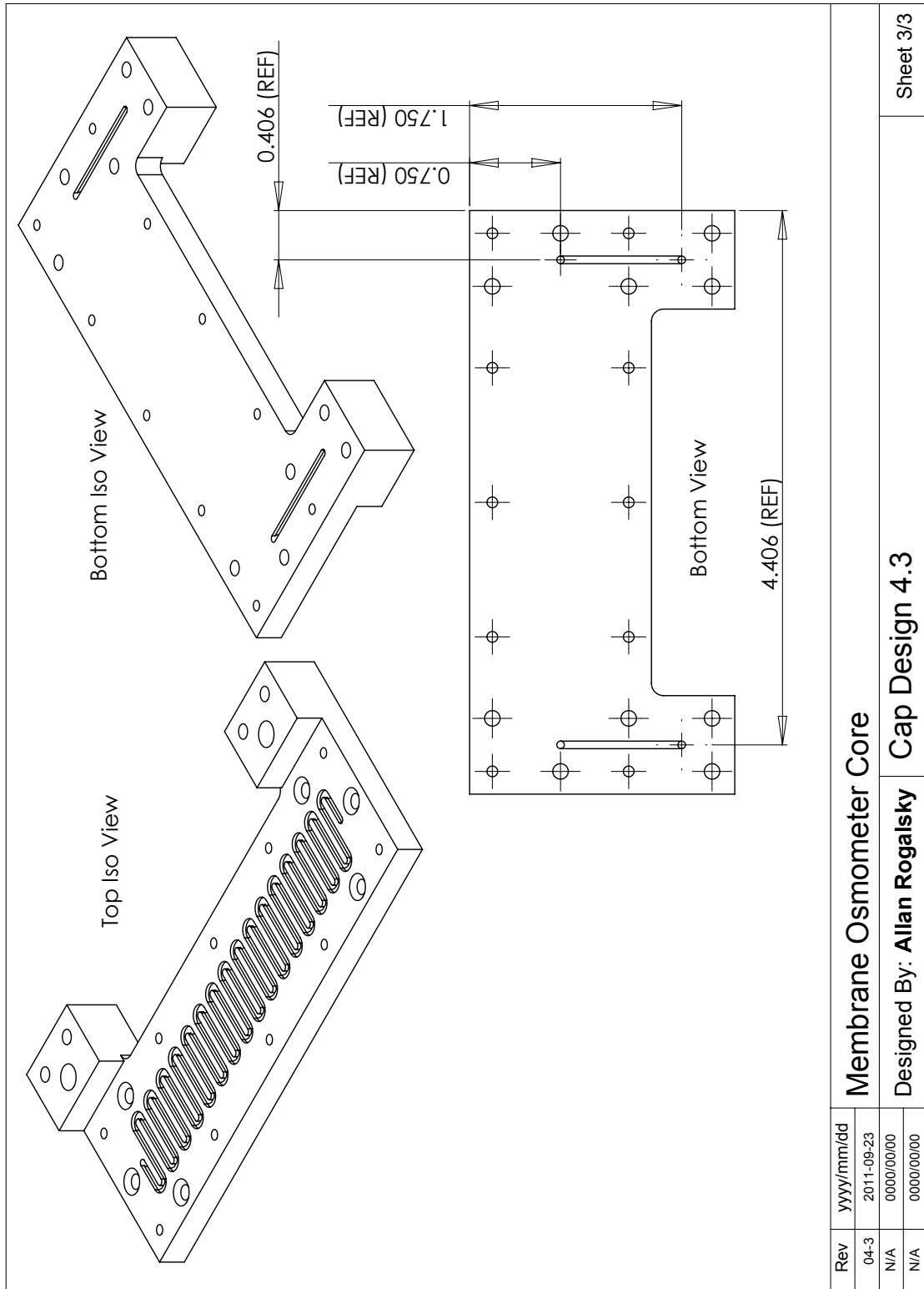


Figure B.12: Osmometer Top Level 4.0 / Core Assembly / Cap / Sheet 3

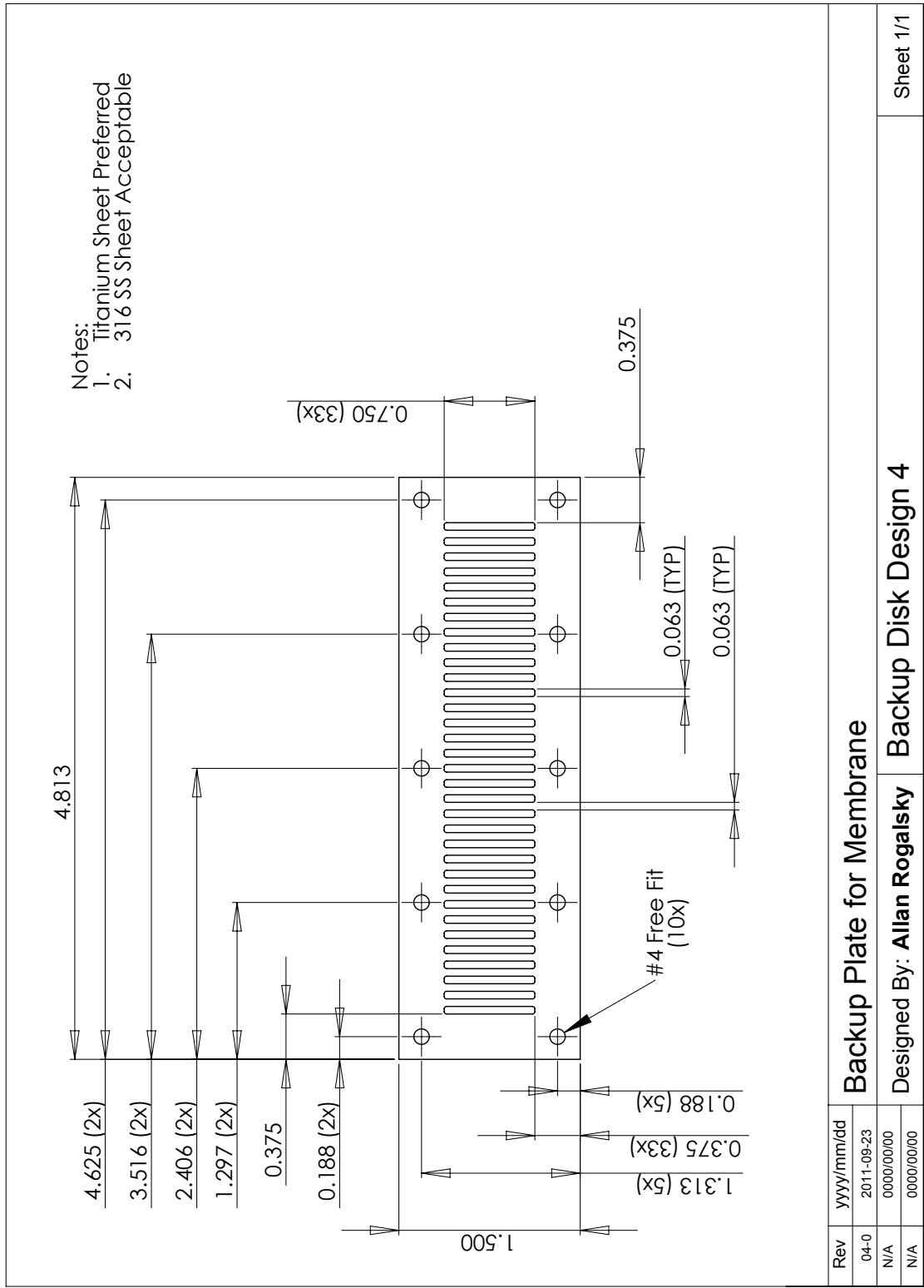


Figure B.13: Osmometer Top Level 4.0 / Backup Disk

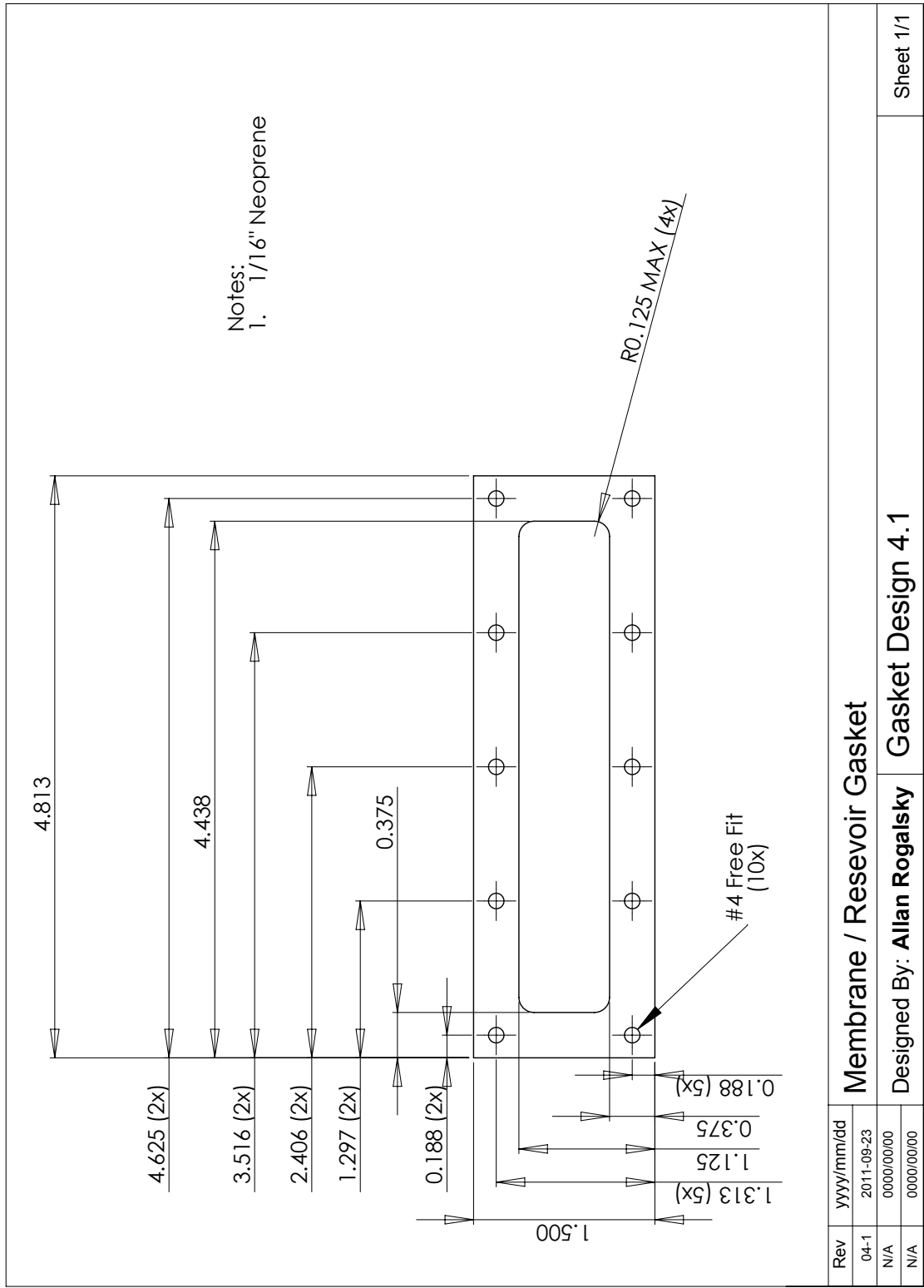


Figure B.14: Osmometer Top Level 4.0 / Gasket

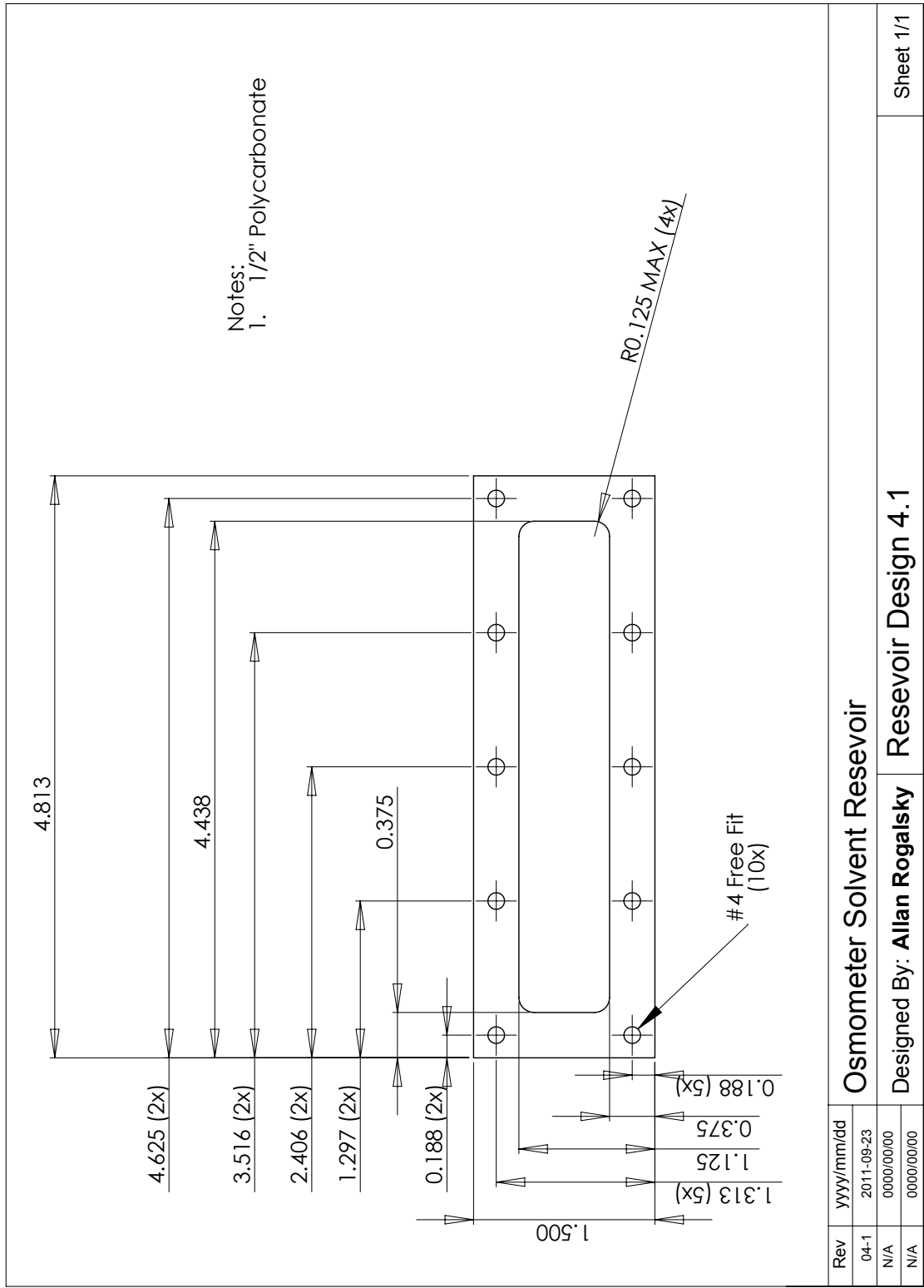


Figure B.15: Osmometer Top Level 4.0 / Reservoir

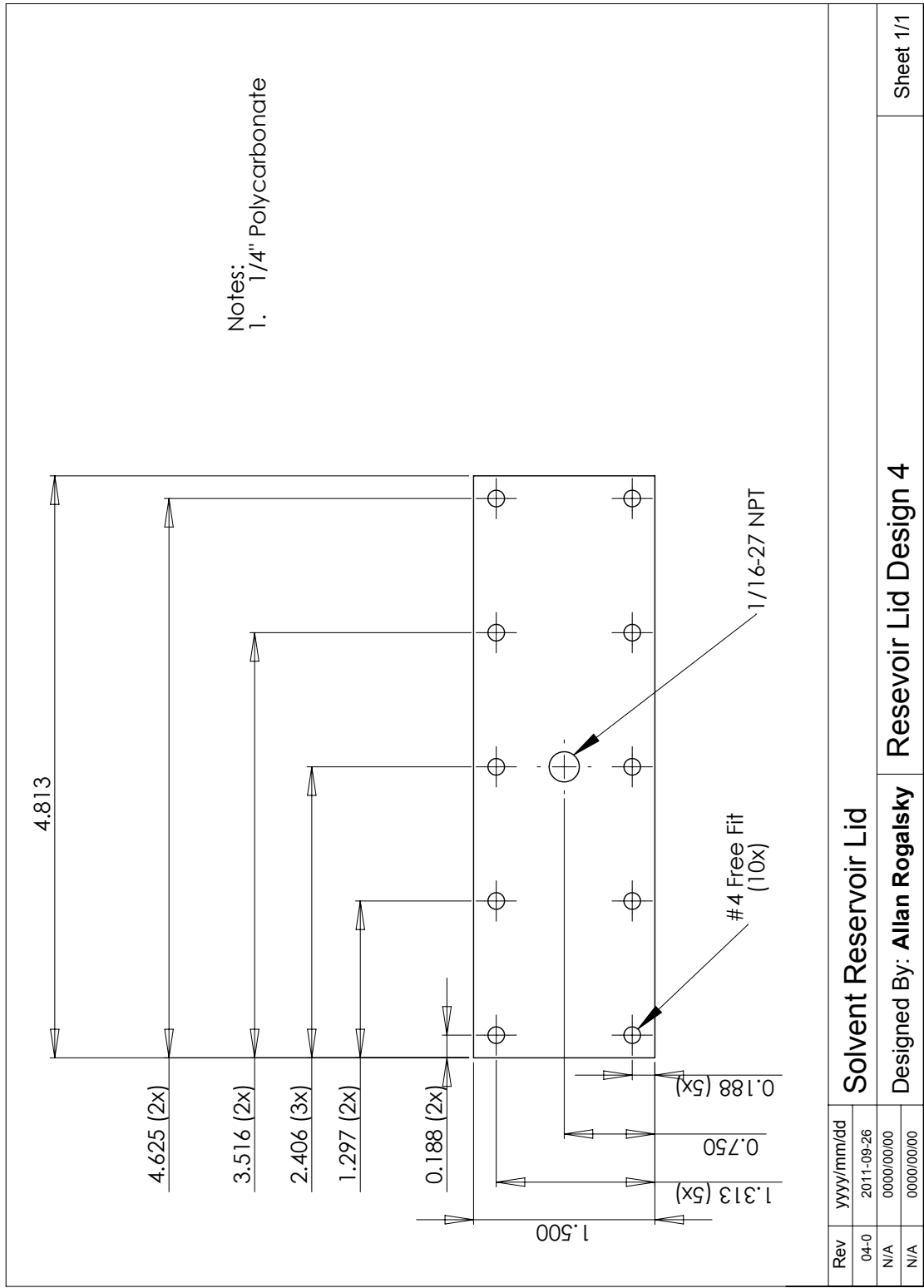


Figure B.16: Osmometer Top Level 4.0 / Reservoir Lid

B.3 Design 4.2 - Changes For First Part Manufacture

Change Top Level Assembly 4.2 was 4.0

In Top Level Assembly 4.2

Change Water-bath Base 4.1 was 4.0

Change Backup Disk 4.2 was 4.0

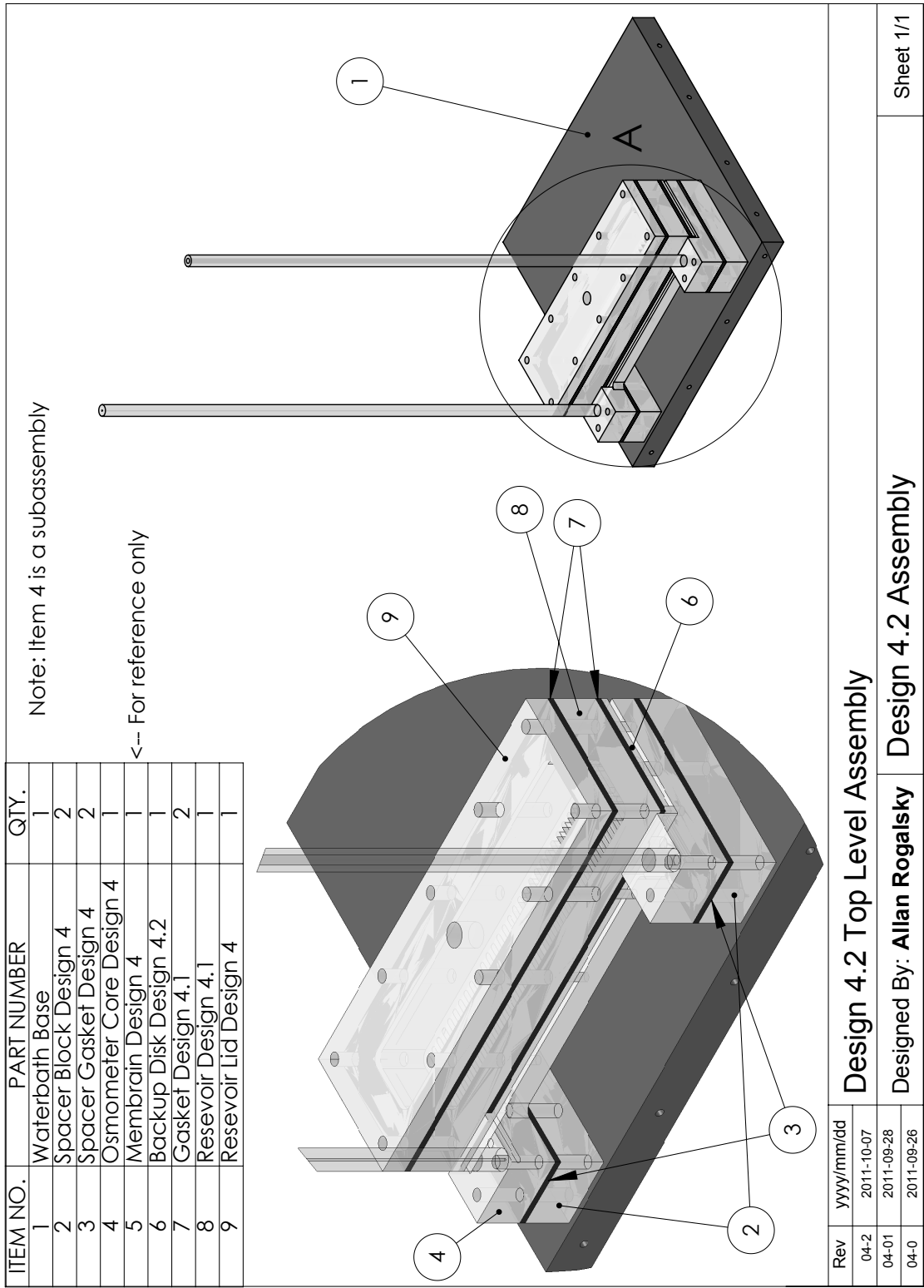


Figure B.17: Osmometer Top Level 4.2

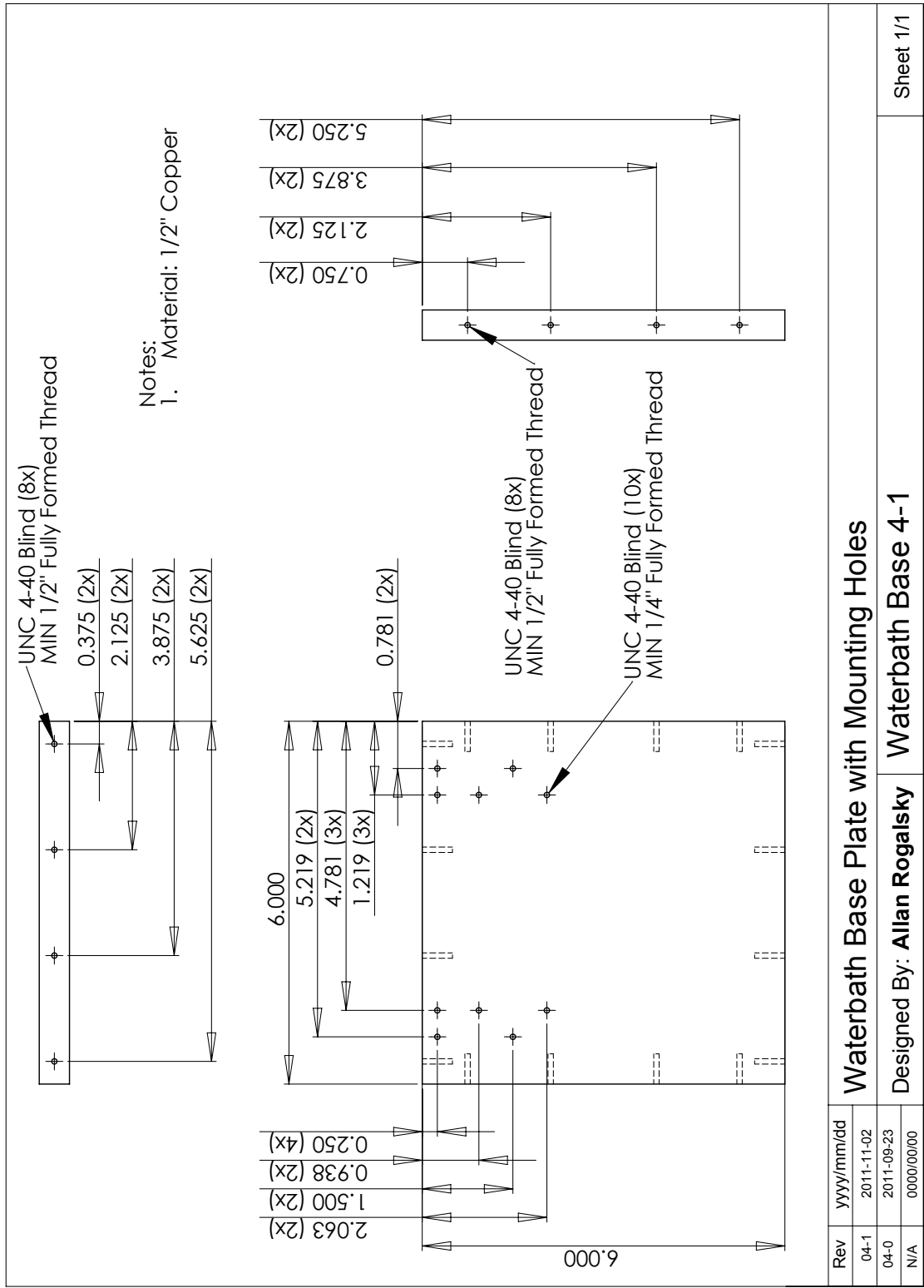
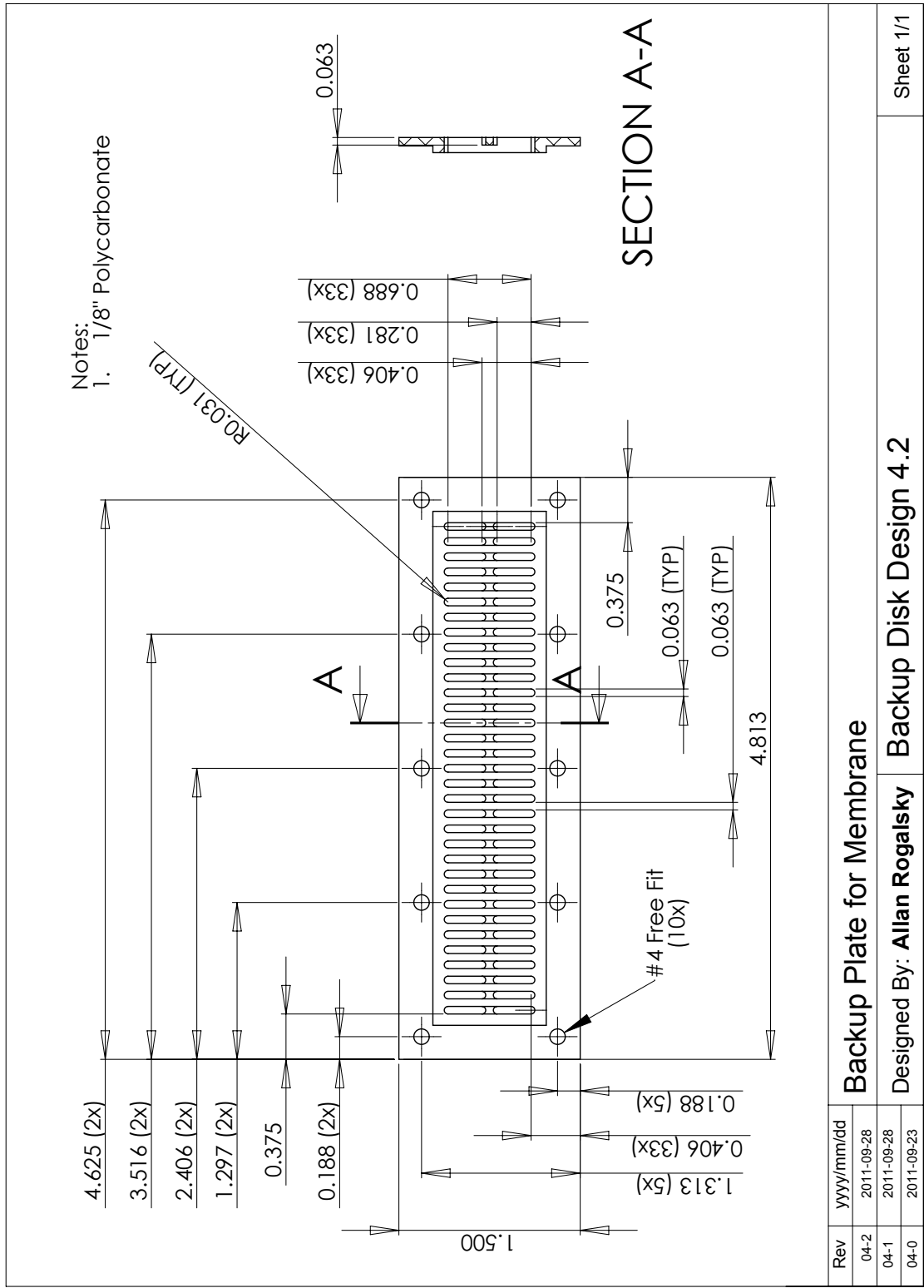


Figure B.18: Osmometer Top Level 4.2 / Waterbath Assembly / Waterbath Base 4.1



Sheet 1/1

Backup Plate for Membrane

Designed By: Allan Rogalsky Backup Disk Design 4.2

Figure B.19: Osmometer Top Level 4.2 / Backup Disk 4.2

B.4 Design 5.2 - Capillary Seating

Change Top Level Assembly 5.2 was 4.2

In Top Level Assembly 5.2

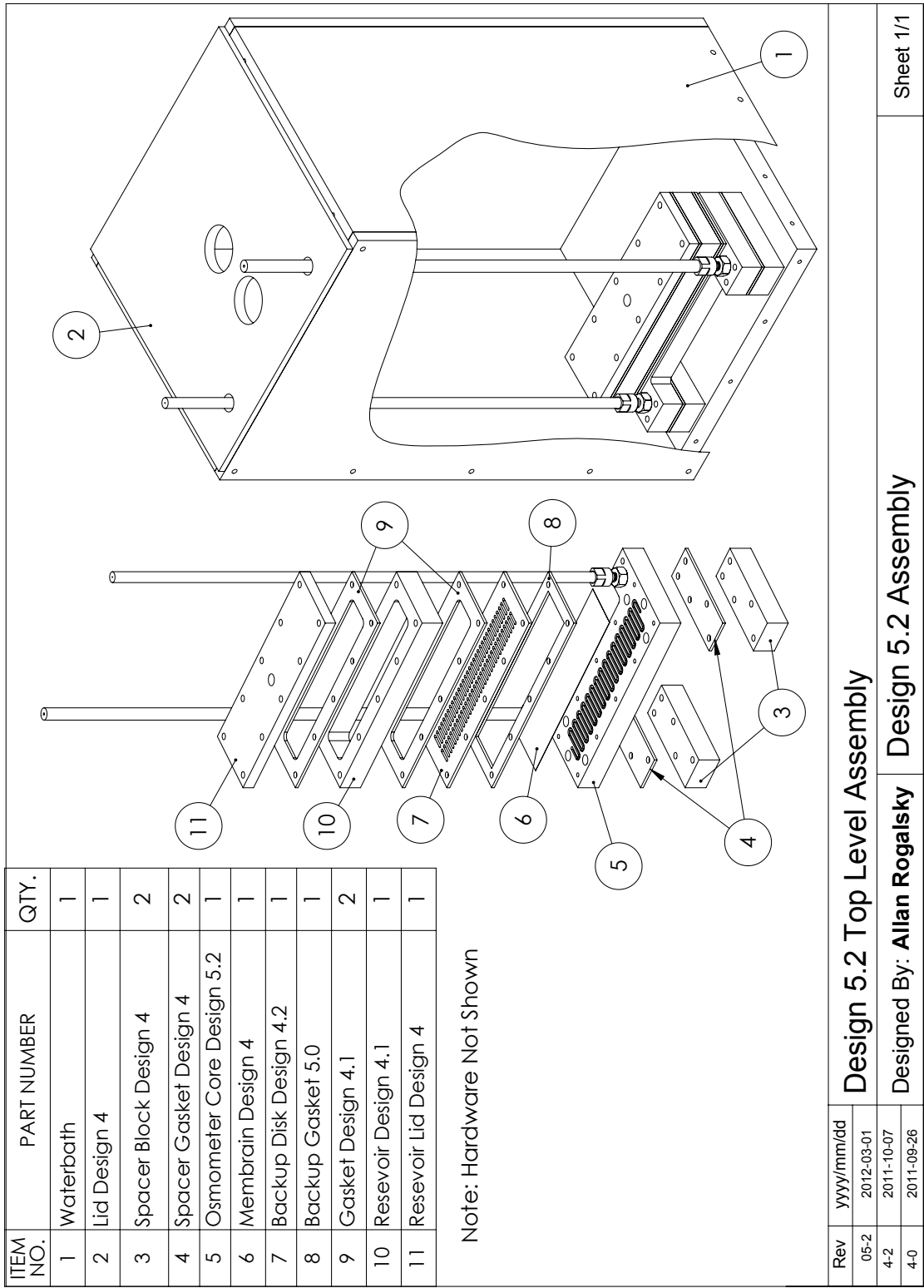
-Change Osmometer Core Assembly 5.2 was 4.0

-Add Backup Gasket 5.0

In Osmometer Core Assembly 5.2

-Change Cap 5.2 was 4.3

-Add Tube Fitting 5.1 (2x)



ITEM NO.	PART NUMBER	QTY.
1	Waterbath	1
2	Lid Design 4	1
3	Spacer Block Design 4	2
4	Spacer Gasket Design 4	2
5	Osmometer Core Design 5.2	1
6	Membrain Design 4	1
7	Backup Disk Design 4.2	1
8	Backup Gasket 5.0	1
9	Gasket Design 4.1	2
10	Reservoir Design 4.1	1
11	Reservoir Lid Design 4	1

Note: Hardware Not Shown

Design 5.2 Top Level Assembly		Sheet 1/1
Designed By: Allan Rogalsky Design 5.2 Assembly		
Rev	yyyy/mm/dd	
05-2	2012-03-01	
4-2	2011-10-07	
4-0	2011-09-26	

Figure B.20: Osmometer Top Level 5.2

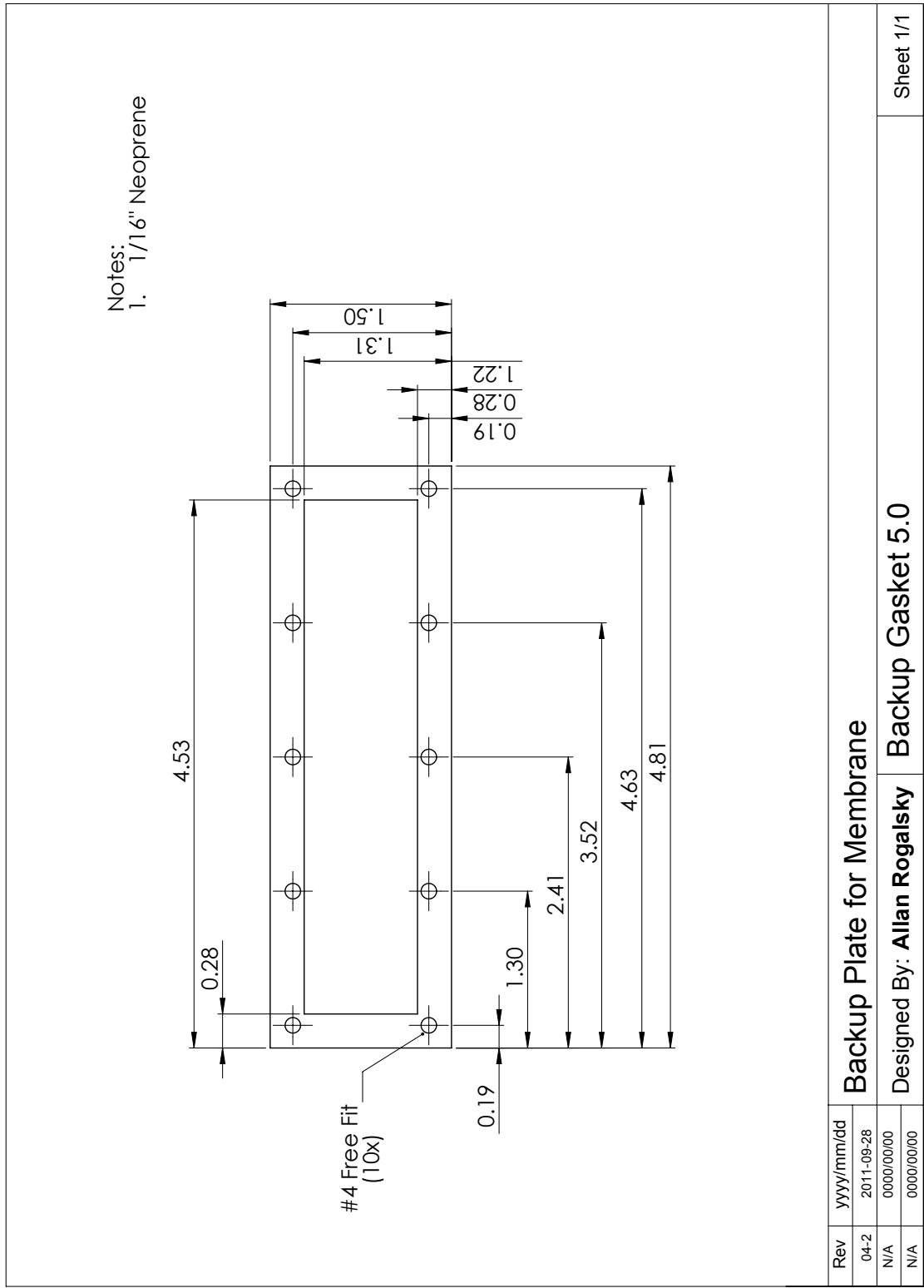


Figure B.21: Osmometer Top Level 5.2 / Membrane Backup Gasket 5.0

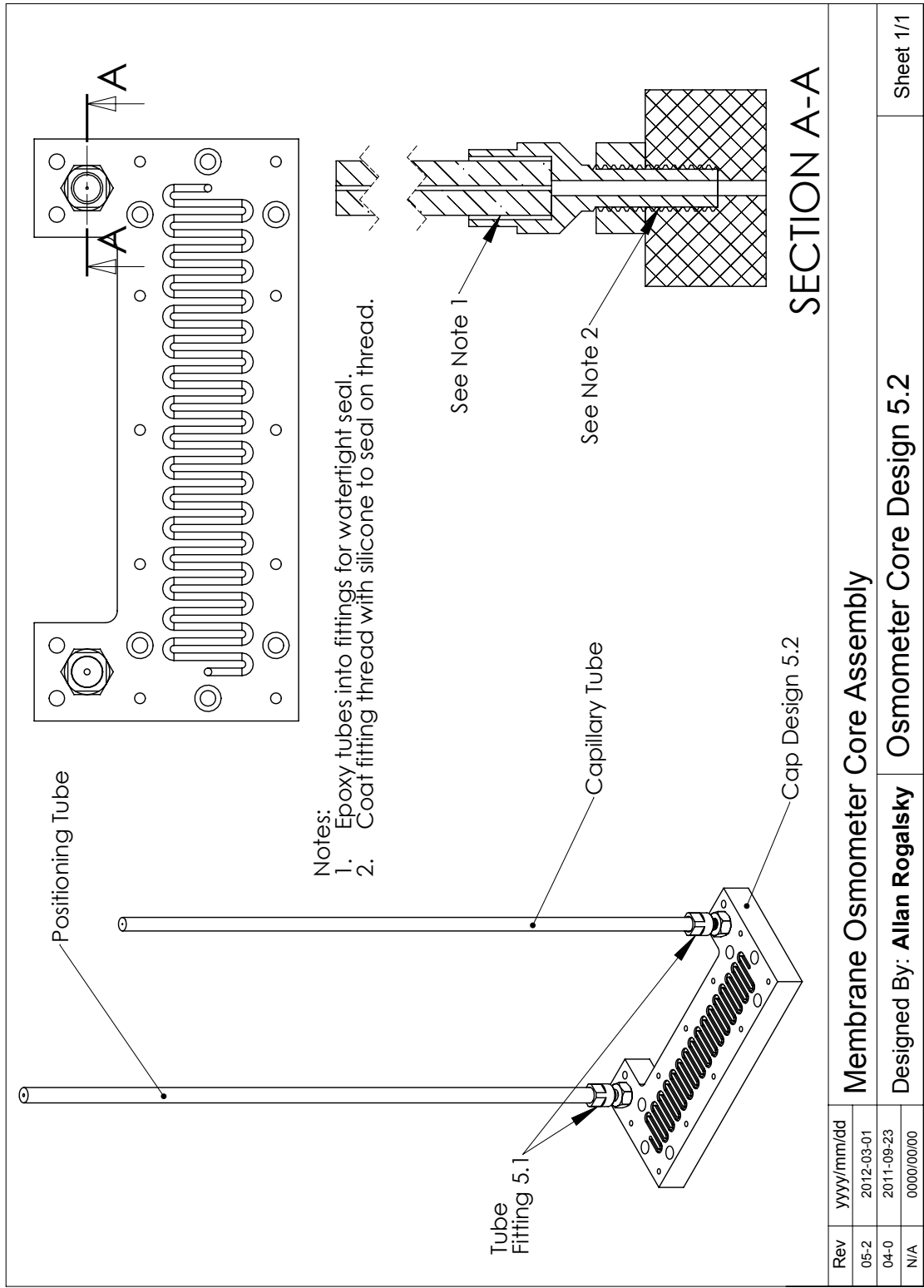


Figure B.22: Osmometer Top Level 5.2 / Core Assembly 5.2

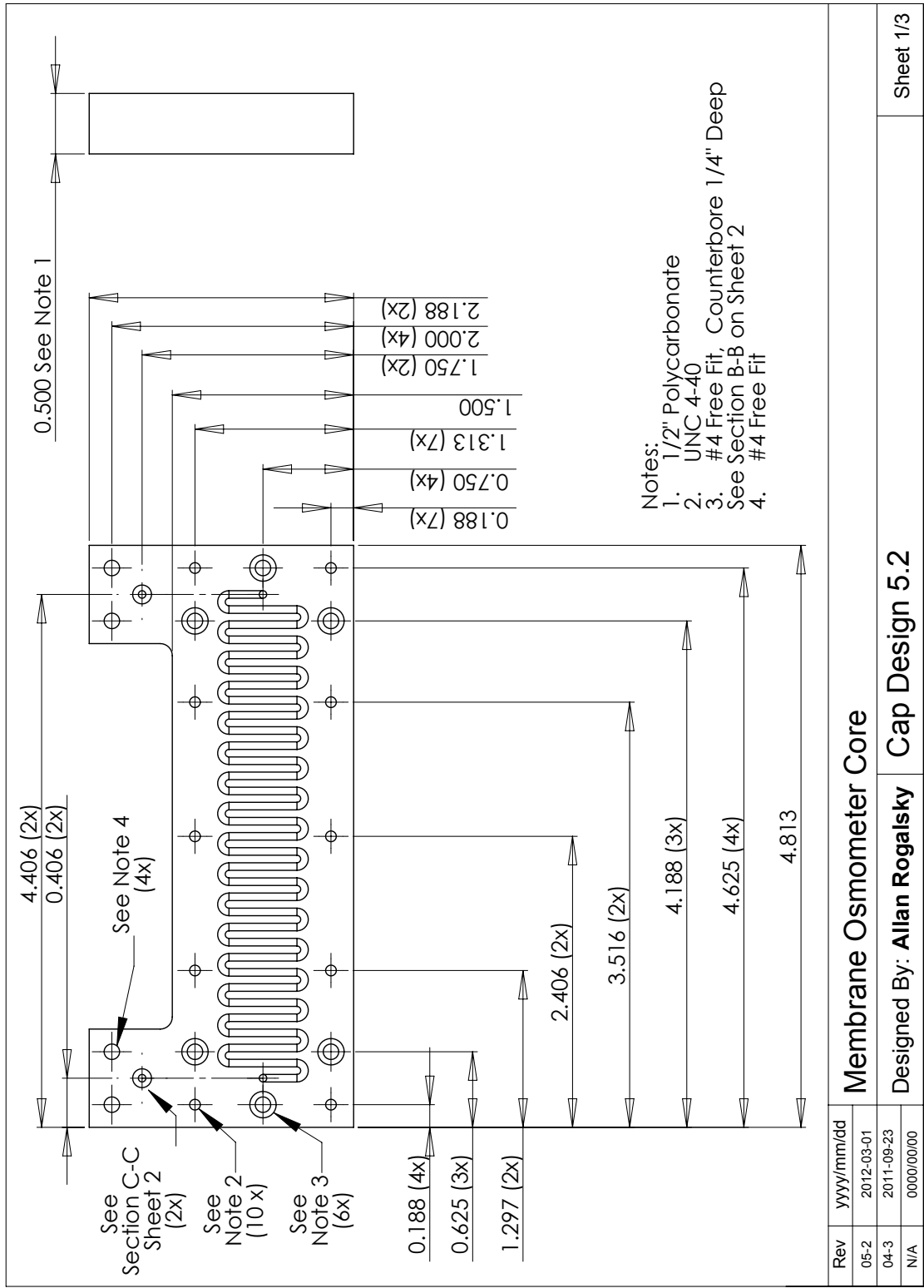


Figure B.23: Osmometer Top Level 5.2 / Core Assembly 5.2 / Cap 5.2 / Sheet 1

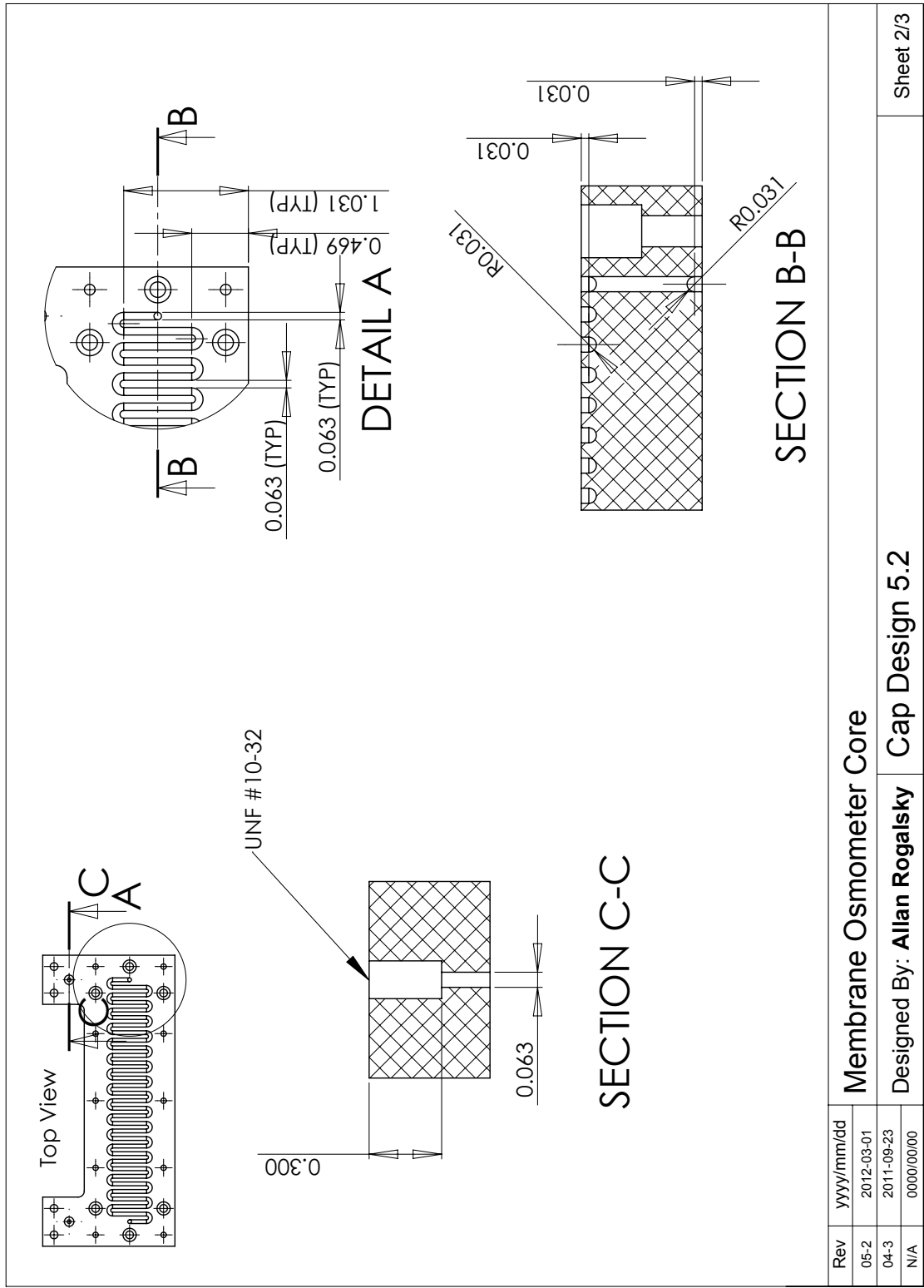


Figure B.24: Osmometer Top Level 5.2 / Core Assembly 5.2 / Cap 5.2 / Sheet 2

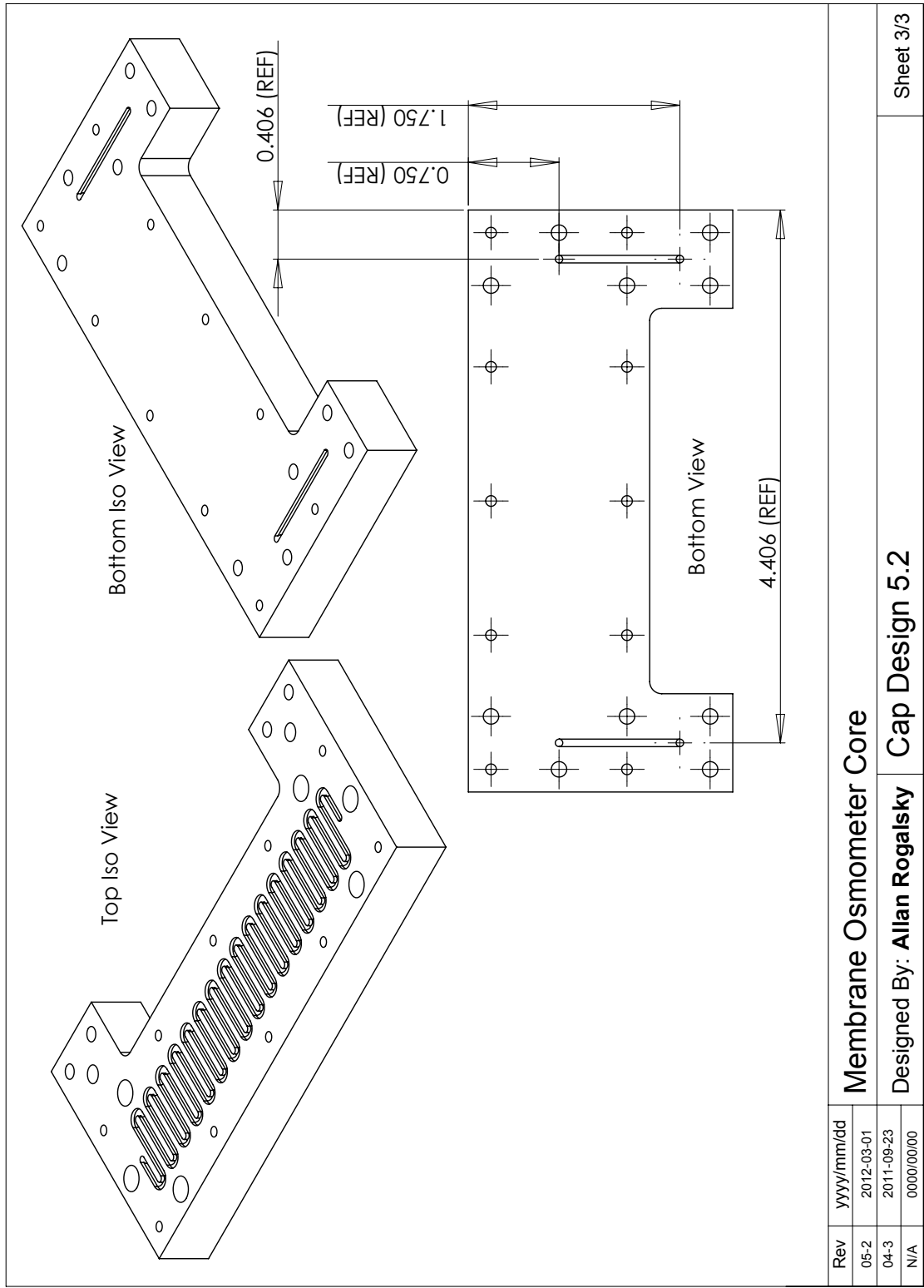


Figure B.25: Osmometer Top Level 5.2 / Core Assembly 5.2 / Cap 5.2 / Sheet 3

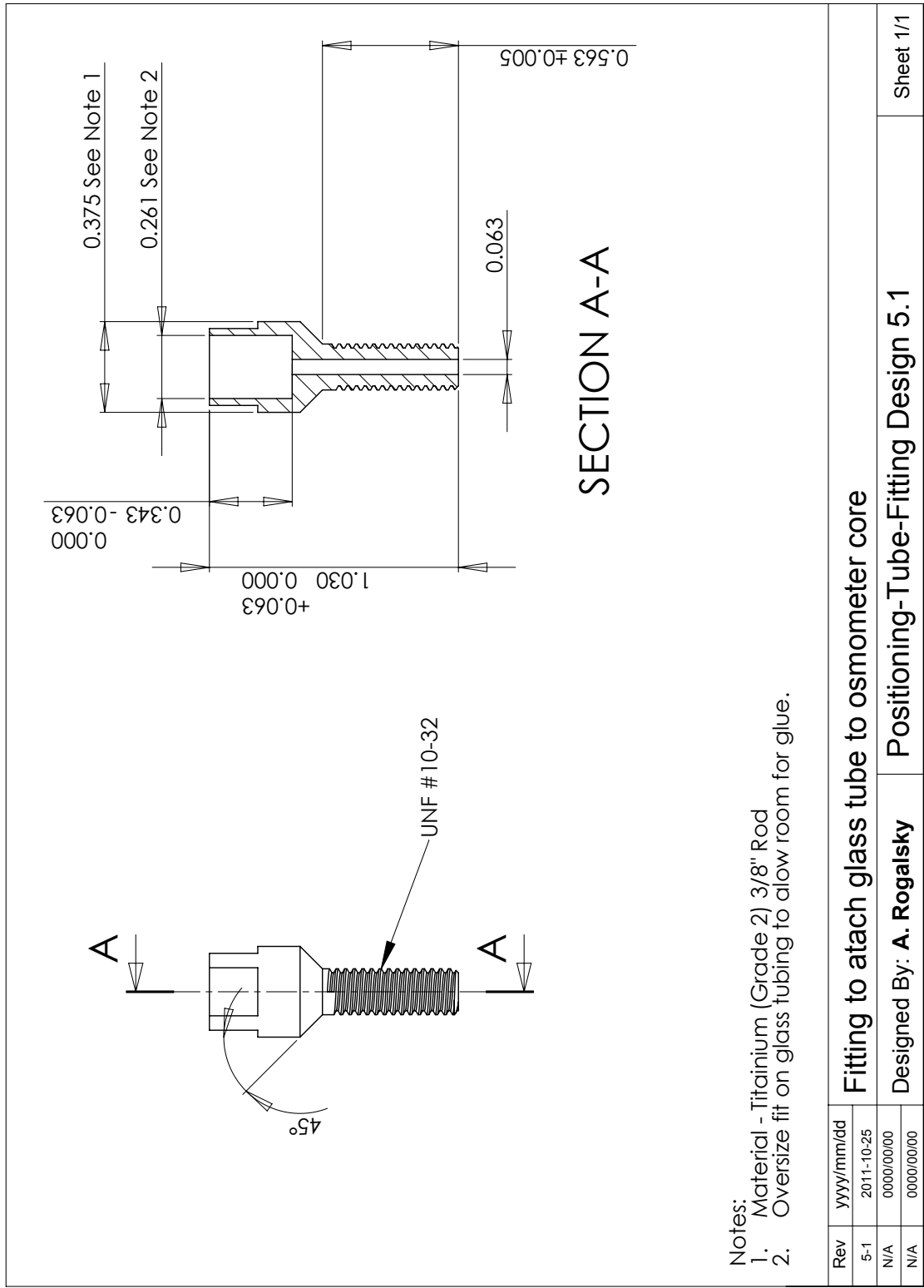


Figure B.26: Osmometer Top Level 5.2 / Core Assembly 5.2 / Tube Fitting 5.1

B.5 Design 8.0 - Cast Silicone Gaskets

Change Top Level Assembly 8.0

Change Water bath Lid 8.0 was 4.0

Change Backup Disk 8.0 was 4.2

Add Spacer Block RHS 8.0

Add Spacer Block LHS 8.0

Add Scale 8.0

Remove Spacer Block 4.0 (2x)

Remove Spacer Gasket 4.0 (2x)

Remove Backup Gasket 5.0

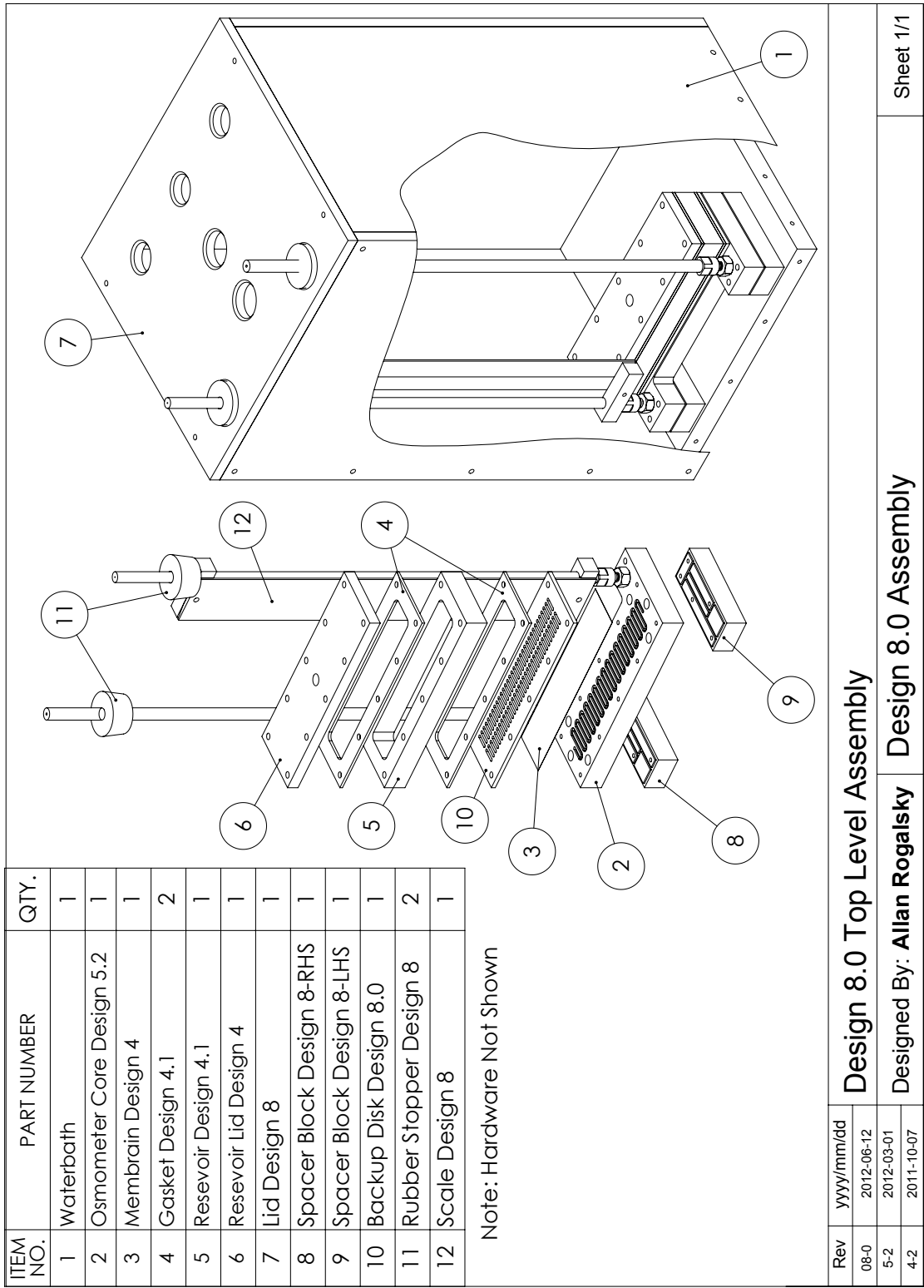


Figure B.27: Osmometer Top Level 8.0

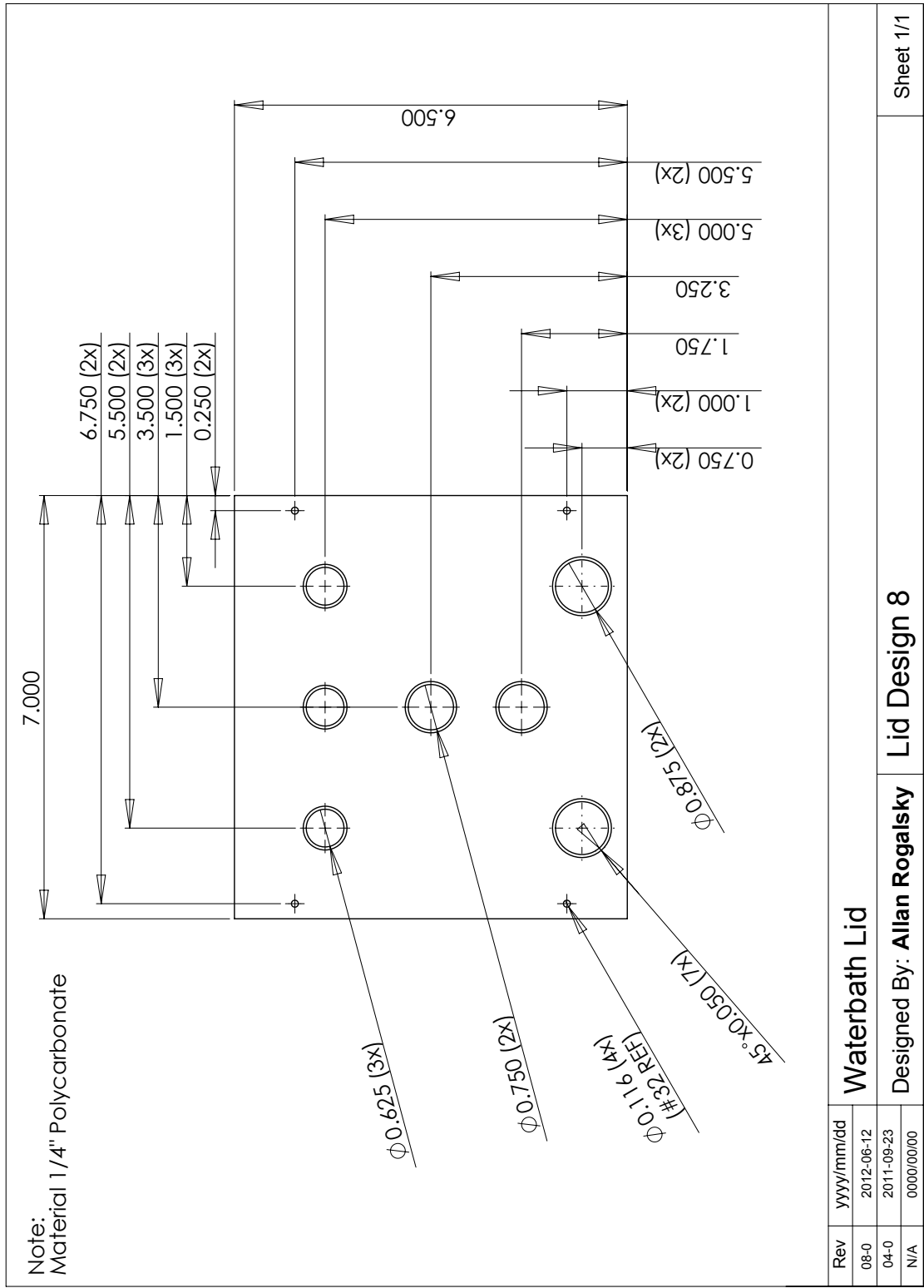
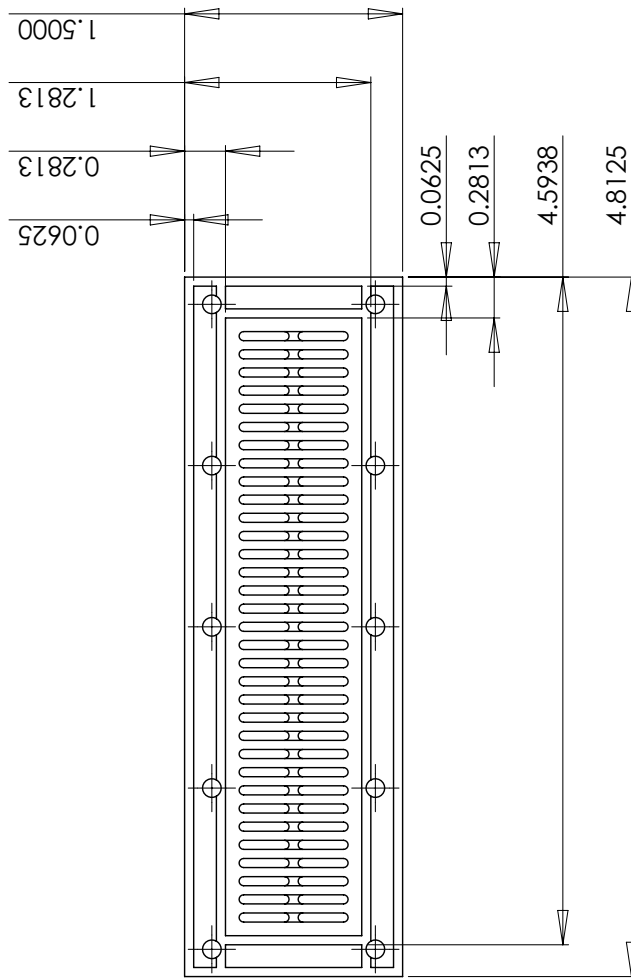


Figure B.28: Osmometer Top Level 8.0 / Water bath Lid 8.0

Notes:
 1. Changes to Backup Disk Design 4-2



Rev	yyyy/mm/dd
08-0	2012-06-12
04-2	2011-09-28
N/A	0000/00/00

Backup Plate for Membrane

Designed By: **Allan Rogalsky** Backup Disk Design 8.0

Sheet 1/1

Figure B.29: Osmometer Top Level 8.0 / Backup Disk 8.0

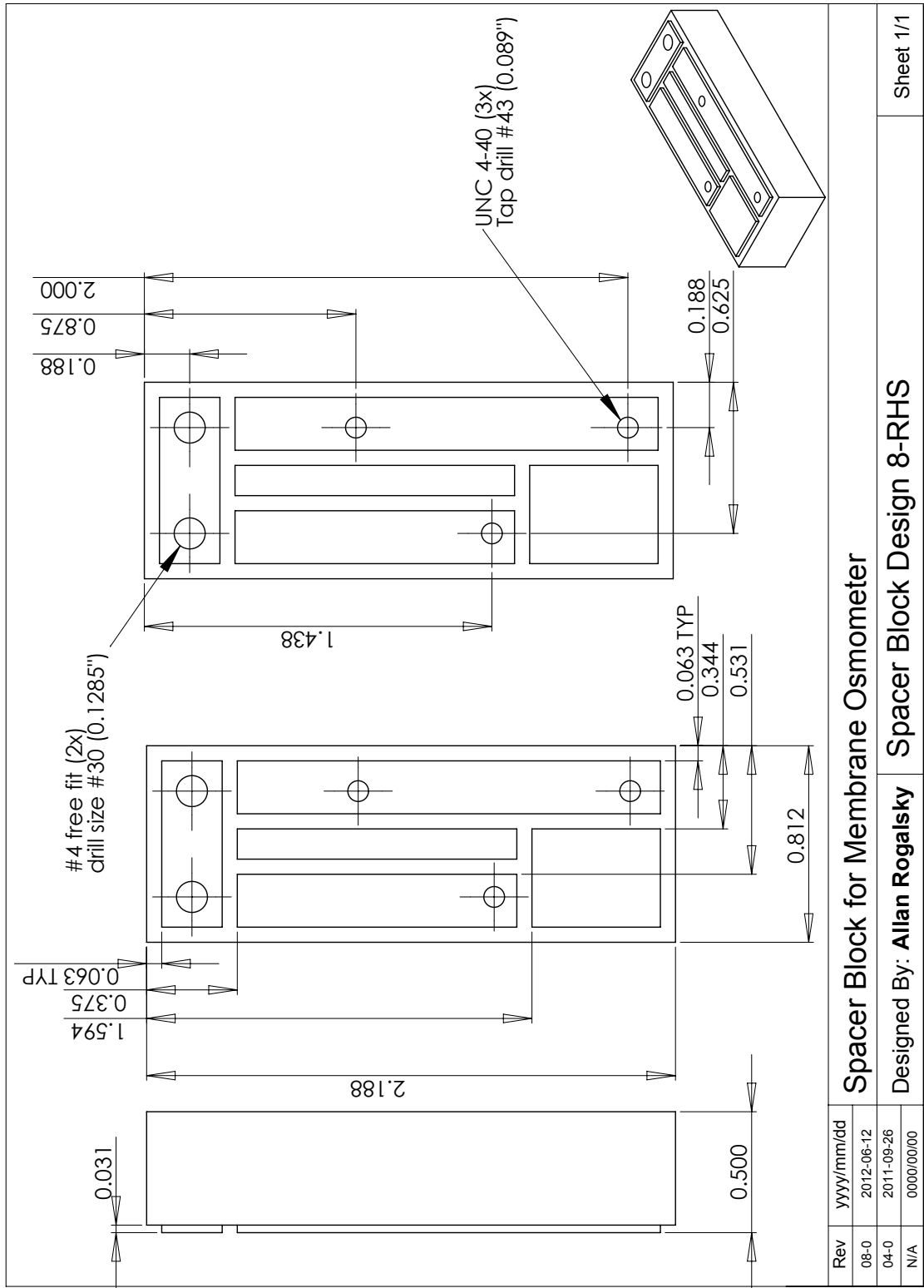
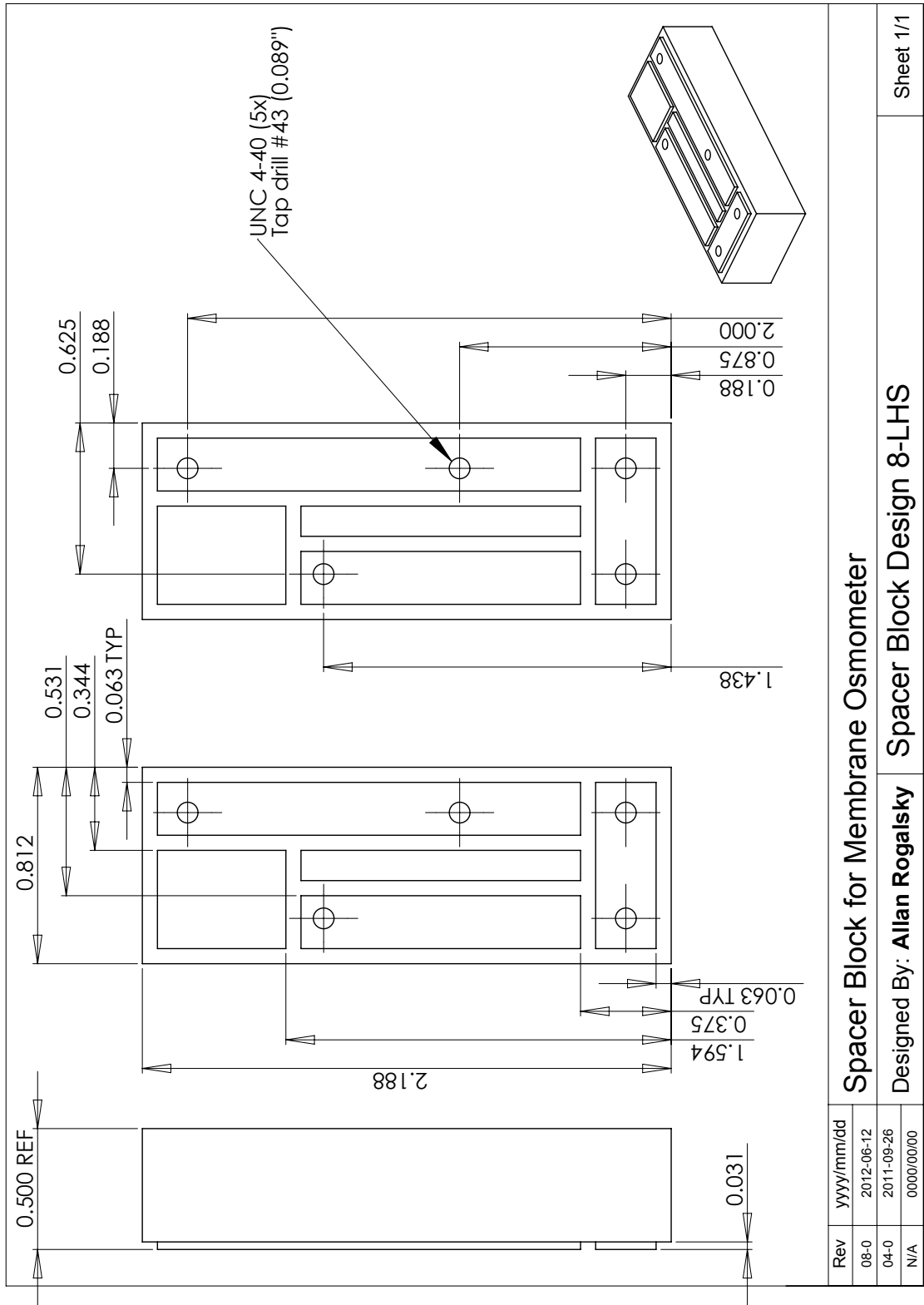


Figure B.30: Osmometer Top Level 8.0 / Spacer Block RHS 8.0



Sheet 1/1

Spacer Block for Membrane Osmometer

Designed By: Allan Rogalsky Spacer Block Design 8-LHS

Figure B.31: Osmometer Top Level 8.0 / Spacer Block LHS 8.0

B.6 Design 9.0 - Glass Reference Snorkel

Change Top Level Assembly 9.0 was 4.2

In Top Level Assembly 9.0 was 4.2

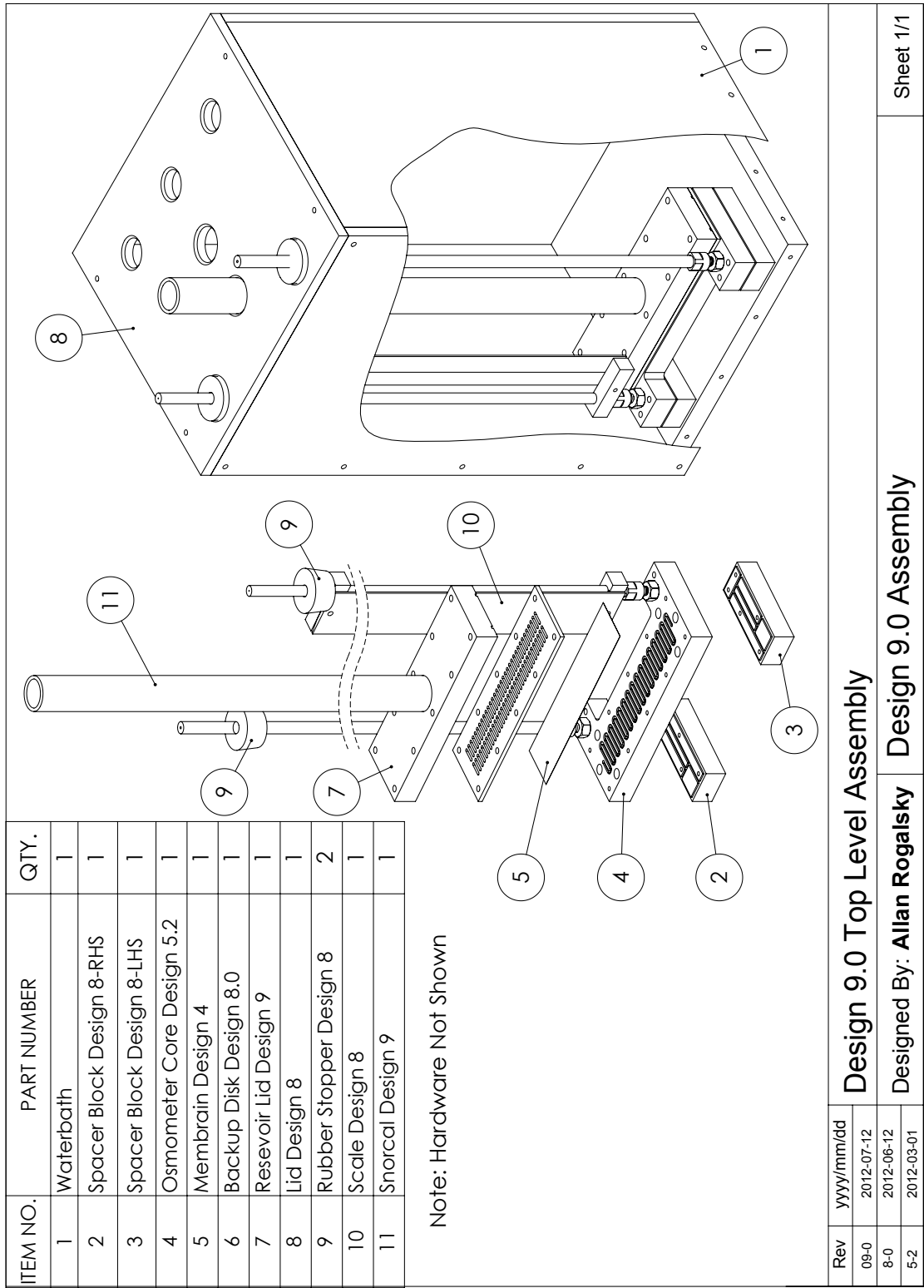
Change Reservoir Lid 9.0 was 4.0

Add Reference Snorkel

Remove Reservoir 4.1

Remove Gasket 4.1 (2x)

Note Fixture Required to make Reservoir Lid using conventional mill.



ITEM NO.	PART NUMBER	QTY.
1	Waterbath	1
2	Spacer Block Design 8-RHS	1
3	Spacer Block Design 8-LHS	1
4	Osmometer Core Design 5.2	1
5	Membrain Design 4	1
6	Backup Disk Design 8.0	1
7	Reservoir Lid Design 9	1
8	Lid Design 8	1
9	Rubber Stopper Design 8	2
10	Scale Design 8	1
11	Snorcal Design 9	1

Note: Hardware Not Shown

Design 9.0 Top Level Assembly		Sheet 1/1
Designed By: Allan Rogalsky		
Rev	yyyy/mm/dd	
09-0	2012-07-12	
8-0	2012-06-12	
5-2	2012-03-01	

Figure B.32: Osmometer Top Level 9.0

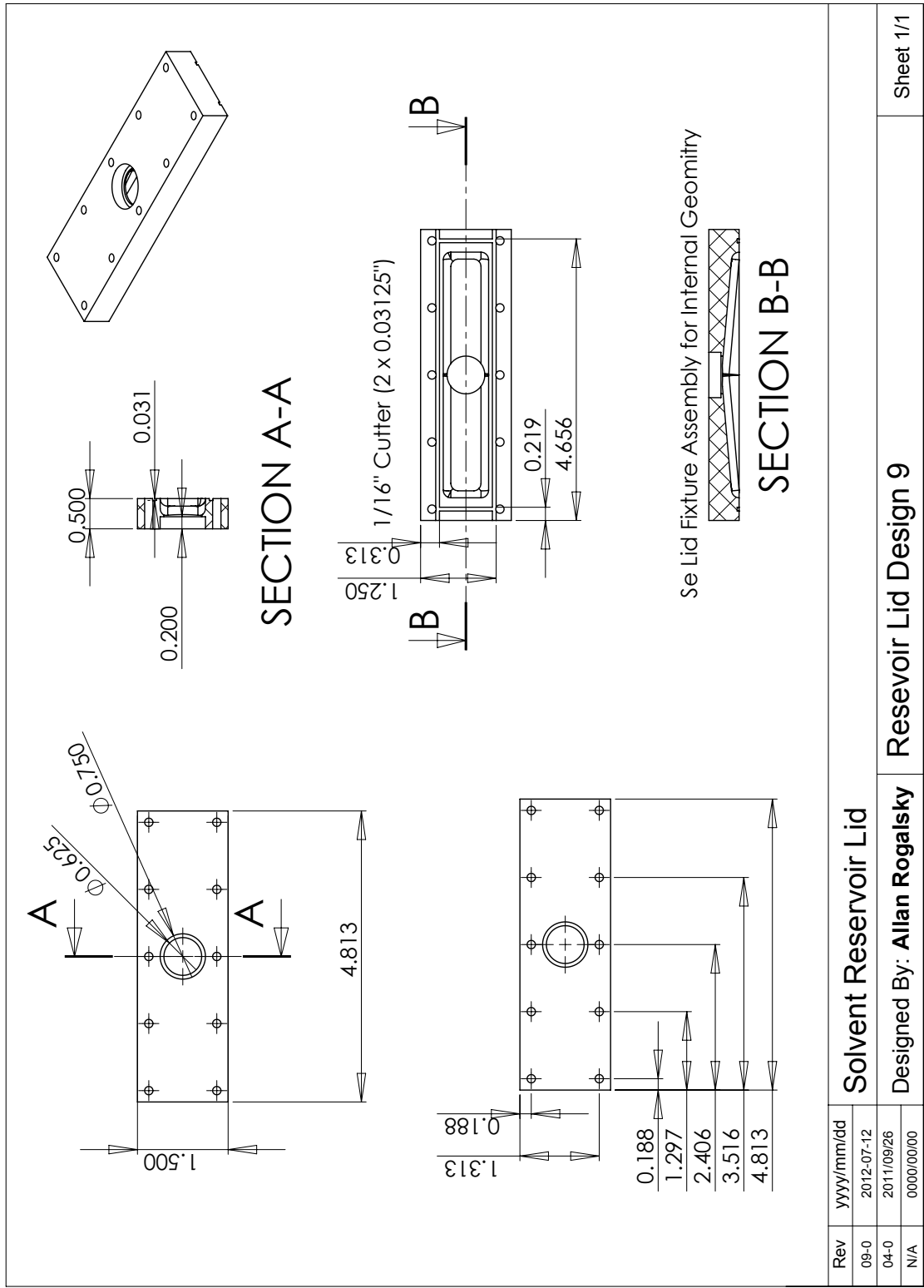


Figure B.33: Osmometer Top Level 9.0 / Reservoir Lid 9.0

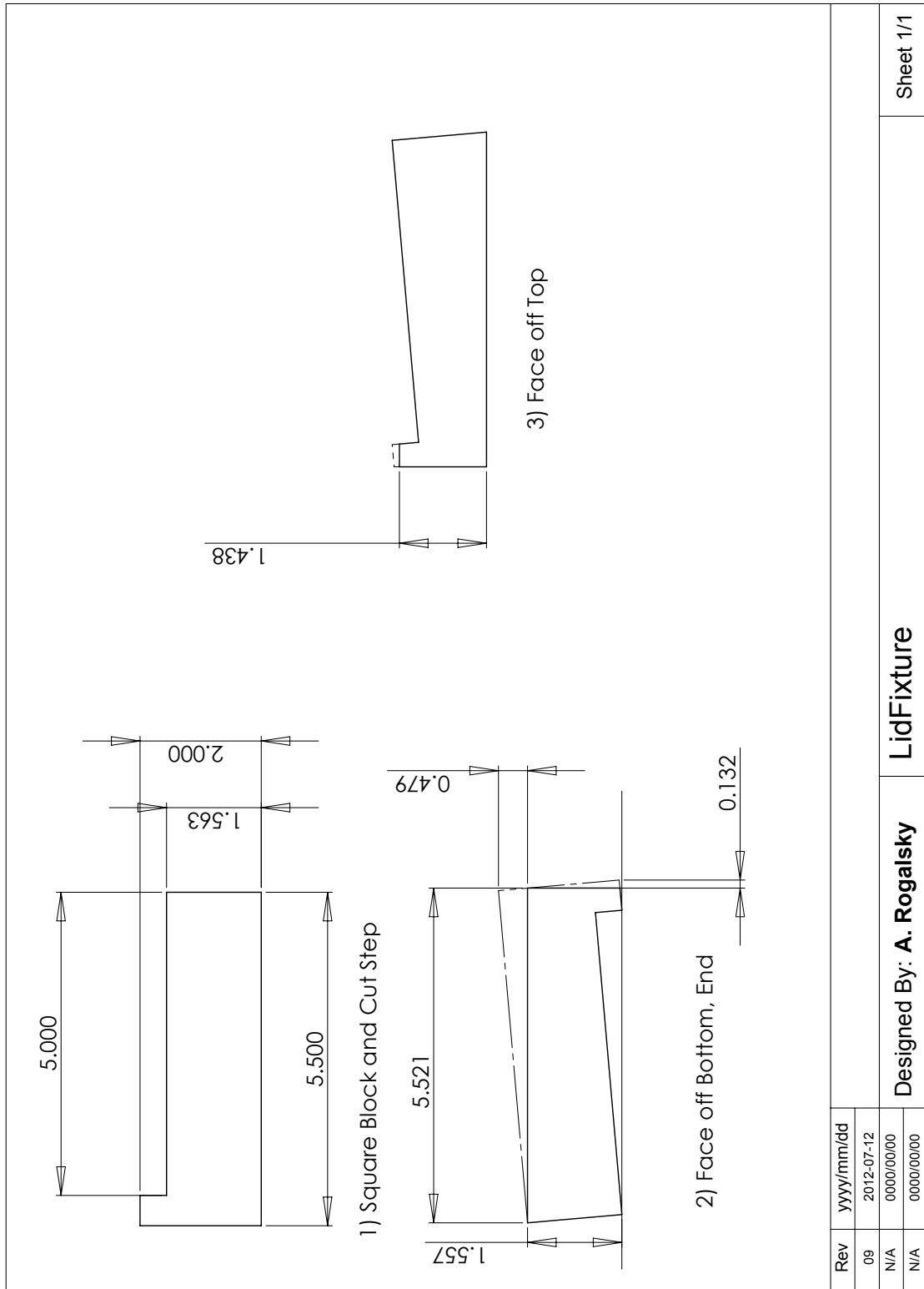


Figure B.34: Osmometer Top Level 9.0 / Reservoir Lid 9.0 / Lid Fixture 9.0

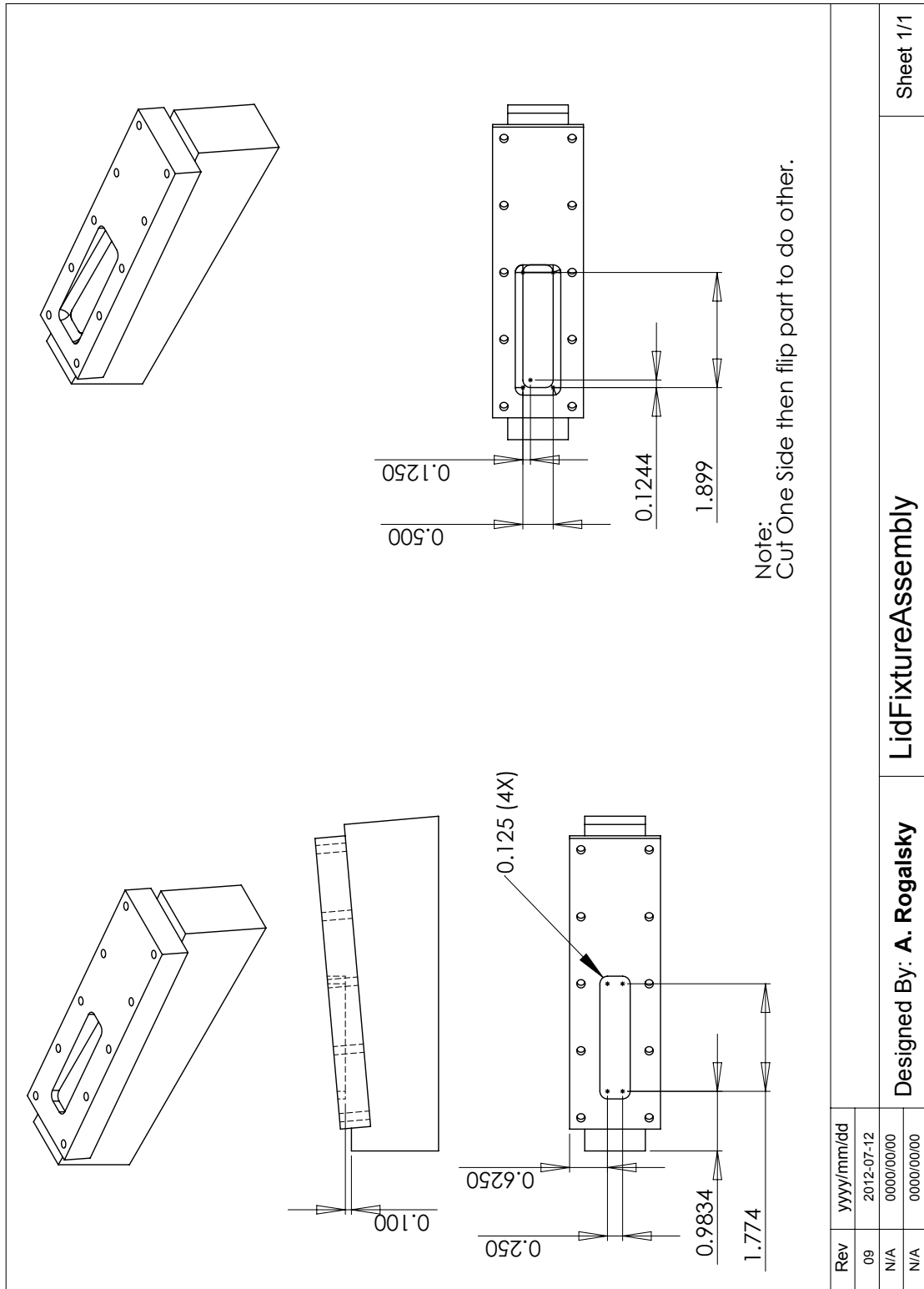


Figure B.35: Osmometer Top Level 9.0 / Reservoir Lid 9.0 / Lid Fixture Assembly 9.0

Appendix C

Transducer Osmometer Design

C.1 Top Level Assemblies

Initial Design: Revision 2-00

1. Water Bath from Manual Design
2. Lid Design 1-0
3. Osmometer Core Assembly 2-0
4. Transducer Well 2-00

Improved Thermal Isolation: Revision 3-00

1. Water Bath 2-0 (was Water Bath from Manual Design)
2. Transducer Well 2-00 (was item 4)
3. Osmometer Core Assembly 2-0
4. Transducer Spacer 2-0 (new)
5. Spacer Lid 1-0 (new)
6. Tank Lid 1-0 (was Lid Design 1-0)

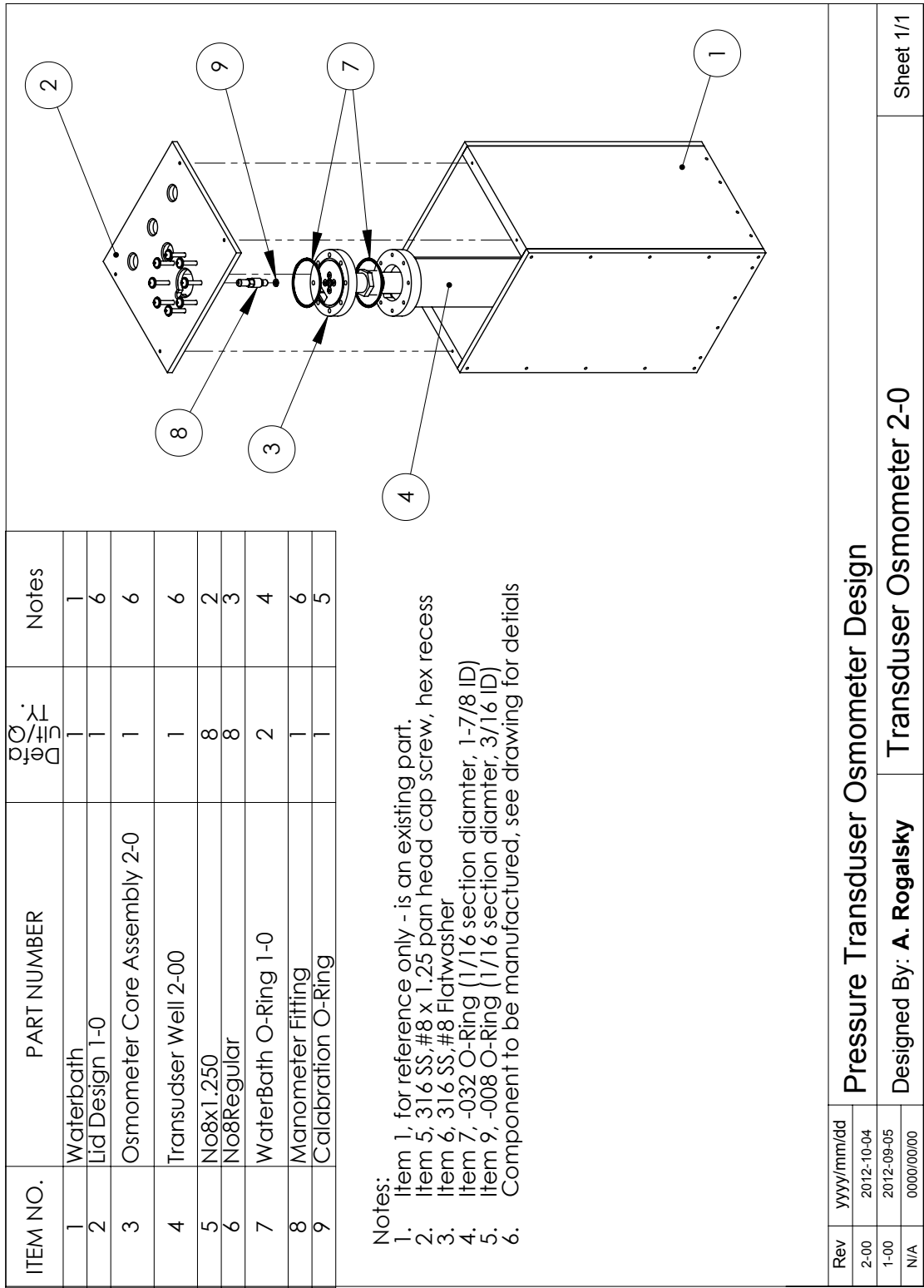


Figure C.1: Initial Design: Revision 2-00

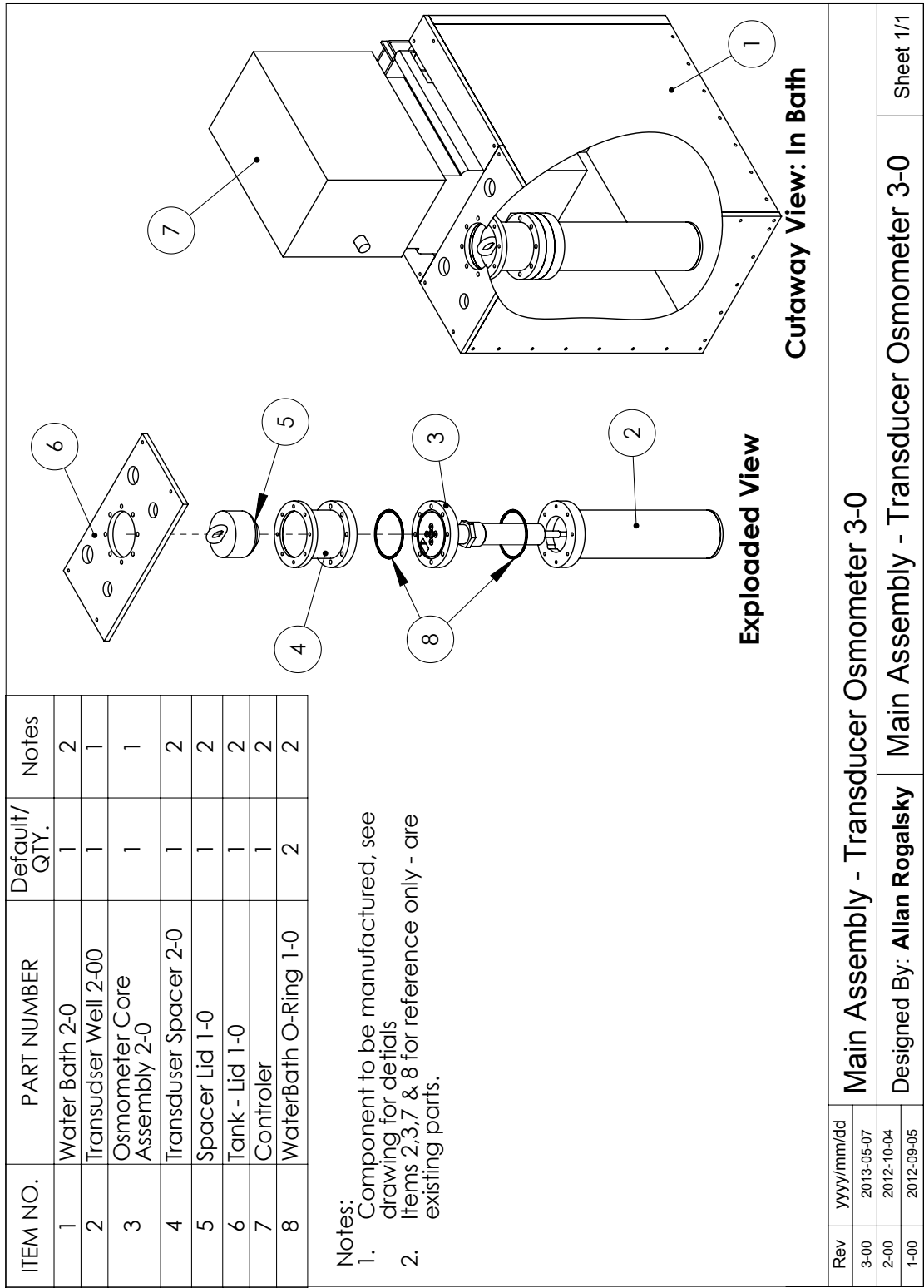


Figure C.2: Improved Thermal Isolation: Revision 3-00

C.2 Core Design

Transducer Osmometer Core Assembly 2-00

1. Osmometer Core
2. Membrane Support
3. Sample Chamber

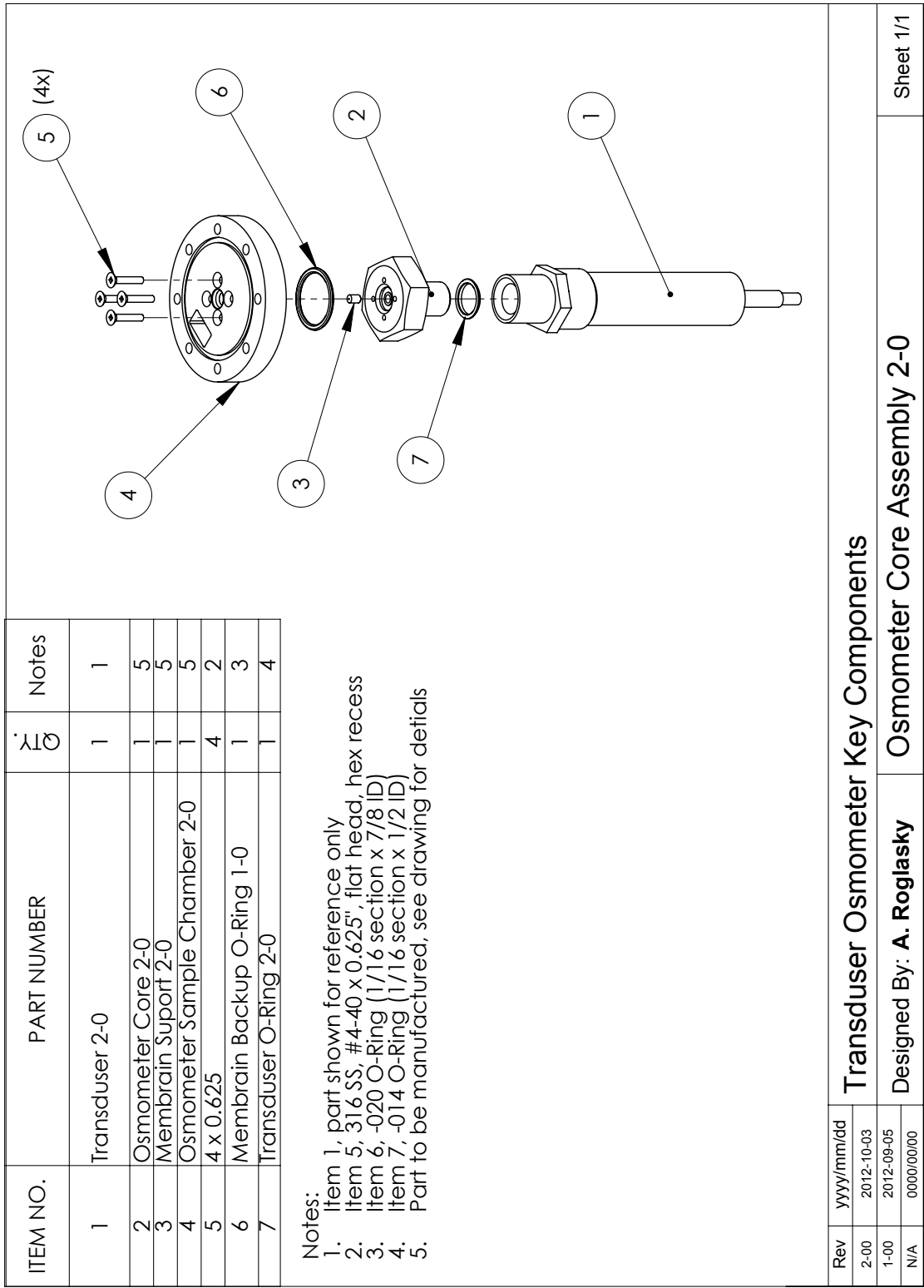


Figure C.3: Transducer Osmometer Core Assembly

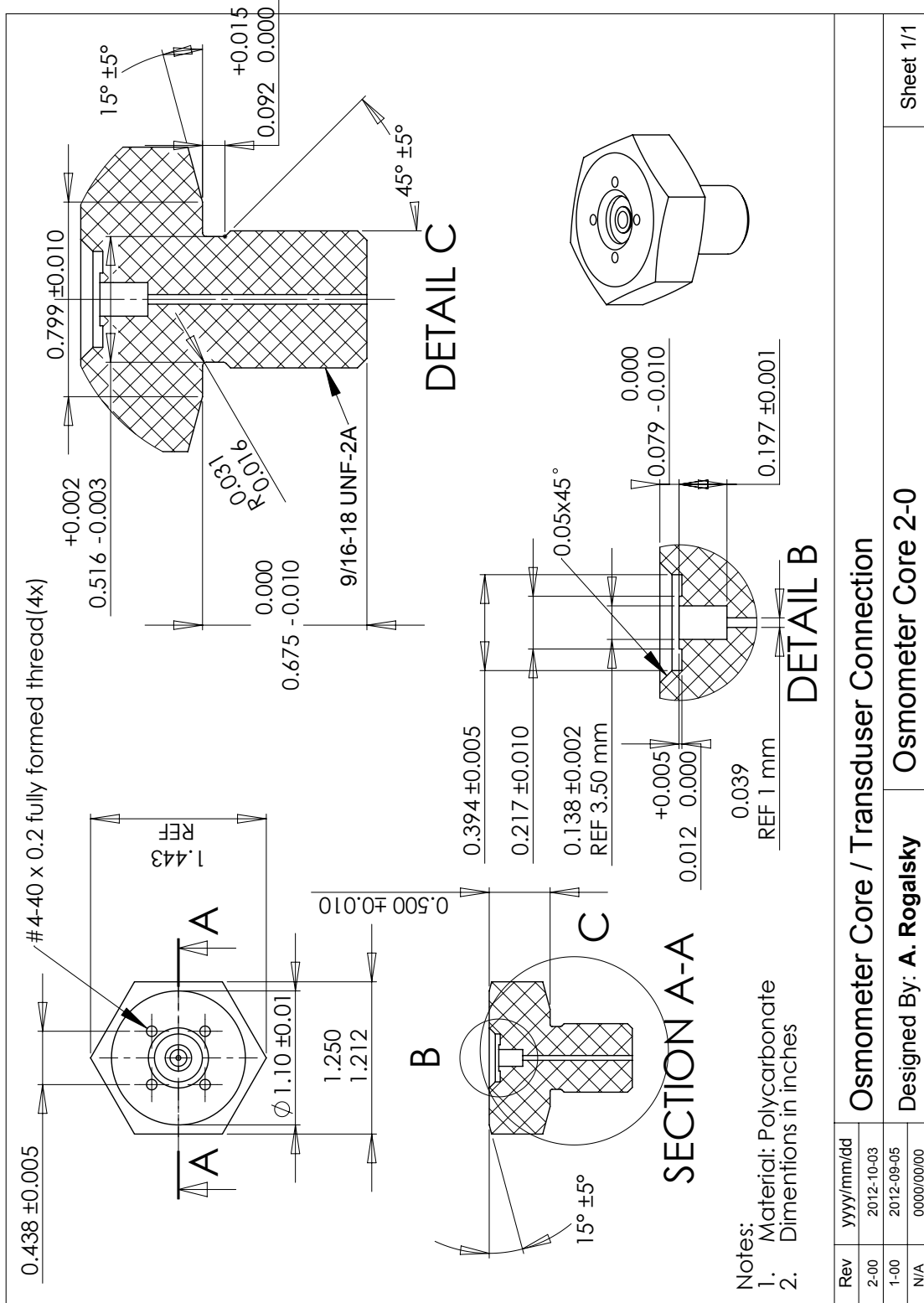


Figure C.4: Transducer Osmometer Core Assembly / Osmometer Core

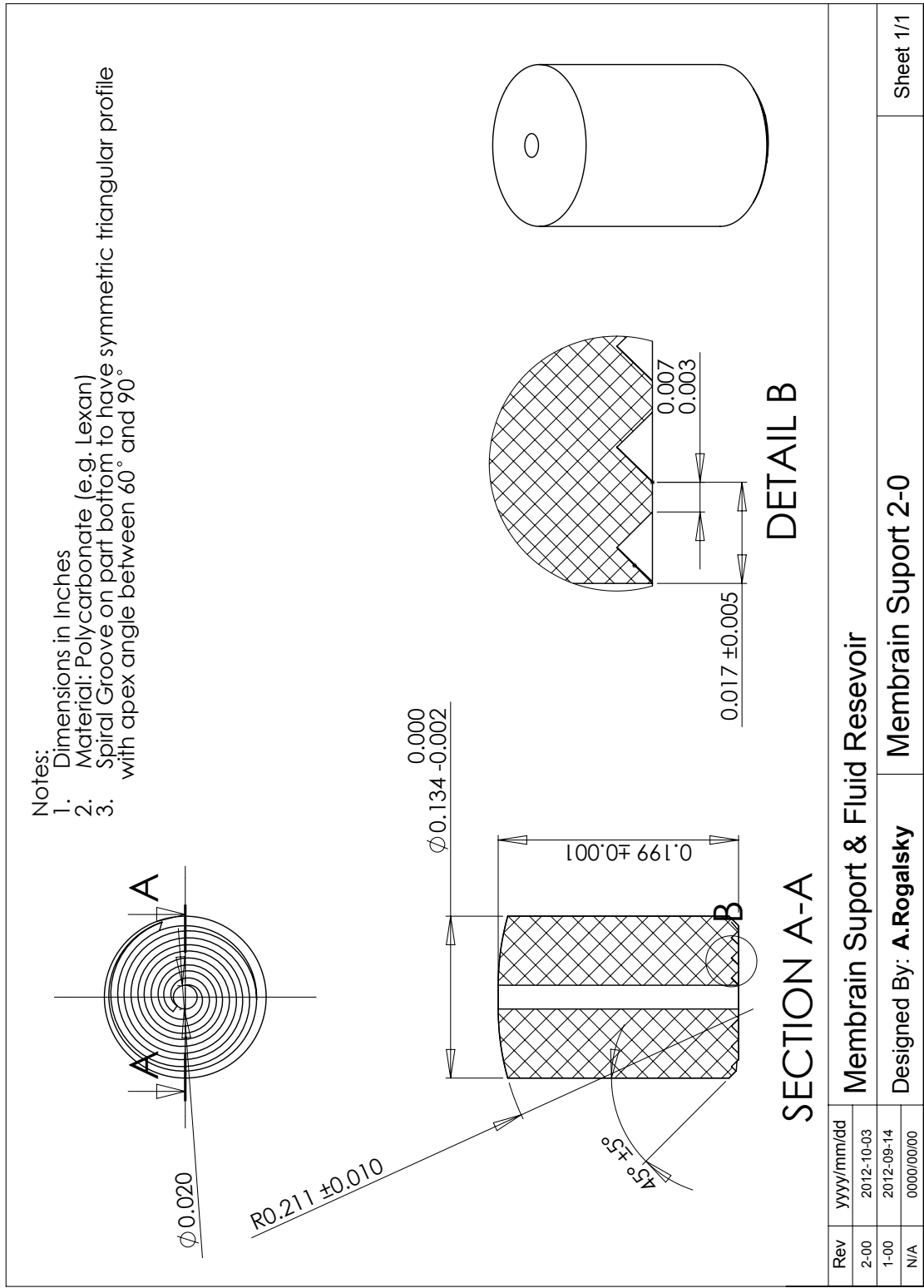


Figure C.5: Transducer Osmometer Core Assembly / Membrane Support

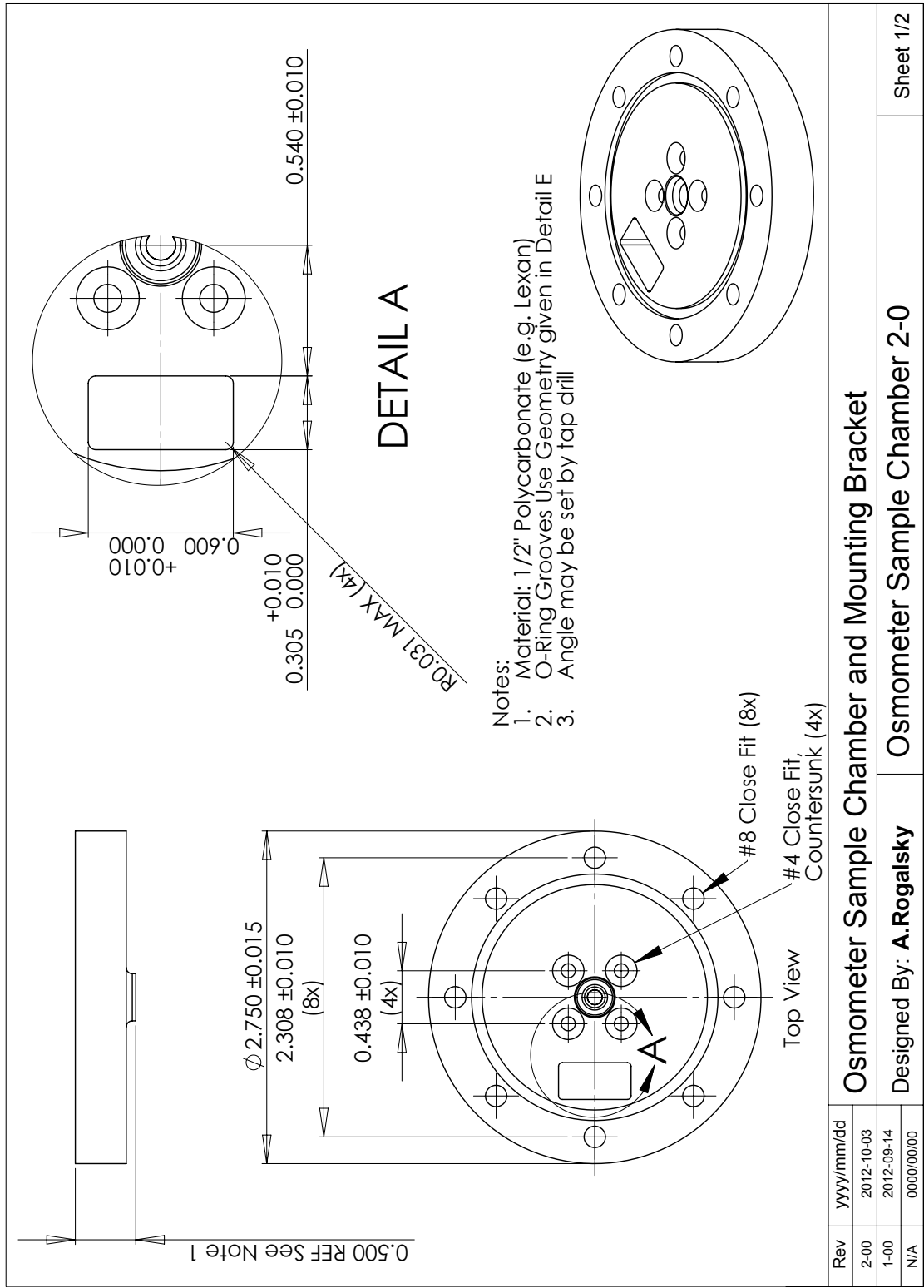


Figure C.6: Transducer Osmometer Core Assembly / Sample Chamber / Sheet 1

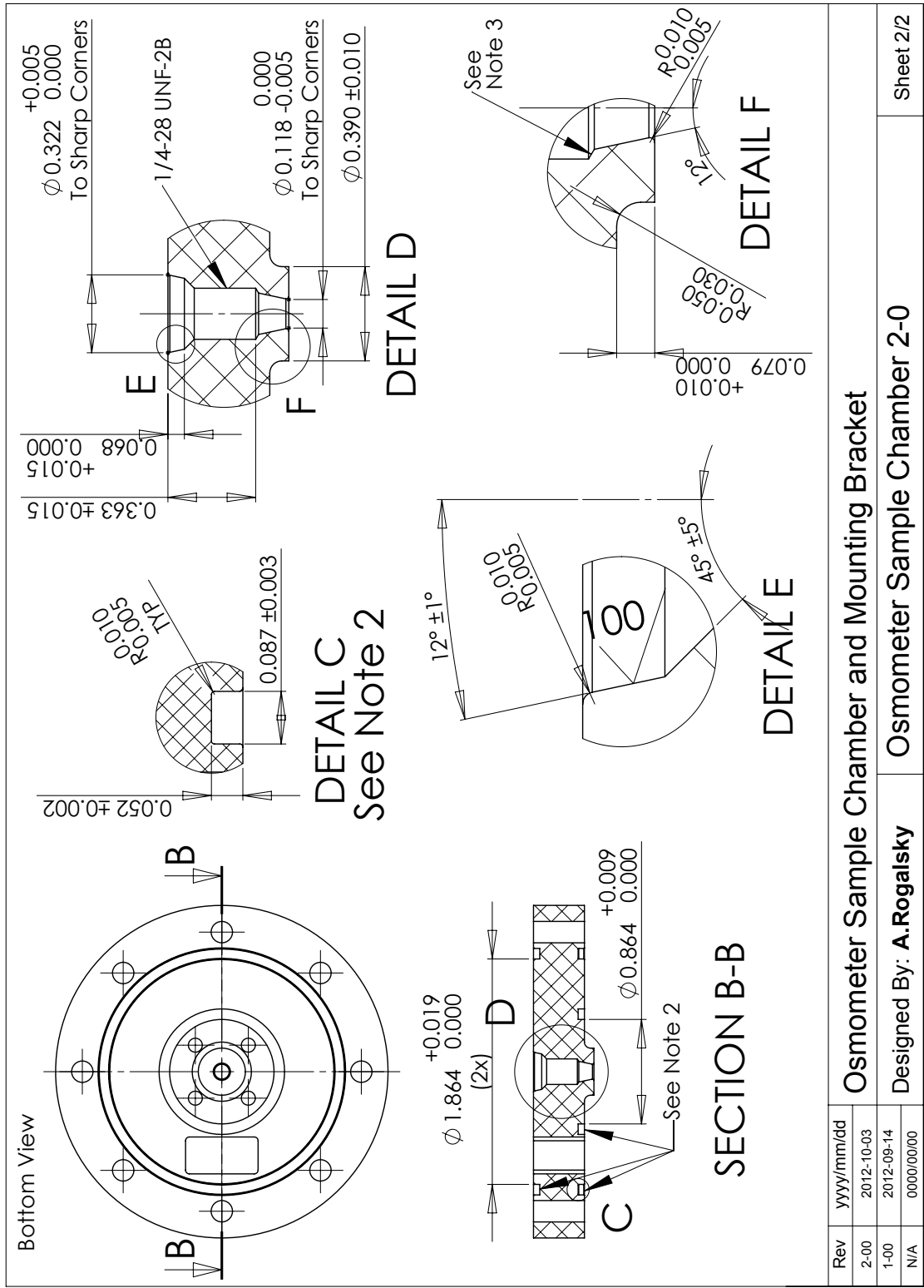


Figure C.7: Transducer Osmometer Core Assembly / Sample Chamber / Sheet 2

C.3 Transducer Well

Transducer Well Assembly 2-00

1. Flange
2. Tube
3. Plug

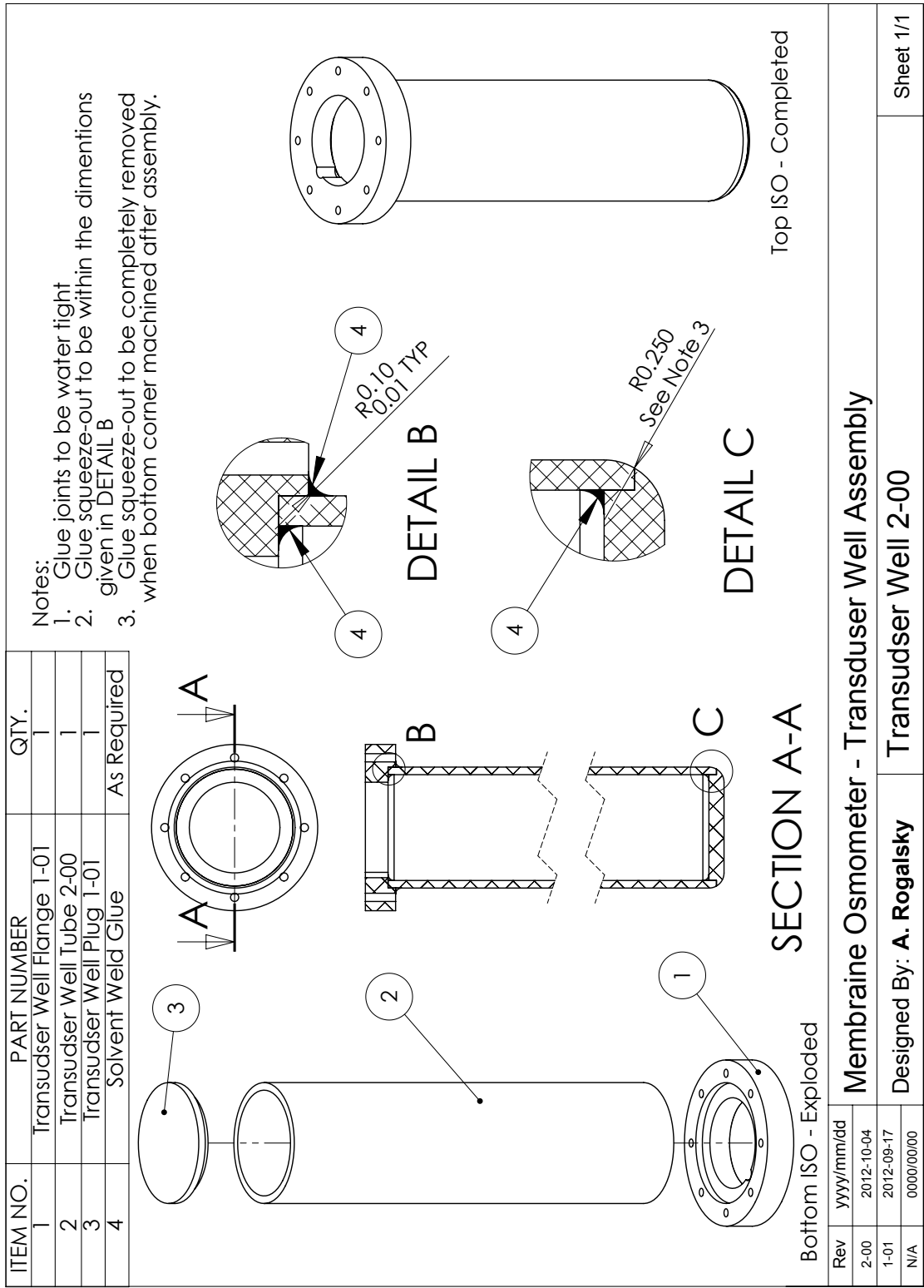


Figure C.8: Transducer Well Assembly

Membrane Osmometer - Transducer Well Assembly	
Designed By: A. Rogalsky	Transducer Well 2-00
Rev	yyyy/mm/dd
2-00	2012-10-04
1-01	2012-09-17
N/A	0000/00/00
Sheet 1/1	

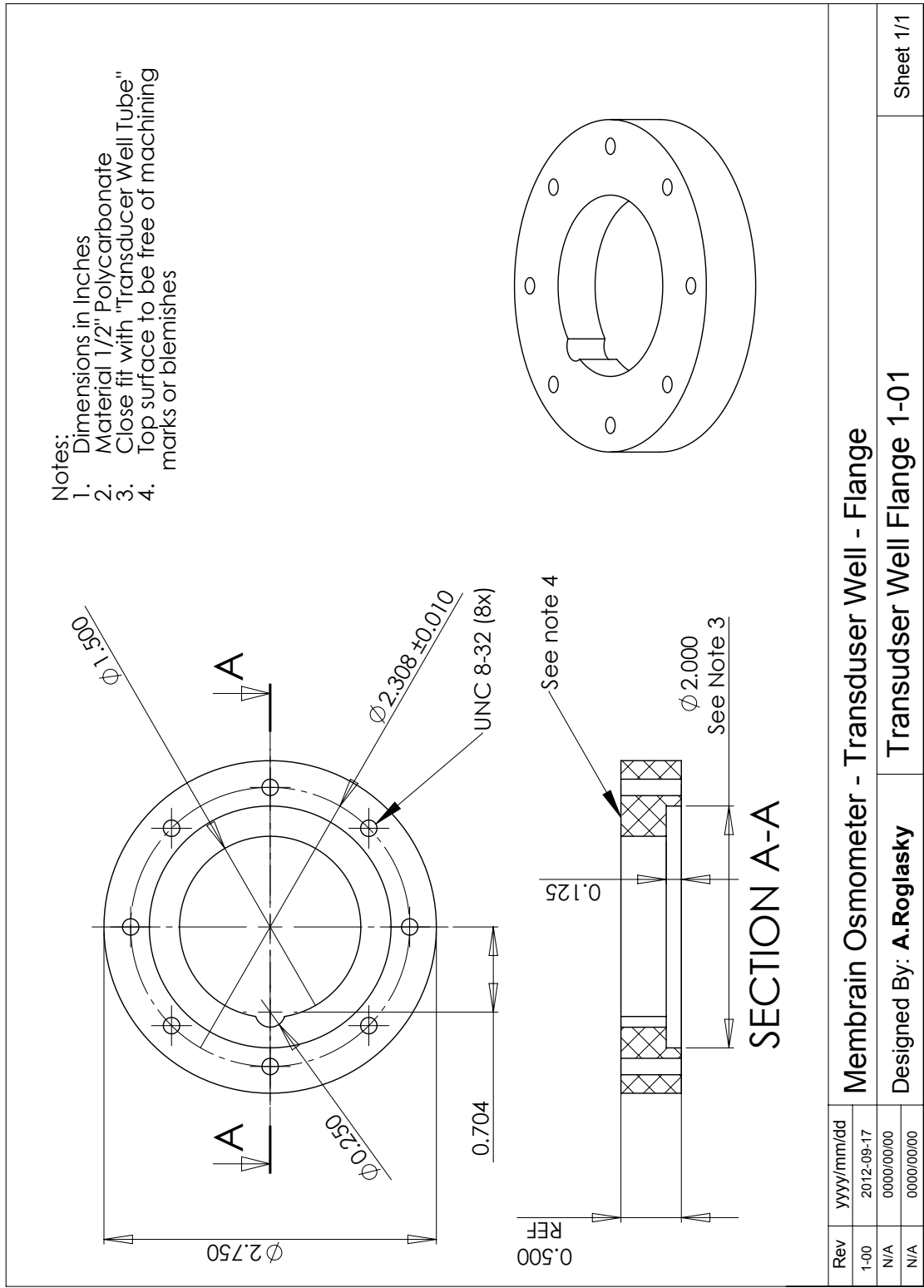


Figure C.9: Transducer Well Assembly / Flange

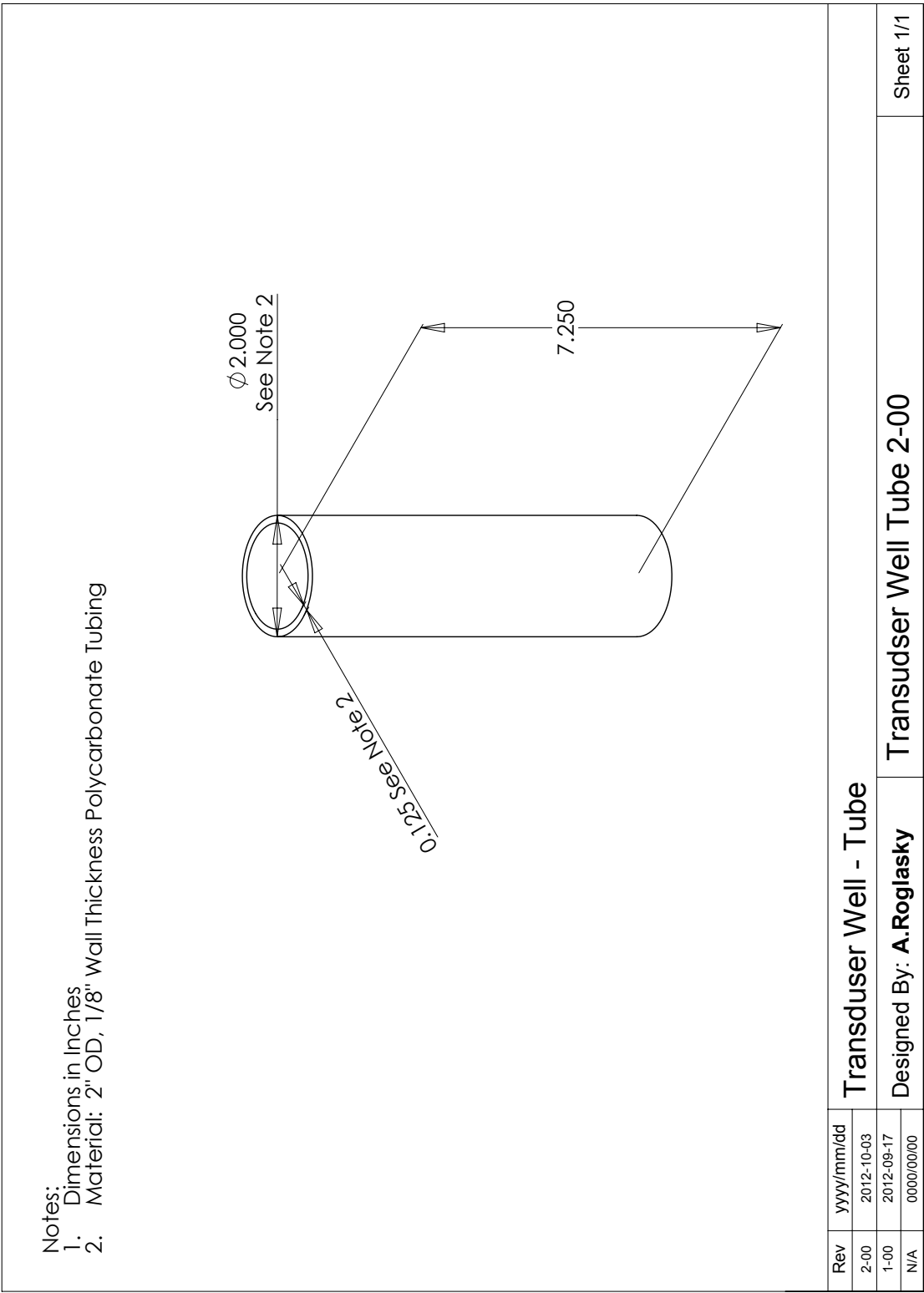


Figure C.10: Transducer Well Assembly / Tube

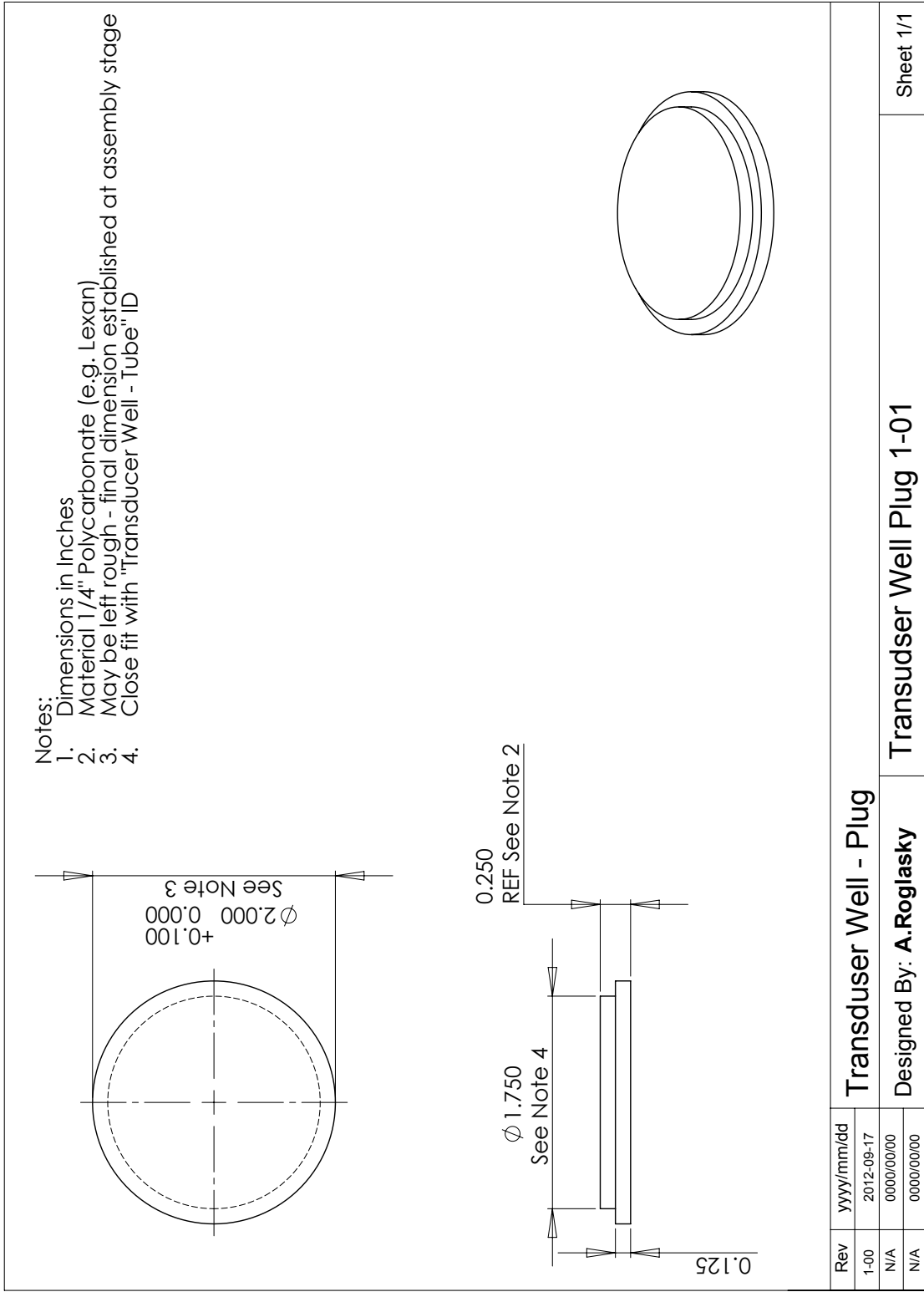


Figure C.11: Transducer Well Assembly / Plug

C.4 Thermal Isolation Spacer

Thermal Isolation Spacer Assembly 2-00

1. Top Flange
2. Tube
3. Bottom Flange
4. Thermal Spacer Lid

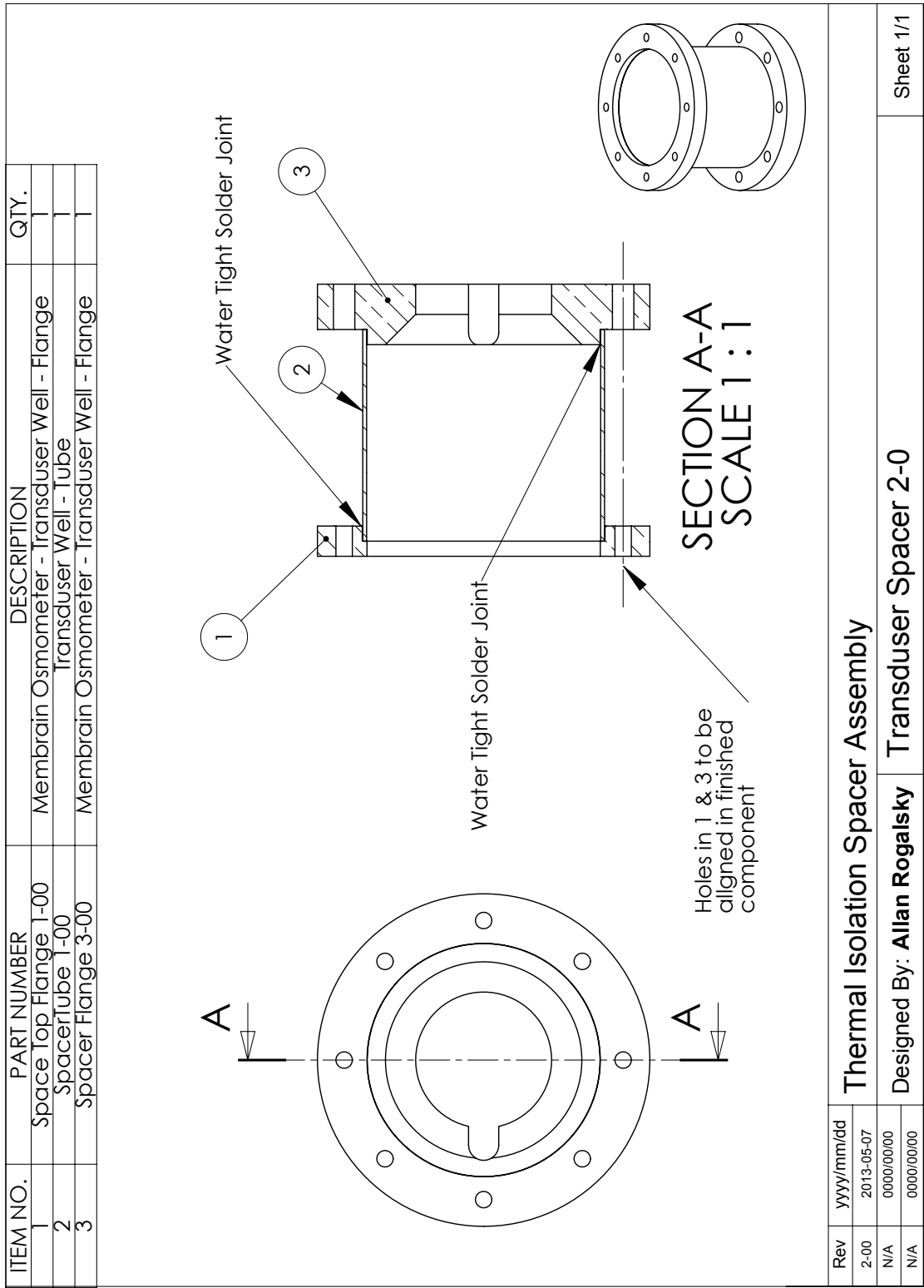


Figure C.12: Thermal Isolation Spacer Assembly

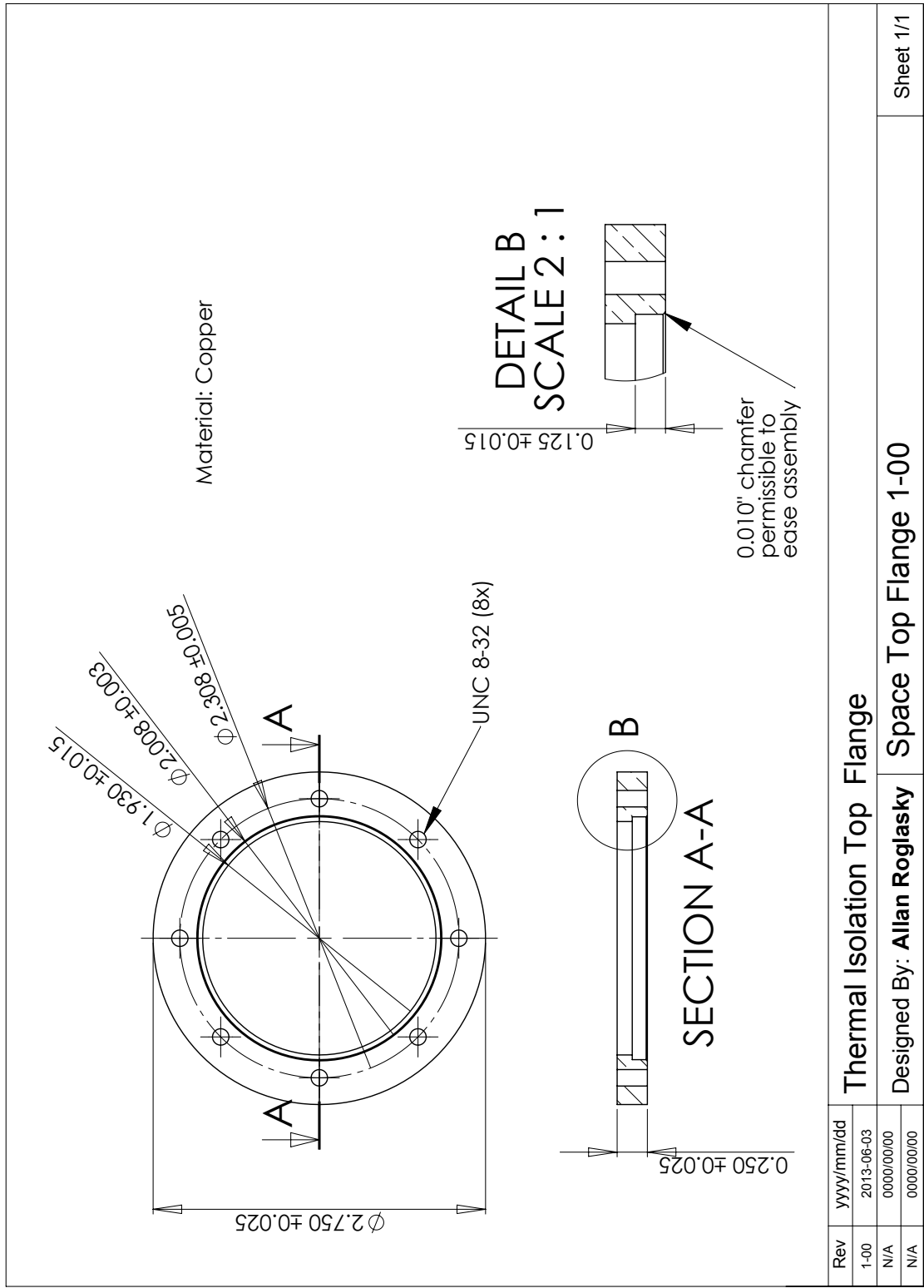


Figure C.13: Thermal Isolation Spacer Assembly / Top Flange

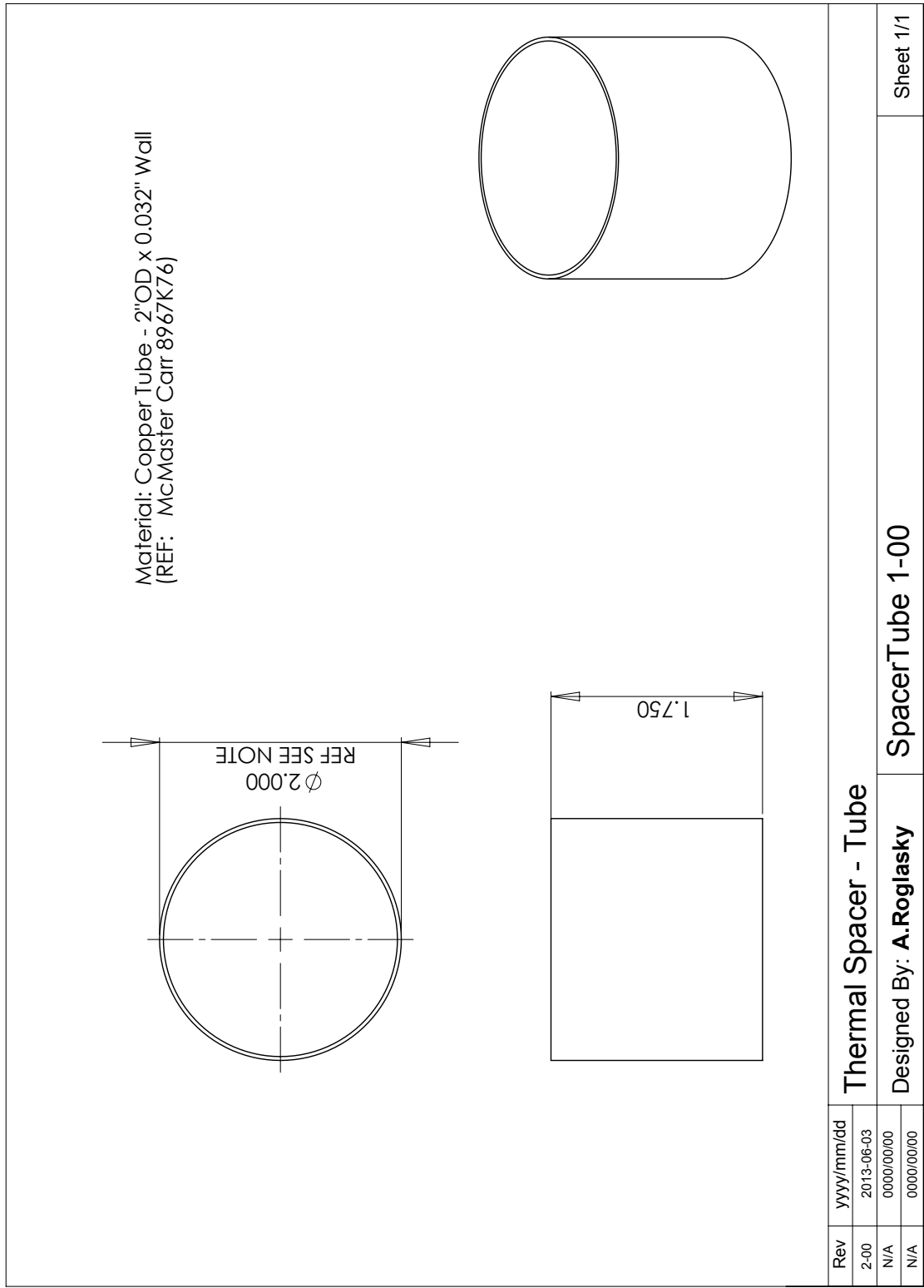


Figure C.14: Thermal Isolation Spacer Assembly / Tube

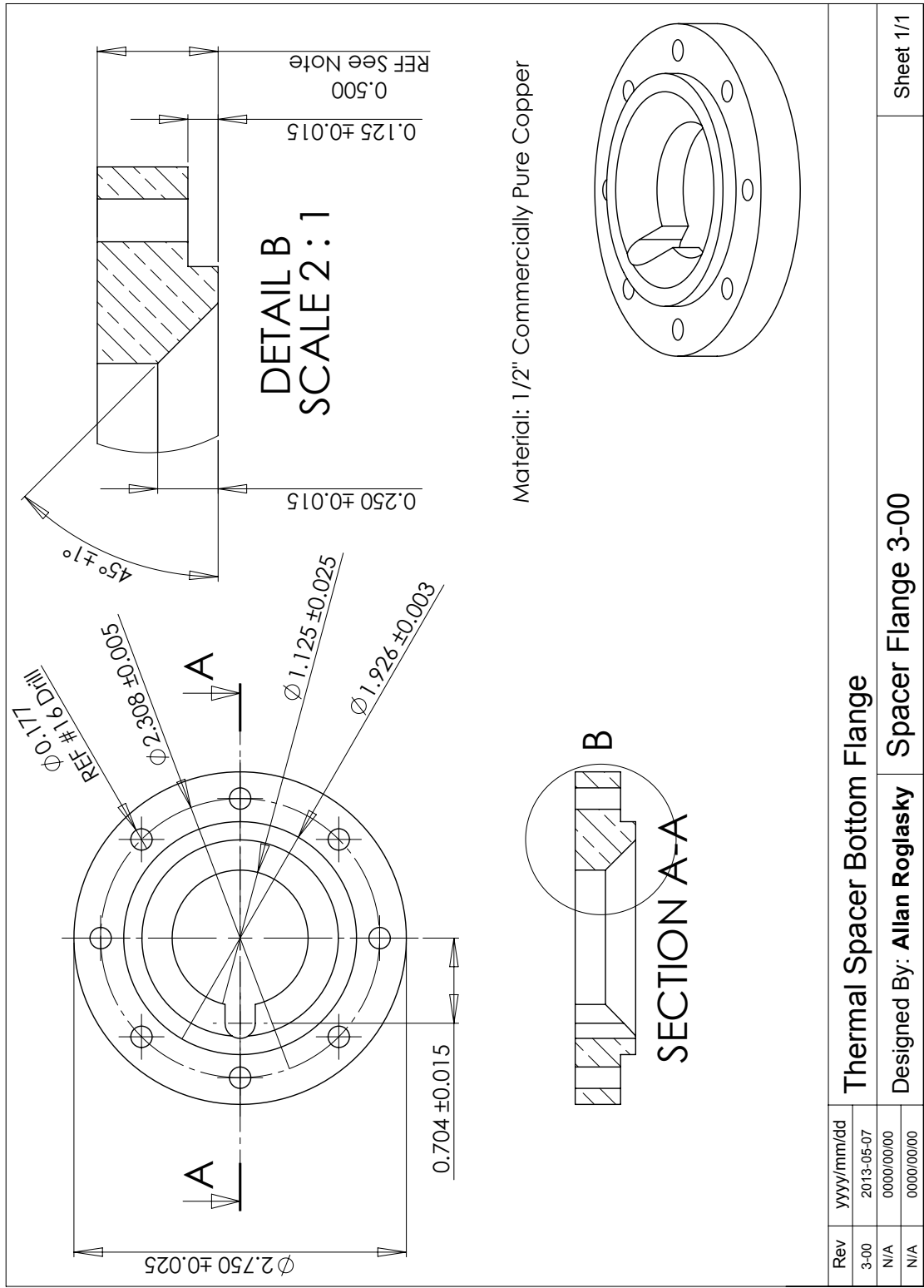


Figure C.15: Thermal Isolation Spacer Assembly / Bottom Flange

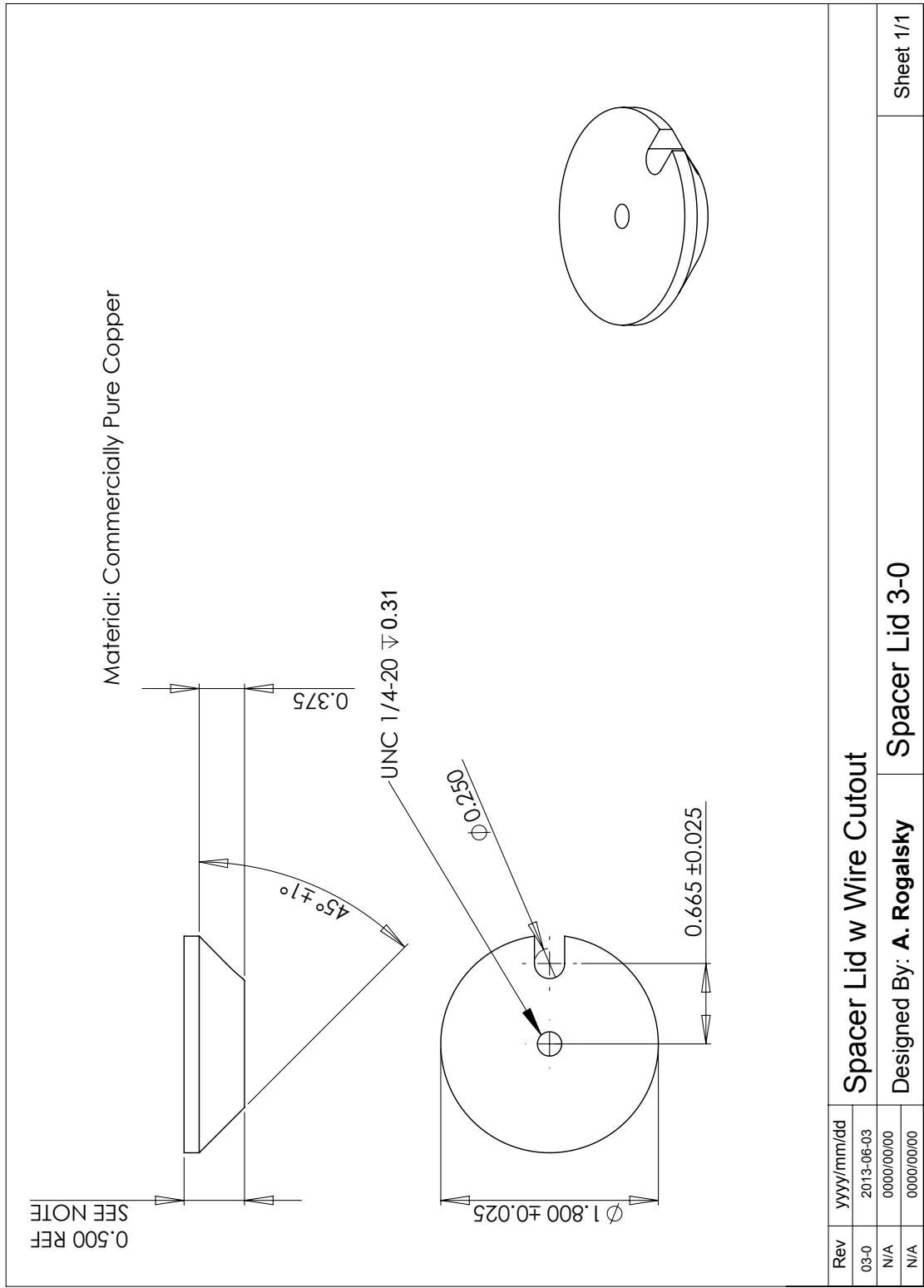


Figure C.16: Thermal Spacer Lid

C.5 Water Bath Components

Waterbath Lid 1-00

Hotplate Based Bath Lid

Circulating Bath Lid 1-00

Adapter for Circulating Bath

Circulating Bath Assembly 2-00

1. Thermal Spacer Lid
2. Bottom
3. Side
4. Front
5. Back
6. Brace

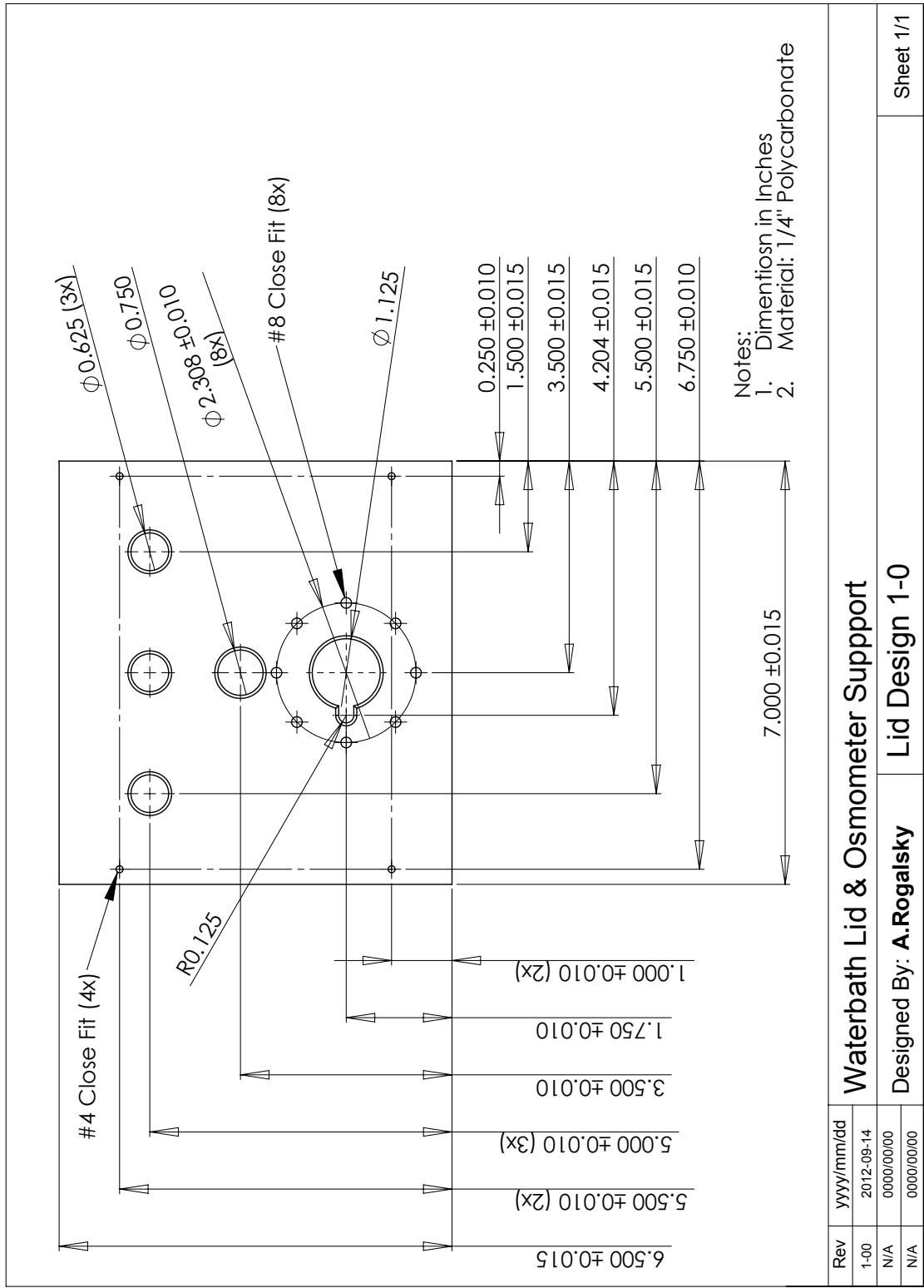


Figure C.17: Hotplate Based Bath Lid

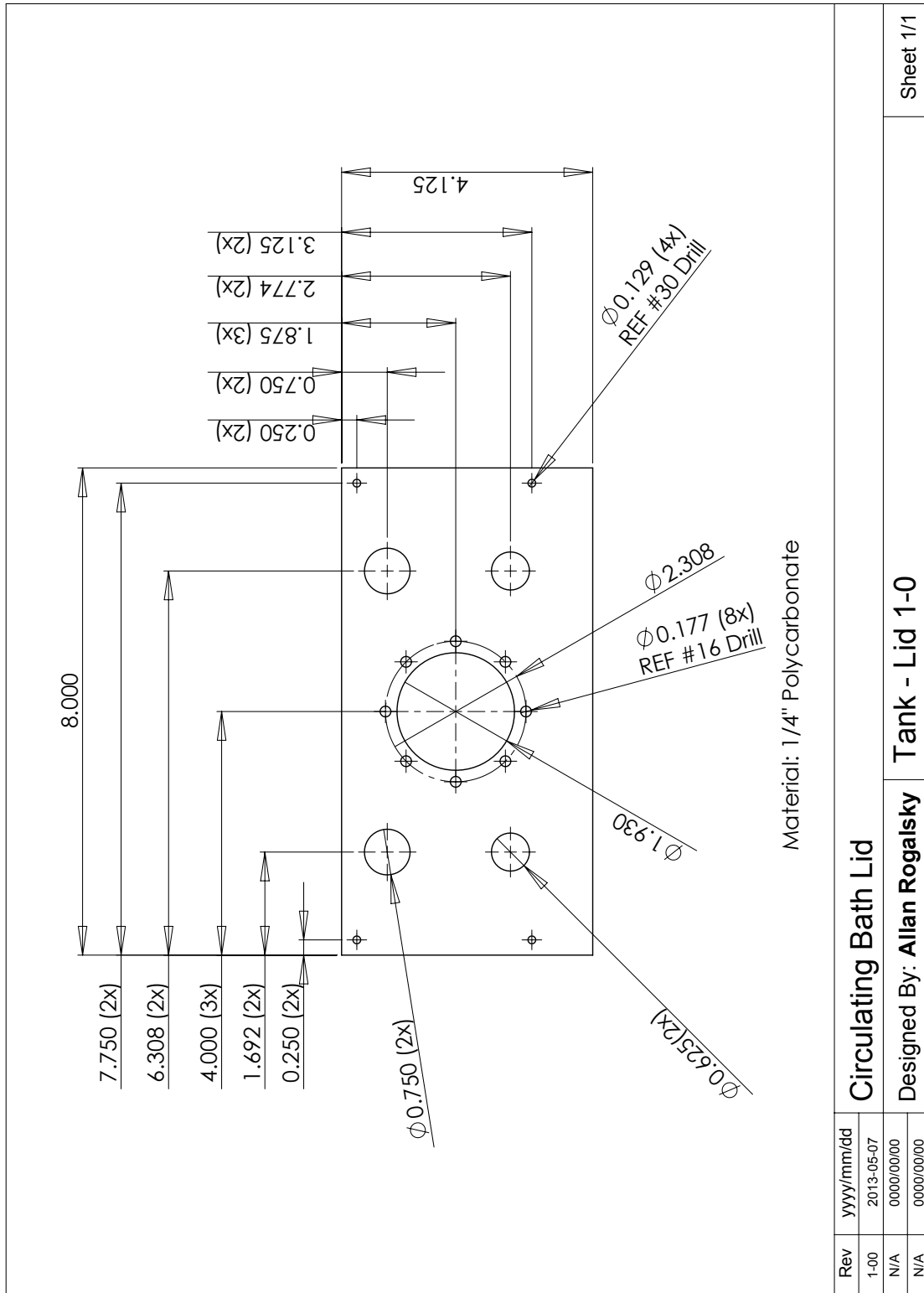


Figure C.18: Circulating Bath Lid

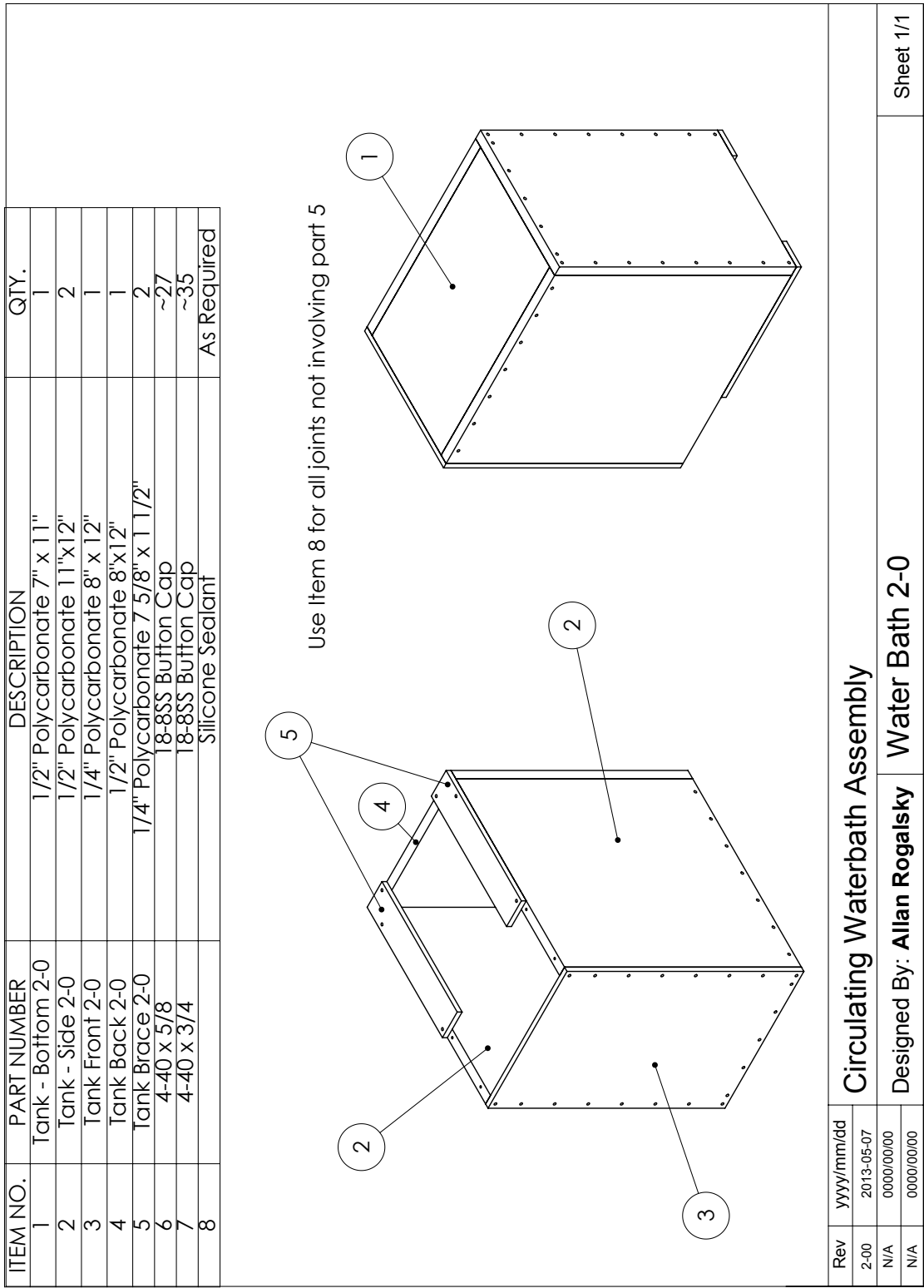


Figure C.19: Circulating Bath Assembly

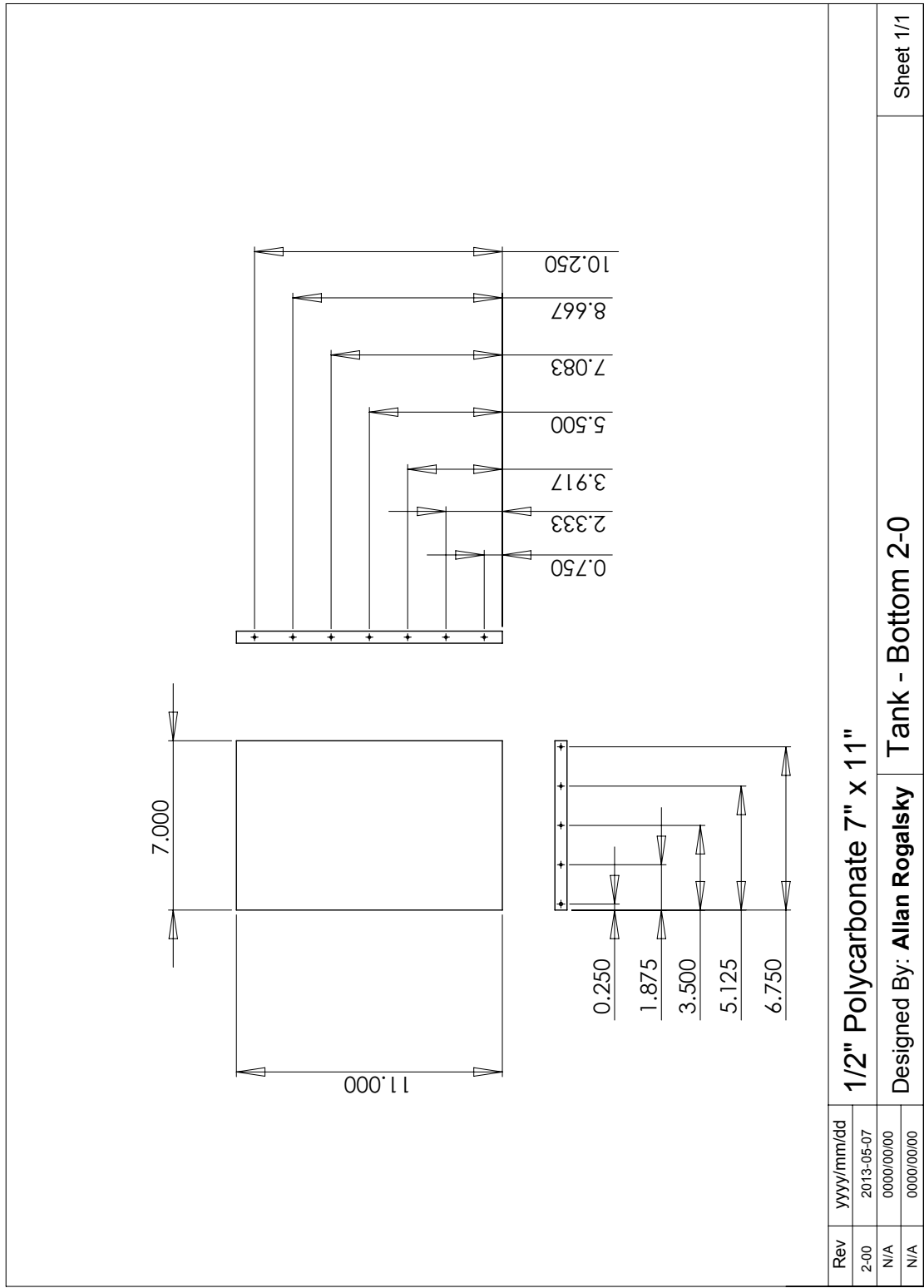


Figure C.20: Circulating Bath Assembly / Bottom

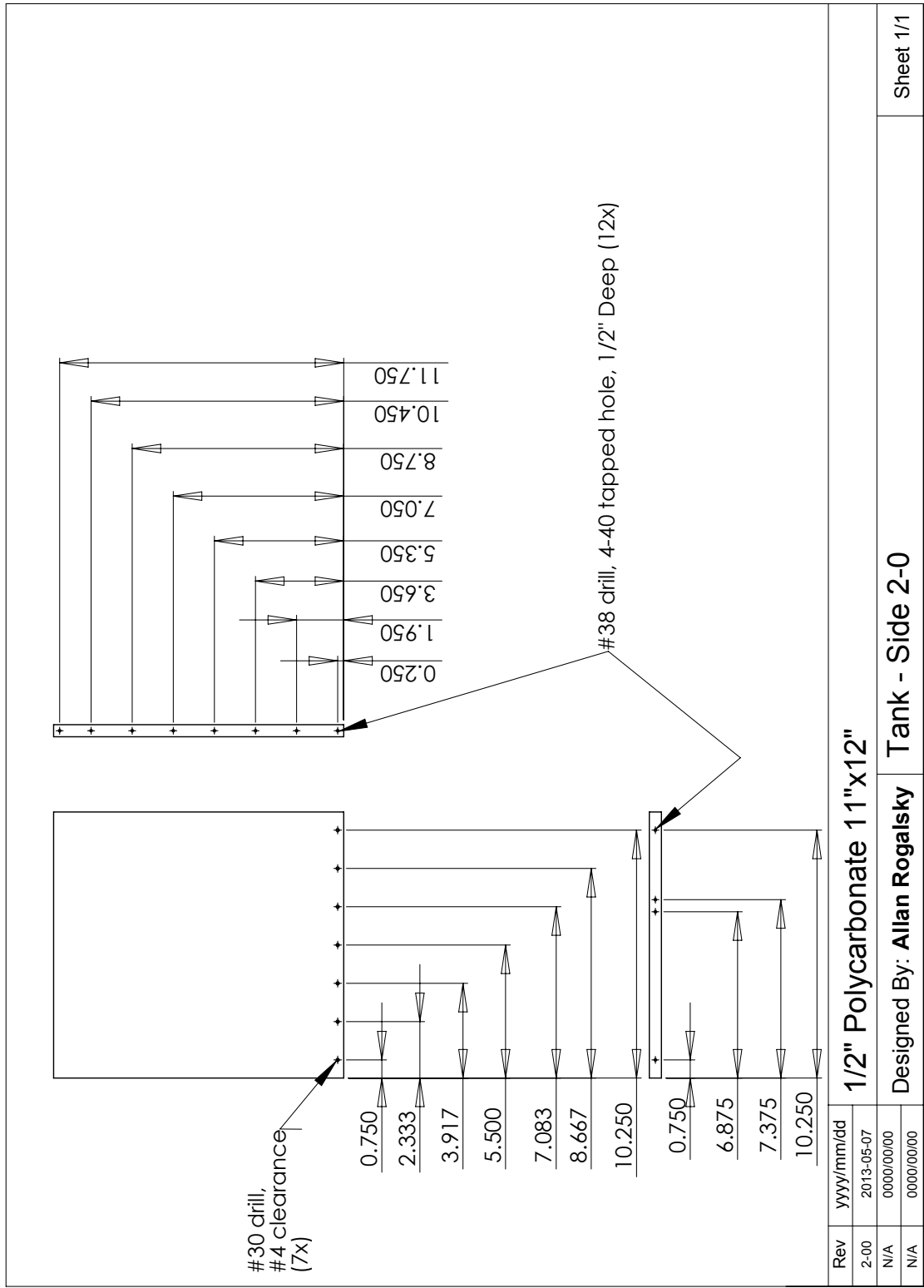


Figure C.21: Circulating Bath Assembly / Side

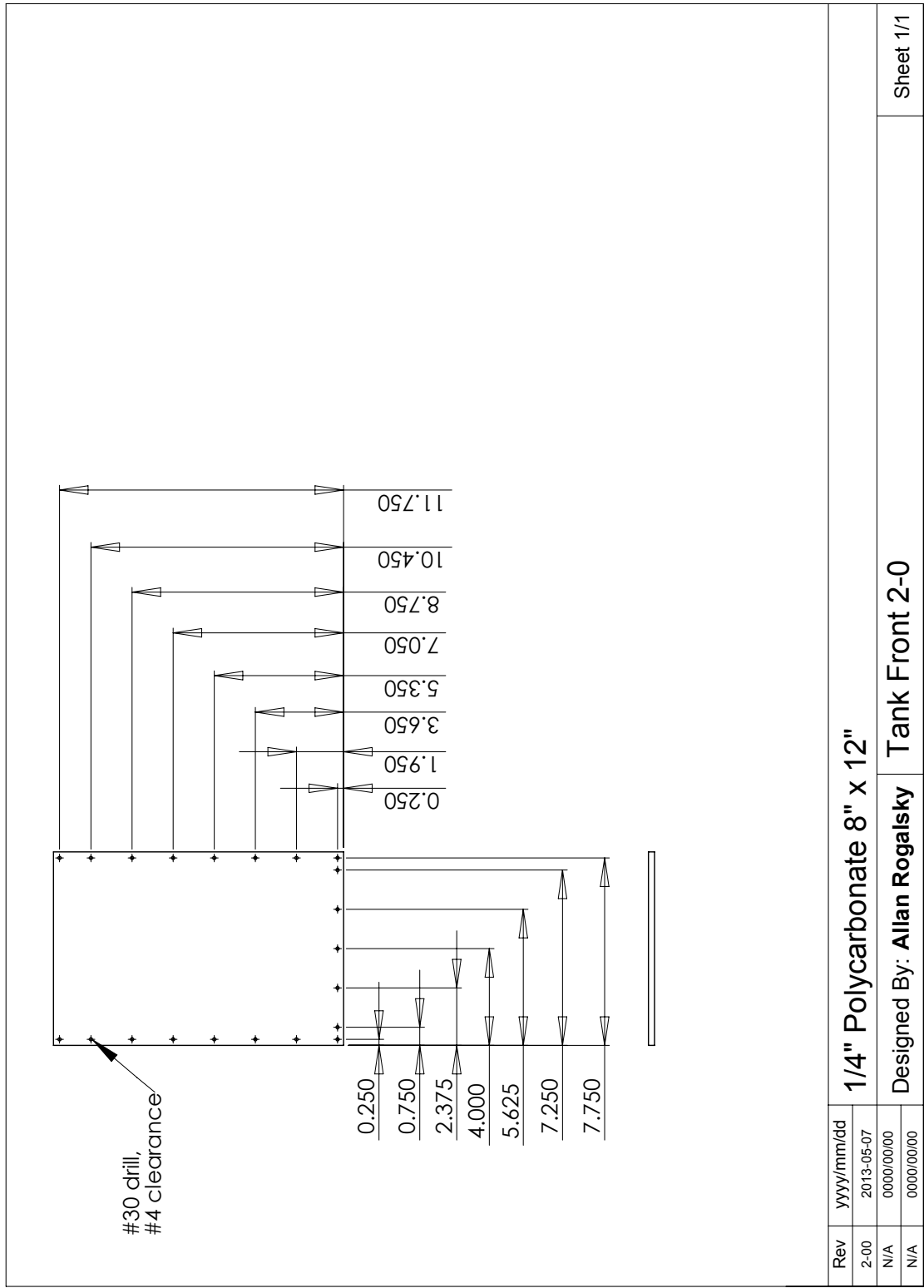


Figure C.22: Circulating Bath Assembly / Front

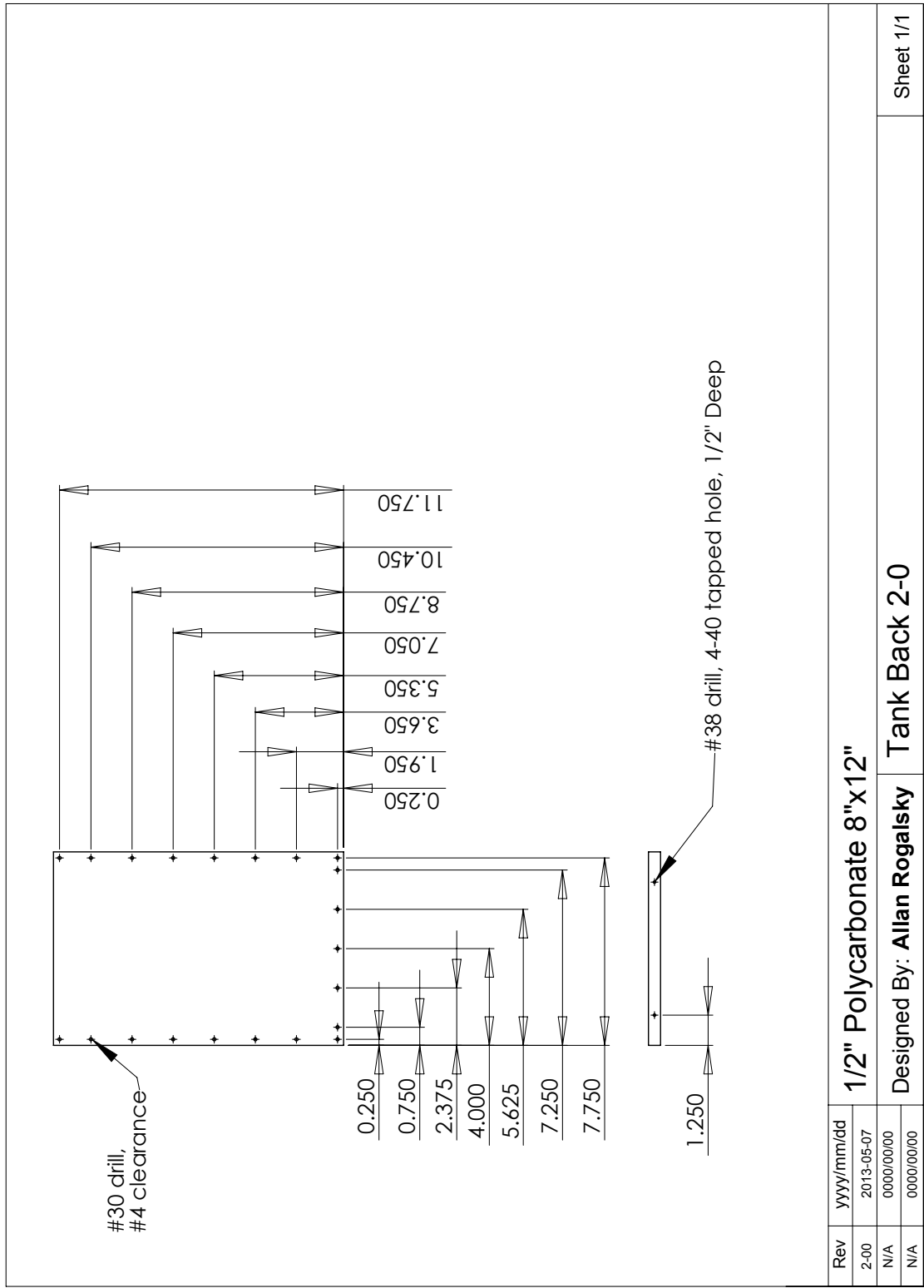


Figure C.23: Circulating Bath Assembly / Back

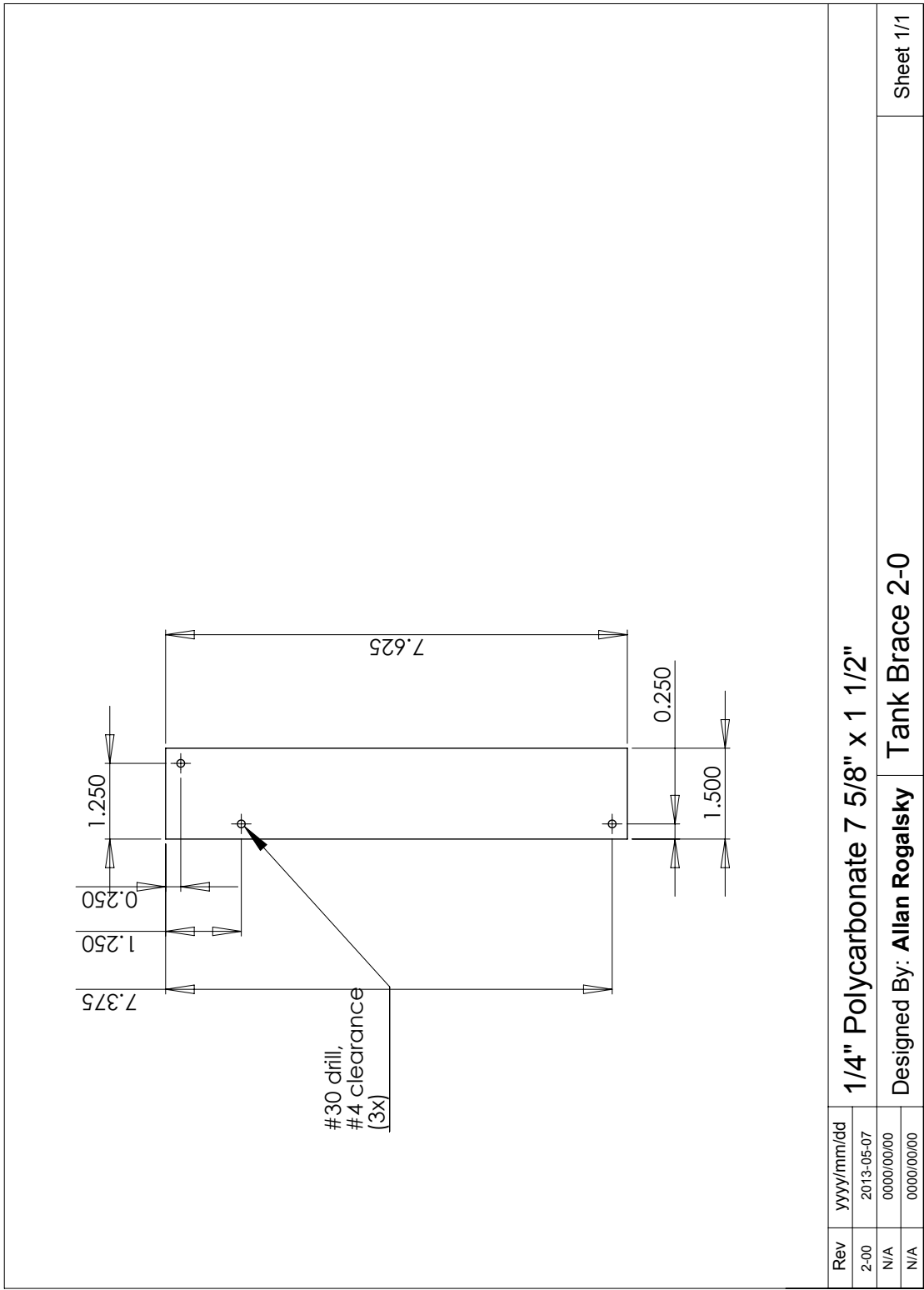


Figure C.24: Circulating Bath Assembly / Brace

C.6 Miscellaneous Tools

Manometer Fitting

Fitting for attaching a calibration manometer

Membrane and Gasket Preparation Tools

1. Membrane and Gasket OD Punch
2. Gasket ID Punch
3. Membrane Template
4. Gasket Template

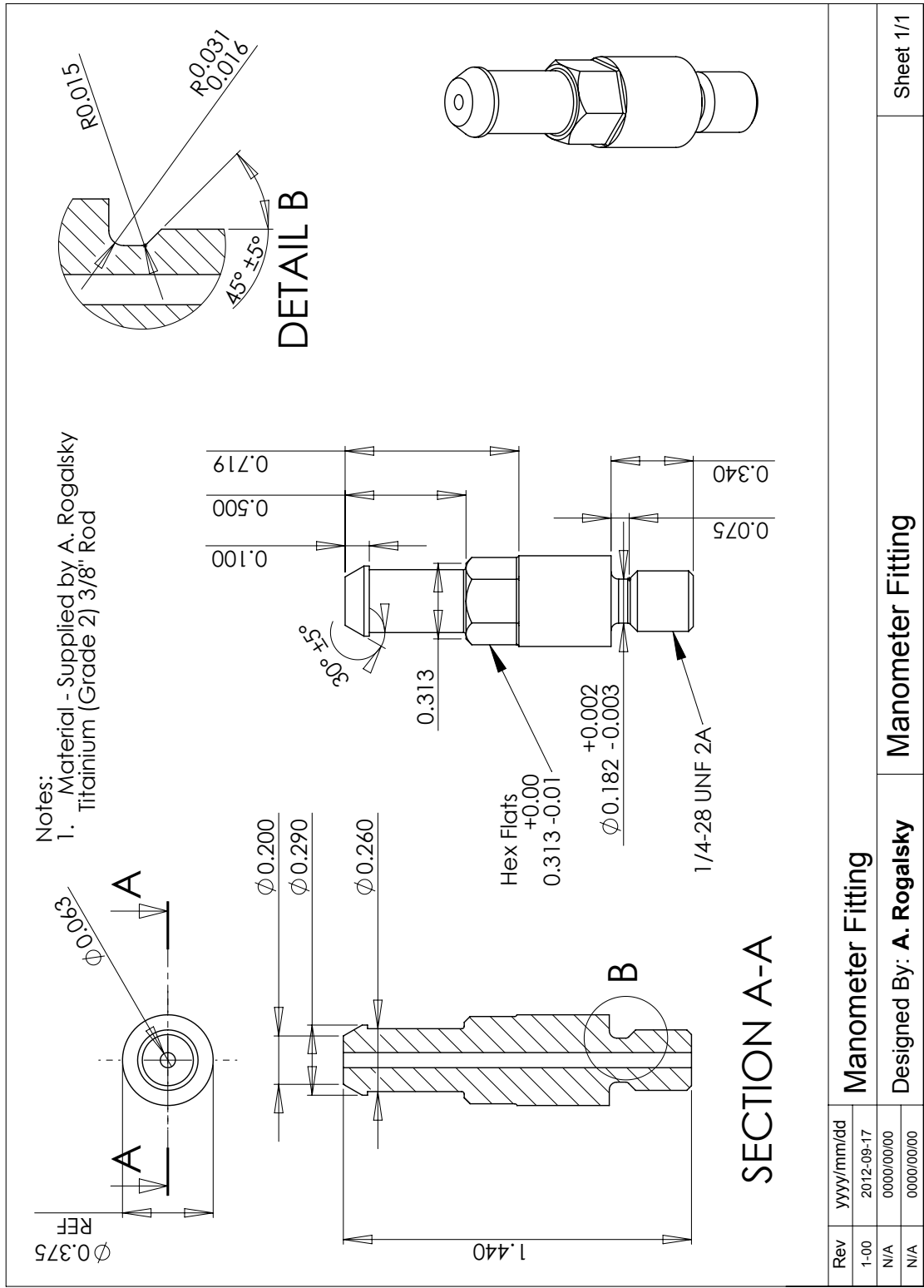


Figure C.25: Manometer Fitting to Check Transducer Calibration

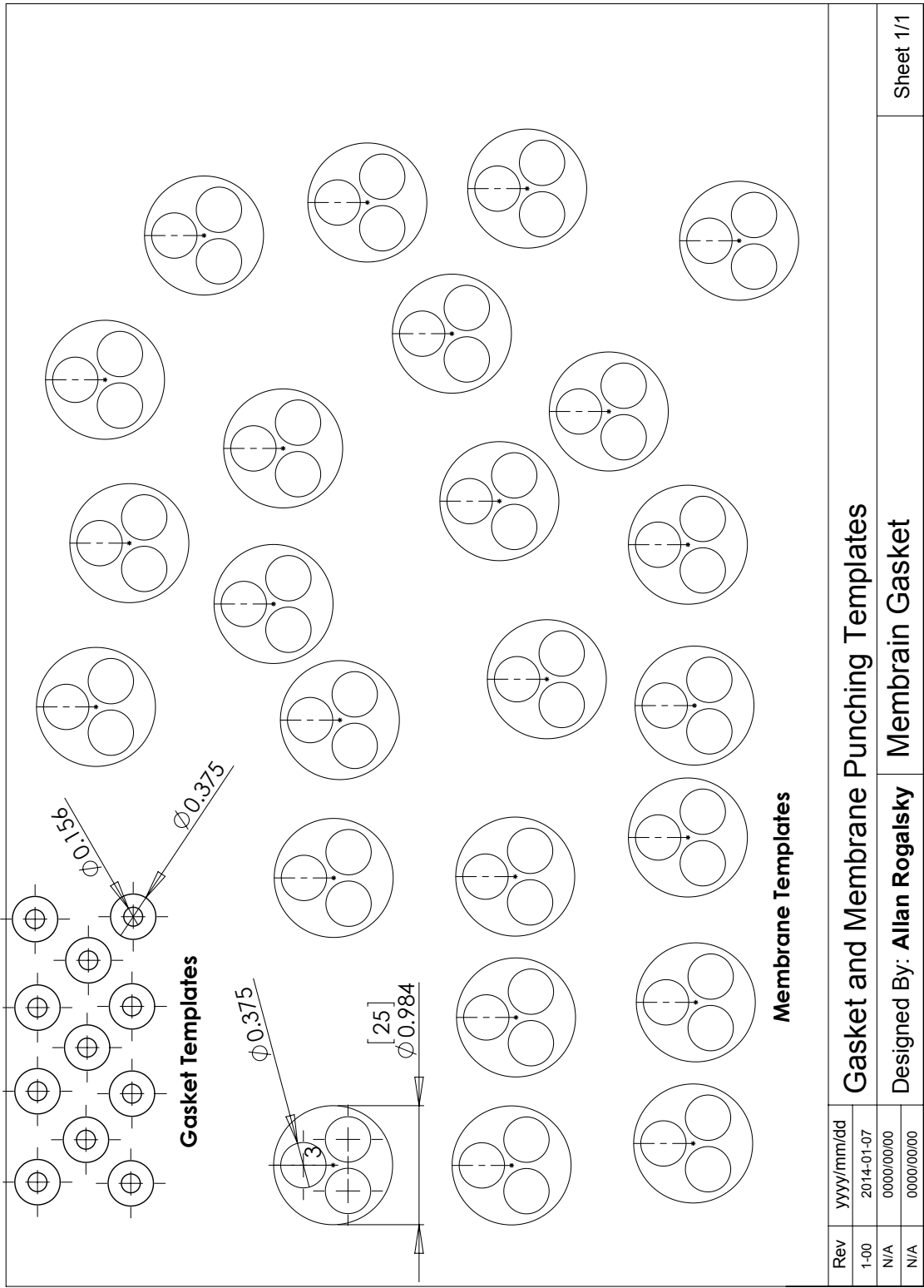


Figure C.26: Template for Punching Membrane and Gasket

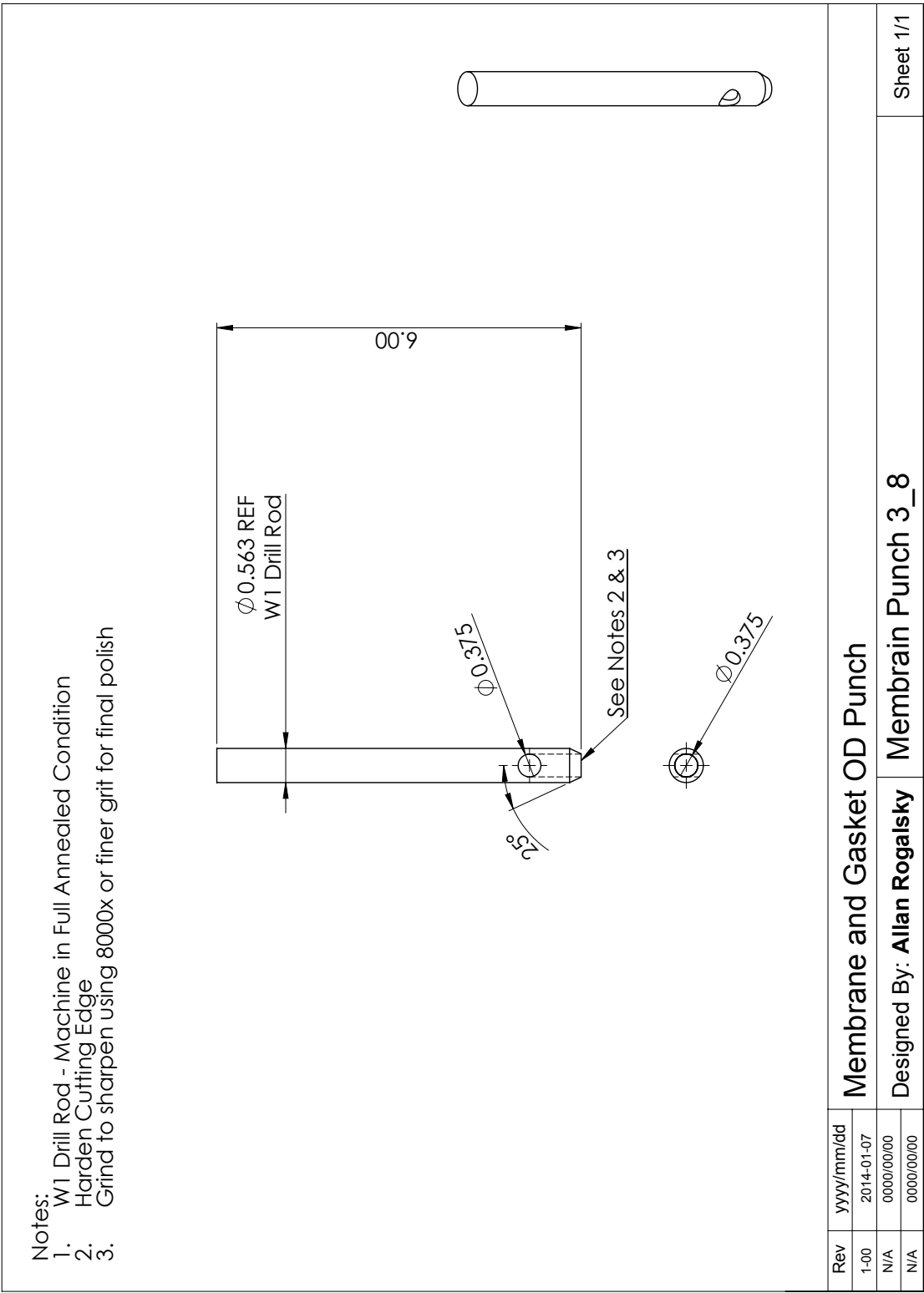


Figure C.27: Membrane and Gasket OD Punch

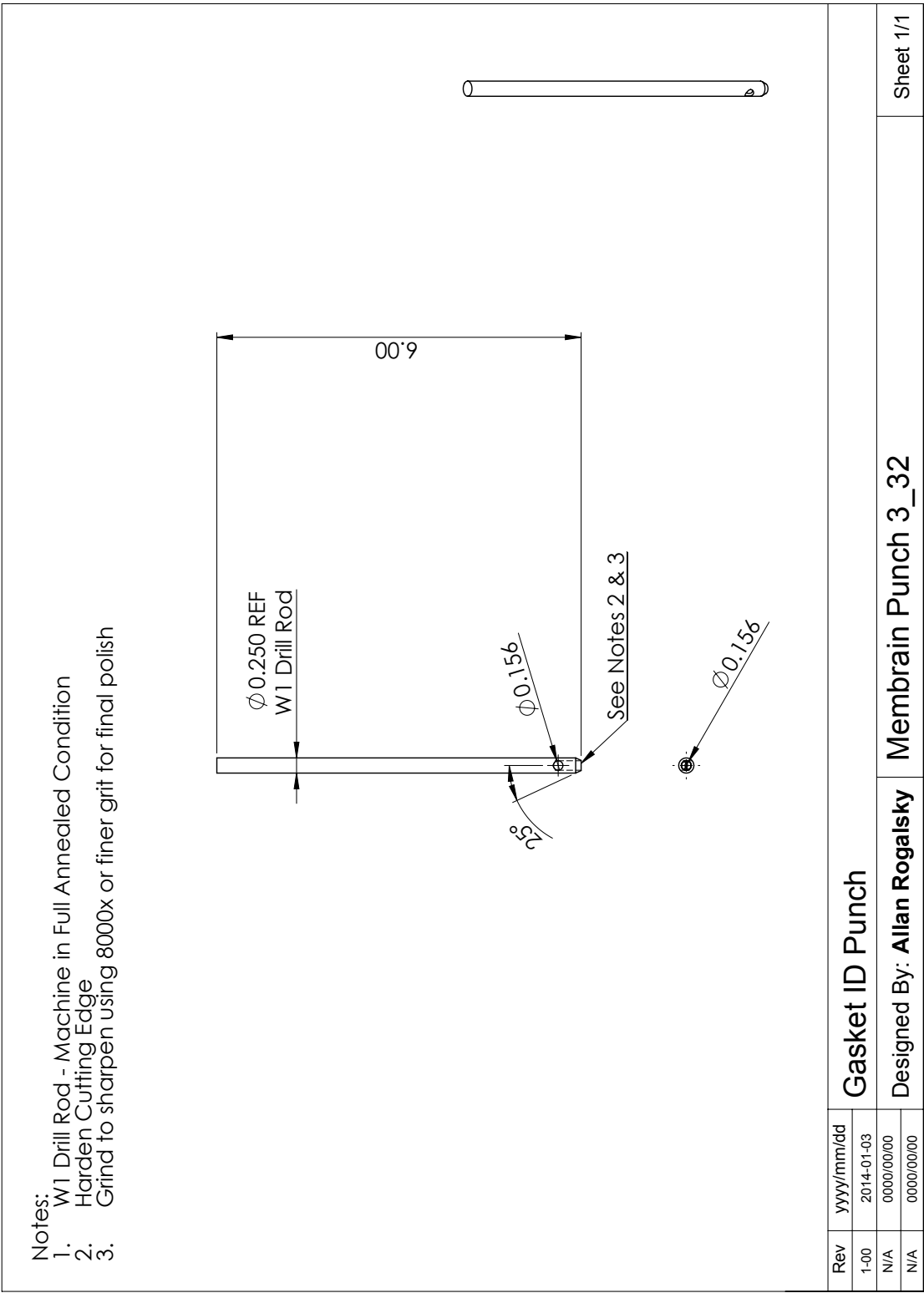


Figure C.28: Gasket ID Punch

C.7 Solution Degassing

Table C.1: Degassing Lid Bill of Materials

Item Number	Part Number	Description	Quantity
1	5478K311 ^a	Quick Connect, 1/8" NPT to 1/8" Plug	1
2	4912K71 ^a	Valve, 1/8" NPT Male to Female	1
3	93303A106 ^a	Gasket, Aramid fiber reinforced Buna-N, 3/8" ID	1
4	430829 ^b	Lid, 50ml Centrifuge Vial, 0.413" \varnothing hole added	1
5	50785K141 ^a	Nut, 1/8" NPT	1

^a McMaster-Carr

^b Corning Life Sciences

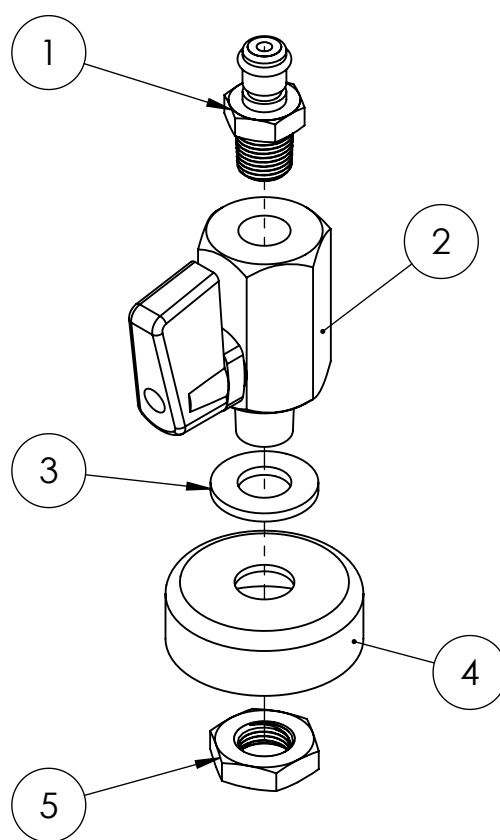


Figure C.29: Degassing Tube Lid Design: Numbers correspond to items in Table C.1

C.8 Detailed Setup Procedure

1. Reference Solution Degas, Water bath start.
2. Transducer Fill/Initial Rinse (held upright in retort stand)
3. Support and gasket rinse
4. Membrane Rinse (Degassed solution not too hot)
5. Core O-Ring Installation
 - (a) Immerse O-ring in degassed solution
 - (b) Fill groove area with ref solution
 - (c) Bring o-ring with suspended drop of ref solution into grove area and press into groove under film of water.
6. Flush and install core
 - (a) Wear clean gloves.
 - (b) With thumb lightly over membrane seat, use blunt needle to flush center channel with ref solution, should feel bubbles and then stream of solution against thumb.
 - (c) Keeping channel sealed add ref to bottom of core until maximum hanging drop size achieved.
 - (d) Bring drop on core into contact with drop on transducer and smoothly lower core to minimize chance of trapped air bubbles.
 - (e) Start screw, keeping channel sealed until well into first turn.
 - (f) Rapidly screw down core allowing escaping ref solution to further flush channel.
7. Final rinse
 - (a) Obtain fresh tube of degassed ref direct from degassing operation (ideally still at temp and boiling under vacuum).
 - (b) Open and fill syringe.
 - (c) Run needle down into osmometer core being careful with depth so as to not touch the transducer.
 - (d) Depress plunger gently while withdrawing needle to thoroughly flush core with fresh degassed solution.
8. Install Membrane Support
 - (a) Tip support from rinse solution into dish used to fill core.

- (b) Pick up support along with hanging drop and push into its socket
- (c) Refill syringe from hot degassed ref and flush support (pressure should partially lift support out of socket, use syringe tip to keep it in place).

9. Install Membrane

- (a) Tip membrane into dish used for core assembly, flip and weight down with gasket.
- (b) Pick up membrane and gasket insuring hanging drop.
- (c) Slip edgewise into pool over support.
- (d) Use tweezers to prevent membrane escape while core area is rinsed with hot degassed ref
- (e) Lower sample chamber and lightly tighten 4 screws.
- (f) Insure sample side of membrane is topped up with degassed ref.

10. Lower assembly into thermal well, add thermal isolation spacer, check o-rings, bolt down.

11. Using sides of thermal well as guide align transducer / core assembly by manipulating membrane clamp screws.

12. Attach to cover plate and lower into bath

13. Wait for thermal equilibrium (~45 min)

14. Tighten clamping screws in 4 stages. (torques and timings are dependent on membrane permeability, experimentally determine)

15. Leave overnight to reach thermal, mechanical and chemical (dissolved gas) equilibrium

References

- [1] W. M. Haynes, Ed., *CRC handbook of chemistry and physics, 95th Ed.* CRC Press/Taylor and Francis, 2015, [E-book] Available: CRCnetBASE.
- [2] T. R. Hoare and D. S. Kohane, “Hydrogels in drug delivery: progress and challenges,” *Polymer*, vol. 49, no. 8, pp. 1993–2007, 2008. DOI: <http://dx.doi.org/10.1016/j.polymer.2008.01.027>.
- [3] J. L. Drury and D. J. Mooney, “Hydrogels for tissue engineering: scaffold design variables and applications,” *Biomaterials*, vol. 24, no. 24, pp. 4337–4351, 2003, Synthesis of Biomimetic Polymers. DOI: [http://dx.doi.org/10.1016/S0142-9612\(03\)00340-5](http://dx.doi.org/10.1016/S0142-9612(03)00340-5).
- [4] M. S. Shoichet, “Polymer scaffolds for biomaterials applications,” *Macromolecules*, vol. 43, no. 2, pp. 581–591, 2010. DOI: [10.1021/ma901530r](http://dx.doi.org/10.1021/ma901530r).
- [5] S. V. Vlierberghe, P. Dubruel, and E. Schacht, “Biopolymer-based hydrogels as scaffolds for tissue engineering applications: a review,” *Biomacromolecules*, vol. 12, no. 5, pp. 1387–1408, 2011, PMID: 21388145. DOI: [10.1021/bm200083n](http://dx.doi.org/10.1021/bm200083n).
- [6] D. E. Discher, P. Janmey, and Y.-l. Wang, “Tissue cells feel and respond to the stiffness of their substrate,” *Science*, vol. 310, no. 5751, pp. 1139–1143, 2005. DOI: [10.1126/science.1116995](http://dx.doi.org/10.1126/science.1116995).
- [7] Q.-Z. Chen, S. E. Harding, N. N. Ali, A. R. Lyon, and A. R. Boccaccini, “Biomaterials in cardiac tissue engineering: ten years of research survey,” *Materials Science and Engineering: R: Reports*, vol. 59, pp. 1–37, 2008. DOI: <http://dx.doi.org/10.1016/j.mser.2007.08.001>.
- [8] M. Mekhail and M. Tabrizian, “Injectable chitosan-based scaffolds in regenerative medicine and their clinical translatability,” *Advanced Healthcare Materials*, vol. 3, no. 10, pp. 1529–1545, 2014. DOI: [10.1002/adhm.201300586](http://dx.doi.org/10.1002/adhm.201300586).
- [9] C. Wang, R. J. Stewart, and J. Kopeček, “Hybrid hydrogels assembled from synthetic polymers and coiled-coil protein domains,” *Nature*, vol. 397, no. 6718, pp. 417–420, Feb. 1999. DOI: [10.1038/17092](http://dx.doi.org/10.1038/17092).
- [10] M. Santin, Ed., *Strategies in Regenerative Medicine*. Springer New York, 2009. DOI: [10.1007/978-0-387-74660-9](http://dx.doi.org/10.1007/978-0-387-74660-9).

- [11] H. Tan and K. G. Marra, "Injectable, biodegradable hydrogels for tissue engineering applications," *Materials*, vol. 3, no. 3, p. 1746, 2010. DOI: 10.3390/ma3031746.
- [12] G. Vunjak-Novakovic, K. O. Lui, N. Tandon, and K. R. Chien, "Bioengineering heart muscle: a paradigm for regenerative medicine," *Annual Review of Biomedical Engineering*, vol. 13, no. 1, pp. 245–267, 2011, PMID: 21568715. DOI: 10.1146/annurev-bioeng-071910-124701.
- [13] N. Annabi, J. W. Nichol, X. Zhong, C. Ji, S. Koshy, A. Khademhosseini, and F. Dehghani, "Controlling the porosity and microarchitecture of hydrogels for tissue engineering," *Tissue Engineering Part B: Reviews*, vol. 16, no. 4, pp. 371–383, 2010. DOI: 10.1089=ten.teb.2009.0639.
- [14] A. W.-J. Chan, "Controlled synthesis of stimuli-responsive network alginate," PhD thesis, Queens University, Kingston, Ontario, Canada, Jul. 2009.
- [15] L. Brannon-Peppas and N. A. Peppas, "Equilibrium swelling behavior of ph-sensitive hydrogels," *Chemical Engineering Science*, vol. 46, no. 3, pp. 715–722, 1991. DOI: [http://dx.doi.org/10.1016/0009-2509\(91\)80177-Z](http://dx.doi.org/10.1016/0009-2509(91)80177-Z).
- [16] L. Brannon-Peppas and N. A. Peppas, "Equilibrium swelling behavior of dilute ionic hydrogels in electrolytic solutions," *Journal of Controlled Release*, vol. 16, no. 3, pp. 319–329, 1991. DOI: [http://dx.doi.org/10.1016/0168-3659\(91\)90009-3](http://dx.doi.org/10.1016/0168-3659(91)90009-3).
- [17] A. Keller, "Introductory lecture: aspects of polymer gels," *Faraday Discuss.*, vol. 101, pp. 1–49, 0 1995. DOI: 10.1039/FD9950100001.
- [18] K. S. Anseth, C. N. Bowman, and L. Brannon-Peppas, "Mechanical properties of hydrogels and their experimental determination," *Biomaterials*, vol. 17, no. 17, pp. 1647–1657, 1996. DOI: [http://dx.doi.org/10.1016/0142-9612\(96\)87644-7](http://dx.doi.org/10.1016/0142-9612(96)87644-7).
- [19] N. A. Peppas, *Hydrogels in Medicine and Pharmacy*. CRC Pres, Inc., 2000.
- [20] A. V. Dobrynin, R. H. Colby, and M. Rubinstein, "Polyampholytes," *Journal of Polymer Science Part B: Polymer Physics*, vol. 42, no. 19, pp. 3513–3538, 2004. DOI: 10.1002/polb.20207.
- [21] T. Painter and B. Larsen, "Formation of hemiacetals between neighbouring hexuronic acid residues during the periodate oxidation of alginate," *acta Chemica Scandinavica.*, vol. 24, pp. 813–833, 1970. DOI: <http://actachemscand.org/doi/10.3891/acta.chem.scand.24-0813>.
- [22] M. George and T. E. Abraham, "Polyionic hydrocolloids for the intestinal delivery of protein drugs: alginate and chitosan a review," *Journal of Controlled Release*, vol. 114, no. 1, pp. 1–14, 2006. DOI: <http://dx.doi.org/10.1016/j.jconrel.2006.04.017>.
- [23] C. Gomez, M. Rinaudo, and M. Villar, "Oxidation of sodium alginate and characterization of the oxidized derivatives," *Carbohydrate Polymers*, vol. 67, pp. 296–304, 2007. DOI: <http://dx.doi.org/10.1016/j.carbpol.2006.05.025>.

- [24] R. Yamaguchi, Y. Arai, T. Itoh, and S. Hirano, "Preparation of partiality N-succinylated chitosans and their cross-linked gels," *Carbohydr. Res.*, vol. 88, pp. 172–175, 1970.
- [25] B. Erman and J. Mark, *Structures and Properties of Rubberlike Networks*, ser. Topics in polymer science : a series of advanced textbooks and monographs. Oxford University Press, 1997.
- [26] P. J. Flory, *Principles of Polymer Chemistry*. Cornell University Press, 1953.
- [27] B. Guo, A. Elgsaeter, and B. T. Stokke, "Gelation kinetics of scleraldehyde-chitosan co-gels," *Polymer Gels and Networks*, vol. 6, no. 2, pp. 113–135, 1998. DOI: [http://dx.doi.org/10.1016/S0966-7822\(98\)00005-7](http://dx.doi.org/10.1016/S0966-7822(98)00005-7).
- [28] H. Tan, C. R. Chu, K. A. Payne, and K. G. Marra, "Injectable in situ forming biodegradable chitosan-hyaluronic acid based hydrogels for cartilage tissue engineering," *Biomaterials*, vol. 30, no. 13, pp. 2499–2506, 2009. DOI: <http://dx.doi.org/10.1016/j.biomaterials.2008.12.080>.
- [29] S. L. M. Liu, and B. Ni, "An injectable oxidized carboxymethylcellulose/N-succinyl-chitosan hydrogel system for protein delivery," *Chemical Engineering Journal*, vol. 160, no. 2, pp. 779–787, 2010. DOI: <http://dx.doi.org/10.1016/j.cej.2010.03.072>.
- [30] A. Serrero, S. Trombotto, P. Cassagnau, Y. Bayon, P. Gravagna, S. Montanari, and L. David, "Polysaccharide gels based on chitosan and modified starch: structural characterization and linear viscoelastic behavior," *Biomacromolecules*, vol. 11, no. 6, pp. 1534–1543, 2010, PMID: 20507059. DOI: [10.1021/bm1001813](https://doi.org/10.1021/bm1001813).
- [31] A. D. Rogalsky, H. J. Kwon, and P. Lee-Sullivan, "Compressive stress-strain response of covalently crosslinked oxidized-alginate/N-succinyl-chitosan hydrogels," *Journal of Biomedical Materials Research Part A*, vol. 99A, pp. 367–375, 2011.
- [32] L.-H. Fan, X.-R. Pan, Y. Zhou, L.-Y. Chen, W.-G. Xie, Z.-H. Long, and H. Zheng, "Preparation and characterization of crosslinked carboxymethyl chitosan-oxidized sodium alginate hydrogels," *Journal of Applied Polymer Science*, vol. 122, no. 4, pp. 2331–2337, 2011. DOI: [10.1002/app.34041](https://doi.org/10.1002/app.34041).
- [33] E. A. Kamoun, "N-succinyl chitosan-dialdehyde starch hybrid hydrogels for biomedical applications," *Journal of Advanced Research*, pp. 2090–1232, 2015. DOI: <http://dx.doi.org/10.1016/j.jare.2015.02.002>.
- [34] K. A. Kristiansen, A. Potthast, and B. E. Christensen, "Periodate oxidation of polysaccharides for modification of chemical and physical properties," *Carbohydrate Research*, vol. 345, no. 10, pp. 1264–1271, 2010, Special Issue: Selected Papers from the 15th European Carbohydrate Symposium, Vienna 2009. DOI: <http://dx.doi.org/10.1016/j.carres.2010.02.011>.

- [35] B. V. Slaughter, S. S. Khurshid, O. Z. Fisher, A. Khademhosseini, and N. A. Peppas, "Hydrogels in regenerative medicine," *Advanced Materials*, vol. 21, no. 32-33, pp. 3307–3329, 2009. DOI: [10.1002/adma.200802106](https://doi.org/10.1002/adma.200802106).
- [36] K. S. Anseth, A. T. Metters, S. J. Bryant, P. J. Martens, J. H. Elisseeff, and C. N. Bowman, "In situ forming degradable networks and their application in tissue engineering and drug delivery," *Journal of Controlled Release*, vol. 78, no. 1-3, pp. 199–209, 2002, Proceedings on the Tenth International Symposium on Recent Advances in Drug Delivery Systems. DOI: [http://dx.doi.org/10.1016/S0168-3659\(01\)00500-4](http://dx.doi.org/10.1016/S0168-3659(01)00500-4).
- [37] J. Li, W. R. K. Illeperuma, Z. Suo, and J. J. Vlassak, "Hybrid hydrogels with extremely high stiffness and toughness," *ACS Macro Letters*, vol. 3, no. 6, pp. 520–523, 2014. DOI: [10.1021/mz5002355](https://doi.org/10.1021/mz5002355).
- [38] C. Wang, J. Kopecek, and R. J. Stewart, "Hybrid hydrogels cross-linked by genetically engineered coiled-coil block proteins," *Biomacromolecules*, vol. 2, no. 3, pp. 912–920, 2001, PMID: 11710049. DOI: [10.1021/bm0155322](https://doi.org/10.1021/bm0155322).
- [39] J. Sun, C. Xiao, H. Tan, and X. Hu, "Covalently crosslinked hyaluronic acid-chitosan hydrogel containing dexamethasone as an injectable scaffold for soft tissue engineering," *Journal of Applied Polymer Science*, vol. 129, no. 2, pp. 682–688, 2013. DOI: [10.1002/app.38779](https://doi.org/10.1002/app.38779).
- [40] C. M. Hwang, S. Sant, M. Masaeli, N. N. Kachouie, B. Zamanian, S.-H. Lee, and A. Khademhosseini, *Biofabrication*, vol. 2, no. 3, p. 035 003, 2010. DOI: [10.1088/1758-5082/2/3/035003](https://doi.org/10.1088/1758-5082/2/3/035003).
- [41] T. D. Dziubla, "Macroporous hydrogels as vascularizable soft tissue - implant interfaces: materials characterization, in vitro evaluation, computer simulations, and applications in implantable drug delivery devices," PhD thesis, Drexel University, Philadelphia, Pennsylvania, USA, Nov. 2002.
- [42] P. C. Hiemenz, *Polymer Chemistry The Basic Concepts*. Marcel Dekker, Inc., 1984.
- [43] R. Stokes, "Thermodynamics of solutions," in *Activity Coefficients in Electrolyte Solutions*, K. Pitzer, Ed., CRC Press, 1991, pp. 1–28.
- [44] C. Gao, M. Liu, J. Chen, and X. Zhang, "Preparation and controlled degradation of oxidized sodium alginate hydrogel," *Polymer Degradation and Stability*, vol. 94, no. 9, pp. 1405–1410, 2009. DOI: <http://dx.doi.org/10.1016/j.polyimdegradstab.2009.05.011>.
- [45] ASTM Standard D3750-79 (1985), *Standard practice for determination of number-average molecular weight of polymers by membrane osmometry*, ASTM International, West Conshohocken, PA, 1990.

- [46] A. V. Dobrynin and M. Rubinstein, "Theory of polyelectrolytes in solutions and at surfaces," *Progress in Polymer Science*, vol. 30, no. 11, pp. 1049–1118, 2005. DOI: <http://dx.doi.org/10.1016/j.progpolymsci.2005.07.006>.
- [47] S. Kudaibergenov, "Recent advances in the study of synthetic polyampholytes in solutions," in *Polymer Latexes - Epoxide Resins - Polyampholytes*, ser. Advances in Polymer Science, vol. 144, Springer Berlin Heidelberg, 1999, pp. 115–197. DOI: 10.1007/3-540-68384-4_3.
- [48] E. F. S. Vieira, A. R. Cestari, C. Airoidi, and W. Loh, "Polysaccharide-based hydrogels: preparation, characterization, and drug interaction behaviour," *Biomacromolecules*, vol. 9, no. 4, pp. 1195–1199, 2008, PMID: 18345637. DOI: 10.1021/bm7011983.
- [49] J. Wang, W. Fu, D. Zhang, X. Yu, J. Li, and C. Wan, "Evaluation of novel alginate dialdehyde cross-linked chitosan/calcium polyphosphate composite scaffolds for meniscus tissue engineering," *Carbohydrate Polymers*, vol. 79, no. 3, pp. 705–710, 2010. DOI: <http://dx.doi.org/10.1016/j.carbpol.2009.09.026>.
- [50] Y. Wang, W. Peng, X. Liu, M. Zhu, T. Sun, Q. Peng, Y. Zeng, B. Feng, W. Zhi, J. Weng, and J. Wang, "Study of bilineage differentiation of human-bone-marrow-derived mesenchymal stem cells in oxidized sodium alginate/N-succinyl chitosan hydrogels and synergistic effects of RGD modification and low-intensity pulsed ultrasound," *Acta Biomaterialia*, vol. 10, no. 6, pp. 2518–2528, 2014. DOI: <http://dx.doi.org/10.1016/j.actbio.2013.12.052>.
- [51] I. M. N. Vold, "Periodate oxidised chitosans: structure and solution properties," PhD thesis, Norwegian University of Science and Technology, Trondheim Norway, Sep. 2004.
- [52] M. Fujihara, N. Iizima, I. Yamamoto, and T. Nagumo, "Purification and chemical and physical characterisation of an antitumour polysaccharide from the brown seaweed sargassum fulvellum," *Carbohydrate Research*, vol. 125, no. 1, pp. 97–106, 1984. DOI: [http://dx.doi.org/10.1016/0008-6215\(84\)85145-9](http://dx.doi.org/10.1016/0008-6215(84)85145-9).
- [53] N. Errington, S. Harding, K. Vrum, and L. Illum, "Hydrodynamic characterization of chitosans varying in degree of acetylation," *International Journal of Biological Macromolecules*, vol. 15, no. 2, pp. 113–117, 1993. DOI: [http://dx.doi.org/10.1016/0141-8130\(93\)90008-A](http://dx.doi.org/10.1016/0141-8130(93)90008-A).
- [54] A. Safronov and A. Zubarev, "Flory-huggins parameter of interaction in polyelectrolyte solutions of chitosan and its alkylated derivative," *Polymer*, vol. 43, no. 3, pp. 743–748, 2002, Mattice Special Issue. DOI: [http://dx.doi.org/10.1016/S0032-3861\(01\)00513-4](http://dx.doi.org/10.1016/S0032-3861(01)00513-4).
- [55] F. A. Simsek-Ege, G. M. Bond, and J. Stringer, "Polyelectrolyte complex formation between alginate and chitosan as a function of pH," *Journal of Applied Polymer Science*, vol. 88, no. 2, pp. 346–351, 2003. DOI: 10.1002/app.11989.

- [56] K. Saito and A. Tanioka, "Polyamphoteric membrane study: 1. potentiometric behaviour of succinyl chitosan aqueous solution," *Polymer*, vol. 37, no. 23, pp. 5117–5122, 1996. DOI: [http://dx.doi.org/10.1016/0032-3861\(96\)00335-7](http://dx.doi.org/10.1016/0032-3861(96)00335-7).
- [57] P. Ramirez, S. Maf, A. Tanioka, and K. Saito, "Modelling of membrane potential and ionic flux in weak amphoteric polymer membranes," *Polymer*, vol. 38, no. 19, pp. 4931–4934, 1997. DOI: [http://dx.doi.org/10.1016/S0032-3861\(96\)01090-7](http://dx.doi.org/10.1016/S0032-3861(96)01090-7).
- [58] J. Kielland, "Individual activity coefficients of ions in aqueous solutions," *Journal of the American Chemical Society*, vol. 59, no. 9, pp. 1675–1678, 1937. DOI: 10.1021/ja01288a032.
- [59] D. Patterson, "Free volume and polymer solubility. a qualitative view," *Macromolecules*, vol. 2, no. 6, pp. 672–677, 1969. DOI: 10.1021/ma60012a021.
- [60] Q. Z. Wang, X. G. Chen, N. Liu, S. X. Wang, C. S. Liu, X. H. Meng, and C. G. Liu, "Protonation constants of chitosan with different molecular weight and degree of deacetylation," *Carbohydrate Polymers*, vol. 65, no. 2, pp. 194–201, 2006. DOI: <http://dx.doi.org/10.1016/j.carbpol.2006.01.001>.
- [61] J. Mazur, A. Silberberg, and A. Katchalsky, "Potentiometric behavior of polyampholytes," *Journal of Polymer Science*, vol. 35, no. 128, pp. 43–70, 1959. DOI: 10.1002/pol.1959.1203512805.
- [62] A. Katchalsky and I. R. Miller, "Polyampholytes," *Journal of Polymer Science*, vol. 13, no. 68, pp. 57–68, 1954. DOI: 10.1002/pol.1954.120136805.
- [63] A. Katchalsky, S. Lifson, and J. Mazur, "The electrostatic free energy of polyelectrolyte solutions. i. randomly kinked macromolecules," *Journal of Polymer Science*, vol. 11, no. 5, pp. 409–423, 1953. DOI: 10.1002/pol.1953.120110503.
- [64] K. H. Bouhadir, D. S. Hausman, and D. J. Mooney, "Synthesis of cross-linked poly(aldehyde guluronate) hydrogels," *Polymer*, vol. 40, no. 12, pp. 3575–3584, 1999. DOI: [http://dx.doi.org/10.1016/S0032-3861\(98\)00550-3](http://dx.doi.org/10.1016/S0032-3861(98)00550-3).
- [65] K. Y. Lee, K. H. Bouhadir, and D. J. Mooney, "Degradation behavior of covalently cross-linked poly(aldehyde guluronate) hydrogels," *Macromolecules*, vol. 33, no. 1, pp. 97–101, 2000. DOI: 10.1021/ma991286z.
- [66] K. H. Bouhadir, G. M. Kruger, K. Y. Lee, and D. J. Mooney, "Sustained and controlled release of daunomycin from cross-linked poly(aldehyde guluronate) hydrogels," *Journal of Pharmaceutical Sciences*, vol. 89, no. 7, pp. 910–919, 2000. DOI: 10.1002/1520-6017(200007)89:7<910::AID-JPS8>3.0.CO;2-#.
- [67] K. H. Bouhadir, E. Alsberg, and D. J. Mooney, "Hydrogels for combination delivery of antineoplastic agents," *Biomaterials*, vol. 22, no. 19, pp. 2625–2633, 2001. DOI: [http://dx.doi.org/10.1016/S0142-9612\(01\)00003-5](http://dx.doi.org/10.1016/S0142-9612(01)00003-5).

- [68] K. Y. Lee, K. H. Bouhadir, and D. J. Mooney, “Controlled degradation of hydrogels using multi-functional cross-linking molecules,” *Biomaterials*, vol. 25, no. 13, pp. 2461–2466, 2004. DOI: <http://dx.doi.org/10.1016/j.biomaterials.2003.09.030>.
- [69] T. Ito, Y. Yeo, C. B. Highley, E. Bellas, C. A. Benitez, and D. S. Kohane, “The prevention of peritoneal adhesions by in situ cross-linking hydrogels of hyaluronic acid and cellulose derivatives,” *Biomaterials*, vol. 28, no. 6, pp. 975–983, 2007. DOI: <http://dx.doi.org/10.1016/j.biomaterials.2006.10.021>.
- [70] Y. Yeo, C. B. Highley, E. Bellas, T. Ito, R. Marini, R. Langer, and D. S. Kohane, “In situ cross-linkable hyaluronic acid hydrogels prevent post-operative abdominal adhesions in a rabbit model,” *Biomaterials*, vol. 27, no. 27, pp. 4698–4705, 2006. DOI: <http://dx.doi.org/10.1016/j.biomaterials.2006.04.043>.
- [71] T. Ito, I. P. Fraser, Y. Yeo, C. B. Highley, E. Bellas, and D. S. Kohane, “Anti-inflammatory function of an in situ cross-linkable conjugate hydrogel of hyaluronic acid and dexamethasone,” *Biomaterials*, vol. 28, no. 10, pp. 1778–1786, 2007. DOI: <http://dx.doi.org/10.1016/j.biomaterials.2006.12.012>.
- [72] X. Li, X. Kong, Z. Zhang, K. Nan, L. Li, X. Wang, and H. Chen, “Cytotoxicity and biocompatibility evaluation of n,o-carboxymethyl chitosan/oxidized alginate hydrogel for drug delivery application,” *International Journal of Biological Macromolecules*, vol. 50, no. 5, pp. 1299–1305, 2012. DOI: <http://dx.doi.org/10.1016/j.ijbiomac.2012.03.008>.
- [73] T. P. Martens, A. F. G. Godier, J. J. Parks, L. Q. Wan, M. S. Koeckert, G. M. Eng, B. I. Hudson, W. Sherman, and G. Vunjak-Novakovic, “Percutaneous cell delivery into the heart using hydrogels polymerizing in situ,” *Cell Transplant*, vol. 18, pp. 297–304, 2009. DOI: <http://dx.doi.org/10.3727/096368909788534915>.
- [74] S. Burke, *The composition and function of body fluids*. C.V.Mosby, 1972.
- [75] H. Wuhrmann, “Applicability of ion sensitive electrodes for measurements in blood,” *Biomedizinische Technik/Biomedical Engineering*, vol. 21, no. 1, pp. 191–192, 1977. DOI: [10.1515/bmte.1976.21.s1.191](https://doi.org/10.1515/bmte.1976.21.s1.191).
- [76] A. Covington and M. Ferra, “A pitzer mixed electrolyte solution theory approach to assignment of ph to standard buffer solutions,” *Journal of Solution Chemistry*, vol. 23, no. 1, pp. 1–10, 1994. DOI: [10.1007/BF00972604](https://doi.org/10.1007/BF00972604).
- [77] J. S. Hutchison, R. E. Ward, J. Lacroix, P. C. Hbert, M. A. Barnes, D. J. Bohn, P. B. Dirks, S. Doucette, D. Fergusson, R. Gottesman, A. R. Joffe, H. M. Kirpalani, P. G. Meyer, K. P. Morris, D. Moher, R. N. Singh, and P. W. Skippen, “Hypothermia therapy after traumatic brain injury in children,” *New England Journal of Medicine*, vol. 358, no. 23, pp. 2447–2456, 2008, PMID: 18525042. DOI: [10.1056/NEJMoa0706930](https://doi.org/10.1056/NEJMoa0706930).

- [78] J. J. Schmidt, J. Rowley, and H. J. Kong, “Hydrogels used for cell-based drug delivery,” *Journal of Biomedical Materials Research Part A*, vol. 87A, no. 4, pp. 1113–1122, 2008. DOI: 10.1002/jbm.a.32287.
- [79] K. Felgenhauer, “Protein size and cerebrospinal fluid composition,” English, *Klinische Wochenschrift*, vol. 52, no. 24, pp. 1158–1164, 1974. DOI: 10.1007/BF01466734.
- [80] K. B. Saunders and P. A. D’Amore, “An in vitro model for cell-cell interactions,” English, *In Vitro Cellular & Developmental Biology*, vol. 28A, no. 7/8, pp. 521–528, 1992.
- [81] B.-S. Kim, J. Nikolovski, J. Bonadio, and D. J. Mooney, “Cyclic mechanical strain regulates the development of engineered smooth muscle tissue,” *Nat Biotech*, vol. 17, no. 10, pp. 979–983, Oct. 1999. DOI: 10.1038/13671.
- [82] S. Levenberg, J. Rouwkema, M. Macdonald, E. S. Garfein, D. S. Kohane, D. C. Darland, R. Marini, C. A. van Blitterswijk, R. C. Mulligan, P. A. D’Amore, and R. Langer, “Engineering vascularized skeletal muscle tissue,” *Nat Biotech*, vol. 23, no. 7, pp. 879–884, Jul. 2005, Research.
- [83] F. Cilurzo, F. Selmin, P. Minghetti, M. Adami, E. Bertoni, S. Lauria, and L. Montanari, “Injectability evaluation: an open issue,” *AAPS PharmSciTech*, vol. 12, no. 2, pp. 604–609, 2011. DOI: 10.1208/s12249-011-9625-y.
- [84] O. Smidsrd and T. Painter, “Effect of periodate oxidation upon the stiffness of the alginate molecule in solution,” *Carbohydrate Research*, vol. 26, no. 1, pp. 125–132, 1973. DOI: [http://dx.doi.org/10.1016/S0008-6215\(00\)85029-6](http://dx.doi.org/10.1016/S0008-6215(00)85029-6).
- [85] Y. Kato, H. Onishi, and Y. Machida, “Depolymerization of N-succinyl-chitosan by hydrochloric acid,” *Carbohydrate Research*, vol. 337, no. 6, pp. 561–564, 2002. DOI: [http://dx.doi.org/10.1016/S0008-6215\(02\)00021-6](http://dx.doi.org/10.1016/S0008-6215(02)00021-6).
- [86] J. M. G. Martinho, M. Campos, M. Tencer, and M. A. Winnik, “Transient effects in intermolecular diffusion-controlled polymer-polymer reactions,” *Macromolecules*, vol. 20, no. 7, pp. 1582–1587, 1987. DOI: 10.1021/ma00173a025.
- [87] T. Freier, H. S. Koh, K. Kazazian, and M. S. Shoichet, “Controlling cell adhesion and degradation of chitosan films by n-acetylation,” *Biomaterials*, vol. 26, no. 29, pp. 5872–5878, 2005. DOI: <http://dx.doi.org/10.1016/j.biomaterials.2005.02.033>.
- [88] K. H. Bouhadir, K. Y. Lee, E. Alsberg, K. L. Damm, K. W. Anderson, and D. J. Mooney, “Degradation of partially oxidized alginate and its potential application for tissue engineering,” *Biotechnology Progress*, vol. 17, no. 5, pp. 945–950, 2001. DOI: 10.1021/bp010070p.

- [89] B. Wright, P. A. De Bank, K. A. Luetchford, F. R. Acosta, and C. J. Connon, "Oxidized alginate hydrogels as niche environments for corneal epithelial cells," *Journal of Biomedical Materials Research Part A*, vol. 102, no. 10, pp. 3393–3400, 2014. DOI: [10.1002/jbm.a.35011](https://doi.org/10.1002/jbm.a.35011).
- [90] Y. Kato, H. Onishi, and Y. Machida, "Evaluation of N-succinyl-chitosan as a systemic long-circulating polymer," *Biomaterials*, vol. 21, no. 15, pp. 1579–1585, 2000. DOI: [http://dx.doi.org/10.1016/S0142-9612\(00\)00044-2](http://dx.doi.org/10.1016/S0142-9612(00)00044-2).
- [91] Y. Kato, H. Onishi, and Y. Machida, "N-succinyl-chitosan as a drug carrier: water-insoluble and water-soluble conjugates," *Biomaterials*, vol. 25, no. 5, pp. 907–915, 2004. DOI: [http://dx.doi.org/10.1016/S0142-9612\(03\)00598-2](http://dx.doi.org/10.1016/S0142-9612(03)00598-2).
- [92] X. Zhang, X. Wang, V. Keshav, X. Wang, J. T. Johanas, G. G. Leisk, and D. L. Kaplan, "Dynamic culture conditions to generate silk-based tissue-engineered vascular grafts," *Biomaterials*, vol. 30, no. 19, pp. 3213–3223, 2009. DOI: <http://dx.doi.org/10.1016/j.biomaterials.2009.02.002>.
- [93] S. T. Wall, J. C. Walker, K. E. Healy, M. B. Ratcliffe, and J. M. Guccione, "Theoretical impact of the injection of material into the myocardium: a finite element model simulation," *Circulation*, vol. 114, no. 24, pp. 2627–2635, 2006. DOI: [10.1161/CIRCULATIONAHA.106.657270](https://doi.org/10.1161/CIRCULATIONAHA.106.657270).
- [94] J. F. Wenk, S. T. Wall, R. C. Peterson, S. L. Helgersson, H. N. Sabbah, M. Burger, N. Stander, M. B. Ratcliffe, and J. M. Guccione, "A method for automatically optimizing medical devices for treating heart failure: designing polymeric injection patterns," *Journal of biomechanical engineering*, vol. 131, no. 12, p. 121011, 2009. DOI: [10.1115/1.4000165](https://doi.org/10.1115/1.4000165).
- [95] D. M. Nelson, Z. Ma, K. L. Fujimoto, R. Hashizume, and W. R. Wagner, "Intramyocardial biomaterial injection therapy in the treatment of heart failure: materials, outcomes and challenges," *Acta Biomaterialia*, vol. 7, no. 1, pp. 1–15, 2011. DOI: <http://dx.doi.org/10.1016/j.actbio.2010.06.039>.
- [96] ASTM Standard F2450-10, *Standard guide for assessing microstructure of polymeric scaffolds for use in tissue-engineered medical products*, ASTM International, West Conshohocken, PA, www.astm.org, 2008. DOI: [10.1520/F2450-10](https://doi.org/10.1520/F2450-10).
- [97] Sigma Aldrich, *202371-1kg - poly(ethylene glycol) average Mn 300*, www.sigmaaldrich.com, May 2011.
- [98] Sigma Aldrich, *81365-1kg Mowiol 18-88, Mw ~130,000*, www.sigmaaldrich.com, May 2011.
- [99] Sigma Aldrich, *48723-500g-f - Gelatin Ph Eur*, www.sigmaaldrich.com, May 2011.
- [100] Sigma Aldrich, *PA2033-250g - Alginic acid sodium salt from brown algae medium viscosity*, www.sigmaaldrich.com, May 2011.
- [101] Sigma Aldrich, *448869-250g - Chitosan low molecular weight*, May 2011.

- [102] Sigma Aldrich, 53747–10g – *Hyaluronic acid sodium salt from streptococcus equi*, www.sigmaaldrich.com, May 2011.
- [103] Sigma Aldrich, F8630–25g – *Fibrinogen from bovine plasma type i-s, 65–85% protein ($\approx 75\%$ of protein is clottable)*, www.sigmaaldrich.com, May 2011.
- [104] E. Chemicals, Emd 234112-250mg – *Collagen, calf skin*, <http://www.emdchemicals.com>, May 2011.
- [105] GenWay, 1g, 15aa sequence, 90% pure, www.genwaybio.com, May 2011.
- [106] S. Vervoort, “Behaviour of hydrogels swollen in polymer solutions under mechanical action.” PhD thesis, École Nationale Supérieure des Mines de Paris, Paris, France, Sep. 2006.
- [107] A. E. English, S. Maf, J. A. Manzanares, X. Yu, A. Y. Grosberg, and T. Tanaka, “Equilibrium swelling properties of polyampholytic hydrogels,” *The Journal of Chemical Physics*, vol. 104, no. 21, 1996.
- [108] F. Oosawa, *Polyelectrolytes*. Marcel Dekker, Inc., 1971.
- [109] A. Katchalsky, Z. Alexandrowicz, and O. Kedem, “Polyelectrolyte solutions,” in *Chemical physics of ionic solutions*. B. E. Conway and R. G. Barradas, Eds., John Wiley and Sons, Inc., 1966, pp. 295–343. DOI: 10.1002/pol.1968.160061111.
- [110] J. Mark, *Physical Properties of Polymers*, ser. Physical Properties of Polymers. Cambridge University Press, 2004.
- [111] W. Hong, X. Zhao, J. Zhou, and Z. Suo, “A theory of coupled diffusion and large deformation in polymeric gels,” *Journal of the Mechanics and Physics of Solids*, vol. 56, no. 5, pp. 1779–1793, 2008. DOI: <http://dx.doi.org/10.1016/j.jmps.2007.11.010>.
- [112] K. Saito and A. Tanioka, “Ionic behaviour and membrane potential in weakly amphoteric polymer membranes,” *Polymer*, vol. 37, no. 12, pp. 2299–2302, 1996. DOI: [http://dx.doi.org/10.1016/0032-3861\(96\)85338-9](http://dx.doi.org/10.1016/0032-3861(96)85338-9).
- [113] A. E. English, T. Tanaka, and E. R. Edelman, “Polyampholytic hydrogel swelling transitions: limitations of the debye-hückel law,” *Macromolecules*, vol. 31, no. 6, pp. 1989–1995, 1998. DOI: 10.1021/ma971207o.
- [114] N. Gundogan, D. Melekaslan, and O. Okay, “Rubber elasticity of poly(n-isopropylacrylamide) gels at various charge densities,” *Macromolecules*, vol. 35, no. 14, pp. 5616–5622, 2002. DOI: 10.1021/ma020151h.
- [115] R. P. Gangadharan, “Polyampholyte hydrogel characteristics and detecting the bacterial interactions with these hydrogels using digital image processing methods.” PhD thesis, University of Tennessee, Knoxville, Tennessee, USA, May 2005.

- [116] Z. Alexandrowicz, "Calculation of the thermodynamic properties of polyelectrolytes in the presence of salt," *Journal of Polymer Science*, vol. 56, no. 163, pp. 97–114, 1962. DOI: 10.1002/pol.1962.1205616310.
- [117] Z. Alexandrowicz, "Osmotic and donnan equilibria in polyacrylic acid-sodium bromide solutions," *Journal of Polymer Science*, vol. 56, no. 163, pp. 115–132, 1962. DOI: 10.1002/pol.1962.1205616311.
- [118] Z. Alexandrowicz and A. Katchalsky, "Colligative properties of polyelectrolyte solutions in excess of salt," *Journal of Polymer Science Part A: General Papers*, vol. 1, no. 10, pp. 3231–3260, 1963. DOI: 10.1002/pol.1963.100011017.
- [119] A. Takahashi, N. Kato, and M. Nagasawa, "The osmotic pressure of polyelectrolyte in neutral salt solutions," *The Journal of Physical Chemistry*, vol. 74, no. 4, pp. 944–946, 1970. DOI: 10.1021/j100699a048.
- [120] K. S. Pitzer and G. Mayorga, "Thermodynamics of electrolytes. ii. activity and osmotic coefficients for strong electrolytes with one or both ions univalent," *The Journal of Physical Chemistry*, vol. 77, no. 19, pp. 2300–2308, 1973. DOI: 10.1021/j100638a009.
- [121] R. S. Koene, T. Nicolai, and M. Mandel, "Scaling relations for aqueous polyelectrolyte-salt solutions. 3. osmotic pressure as a function of molar mass and ionic strength in the semidilute regime," *Macromolecules*, vol. 16, no. 2, pp. 231–236, 1983. DOI: 10.1021/ma00236a015.
- [122] K. Pitzer, "Ion interaction approach: theory and data correlation," in *Activity Coefficients in Electrolyte Solutions*, K. Pitzer, Ed., CRC Press, 1991, pp. 75–154.
- [123] K. Arh, C. Pohar, and V. Vlachy, "Osmotic properties of aqueous ionene solutions," *The Journal of Physical Chemistry B*, vol. 106, no. 38, pp. 9967–9973, 2002. DOI: 10.1021/jp025858k.
- [124] J.-M. Y. Carrillo and A. V. Dobrynin, "Salt effect on osmotic pressure of polyelectrolyte solutions: simulation study," *Polymers*, vol. 6, no. 7, pp. 1897–1913, 2014.
- [125] A. V. Dobrynin, "Theory and simulations of charged polymers: from solution properties to polymeric nanomaterials," *Current Opinion in Colloid and Interface Science*, vol. 13, no. 6, pp. 376–388, 2008. DOI: <http://dx.doi.org/10.1016/j.cocis.2008.03.006>.
- [126] K. Binder, *Monte Carlo and Molecular Dynamics Simulations in Polymer Science*, ser. Topics in polymer science. Oxford University Press, 1995.
- [127] J. Zhang and G. Zografi, "Water vapor absorption into amorphous sucrose-poly(vinyl pyrrolidone) and trehalose-poly(vinyl pyrrolidone) mixtures," *Journal of Pharmaceutical Sciences*, vol. 90, no. 9, pp. 1375–1385, 2001. DOI: 10.1002/jps.1090.
- [128] L. Utracki, *Polymer Alloys and Blends: Thermodynamics and Rheology*. Hanser Gardner Publications, 1990.

- [129] J. Bockris and A. Reddy, *Modern Electrochemistry 1: Ionics*, ser. Modern Electrochemistry. Springer, 1998.
- [130] D. Oxtoby, H. Gillis, and N. Nachtrieb, *Principles of Modern Chemistry*. Saunders College Pub., 1999.
- [131] G. S. Manning, “Limiting laws and counterion condensation in polyelectrolyte solutions i. colligative properties,” *The Journal of Chemical Physics*, vol. 51, no. 3, 1969.
- [132] S. L. Clegg and M. Whitefield, “Activity coefficients in natural waters,” in *Activity Coefficients in Electrolyte Solutions*, K. Pitzer, Ed., pp. 279–434.
- [133] W. G. McMillan and J. E. Mayer, “The statistical thermodynamics of multicomponent systems,” *The Journal of Chemical Physics*, vol. 13, no. 7, 1945.
- [134] J. I. Partanen and P. O. Minkkinen, “Redetermination of the second dissociation constant of phosphoric acid and calculation of the pH values of the pH standards based on solutions of dihydrogen and hydrogen phosphate ions at 298.15 K,” *Acta Chemica Scandinavica*, vol. 50, pp. 1081–1086, 1996. DOI: 10.3891/acta.chem.scand.50-1081.
- [135] J. I. Partanen, Y. Mori, M. Louhi-Kultanen, and J. J. Kallas, “Activity coefficients of potassium dihydrogen phosphate in aqueous solutions at 25°C and in aqueous mixtures of urea and this electrolyte in the temperature range 20–35°C,” *Zeitschrift für Physikalische Chemie/International journal of research in physical chemistry and chemical physics.*, vol. 217, no. 6, pp. 723–738, 2003. DOI: 10.1524/zpch.217.6.723.20441.
- [136] B. O’Shaughnessy and Q. Yang, “Manning-Oosawa counterion condensation,” *Phys. Rev. Lett.*, vol. 94, p. 048302, 4 Feb. 2005. DOI: 10.1103/PhysRevLett.94.048302.
- [137] E. Trizac, L. Bocquet, and M. Aubouy, “Simple approach for charge renormalization in highly charged macroions,” *Phys. Rev. Lett.*, vol. 89, p. 248301, 24 Nov. 2002. DOI: 10.1103/PhysRevLett.89.248301.
- [138] R. N. Goldberg, N. Kishore, and R. M. Lennen, “Thermodynamic quantities for the ionization reactions of buffers,” *Journal of Physical and Chemical Reference Data*, vol. 31, no. 2, 2002.
- [139] H. Dong, H. Du, and X. Qian, “Prediction of pKa values for oligo-methacrylic acids using combined classical and quantum approaches,” *The Journal of Physical Chemistry B*, vol. 113, no. 39, pp. 12857–12859, 2009, PMID: 19739649. DOI: 10.1021/jp9060889.
- [140] F. G. Donnan, “Theory of membrane equilibria and membrane potentials in the presence of non-dialysing electrolytes. a contribution to physical-chemical physiology,” *Journal of Membrane Science*, vol. 100, no. 1, pp. 45–55, 1995. DOI: [http://dx.doi.org/10.1016/0376-7388\(94\)00297-C](http://dx.doi.org/10.1016/0376-7388(94)00297-C).

- [141] S. Sarkar, A. K. SenGupta, and P. Prakash, "The donnan membrane principle: opportunities for sustainable engineered processes and materials," *Environmental Science & Technology*, vol. 44, no. 4, pp. 1161–1166, 2010, PMID: 20092307. DOI: 10.1021/es9024029.
- [142] M. Friedman, *Principles and Models of Biological Transport*. Springer, 2008.
- [143] O. Söhnel and P. Novotný, *Densities of aqueous solutions of inorganic substances*, ser. Physical sciences data. Elsevier, 1985.
- [144] R. Dulbecco and M. Vogt, "Plaque formation and isolation of pure lines with poliomyelitis viruses," *The Journal of Experimental Medicine*, vol. 99, no. 2, pp. 167–182, 1954. DOI: 10.1084/jem.99.2.167.
- [145] J. G. Kirkwood and F. H. Westheimer, "The electrostatic influence of substituents on the dissociation constants of organic acids. i," *The Journal of Chemical Physics*, vol. 6, no. 9, pp. 506–512, 1938. DOI: <http://dx.doi.org/10.1063/1.1750302>.
- [146] A. C. Ribeiro, M. A. Estes, V. M. Lobo, H. D. Burrows, A. M. Amado, A. M. A. da Costa, A. J. Sobral, E. F. Azevedo, and M. A. Ribeiro, "Mean distance of closest approach of ions: sodium salts in aqueous solutions," *Journal of Molecular Liquids*, vol. 128, no. 1-3, pp. 134–139, 2006. DOI: <http://dx.doi.org/10.1016/j.molliq.2005.12.004>.
- [147] G. Jones, "Intercellular adhesion: modification by dielectric properties of the medium," English, *The Journal of Membrane Biology*, vol. 16, no. 1, pp. 297–312, 1974. DOI: 10.1007/BF01872420.
- [148] Z. Aiping, C. Tian, Y. Lanhua, W. Hao, and L. Ping, "Synthesis and characterization of N-succinyl-chitosan and its self-assembly of nanospheres," *Carbohydrate Polymers*, vol. 66, no. 2, pp. 274–279, 2006. DOI: <http://dx.doi.org/10.1016/j.carbpol.2006.03.014>.
- [149] S. Sun and A. Wang, "Adsorption properties of N-succinyl-chitosan and cross-linked N-succinyl-chitosan resin with Pb(II) as template ions," *Separation and Purification Technology*, vol. 51, no. 3, pp. 409–415, 2006. DOI: <http://dx.doi.org/10.1016/j.seppur.2006.03.004>.
- [150] J. Hornack, *The basics of nmr iii*, <https://www.cis.rit.edu/htbooks/nmr/bnmr.htm>, Magnetic Resonance Laboratory, Center for Imaging Science, Rochester Institute of Technology, Rochester, NY 14623-5604, 1999.
- [151] H. E. Gottlieb, V. Kotlyar, and A. Nudelman, "Nmr chemical shifts of common laboratory solvents as trace impurities," *The Journal of Organic Chemistry*, vol. 62, no. 21, pp. 7512–7515, 1997, PMID: 11671879. DOI: 10.1021/jo971176v.
- [152] A. Hirai, H. Odani, and A. Nakajima, "Determination of degree of deacetylation of chitosan by 1h nmr spectroscopy," English, *Polymer Bulletin*, vol. 26, no. 1, pp. 87–94, 1991. DOI: 10.1007/BF00299352.

- [153] M. Lavertu, Z. Xia, A. Serreqi, M. Berrada, A. Rodrigues, D. Wang, M. Buschmann, and A. Gupta, "A validated 1h {nmr} method for the determination of the degree of deacetylation of chitosan," *Journal of Pharmaceutical and Biomedical Analysis*, vol. 32, no. 6, pp. 1149–1158, 2003. DOI: [http://dx.doi.org/10.1016/S0731-7085\(03\)00155-9](http://dx.doi.org/10.1016/S0731-7085(03)00155-9).
- [154] C. Zhang, Q. Ping, H. Zhang, and J. Shen, "Synthesis and characterization of water-soluble o-succinyl-chitosan," *European Polymer Journal*, vol. 39, no. 8, pp. 1629–1634, 2003. DOI: [http://dx.doi.org/10.1016/S0014-3057\(03\)00068-5](http://dx.doi.org/10.1016/S0014-3057(03)00068-5).
- [155] C. Zhang, Q. Ping, Y. Ding, Y. Cheng, and J. Shen, "Synthesis, characterization, and microsphere formation of galactosylated chitosan," *Journal of Applied Polymer Science*, vol. 91, no. 1, pp. 659–665, 2004. DOI: [10.1002/app.13232](http://dx.doi.org/10.1002/app.13232).
- [156] ASTM Standard F2260-03 (2008), *Standard test method for determining degree of deacetylation in chitosan salts by proton nuclear magnetic resonance (¹H NMR) spectroscopy*, ASTM International, West Conshohocken, PA, www.astm.org, 2008. DOI: [10.1520/F2260-03R12E01](http://dx.doi.org/10.1520/F2260-03R12E01).
- [157] Y Shigemasa, H Usui, M Morimoto, H Saimoto, Y Okamoto, S Minami, and H Sashiwa, "Chemical modification of chitin and chitosan 1: preparation of partially deacetylated chitin derivatives via a ring-opening reaction with cyclic acid anhydrides in lithium chloride/n,n-dimethylacetamide," *Carbohydrate Polymers*, vol. 39, no. 3, pp. 237–243, 1999. DOI: [http://dx.doi.org/10.1016/S0144-8617\(99\)00007-7](http://dx.doi.org/10.1016/S0144-8617(99)00007-7).
- [158] C. Yan, D. Chen, J. Gu, H. Hu, X. Zhao, and M. Qiao, "Preparation of N-succinyl-chitosan and their physical-chemical properties as a novel excipient," *Yakugaku Zasshi*, vol. 126, no. 9, pp. 789–793, 2006. DOI: [10.1248/yakushi.126.789](http://dx.doi.org/10.1248/yakushi.126.789).
- [159] G. Q. Ying, H. Yang, Y. Yi, and F. Xu, "Relationships between the molecular structure and moisture-absorption and moisture-retention abilities of succinyl chitosan," English, *Polymer Bulletin*, vol. 59, no. 4, pp. 509–516, 2007. DOI: [10.1007/s00289-007-0790-9](http://dx.doi.org/10.1007/s00289-007-0790-9).
- [160] J. P. Soares, J. E. Santos, G. O. Chierice, and E. T. G. Cavaleiro, "Thermal behavior of alginic acid and its sodium salt," *Ecl. Qum., So Paulo*, vol. 29, pp. 53–56, 2004.
- [161] M. Pikal, S. Shah, M. Roy, and R. Putman, "The secondary drying stage of freeze drying: drying kinetics as a function of temperature and chamber pressure," *International Journal of Pharmaceutics*, vol. 60, no. 3, pp. 203–207, 1990. DOI: [http://dx.doi.org/10.1016/0378-5173\(90\)90074-E](http://dx.doi.org/10.1016/0378-5173(90)90074-E).
- [162] Z. Ping, Q. Nguyen, S. Chen, J. Zhou, and Y. Ding, "States of water in different hydrophilic polymers – dsc and ftir studies," *Polymer*, vol. 42, pp. 8461–8467, 2001.
- [163] W. K. Lewis, "The rate of drying of solid materials," *Journal of Industrial & Engineering Chemistry*, vol. 13, no. 5, pp. 427–432, 1921. DOI: [10.1021/ie50137a021](http://dx.doi.org/10.1021/ie50137a021).

- [164] ASTM Standard D570-98 (2010)e1, *Standard test method for water absorption of plastics*, ASTM International, West Conshohocken, PA, www.astm.org, 2010. DOI: 10.1520/D0570-98R10E01.
- [165] ASTM Standard D6980-12, *Standard test method for determination of moisture in plastics by loss in weight*, ASTM International, West Conshohocken, PA, www.astm.org, 2012. DOI: 10.1520/D6980-12.
- [166] ASTM Standard F2259-03 (2008), *Standard test method for determining the chemical composition and sequence in alginate by proton nuclear magnetic resonance (1H NMR) spectroscopy*, ASTM International, West Conshohocken, PA, www.astm.org, 2008. DOI: 10.1520/F2259-03R08.
- [167] D. Montgomery, *Design and Analysis of Experiments, 6th Ed.* Jon Wiley and Sons, INC., 2005.
- [168] F. M. White, *Fluid Mechanics, 5th Ed.* McGraw Hill, 2003.
- [169] Eshelman School of Pharmacy, University of North Carolina at Chapel Hill, *The pharmaceuticals and compounding laboratory: sterile compounding, injection dependent routes*, <http://pharmlabs.unc.edu/labs/parenterals/dependent.htm>, Chapel Hill, NC, United States, Dec. 2013.
- [170] TA Instruments: Rheology Applications Note, *RN014 - the principles and applications of the Cox-Merz rule*, 1998.
- [171] R. McKennell, "Cone-plate viscometer: comparison with coaxial cylinder viscometer," *Analytical Chemistry*, vol. 28, pp. 297-304, 1956. DOI: <http://dx.doi.org/10.1021/ac60119a021>.
- [172] M. E. Fewell and J. D. Hellums, "The secondary flow of newtonian fluids in cone and plate viscometers," *Transactions of The Society of Rheology (1957-1977)*, vol. 21, no. 4, 1977.
- [173] *DV2T Viscometer Operating Instructions M13-167*, BROOKFIELD, 2013.
- [174] *DV3T Rheometer Operating Instructions M13-2100*, BROOKFIELD, 2013.
- [175] F. Incropera and D. Dewitt, *Fundamentals of Heat and Mass Transfer 5th ed.* John Wiley and Sons, 2002.
- [176] Q.-H. Nguyen and N.-D. Nguyen, "Incompressible non-newtonian fluid flows," in *Continuum Mechanics - Progress in Fundamentals and Engineering Applications*, Y. Gan, Ed., InTech, 2012, pp. 47-72. DOI: 10.5772/26091.
- [177] *GenieTouch Syringe Pump Users Guide Version 1.00*, Kent Scientific, Feb. 2012.
- [178] D. C. Hoaglin and R. E. Welsch, "The hat matrix in regression and anova," *The American Statistician*, vol. 32, no. 1, pp. 17-22, 1978. DOI: 10.1080/00031305.1978.10479237.

- [179] G. P. Association, *Physical Properties of Glycerine and Its Solutions*. Glycerine Producers' Association, 1963.
- [180] J. B. Segur and H. E. Oberstar, "Viscosity of glycerol and its aqueous solutions," *Industrial & Engineering Chemistry*, vol. 43, no. 9, pp. 2117–2120, 1951. DOI: 10.1021/ie50501a040.
- [181] ASTM Standard E928-08, *Standard test method for purity by differential scanning calorimetry*, ASTM International, West Conshohocken, PA, www.astm.org, 2008. DOI: 10.1520/E0928-08.
- [182] S. C. MARVEL and M. V. KEPLER, "A simple membrane osmometer system & experiments that quantitatively measure osmotic pressure," *THE AMERICAN BIOLOGY TEACHER*, vol. 71, pp. 355–362, 2009.
- [183] A. T. Hansen, "A self-recording electronic osmometer for quick, direct measurement of colloid osmotic pressure in small samples," *Acta Physiologica Scandinavica*, vol. 53, no. 3-4, pp. 197–213, 1961. DOI: 10.1111/j.1748-1716.1961.tb02278.x.
- [184] C. Dessy and K.-D. Bures, *A new membrane osmometry detector for GPC*.
- [185] B. H. Zimm and I. Myerson, "A convenient small osmometer," *Journal of the American Chemical Society*, vol. 68, no. 5, pp. 911–912, 1946. DOI: 10.1021/ja01209a509.
- [186] R. M. Fuoss and D. J. Mead, "Osmotic pressures of polyvinyl chloride solutions by a dynamic method," *The Journal of Physical Chemistry*, vol. 47, no. 1, pp. 59–70, 1943. DOI: 10.1021/j150424a008.
- [187] D. M. French and R. H. Ewart, "Molecular weight of GR-S fractions," *Analytical Chemistry*, vol. 19, no. 3, pp. 165–167, 1947. DOI: 10.1021/ac60003a010.
- [188] G. Hanks and S. Weissberg, "A convenient small osmometer," *Journal of Research of the National Bureau of Standards*, vol. 49, no. 6, pp. 393–369, 1952. DOI: 10.6028/jres.049.042.
- [189] J. V. Stabin and E. H. Immergut, "A high-speed glass osmometer," *Journal of Polymer Science*, vol. 14, no. 74, pp. 209–212, 1954. DOI: 10.1002/pol.1954.120147407.
- [190] P. T. Gilbert, "Osmometer," Patent 3 635 075, Jan. 1972.
- [191] C. A. Wiederhielm, D. R. Lee, and D. D. Stromberg, "A membrane osmometer for microliter samples," *Journal of Applied Physiology*, vol. 35, no. 3, pp. 432–435, 1973.
- [192] K. Aukland and H. M. Johnsen, "A colloid osmometer for small fluid samples," *Acta Physiologica Scandinavica*, vol. 90, no. 2, pp. 485–490, 1974. DOI: 10.1111/j.1748-1716.1974.tb05611.x.

- [193] A. Grattoni, G. Canavese, F. M. Montevecchi, and M. Ferrari, “Fast membrane osmometer as alternative to freezing point and vapor pressure osmometry,” *Analytical Chemistry*, vol. 80, no. 7, pp. 2617–2622, 2008, PMID: 18315010. DOI: 10.1021/ac7023987.
- [194] J. E. Shiley, C. R. Mischke, and R. G. Budynas.
- [195] S. Hansen, “Leaks: the good, the bad and the ugly: what leaks are, how to classify and size them, and how to make useful leaks.,” *the Bell Jar*, vol. 7, no. 1, pp. 1–8, 1998.
- [196] Y. Kawashima, K. Murai, and T. Hosokawa, “A study on flow patterns and fluid mixing for water purification in a rectangular water tank,” in *Proc. Second International Conference on CFD in the Minerals and Process Industries*, CSIRO, Melbourne, Australia, Dec. 1999, pp. 119–122.
- [197] E. Wilhelm, R. Battino, and R. J. Wilcock, “Low-pressure solubility of gases in liquid water,” *Chemical Reviews*, vol. 77, no. 2, pp. 219–262, 1977. DOI: 10.1021/cr60306a003.
- [198] C. L. Yaws, P. K. Narasimhan, and C. Gabbula, *Yaws’ Handbook of Antoine Coefficients for Vapor Pressure (2nd Electronic Edition)*. Knovel, 2009, [E-book].
- [199] F. Seglenieks, *UW weather station data archives*, <http://weather.uwaterloo.ca/data.html>, Waterloo, Ontario, Canada, Feb. 2013.
- [200] R. Battino, T. R. Rettich, and T. Tominaga, “The solubility of nitrogen and air in liquids,” *Journal of Physical and Chemical Reference Data*, vol. 13, no. 2, 1984.
- [201] H. Ochiai, Y. Fujino, Y. Tadokoro, and I. Murakami, “The partial specific volume and preferential interactions of poly (vinyl alcohol) in aqueous borax solutions,” *Polymer Journal*, vol. 13, no. 4, pp. 351–356, 1981.
- [202] K. Nakanishi and M. Kurata, “Density measurement in dilute aqueous solution of polyvinyl alcohol,” *Bulletin of the Chemical Society of Japan*, vol. 33, no. 2, pp. 152–157, 1960. DOI: 10.1246/bcsj.33.152.
- [203] N. A. Peppas and E. W. Merrill, “Determination of interaction parameter 1, for poly(vinyl alcohol) and water in gels crosslinked from solutions,” *Journal of Polymer Science: Polymer Chemistry Edition*, vol. 14, no. 2, pp. 459–464, 1976. DOI: 10.1002/pol.1976.170140216.
- [204] S. Saxena, *61st JECFA - polyvinyl alcohol (PVA) chemical and technical assessment (CTA)*, 2004.
- [205] W. G. Martin, W. H. Cook, and C. A. Winkler, “The determination of partial specific volumes by differential sedimentation,” *Canadian Journal of Chemistry*, vol. 34, no. 6, pp. 809–814, 1956. DOI: 10.1139/v56-104.

- [206] ASTM Standard ASTM E542-01 (2007), *Standard practice for calibration of laboratory volumetric apparatus*, ASTM International, West Conshohocken, PA, www.astm.org, 2007. DOI: 10.1520/E0542-01R07.
- [207] ASTM Standard ASTM E288-10, *Standard specification for laboratory glass volumetric flasks*, ASTM International, West Conshohocken, PA, www.astm.org, 2010. DOI: 10.1520/E0288-10.
- [208] L. Masaro and X. Zhu, “Physical models of diffusion for polymer solutions, gels and solids,” *Progress in Polymer Science*, vol. 24, no. 5, pp. 731–775, 1999. DOI: [http://dx.doi.org/10.1016/S0079-6700\(99\)00016-7](http://dx.doi.org/10.1016/S0079-6700(99)00016-7).
- [209] J. Yoon, S. Cai, Z. Suo, and R. C. Hayward, “Poroelastic swelling kinetics of thin hydrogel layers: comparison of theory and experiment,” *Soft Matter*, vol. 6, pp. 6004–6012, 23 2010. DOI: 10.1039/C0SM00434K.
- [210] ASTM Standard D1621-10, *Standard test method for compressive properties of rigid cellular plastics*, ASTM International, West Conshohocken, PA, www.astm.org, 2010. DOI: 10.1520/D1621-10.
- [211] ASTM Standard D5024-07, *Standard test method for plastics: dynamic mechanical properties: in compression*, ASTM International, West Conshohocken, PA, www.astm.org, 2007. DOI: 10.1520/D5024-07.
- [212] M. Rubinstein, R. H. Colby, A. V. Dobrynin, and J.-F. Joanny, “Elastic modulus and equilibrium swelling of polyelectrolyte gels,” *Macromolecules*, vol. 29, no. 1, pp. 398–406, 1996. DOI: 10.1021/ma9511917.